

Decomposition of multicomponent ocean-bottom data into P- and S-waves

Proefschrift

ter verkrijging van de graad van doctor
aan de Technische Universiteit Delft,
op gezag van de Rector Magnificus prof. ir. K. F. Wakker,
voorzitter van het College voor Promoties,
in het openbaar te verdedigen
op dinsdag 13 november 2001 om 16:00 uur

door

Karin Margriet SCHALKWIJK

doctorandus in de geofysica
geboren te San Diego, Verenigde Staten van Amerika



Dit proefschrift is goedgekeurd door de promotoren:

Prof. dr. ir. C.P.A. Wapenaar

Prof. dr. ir. A.J. Berkhout

Toegevoegd promotor:

Dr. ir. D.J. Verschuur

Samenstelling Promotiecommissie:

Rector Magnificus,	voorzitter
Prof. dr. ir. C.P.A. Wapenaar,	Technische Universiteit Delft, promotor
Prof. dr. ir. A.J. Berkhout,	Technische Universiteit Delft, promotor
Dr. ir. D.J. Verschuur,	Technische Universiteit Delft, toegevoegd promotor
Prof. dr. ir. A. Gisolf,	Technische Universiteit Delft
Prof. dr. ir. J.T. Fokkema,	Technische Universiteit Delft
Prof. dr. W. Spakman,	Universiteit Utrecht
Dr. L. Amundsen,	Statoil/University of Trondheim, Noorwegen

ISBN 90-9015261-X

Copyright ©2001, by K.M. Schalkwijk, Delft University of Technology, Delft, The Netherlands.

All rights reserved. No part of this publication may be reproduced, stored in a retrieval system or transmitted in any form or by any means, electronic, mechanical, photocopying, recording or otherwise, without the prior written permission of the author K.M. Schalkwijk, Delft University of Technology, Faculty of Applied Sciences, P.O. Box 5046, 2600 GA Delft, The Netherlands.

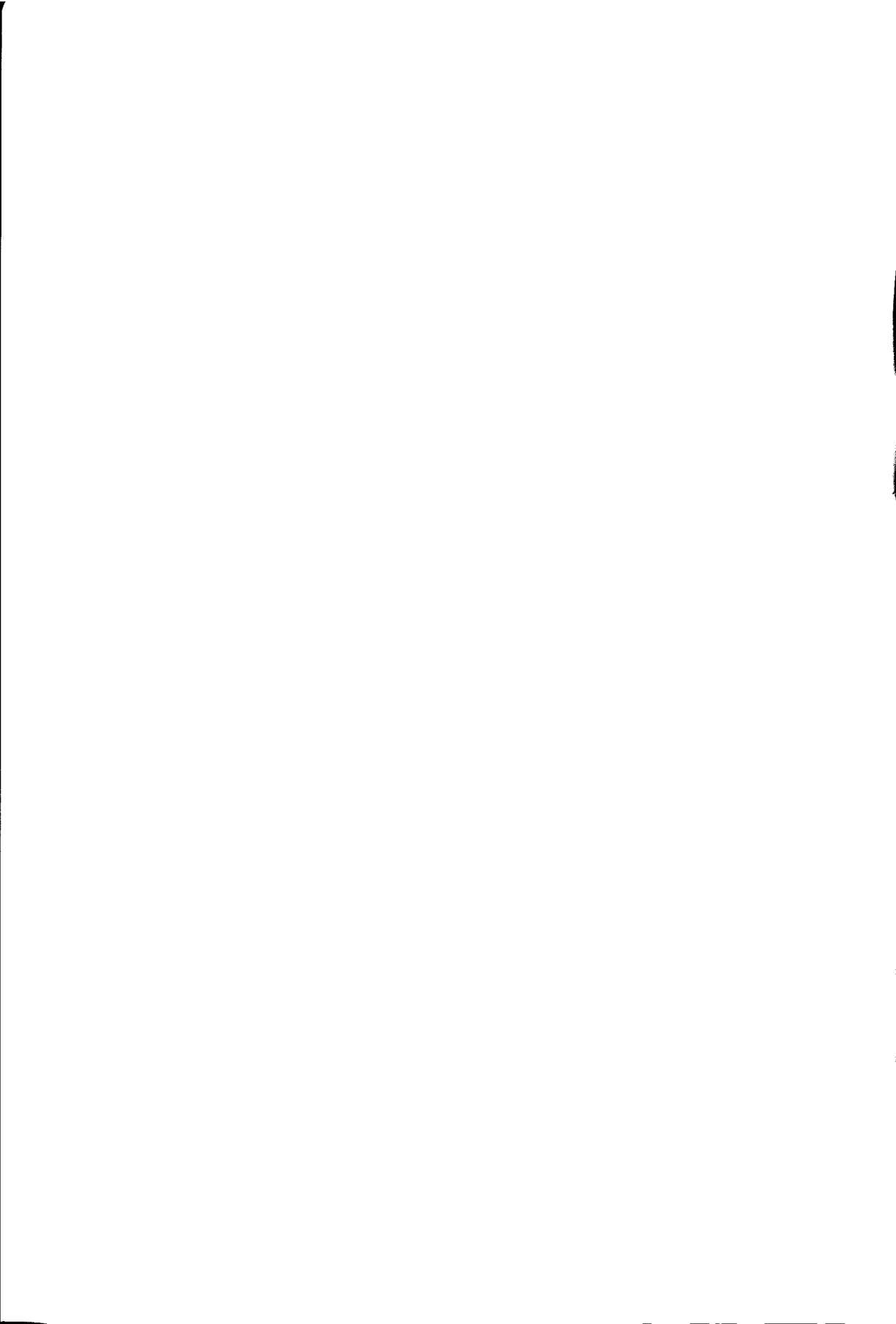
SUPPORT

The research for this thesis was financially supported by the DELPHI consortium.

Typesetting system: L^AT_EX

Printed in The Netherlands by: DocVision BV. Technische Universiteit Delft.

*I don't know where I'm going
but I'm not lost.*



Preface

I chose to apply wavefield decomposition to multicomponent ocean-bottom data by the fact that it was a more practically oriented research, and because of the presence of the word *ocean* in the subject. Application of an existing theoretical framework to field data was not so straightforward as it appeared at first. But the satisfaction when step by step things started to work on field data more than made up for the difficult times.

In the first place I would like to thank my promoter Prof. Kees Wapenaar, for his continuous encouragement and advice. I also greatly appreciate the thoroughness of the proofreading for this thesis, and the fact that I could always come in for discussions and questions. The same is true for my copromoter Eric Verschuur, who would not hesitate to help when every tactic seemed to fail on field data; Eric would always suggest yet another option. Also his generous help with Chapter 5 of this thesis is gratefully acknowledged. The theoretical framework and software on wavefield decomposition already available from Kees, Eric and Philippe Herrmann gave me a big headstart into this research.

I am greatly indebted to my other promoter Prof. Berkhouit for the opportunity to be part of the DELPHI consortium. I have enjoyed working within the DELPHI team.

Through the different sponsoring companies, I had never any lack of data. I would like to mention SAGA Petroleum and BP Amoco for providing me with the OBC data I have used in this research. I would like to thank Schlumberger Geco-Prakla and especially Richard Bale and Dave Allen for inviting me over for a summer internship. I greatly appreciated working with them and value their input and ideas over my research. I thank prof. Ursin for his hospitality during my visit to the University of Trondheim in Norway, and Lasse Amundsen and Are Osen of Statoil for kindly sharing with me their earlier work on wavefield decomposition. During my time in Delft I have been able to visit several more companies and present my work, I thank SAGA Petroleum (Oslo), Amoco (New Orleans) and Chevron (La Habra) for their interest and hospitality. And finally I would like to thank all the

sponsors with whom I have spoken at the sponsormeetings and conferences for their input and just in general for a good time.

The positive experience of team work, depends of course on the people making up the team. I know I have been very lucky with my present and former colleagues. I would like to thank the old division, Riaz Alá'i, Frank Dessing, Maurits van der Heiden, Felix Herrmann, Nurul Kabir, Alexander Koek, Jan Thorbecke, Frederic Verhelst, and Aart-Jan van Wijngaarden for their kind acceptance and for initiating me into sponsormeeting procedures and other kind of DELPHI peculiarities. I thank my present colleagues John Bolte, Barbara Cox, Ewoud van Dedem, Kees Hindriks, Remco Romijn, Arno Volker and Paul Zwartjes for the great working atmosphere. And though not current members of the group anymore, I should not forget to mention Jeroen Goudswaard and Johan Vos.

I would especially like to thank Ewoud van Dedem for discussions on surface related multiple elimination which led to the figure on page 149, Kees Hindriks for helping to make the 3-D MATLAB picture on page 120, Remco Romijn for helping with the processing for the stacked and the poststack time migrated sections in Chapter 4, and Johan Vos for discussions on optimization and for taking the time to proofread the thesis.

Besides doing a decomposition of wavefields I have also had to do a decomposition of time over my other interests and social activities. My horse Jet has received by far the greatest part of this decomposed time. Giuseppe, my parents, brother and sisters had to share the rest. My parents have been a source of inspiration and have always encouraged me to follow my interests. They have also provided me with the main tools for completing a Ph.D. research: mathematics, public speaking and ten-finger blind typing. Without all the help and support of Giuseppe, I would not have been able to do all the things I am doing.

Contents

Preface	vii
1 Introduction	1
1.1 History	1
1.2 Acoustic versus elastic data processing	3
1.3 Wavefield decomposition methods	4
1.4 Outline of this thesis	6
2 Wavefield decomposition: theoretical aspects	9
2.1 Relations between two-way and one-way wavefields	12
2.1.1 Acoustic case	12
2.1.2 Elastic case	16
2.1.3 Special case ($k_y = 0$)	27
2.2 Wavefield decomposition for the special case of ocean-bottom data .	28
2.2.1 Acoustic wavefield vectors and composition/decomposition operators	29
2.2.2 Synthetic data	30
2.2.3 Elastic wavefield vectors and composition/decomposition operators	32
2.3 Wavefield decomposition in two steps	35

2.4	An adaptive decomposition scheme	38
2.4.1	Frequency independent inversion of $\tilde{F}(p)$	50
2.5	Combined extrapolation/decomposition operators	53
2.5.1	Analytic expression for $\tilde{F}(p, \omega)$: forward model with thin layer	54
2.5.2	Frequency-dependent inversion	57
2.6	Incorporation of a thin layer in the adaptive decomposition scheme .	59
2.7	Limitations in the application of the decomposition operators.	63
3	Wavefield decomposition: practical aspects for the deep to medium-depth ocean-bottom	67
3.1	A deep ocean-bottom example: Vørting	67
3.2	Comparison before and after decomposition	74
3.3	A medium-depth ocean-bottom example: Snorre	77
3.4	Comparison before and after decomposition	83
3.5	Application of the adaptive decomposition scheme to the 2-D line . .	85
3.5.1	Choosing optimization windows	88
3.5.2	Decomposition results for all common receiver gathers	89
3.6	Conclusions	90
4	Wavefield decomposition: practical aspects for the shallow ocean-bottom	95
4.1	A shallow ocean-bottom example: Mahogany	95
4.2	Decomposition of one common-receiver gather	104
4.3	Application to part of the 2-D data	116
4.4	Estimation of the medium parameters	117
4.4.1	Importance of medium parameters in total decomposition scheme	127
4.4.2	Inversion strategy for Mahogany	128
4.5	Comparison before and after decomposition	130
4.6	Conclusions	138

5	Multiple elimination for ocean-bottom data	143
5.1	Theory of multiple elimination for OBS data	144
5.1.1	Matrix notation for discretized wavefields	144
5.1.2	Forward model for surface data	145
5.1.3	Multiple elimination for surface data	146
5.1.4	Adaptive iterative multiple elimination for ocean-bottom data	147
5.2	Multiple elimination: synthetic data example	149
5.3	Multiple elimination: Mahogany field dataset	154
5.4	Conclusions	155
6	Conclusions and discussion	161
6.1	Conclusions	161
6.2	Discussion and recommendations	165
A	Elastic two-way wavefield extrapolation operator	169
Bibliography		171
Summary		175
Samenvatting		177
Curriculum vitae		179

Chapter 1

Introduction

1.1 History

In conventional seismic exploration, typically a source at or just below the Earth's surface emits a sound wavefield which propagates into the subsurface, where the wavefield is reflected upwards again by layering and structures beneath the surface. The reflected wavefield is then recorded at the surface by geophones or hydrophones (when recording is done on land or in water, respectively). The recorded data have to be processed to obtain an image of the Earth's structures beneath the surface. In this way, for example, oil and gas reservoirs can be found and evaluated.

As the earth is an elastic medium, waves propagating through it are described by the elastic wave equation. In elastic media two types of waves can propagate: longitudinal (P-) and transversal (S-) waves. These waves can convert from one to the other due to inhomogeneities in the earth. To quantify the *elastic* wave motion, it has to be measured in three orthogonal directions at each measuring location (as it is a vector wavefield). And to excite the total elastodynamic earth's response, ideally three-component sources should be used as well. In practice, often only the P-waves are used, other types of waves are then regarded as noise. However, this does not mean that the P-waves can be described by the acoustic wave equation (as for example the elastic P reflection and transmission coefficients at the layers have to be taken into account). The most basic description (i.e. making few *a priori* assumptions) of the seismic experiment is given by a wavefield propagating downwards, which is reflected back upwards at a certain point and then propagates upwards to where it is measured. In Figure 1.1 this process is illustrated in a schematic way (introduced by Berkhout, 1982). The data **P** contains all possible elastic waves, where the sources are arranged in the horizontal direction and the receivers in the vertical direction. The data is generated by a source **S**, two propagation operators **W** and a reflection operator **R**. The data represented by the matrix **P** can be divided in four

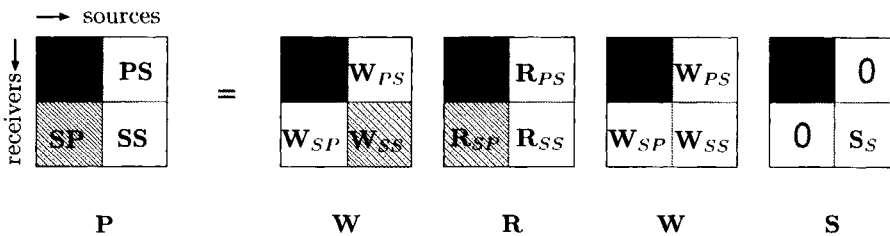


Fig. 1.1 Description of the seismic experiment in terms of matrices (see Berkhouit, 1982; Wapenaar and Berkhouit, 1989, for respectively the acoustic and the full elastic situation).

parts, each part is labeled with the wavetype it contains, where the first character denotes the wavetype at the receiver and the second character the wavetype emitted by the source. In the same way the reflection, propagation and source matrices can be divided, where the matrix \mathbf{R}_{PP} represents for each reflection point the reflection operator of the P-waves, the matrix \mathbf{R}_{SS} represents for each reflection point the reflection operator of the S-waves etc. Note that in practice there are no pure P- and S-wave sources, neither are there pure P- and S-wave receivers, the situation as depicted in Figure 1.1 can be obtained after a wavefield decomposition (Wapenaar et al., 1990).

If only “pure” P-waves are taken into account, just the black part of the matrices in Figure 1.1 is used. This means that only P-wave propagation is considered (kinematics) while elastic reflection effects can be taken into account (dynamics). By also accounting for the S-waves (i.e. the other three parts of the matrix), additional information about the Earth’s subsurface can be obtained. In earthquake seismology, S-wave recordings were already used to infer information about the earth’s interior at a larger scale. The use of S-waves (together with P-waves) in seismic exploration has developed much slower, due to technological difficulties like the development of effective S-wave sources, the increase in size of the recorded data, and the more complex and therefore expensive acquisition of the data. Moreover, the use of S-waves adds additional complexity to the processing of the data, and the necessity of developing new processing methods.

A hybrid data acquisition method, in between the acoustic single component recording and the elastic three-component source and three-component receiver acquisition, is the ocean-bottom data acquisition. With ocean-bottom acquisition, a source, just below the sea-surface, towed behind a boat, emits a pressure wavefield into the water. This pressure wavefield propagates through the water into the subsurface where

the wavefield is reflected upwards again by the ocean-bottom and structures beneath it. The wavefield is recorded by multicomponent geophones at the ocean-bottom. A commonly used method of ocean-bottom acquisition utilises geophones fastened at regular intervals on a long cable which is laid at the bottom; therefore data acquired at the ocean-bottom are often called OBC (ocean-bottom cable) data. Contrary to conventional marine seismic data acquisition, where the (acoustic) wavefield is recorded by hydrophones floating just below the water surface behind a boat, in the case of OBC data the elastic wavefield can be recorded. Usually, the acoustic pressure is also measured by hydrophones coincident with the three-component geophones (which is also called 4C(omponent) OBC data). From these 4 components the total wavefield can be reconstructed. As the source is in the water, it will emit only P-waves. Therefore, the S-waves as recorded by the ocean-bottom geophones have always been converted from P-waves somewhere along the propagation path and therefore are also called converted waves or C-waves. In Figure 1.1 the shaded square denotes the data that is added when using OBC-type acquisition; it is assumed to be generated by PS conversion at reflection. In this thesis, OBC-type data will be considered.

Recently, there has been a lot of interest for OBC recording. One reason for this is the fact that areas of interest have become obstructed by oil producing platforms. Data-acquisition vessels towing long streamers of hydrophones behind them cannot enter these areas. But with ocean-bottom recording, these areas can be covered. In addition, stationary receivers on the ocean-bottom allow monitoring a reservoir during a longer period of time, so that changes in the reservoir can be detected (this is called 4-D seismics). First experience shows that 4-D seismics will lead to a more efficient production of a reservoir. By using geophones at the ocean-bottom instead of at the water surface, it is possible to record the elastic wavefield in marine environments, still keeping the acquisition fairly economic by letting the source remain easily moveable near the water surface.

1.2 Acoustic versus elastic data processing

By accounting for additional wave types in the processing of seismic data, a sharper image of the Earth's structure and additional or more reliable information on its properties could be obtained.

Multicomponent data require a different kind of processing than the conventional data processing, based on the acoustic wavefield. Figure 1.2 shows the approach that was taken in this study (after Berkhouwt and Wapenaar, 1990). In this approach the P- and S-waves are separated in the first step so that (optionally after multiple elimination) the separated wavefields can then be approximately treated as scalar

wavefields, and further processing steps can be along similar lines as in the acoustic processing sequence. If the processing is correct the migration results for the P- and S-waves should give a consistent image of the earth, and additional information for the inversion process. The other option, not considered here, would be to do full vector wavefield processing. The reason for choosing the approach as given in Figure 1.2, is that this formulation gives simpler equations. Another consideration is that when using the separated wavefields, the sensitivity to errors in the macro velocity model is not as high as in full vector wave field processing. In this thesis, only the first two steps in Figure 1.2, up to the surface related multiple elimination, are treated.

The implementation and theoretical aspects of the wavefield separation step of the elastic processing method as described above, were investigated by Herrmann (1992) for the situation of three-component source and receiver data. Despite the rather simple appearance of the wavefield decomposition equations, application to measured multicomponent land data was not very successfull, mainly due to the low quality of multicomponent land data and problems related to geophone coupling and the weathered layer. Therefore, the aim of this study was the application of the wavefield decomposition to the relatively more simple and often high quality OBC-type data.

1.3 Wavefield decomposition methods

In order to process elastic seismic data according to the approach in Figure 1.2, the wavefield decomposition plays an important role. There exist several (variants of) methods for performing a wavefield separation, not all with the same result. To avoid confusion an attempt is made to categorize the most common methods. Decomposition methods can roughly be divided into two categories:

- Methods that perform wave-equation based decomposition. In this category are the methods similar to the decomposition investigated in this thesis. Elastic wave-equation based decomposition methods not only perform a separation of P- and S-waves, but a separation into down- and upgoing wavefields as well. The methods are often applied in the $\omega - k$ or $\tau - p$ domain and are therefore correct for all angles of incidence. In the presence of lateral variations these methods can also be formulated in the space-frequency domain as space-variant spatial convolutional operations. Application of this decomposition method to the special case of ocean-bottom acquisition has been discussed in Amundsen and Reitan (1995); Osen et al. (1996); Donati and Stewart (1996), as a modification of multicomponent decomposition schemes by White (1965); Dankbaar (1985); Wapenaar et al. (1990).
- Methods that perform wave-type separation based on polarization. In these

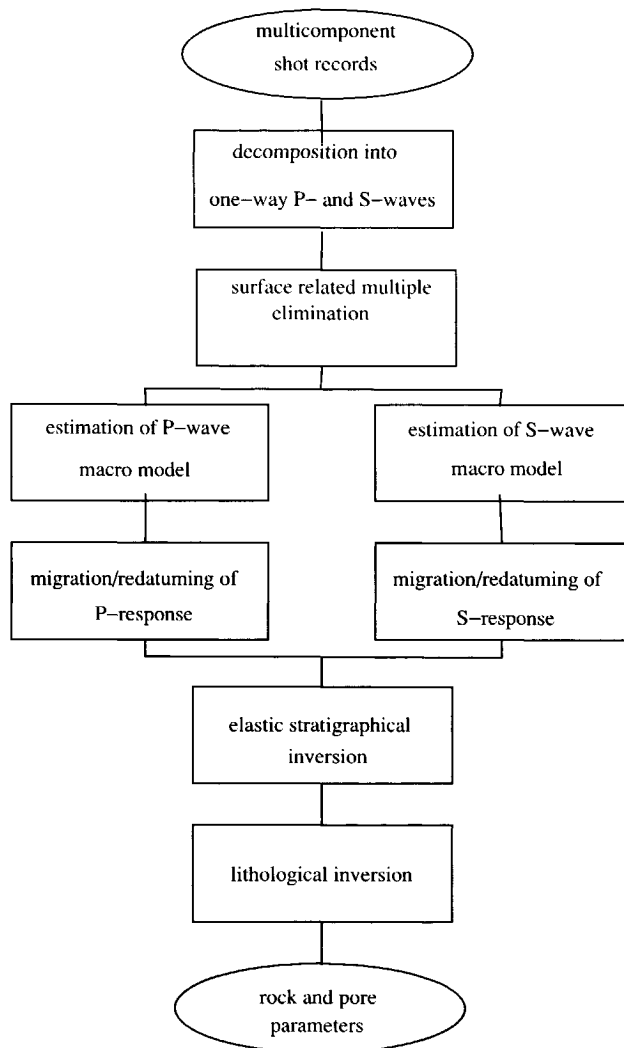


Fig. 1.2 Proposed processing sequence for multicomponent seismic data (after Berkhout and Wapenaar, 1990).

methods the difference in polarization between P- and S-waves is utilized in order to separate the different wave-types. The method is applied in the frequency domain and separates the different wave types present in a window, but not the up- and downgoing wavefields. An advantage is that no a priori knowledge about the elastic parameters just below the ocean-bottom is needed, but it is rather tedious to apply to large datasets. This method is explained in Richwalski (2000) for multicomponent data in general, and in Cho and Spencer (1992).

The previously mentioned methods separate P- and S-waves. For OBC-type data there also have been developed several methods that separate water multiples from primary reflections. In literature these are often classified as decomposition methods too:

- Methods that aim at removing/attenuating reverberations of the wavefield in the water (demultiple). These methods aim at removing the reverberations caused by energy trapped in the water layer, and energy that is reflected downward again by the water surface. An example is the dual-sensor summation (Barr and Sanders, 1989) where the hydrophone and the scaled vertical geophone recordings are summed. The scaling factor is a function of the ocean-bottom reflectivity and causes the surface-related reverberations to cancel out. The summation procedure as described in Barr and Sanders (1989) is derived for normal incidence and is applied in the time-domain. Some of these methods are variants of wave equation based decomposition methods, limited to the separation of up- and downgoing wavefields.

In addition, full surface-related multiple removal methods adapted to the special case of ocean-bottom acquisition (e.g. Ikelle, 1998) are also ordered under wavefield decomposition methods. As can be seen in Figure 1.2 it is chosen not to place multiple removal under decomposition here. Multiple removal necessitates a considerably larger data volume, whereas wavefield decomposition typically acts on one shot gather. Moreover, multiple removal and wavefield decomposition can be performed independently of each other.

1.4 Outline of this thesis

The aim of this thesis is to apply the wavefield decomposition theory to OBC data. Further processing results of the elastic wavefield processing strategy followed here depend on a good separation of P- and S-waves. A bad decomposition result will influence the reliability of further processing steps. Therefore, a lot of attention is paid to the wavefield decomposition, and it is tested on several different datasets.

In chapter 2, the theory of the wavefield decomposition is reviewed with adaptations to the special case of OBC acquisition. Decomposition results are shown on synthetic data. As it turns out that the application of the decomposition theory to field data is not straightforward, an adaptive decomposition strategy for application to field data will be developed as well, which is also tested on the synthetic data.

In chapter 3 this strategy will then be verified on some field data examples from the North Sea with relatively large water depths. These datasets allow an easy evaluation of the quality and issues of the wavefield decomposition for field data.

Chapter 4 continues with a demonstration of the wavefield decomposition on a more challenging dataset (shallower water layer). This dataset poses some additional issues - due to the stronger interference between different events. It is also demonstrated that it is possible to apply the decomposition to an entire 2-D dataset. After wavefield decomposition, this dataset is taken through some additional (conventional) processing steps to obtain a rough image of the subsurface. This makes it possible to compare the quality of an image with and without wavefield decomposition.

In chapter 5, the decomposed data obtained in chapter 4 are subjected to the next processing step: surface related multiple elimination. This is done to obtain a dataset with all water related events removed. The decomposed data still contain some water related multiples (so called source-side peg legs). First the surface related multiple elimination procedure developed for surface seismic data (Verschuur, 1991; Verschuur et al., 1992) has to be slightly modified to accomodate ocean-bottom acquisition. The multiple elimination is demonstrated on synthetic data. It is then investigated how important the removal of left-over multiples is in practice on a field data example.

Finally, in chapter 6 it is concluded that the wavefield decomposition can be successfully applied to OBC data acquired over a relatively flat ocean-bottom for various water depths. The method is easily extended to data aquired with the shot line in the same vertical plane as the ocean-bottom cable. In addition the possible extension to 3D acquisition geometries is discussed. The extra effort required for a wavefield decomposition is compensated by cleaner data components and a better subsurface image. Additional multiple elimination can be beneficial in the case of strong reflecting structures, otherwise the decomposition in itself will already attenuate most of the multiple energy.

Chapter 2

Wavefield decomposition: theoretical aspects

In the case of a decomposition at the ocean-bottom there is the choice of performing a decomposition just above the bottom (acoustic decomposition) or just below the bottom (elastic decomposition). In the former case the down- and upgoing pressure wavefields in the water-layer are obtained; the latter case results in the down- and upgoing P- and S-waves just below the receiver level. The composition and decomposition equations [equations (2.156) and (2.157) below] give the relations between the two-way wavefield vectors (in terms of the total particle velocity and traction) and one-way wavefield vectors (acoustically in terms of downgoing and upgoing pressure wavefields, elastically in terms of potentials for downgoing and upgoing P- and S-waves). In this chapter, horizontally layered media will be considered. In the last section, the limitations of the decomposition operators with respect to non-horizontally layered media will be discussed.

Notation

Time-derivatives will be denoted by ∂_t which is short for $\frac{\partial}{\partial t}$ and spatial-derivatives by ∂_k which is short for $\frac{\partial}{\partial k}$, $k = x, y, z$. The gradient operator is denoted by $\nabla = (\partial_x, \partial_y, \partial_z)^T$, where T denotes transposition.

Einstein's summation convention applies for repeated subscripts (except for subscripts x , y , z and t). When the word frequency is used, the angular frequency $\omega = 2\pi f$ is meant, unless it is explicitly mentioned to be otherwise.

Transformations

In this chapter, wavefield decomposition is derived in the horizontal wavenumber-frequency (k_x, k_y, ω) domain. Application of the decomposition is done in the

slowness-frequency (p, ω) domain. To convert between the different domains, the following transformations are used.

Temporal Fourier transformation. The forward temporal Fourier Transform $U(\omega)$ of a function of time $u(t)$ is defined as

$$U(\omega) = \int_{-\infty}^{+\infty} \exp(-j\omega t) u(t) dt, \quad (2.1)$$

and the inverse temporal Fourier Transform as

$$u(t) = \frac{1}{2\pi} \int_{-\infty}^{+\infty} \exp(j\omega t) U(\omega) d\omega, \quad (2.2)$$

where ω denotes the angular frequency. The equivalent of a derivative with respect to time in the time domain is a multiplication with $j\omega$ in the frequency domain: $\partial_t \leftrightarrow j\omega$.

If $u(t)$ is a real-valued function in time, then

$$u(t) = \frac{1}{\pi} \operatorname{Re} \left[\int_0^{+\infty} \exp(j\omega t) U(\omega) d\omega \right], \quad (2.3)$$

hence, only positive frequencies have to be taken into account. From here onward ω will always be taken positive.

One-dimensional spatial Fourier transformation. The one-dimensional spatial Fourier transform with respect to the horizontal Cartesian coordinate x is defined as

$$\tilde{U}(k_x, \omega) = \int_{-\infty}^{+\infty} \exp(jk_x x) U(x, \omega) dx, \quad (2.4)$$

and the inverse spatial Fourier Transform as

$$U(x, \omega) = \frac{1}{2\pi} \int_{-\infty}^{+\infty} \exp(-jk_x x) \tilde{U}(k_x, \omega) dk_x, \quad (2.5)$$

where k_x denotes the horizontal wavenumber, and \tilde{U} denotes the function in the wavenumber-frequency domain. The equivalent of a spatial derivative in the space-frequency domain is a multiplication with $-jk_x$ in the wavenumber-frequency domain: $\partial_x \leftrightarrow -jk_x$.

Two-dimensional spatial Fourier transformation. The two-dimensional spatial Fourier transform with respect to the horizontal Cartesian coordinates x and y is defined as

$$\tilde{U}(k_x, k_y, \omega) = \int_{-\infty}^{+\infty} \int_{-\infty}^{+\infty} \exp(j(k_x x + k_y y)) U(x, y, \omega) dx dy, \quad (2.6)$$

and the inverse spatial Fourier Transform as

$$U(x, y, \omega) = \frac{1}{4\pi^2} \int_{-\infty}^{+\infty} \int_{-\infty}^{+\infty} \exp(-j(k_x x + k_y y)) \tilde{U}(k_x, k_y, \omega) dk_x dk_y, \quad (2.7)$$

where k_x, k_y denote the horizontal wavenumbers in the x and y directions, and \tilde{U} denotes the function in the wavenumber-frequency domain. The equivalent of a spatial derivative in the space-frequency domain is a multiplication with $-jk_i$, $i = x, y$, in the wavenumber-frequency domain: $\partial_i \leftrightarrow -jk_i$, $i = x, y$.

One-dimensional Radon transformation. In this thesis, also the one-dimensional Radon transform is used for a two-dimensional geometry. Starting from a one-dimensional spatial Fourier transform with respect to the horizontal coordinate x and using the relation between the horizontal slowness p and the wavenumber k_x

$$p = k_x / \omega, \quad (2.8)$$

the one-dimensional Radon transform can be written as

$$\tilde{U}(wp, \omega) = \int_{-\infty}^{+\infty} \exp(j\omega p x) U(x, \omega) dx, \quad (2.9)$$

and

$$U(x, \omega) = \frac{\omega}{2\pi} \int_{-\infty}^{+\infty} \exp(-j\omega p x) \tilde{U}(wp, \omega) dp. \quad (2.10)$$

The time-domain equivalent is given by

$$\hat{u}(p, \tau) = \int_{-\infty}^{+\infty} u(x, \tau + px) dx, \quad (2.11)$$

and

$$u(x, t) = \frac{1}{2\pi} \frac{\partial}{\partial t} \int_{-\infty}^{+\infty} \mathcal{H}[\hat{u}(p, t - px)] dp, \quad (2.12)$$

where $\mathcal{H}(\hat{u})$ denotes the Hilbert transform of \hat{u} and τ is the intercept time defined as $\tau = t - px$. This transform represents a plane wave decomposition of a wavefield due to a line source in a horizontally layered medium. Each plane wave is characterized by a constant horizontal slowness or ray parameter p . Equations (2.11) and (2.12) are also known as the forward and inverse $\tau - p$ transform.

Overview of domains

Throughout this thesis the wavefields will be described with respect to the Cartesian coordinates x , y and z . A wavefield is written as $u(x, y, z, t)$ in the time domain. The same wavefield in the frequency domain is denoted by capital characters, unless otherwise noted. The wavefield notation in the different domains is summarized in Table 2.

$u(x, y, z, t)$	space-time domain
$U(x, y, z, \omega)$	space-frequency domain
$\tilde{U}(k_x, k_y, z, \omega)$	wavenumber-frequency domain
$\tilde{U}(\omega p, z, \omega)$	horizontal slowness-frequency domain
$\hat{u}(p, z, \tau)$	$\tau - p$ domain

Table 2.1 Wavefield notation in the different domains.

For the decomposition theory formulated in this thesis media are considered in which the medium parameters vary in the vertical direction only, i.e. there are no lateral variations (in section 2.7 it will be discussed to what extent this assumption can be relaxed). Therefore, often only the z -dependency is written explicitly, e.g. $\tilde{U}(z)$ is short for $\tilde{U}(k_x, k_y, z, \omega)$. The positive z -direction is chosen downward. The down-going wavefield is therefore denoted as $\tilde{U}^+(z)$ and the upgoing wavefield as $\tilde{U}^-(z)$. Vectors and matrices are denoted by bold characters.

2.1 Relations between two-way and one-way wavefields

2.1.1 Acoustic case

The equations that govern linear two-way wavefield propagation in an acoustic medium (for this thesis, above the ocean-bottom), derived under specific assumptions (de Hoop, 1995; Vos, 2000), are the equation of motion and the deformation equation, given by:

$$\partial_k p + \varrho \partial_t v_k = f_k \quad (2.13)$$

$$\partial_k v_k + \kappa \partial_t p = q, \quad (2.14)$$

where p is the acoustic pressure, v_k the particle velocity, ϱ the volume density of mass, κ the compressibility, f_k the volume source density of volume force and q the volume source density of injection rate. Assuming no sources are present and writing

the above equations in vector notation gives

$$\nabla p(x, y, z, t) = -\varrho \partial_t \mathbf{v}(x, y, z, t) \quad (2.15)$$

$$\nabla \cdot \mathbf{v}(x, y, z, t) = -\kappa \partial_t p(x, y, z, t). \quad (2.16)$$

As mentioned previously, a horizontally layered medium will be considered. This means the medium parameters vary only in the vertical direction, i.e. $\kappa = \kappa(z)$ and $\varrho = \varrho(z)$. Transforming equations (2.15) and (2.16) to the wavenumber-frequency domain and writing each component gives

$$-jk_x \tilde{P} = -j\omega \varrho \tilde{V}_x \quad (2.17)$$

$$-jk_y \tilde{P} = -j\omega \varrho \tilde{V}_y \quad (2.18)$$

$$\partial_z \tilde{P} = -j\omega \varrho \tilde{V}_z \quad (2.19)$$

$$-jk_x \tilde{V}_x - jk_y \tilde{V}_y + \partial_z \tilde{V}_z = -j\omega \kappa \tilde{P}, \quad (2.20)$$

where it is implicitly assumed that \tilde{V}_x , \tilde{V}_y , \tilde{V}_z , \tilde{P} , ϱ and κ are z -dependent. The above equations can be combined to a second-order differential equation by elimination of \tilde{V}_x , \tilde{V}_y and \tilde{V}_z , or written as a system of first-order differential equations by eliminating only \tilde{V}_x and \tilde{V}_y . For the derivation of the one-way wave equations the latter approach is followed:

$$\partial_z \begin{pmatrix} \tilde{P} \\ \tilde{V}_z \end{pmatrix} = \begin{pmatrix} 0 & -j\omega \varrho \\ \frac{k_z^2}{j\omega \varrho} & 0 \end{pmatrix} \begin{pmatrix} \tilde{P} \\ \tilde{V}_z \end{pmatrix} \quad (2.21)$$

with

$$k_z^2 = \frac{\omega^2}{c^2} - k_x^2 - k_y^2 \quad (2.22)$$

$$c^2 = (\kappa \varrho)^{-1}, \quad (2.23)$$

where $c(z)$ is the acoustic propagation velocity. Equation (2.21) can be written as

$$\partial_z \tilde{\mathbf{Q}}(z) = \tilde{\mathbf{A}}(z) \tilde{\mathbf{Q}}(z) \quad (2.24)$$

where

$$\tilde{\mathbf{Q}}(z) = \begin{pmatrix} \tilde{P}(z) \\ \tilde{V}_z(z) \end{pmatrix}, \quad (2.25)$$

and

$$\tilde{\mathbf{A}}(z) = \begin{pmatrix} 0 & \tilde{A}_{12}(z) \\ \tilde{A}_{21}(z) & 0 \end{pmatrix}, \quad (2.26)$$

with

$$\tilde{A}_{12}(z) = -j\omega \varrho(z) \quad \text{and} \quad \tilde{A}_{21}(z) = \frac{k_z^2(z)}{j\omega \varrho(z)}. \quad (2.27)$$

Eigenvalue decomposition of matrix \mathbf{A} gives

$$\tilde{\mathbf{A}}(z) = \tilde{\mathbf{L}}(z)\tilde{\Lambda}(z)\tilde{\mathbf{L}}^{-1}(z). \quad (2.28)$$

The eigenvalues $\zeta_{1,2}$ are found by solving the characteristic equation

$$\det[\tilde{\mathbf{A}} - \zeta \mathbf{I}] = 0, \quad (2.29)$$

giving $\zeta_{1,2} = \mp jk_z$. The diagonal matrix $\tilde{\Lambda}$ thus becomes

$$\tilde{\Lambda}(z) = \begin{pmatrix} -jk_z(z) & 0 \\ 0 & jk_z(z) \end{pmatrix}. \quad (2.30)$$

The eigenvectors $\vec{\ell}_1$ and $\vec{\ell}_2$ are found using

$$\tilde{\mathbf{A}}\vec{\ell}_1 = \zeta_1 \vec{\ell}_1 \quad (2.31)$$

$$\tilde{\mathbf{A}}\vec{\ell}_2 = \zeta_2 \vec{\ell}_2 \quad (2.32)$$

giving

$$\vec{\ell}_1 = \begin{pmatrix} \tilde{L}_1 \\ \tilde{L}_2 \end{pmatrix}, \quad \vec{\ell}_2 = \begin{pmatrix} \tilde{L}_1 \\ -\tilde{L}_2 \end{pmatrix}, \quad (2.33)$$

with

$$\tilde{L}_2 = \frac{k_z}{\omega\varrho} \tilde{L}_1. \quad (2.34)$$

Thus,

$$\tilde{\mathbf{L}}(z) = \begin{pmatrix} \tilde{L}_1 & \tilde{L}_1 \\ \frac{k_z(z)}{\omega\varrho(z)} \tilde{L}_1 & -\frac{k_z(z)}{\omega\varrho(z)} \tilde{L}_1 \end{pmatrix}, \quad \tilde{\mathbf{L}}^{-1}(z) = \frac{1}{2\tilde{L}_1} \begin{pmatrix} 1 & \frac{\omega\varrho(z)}{k_z(z)} \\ 1 & -\frac{\omega\varrho(z)}{k_z(z)} \end{pmatrix}, \quad (2.35)$$

where the columns of matrix $\tilde{\mathbf{L}}$ contain the eigenvectors of matrix $\tilde{\mathbf{A}}$. In the above equations the normalization of the eigenvectors remains a degree of freedom, determined by the choice of \tilde{L}_1 .

Using the eigenvalue decomposition, equation (2.24) becomes

$$\partial_z \tilde{\mathbf{Q}}(z) = \tilde{\mathbf{L}}(z)\tilde{\Lambda}(z)\tilde{\mathbf{L}}^{-1}(z)\tilde{\mathbf{Q}}(z). \quad (2.36)$$

Making the following definition:

$$\tilde{\mathbf{D}}(z) = \tilde{\mathbf{L}}^{-1}(z)\tilde{\mathbf{Q}}(z), \quad (2.37)$$

and therefore

$$\tilde{\mathbf{Q}}(z) = \tilde{\mathbf{L}}(z)\tilde{\mathbf{D}}(z), \quad (2.38)$$

it follows that

$$\partial_z [\tilde{\mathbf{L}}(z) \tilde{\mathbf{D}}(z)] = \tilde{\mathbf{L}}(z) \tilde{\mathbf{\Lambda}}(z) \tilde{\mathbf{D}}(z) \quad (2.39)$$

or

$$\partial_z \tilde{\mathbf{D}}(z) = \tilde{\mathbf{B}}(z) \tilde{\mathbf{D}}(z) \quad (2.40)$$

with

$$\tilde{\mathbf{B}}(z) = \tilde{\mathbf{\Lambda}}(z) - \tilde{\mathbf{L}}^{-1}(z) \partial_z \tilde{\mathbf{L}}(z). \quad (2.41)$$

The vector $\tilde{\mathbf{D}}(z)$ contains the down- and upgoing (one-way) wavefields with respect to the z -direction. From equations (2.41) and (2.35) it can be seen that when the medium is homogeneous, the partial derivative of $\tilde{\mathbf{L}}$ becomes zero so $\tilde{\mathbf{B}}$ reduces to the diagonal matrix $\tilde{\mathbf{\Lambda}}$, hence the down- and upgoing wavefields decouple. For vertically inhomogeneous media the down- and upgoing wavefields are coupled by the term $\tilde{\mathbf{L}}^{-1} \partial_z \tilde{\mathbf{L}}$. The matrix $\tilde{\mathbf{L}}$ gives a linear relation between the one-way wavefields and the two-way wavefields in terms of pressure and particle velocity and is therefore also called a *composition* matrix. The inverse matrix $\tilde{\mathbf{L}}^{-1}$ is then called a *decomposition* matrix. The normalization of matrix $\tilde{\mathbf{L}}$ depends on how the one-way wavefields are defined. If the one-way wavefields are desired to represent acoustic pressure, i.e.

$$\tilde{\mathbf{D}}(z) = \begin{pmatrix} \tilde{P}^+(z) \\ \tilde{P}^-(z) \end{pmatrix}, \quad (2.42)$$

and using the definition $\tilde{P}(z) = \tilde{P}^+(z) + \tilde{P}^-(z)$, matrix $\tilde{\mathbf{L}}$ becomes

$$\tilde{\mathbf{L}}(z) = \begin{pmatrix} 1 & 1 \\ \frac{k_z(z)}{\omega \rho(z)} & -\frac{k_z(z)}{\omega \rho(z)} \end{pmatrix}. \quad (2.43)$$

This type of normalization is called ‘pressure normalization’.

The one-way wavefields can also be chosen to represent vertical particle velocity,

$$\tilde{\mathbf{D}}(z) = \begin{pmatrix} \tilde{V}_z^+(z) \\ -\tilde{V}_z^-(z) \end{pmatrix}, \quad (2.44)$$

This is called normalization to the vertical particle velocity. Using the definition $\tilde{V}_z(z) = \tilde{V}_z^+(z) + \tilde{V}_z^-(z)$, Matrix $\tilde{\mathbf{L}}$ becomes

$$\tilde{\mathbf{L}}(z) = \begin{pmatrix} \frac{\omega \rho(z)}{k_z(z)} & \frac{\omega \rho(z)}{k_z(z)} \\ 1 & -1 \end{pmatrix}. \quad (2.45)$$

And finally in the vertical acoustic power flux normalization, the amplitudes of the one-way wavefields are normalized in such a way that they are proportional to the

square-root of the power flux in the z -direction (Ursin, 1983; de Hoop, 1992). For propagating waves ($k_x^2 + k_y^2 \leq \omega^2/c^2$), the power flux in the z -direction of flux-normalized one-way wavefields \tilde{P}^+ and \tilde{P}^- is by definition given by

$$\tilde{P}^+(\tilde{P}^+)^* - \tilde{P}^-(\tilde{P}^-)^*, \quad (2.46)$$

where $*$ denotes the complex conjugate. In terms of total wavefields, the power flux is given by

$$\tilde{P}\tilde{V}_z^* + \tilde{P}^*\tilde{V}_z, \quad (2.47)$$

By demanding that equation (2.46) is equal to equation (2.47), the normalization factors can be determined:

$$\tilde{P}^+(\tilde{P}^+)^* - \tilde{P}^-(\tilde{P}^-)^* = \tilde{P}\tilde{V}_z^* + \tilde{P}^*\tilde{V}_z, \quad (2.48)$$

which is equivalent to

$$\tilde{\mathbf{D}}^H \begin{pmatrix} 1 & 0 \\ 0 & -1 \end{pmatrix} \tilde{\mathbf{D}} = \tilde{\mathbf{Q}}^H \begin{pmatrix} 0 & 1 \\ 1 & 0 \end{pmatrix} \tilde{\mathbf{Q}}, \quad (2.49)$$

$$= \tilde{\mathbf{D}}^H \tilde{\mathbf{L}}^H \begin{pmatrix} 0 & 1 \\ 1 & 0 \end{pmatrix} \tilde{\mathbf{L}} \tilde{\mathbf{D}}, \quad (2.50)$$

with

$$\tilde{\mathbf{D}}(z) = \begin{pmatrix} \tilde{P}^+(z) \\ \tilde{P}^-(z) \end{pmatrix}, \quad (2.51)$$

where H denotes the transpose and complex conjugate. It then follows that $\tilde{\mathbf{L}}$ must satisfy

$$\begin{pmatrix} 1 & 0 \\ 0 & -1 \end{pmatrix} = \tilde{\mathbf{L}}^H \begin{pmatrix} 0 & 1 \\ 1 & 0 \end{pmatrix} \tilde{\mathbf{L}}. \quad (2.52)$$

Matrix $\tilde{\mathbf{L}}$ then becomes

$$\tilde{\mathbf{L}}(z) = \begin{pmatrix} \sqrt{\frac{\omega\varrho(z)}{2k_z(z)}} & \sqrt{\frac{\omega\varrho(z)}{2k_z(z)}} \\ \sqrt{\frac{k_z(z)}{2\omega\varrho(z)}} & -\sqrt{\frac{k_z(z)}{2\omega\varrho(z)}} \end{pmatrix}. \quad (2.53)$$

2.1.2 Elastic case

The linear equation of motion and the linear deformation equation in a horizontally layered elastic medium are given by

$$\varrho\partial_t v_i = \partial_j \tau_{ij} + f_i \quad (2.54)$$

$$\partial_t \tau_{ij} = C_{ijkl} \partial_l v_k - \partial_t \sigma_{ij}, \quad (2.55)$$

where C_{ijkl} is the stiffness tensor, τ_{ij} the stress tensor, and σ_{ij} the stress source tensor. The stiffness tensor and the stress tensor are symmetric, i.e. $C_{ijkl} = C_{ijlk} = C_{jikl} = C_{klij}$, and $\tau_{ij} = \tau_{ji}$. Equations (2.54) and (2.55) define the base for the decomposition method below the ocean-bottom.

Assuming no sources are present and using vector notation the above equations become :

$$\varrho \partial_t \mathbf{v} = \partial_j \boldsymbol{\tau}_j \quad (2.56)$$

$$\partial_t \boldsymbol{\tau}_j = \mathbf{C}_{jl} \partial_l \mathbf{v} \quad (2.57)$$

with

$$\mathbf{v} = \begin{pmatrix} v_x \\ v_y \\ v_z \end{pmatrix}, \quad \boldsymbol{\tau}_j = \begin{pmatrix} \tau_{xj} \\ \tau_{yj} \\ \tau_{zj} \end{pmatrix}, \quad \mathbf{C}_{jl} = \begin{pmatrix} C_{xj, xl} & C_{xj, yl} & C_{xj, zl} \\ C_{yj, xl} & C_{yj, yl} & C_{yj, zl} \\ C_{zj, xl} & C_{zj, yl} & C_{zj, zl} \end{pmatrix}. \quad (2.58)$$

Transforming these equations to the two-dimensional wavenumber-frequency (k_x, k_y, ω) domain and writing each component gives for equation (2.56)

$$j\omega \varrho \tilde{V}_x = -jk_x \tilde{T}_{xx} - jk_y \tilde{T}_{xy} + \partial_z \tilde{T}_{xz}, \quad (2.59)$$

$$j\omega \varrho \tilde{V}_y = -jk_x \tilde{T}_{yx} - jk_y \tilde{T}_{yy} + \partial_z \tilde{T}_{yz}, \quad (2.60)$$

$$j\omega \varrho \tilde{V}_z = -jk_x \tilde{T}_{zx} - jk_y \tilde{T}_{zy} + \partial_z \tilde{T}_{zz}. \quad (2.61)$$

Assuming an isotropic medium, the stiffness tensor becomes (Auld, 1973)

$$C_{ijkl} = \lambda \delta_{ij} \delta_{kl} + \mu [\delta_{ik} \delta_{jl} + \delta_{il} \delta_{jk}], \quad (2.62)$$

where δ_{ij} is the Kronecker delta defined as

$$\delta_{ij} = \begin{cases} 0 & \text{if } i \neq j, \\ 1 & \text{if } i = j. \end{cases}$$

Substitution of equation (2.62) into equation (2.57) gives

$$\partial_t \tau_{ij} = \delta_{ij} \lambda \partial_k v_k + \mu (\partial_i v_j + \partial_j v_i) \quad (2.63)$$

or, in the two-dimensional wavenumber-frequency domain,

$$j\omega \tilde{T}_{xx} = -jk_x (\lambda + 2\mu) \tilde{V}_x - jk_y \lambda \tilde{V}_y + \lambda \partial_z \tilde{V}_z, \quad (2.64)$$

$$j\omega \tilde{T}_{yy} = -jk_x \lambda \tilde{V}_x - jk_y (\lambda + 2\mu) \tilde{V}_y + \lambda \partial_z \tilde{V}_z, \quad (2.65)$$

$$j\omega \tilde{T}_{zz} = -jk_x \lambda \tilde{V}_x - jk_y \lambda \tilde{V}_y + (\lambda + 2\mu) \partial_z \tilde{V}_z, \quad (2.66)$$

$$j\omega \tilde{T}_{xz} = j\omega \tilde{T}_{zx} = \mu (-jk_x \tilde{V}_z + \partial_z \tilde{V}_x), \quad (2.67)$$

$$j\omega \tilde{T}_{yz} = j\omega \tilde{T}_{zy} = \mu (-jk_y \tilde{V}_z + \partial_z \tilde{V}_y), \quad (2.68)$$

$$j\omega \tilde{T}_{xy} = j\omega \tilde{T}_{yx} = \mu (-jk_x \tilde{V}_y - jk_y \tilde{V}_x). \quad (2.69)$$

By eliminating the quantities that may be discontinuous at the boundaries (i.e. \tilde{T}_{xx} , \tilde{T}_{yy} , \tilde{T}_{xy}) from equations (2.59-2.61), (2.64-2.66) and (2.67-2.69), a system of first-order differential equations is obtained:

$$\partial_z \tilde{\mathbf{Q}}^p(z) = \tilde{\mathbf{A}}^p(z) \tilde{\mathbf{Q}}^p(z), \quad (2.70)$$

where $\tilde{\mathbf{Q}}^p$ is a permutation of

$$\tilde{\mathbf{Q}} = \begin{pmatrix} -\tilde{\mathbf{T}}_z \\ \tilde{\mathbf{V}} \end{pmatrix}. \quad (2.71)$$

The permutation $\tilde{\mathbf{Q}}^p$ is used in order to be able to derive the composition/decomposition equations along similar lines as in the acoustic case.

$$\tilde{\mathbf{Q}}^p(z) = \begin{pmatrix} \tilde{V}_x(z) \\ \tilde{V}_y(z) \\ -\tilde{T}_{zz}(z) \\ -\tilde{T}_{xz}(z) \\ -\tilde{T}_{yz}(z) \\ \tilde{V}_z(z) \end{pmatrix}, \quad (2.72)$$

and

$$\tilde{\mathbf{A}}^p(z) = \begin{pmatrix} 0 & \tilde{\mathbf{A}}_{12}(z) \\ \tilde{\mathbf{A}}_{21}(z) & 0 \end{pmatrix} \quad (2.73)$$

with

$$\tilde{\mathbf{A}}_{12}(z) = \begin{pmatrix} -j\frac{\omega}{\mu} & 0 & jk_x \\ 0 & -j\frac{\omega}{\mu} & jk_y \\ jk_x & jk_y & -j\omega\varrho \end{pmatrix} \quad (2.74)$$

and

$$\tilde{\mathbf{A}}_{21}(z) = \begin{pmatrix} -j\omega\varrho - \frac{1}{j\omega}[\alpha_1 k_x^2 + \mu k_y^2] & -\frac{1}{j\omega}\alpha_2 k_x k_y & jk_x \frac{\lambda}{\lambda+2\mu} \\ -\frac{1}{j\omega}\alpha_2 k_x k_y & -j\omega\varrho - \frac{1}{j\omega}[\mu k_x^2 + \alpha_1 k_y^2] & jk_y \frac{\lambda}{\lambda+2\mu} \\ jk_x \frac{\lambda}{\lambda+2\mu} & jk_y \frac{\lambda}{\lambda+2\mu} & -j \frac{\omega}{\lambda+2\mu} \end{pmatrix}, \quad (2.75)$$

where

$$\alpha_1 = 4\mu\left(\frac{\lambda + \mu}{\lambda + 2\mu}\right) \quad (2.76)$$

$$\alpha_2 = \mu\left(\frac{3\lambda + 2\mu}{\lambda + 2\mu}\right). \quad (2.77)$$

Because an isotropic medium is considered and because of the way in which $\tilde{\mathbf{Q}}^p$ is ordered, matrix $\tilde{\mathbf{A}}^p$ has the same antidiagonal form as the matrix $\tilde{\mathbf{A}}$ in the acoustic

case. Therefore, the eigenvalue decomposition of matrix $\tilde{\mathbf{A}}^p$ can be performed in a similar way as in the acoustic case.

Eigenvalue decomposition of matrix $\tilde{\mathbf{A}}^p$ gives

$$\tilde{\mathbf{A}}^p(z) = \tilde{\mathbf{L}}^p(z)\tilde{\mathbf{\Lambda}}(z)[\tilde{\mathbf{L}}^p(z)]^{-1}. \quad (2.78)$$

The eigenvalues $\zeta_{i=1,6}$ are found by solving the characteristic equation

$$\det[\tilde{\mathbf{A}}^p - \zeta \mathbf{I}] = 0. \quad (2.79)$$

Because of the special structure of $\tilde{\mathbf{A}}^p$ (equation 2.73), this is equivalent with solving

$$\det(\tilde{\mathbf{A}}_{12}\tilde{\mathbf{A}}_{21} - \zeta^2 \mathbf{I}) = 0, \quad (2.80)$$

giving six eigenvalues, $\pm jk_{z,p}, \pm jk_{z,s}, \pm jk_{z,s}$, where

$$k_{z,p} = \sqrt{k_p^2 - k_x^2 - k_y^2}, \quad (2.81)$$

$$k_{z,s} = \sqrt{k_s^2 - k_x^2 - k_y^2}, \quad (2.82)$$

$$k_p^2 = \omega^2/c_p^2 = \varrho\omega^2/(\lambda + 2\mu), \quad (2.83)$$

$$k_s^2 = \omega^2/c_s^2 = \varrho\omega^2/\mu. \quad (2.84)$$

The diagonal matrix $\tilde{\mathbf{\Lambda}}$ becomes

$$\tilde{\mathbf{\Lambda}}(z) = \begin{pmatrix} -jk_{z,p}(z) & 0 & 0 & 0 & 0 & 0 \\ 0 & -jk_{z,s}(z) & 0 & 0 & 0 & 0 \\ 0 & 0 & -jk_{z,s}(z) & 0 & 0 & 0 \\ 0 & 0 & 0 & jk_{z,p}(z) & 0 & 0 \\ 0 & 0 & 0 & 0 & jk_{z,s}(z) & 0 \\ 0 & 0 & 0 & 0 & 0 & jk_{z,s}(z) \end{pmatrix}. \quad (2.85)$$

The six eigenvectors of matrix $\tilde{\mathbf{A}}^p$ are found using

$$\tilde{\mathbf{A}}^p \begin{pmatrix} \vec{\ell}_1 \\ \vec{\ell}_2 \end{pmatrix} = \zeta \begin{pmatrix} \vec{\ell}_1 \\ \vec{\ell}_2 \end{pmatrix}, \quad (2.86)$$

or

$$\tilde{\mathbf{A}}_{12}\tilde{\mathbf{A}}_{21}\vec{\ell}_1 = \zeta^2 \vec{\ell}_1 \quad (2.87)$$

$$\tilde{\mathbf{A}}_{21}\tilde{\mathbf{A}}_{12}\vec{\ell}_2 = \zeta^2 \vec{\ell}_2, \quad (2.88)$$

where equation (2.87) and (2.88) each solve three “sub-eigenvectors”, which will be called $\vec{\ell}_{1,p}$, $\vec{\ell}_{1,s}$, $\vec{\ell}'_{1,s}$, and $\vec{\ell}_{2,p}$, $\vec{\ell}_{2,s}$, and $\vec{\ell}'_{2,s}$, with the subscript referring to whether $\zeta^2 = -k_{z,p}^2$ or $-k_{z,s}^2$ was used.

Similar to the acoustic case, the eigenvector matrix $\tilde{\mathbf{L}}^p$ is given by

$$\tilde{\mathbf{L}}^p = \begin{pmatrix} \tilde{\mathbf{L}}_1^p & \tilde{\mathbf{L}}_2^p \\ \tilde{\mathbf{L}}_2^p & -\tilde{\mathbf{L}}_1^p \end{pmatrix}, \quad (2.89)$$

$$\tilde{\mathbf{L}}_1^p = \begin{pmatrix} \vec{\ell}_{1,p} & \vec{\ell}_{1,s} & \vec{\ell}_{1,s}' \end{pmatrix}, \quad (2.90)$$

$$\tilde{\mathbf{L}}_2^p = \begin{pmatrix} \vec{\ell}_{2,p} & \vec{\ell}_{2,s} & \vec{\ell}_{2,s}' \end{pmatrix}, \quad (2.91)$$

where the columns of matrix $\tilde{\mathbf{L}}^p$ contain the eigenvectors of matrix $\tilde{\mathbf{A}}^p$.

The matrix $\tilde{\mathbf{A}}_{12}\tilde{\mathbf{A}}_{21}$ is given by

$$\begin{aligned} \tilde{\mathbf{A}}_{12}\tilde{\mathbf{A}}_{21} = & \begin{pmatrix} -k_s^2 + (\frac{3\lambda+4\mu}{\lambda+2\mu})k_x^2 + k_y^2 & 2(\frac{\lambda+\mu}{\lambda+2\mu})k_x k_y & \frac{k_x \omega}{\mu}(\frac{\lambda+\mu}{\lambda+2\mu}) \\ 2(\frac{\lambda+\mu}{\lambda+2\mu})k_x k_y & -k_s^2 + k_x^2 + (\frac{3\lambda+4\mu}{\lambda+2\mu})k_y^2 & \frac{k_y \omega}{\mu}(\frac{\lambda+\mu}{\lambda+2\mu}) \\ 2(\frac{\lambda+\mu}{\lambda+2\mu})\frac{k_x \mu}{\omega}[k_s^2 - 2k_x^2 - 2k_y^2] & 2(\frac{\lambda+\mu}{\lambda+2\mu})\frac{k_y \mu}{\omega}[k_s^2 - 2k_x^2 - 2k_y^2] & -k_p^2 - \frac{\lambda(k_x^2 + k_y^2)}{\lambda+2\mu} \end{pmatrix}. \end{aligned} \quad (2.92)$$

As the matrices $\tilde{\mathbf{A}}_{12}$ and $\tilde{\mathbf{A}}_{21}$ are both symmetric, $\tilde{\mathbf{A}}_{21}\tilde{\mathbf{A}}_{12}$ obeys the symmetry relation

$$\tilde{\mathbf{A}}_{21}\tilde{\mathbf{A}}_{12} = (\tilde{\mathbf{A}}_{12}\tilde{\mathbf{A}}_{21})^T. \quad (2.93)$$

The eigenvector $\vec{\ell}_{1,p}$ is then obtained from equations (2.87), (2.81) and (2.92) as

$$\vec{\ell}_{1,p} = \begin{pmatrix} \ell_{1p} \\ \frac{k_y}{k_x}\ell_{1p} \\ \frac{\mu}{\omega k_x}[k_s^2 - 2k_x^2 - 2k_y^2]\ell_{1p} \end{pmatrix}. \quad (2.94)$$

From equation (2.87), using $\zeta^2 = -k_{z,s}^2$, where $k_{z,s}$ is defined in equation (2.82), it can be seen that all three rows of $\tilde{\mathbf{A}}_{12}\tilde{\mathbf{A}}_{21} - \zeta^2\mathbf{I}$ become dependent:

$$(\tilde{\mathbf{A}}_{12}\tilde{\mathbf{A}}_{21} - \zeta^2\mathbf{I})\vec{\ell}_{1,s} = 0, \quad \text{or} \quad (2.95)$$

$$2k_x k_y a + 2k_y^2 b + \frac{k_y \omega}{\mu} c = 0 \quad (2.96)$$

if $\vec{\ell}_{1,s} = (a, b, c)^T$. Two independent eigenvectors that satisfy this equation are easily found:

$$\langle e_1 \rangle = \begin{pmatrix} 1 \\ -\frac{k_x}{k_y} \\ 0 \end{pmatrix}, \quad \langle e_2 \rangle = \begin{pmatrix} 1 \\ 0 \\ -\frac{2k_x \mu}{\omega} \end{pmatrix}. \quad (2.97)$$

A general solution for the eigenvector is given by a linear combination of $\langle e_1 \rangle$ and $\langle e_2 \rangle$:

$$\eta_1 \langle e_1 \rangle + \eta_2 \langle e_2 \rangle = \begin{pmatrix} \eta_1 + \eta_2 \\ -\frac{k_x}{k_y} \eta_1 \\ -\frac{2k_x \mu}{\omega} \eta_2 \end{pmatrix}, \quad (2.98)$$

where η_1 and η_2 are arbitrary scaling factors. The eigenvectors $\vec{\ell}_{1,s}$ and $\vec{\ell}'_{1,s}$ are then given by

$$\vec{\ell}_{1,s} = \begin{pmatrix} \eta_1 + \eta_2 \\ -\frac{k_x}{k_y} \eta_1 \\ -\frac{2k_x \mu}{\omega} \eta_2 \end{pmatrix}, \quad \vec{\ell}'_{1,s} = \begin{pmatrix} \eta'_1 + \eta'_2 \\ -\frac{k_x}{k_y} \eta'_1 \\ -\frac{2k_x \mu}{\omega} \eta'_2 \end{pmatrix}. \quad (2.99)$$

Matrix $\tilde{\mathbf{L}}_1^p$ then becomes

$$\tilde{\mathbf{L}}_1^p = \begin{pmatrix} \ell_{1p} & \eta_1 + \eta_2 & \eta'_1 + \eta'_2 \\ \frac{k_y}{k_x} \ell_{1p} & -\frac{k_x}{k_y} \eta_1 & -\frac{k_x}{k_y} \eta'_1 \\ \frac{\mu}{\omega k_x} [k_s^2 - 2k_x^2 - 2k_y^2] \ell_{1p} & -\frac{2k_x \mu}{\omega} \eta_2 & -\frac{2k_x \mu}{\omega} \eta'_2 \end{pmatrix}, \quad (2.100)$$

where ℓ_{1p} , η_1 , η_2 , η'_1 , and η'_2 are normalization factors still to be determined.

Using equation (2.88) and (2.93) the eigenvectors $\vec{\ell}_{2,p}$, $\vec{\ell}_{2,s}$ and $\vec{\ell}'_{2,s}$ are found:

$$\tilde{\mathbf{L}}_2^p = \begin{pmatrix} \ell_{2p} & \xi_1 + \xi_2 & \xi'_1 + \xi'_2 \\ \frac{k_y}{k_x} \ell_{2p} & -\frac{k_x}{k_y} \xi_1 & -\frac{k_x}{k_y} \xi'_1 \\ \frac{\omega}{2k_x \mu} \ell_{2p} & -\frac{k_x \omega}{\mu [k_s^2 - 2k_x^2 - 2k_y^2]} \xi_2 & -\frac{k_x \omega}{\mu [k_s^2 - 2k_x^2 - 2k_y^2]} \xi'_2 \end{pmatrix}, \quad (2.101)$$

where ℓ_{2p} , ξ_1 , ξ_2 , ξ'_1 , and ξ'_2 are normalization factors still to be determined.

In this thesis, the normalization will be performed in such a way that the one-way wavefields represent compressional (P) and shear-wave (S) potentials. The particle velocity can be written as the sum of a compressional component \mathbf{v}_p and a shear component \mathbf{v}_s :

$$-\varrho \partial_t \mathbf{v}_p = \nabla \phi, \quad (2.102)$$

$$-\varrho \partial_t \mathbf{v}_s = \nabla \times \boldsymbol{\psi}, \quad (2.103)$$

$$(2.104)$$

$$\boldsymbol{\psi} = (\psi_x, \psi_y, \psi_z)^T, \quad (2.105)$$

where ϕ is the scalar P-wave potential and $\boldsymbol{\psi}$ the vector S-wave potential; ψ_x is the potential for S-waves polarized in the y, z -plane, ψ_y is the potential for S-waves

polarized in the x, z -plane, and ψ_z is the potential for S-waves polarized in the x, y -plane. The P- and S-wave potentials therefore satisfy

$$\mathbf{V} = -\frac{1}{j\omega\rho}(\nabla\Phi + \nabla \times \Psi), \quad (2.106)$$

in the frequency domain. Written in its components this becomes in the wavenumber-frequency domain

$$\tilde{\mathbf{V}} = -\frac{1}{j\omega\rho} \begin{pmatrix} -jk_x\tilde{\Phi} - jk_y\tilde{\Psi}_z - \partial_z\tilde{\Psi}_y \\ -jk_y\tilde{\Phi} + jk_x\tilde{\Psi}_z + \partial_z\tilde{\Psi}_x \\ \partial_z\tilde{\Phi} - jk_x\tilde{\Psi}_y + jk_y\tilde{\Psi}_x \end{pmatrix}. \quad (2.107)$$

In addition the divergence of ψ is zero, or

$$-jk_x\tilde{\Psi}_x - jk_y\tilde{\Psi}_y + \partial_z\tilde{\Psi}_z = 0. \quad (2.108)$$

Substituting the following equations into equations (2.107) and (2.108):

$$\Phi = \tilde{\Phi}^+ + \tilde{\Phi}^-, \quad \Psi = \tilde{\Psi}^+ + \tilde{\Psi}^-, \quad (2.109)$$

and

$$\partial_z\tilde{\Phi}^\pm = \mp jk_{z,p}\tilde{\Phi}^\pm, \quad \partial_z^\pm\tilde{\Psi} = \mp jk_{z,s}\tilde{\Psi}^\pm, \quad (2.110)$$

and eliminating $\tilde{\Psi}_z^\pm$, the desired relation between the particle velocity and the P- and S-wave potentials is found

$$\begin{pmatrix} \tilde{V}_x \\ \tilde{V}_y \\ \tilde{V}_z \end{pmatrix} = \frac{1}{\omega\rho} \begin{pmatrix} k_x & \frac{-k_x k_y}{k_{z,s}} & \frac{-(k_s^2 - k_x^2)}{k_{z,s}} \\ k_y & \frac{(k_s^2 - k_y^2)}{k_{z,s}} & \frac{k_x k_y}{k_{z,s}} \\ k_{z,p} & -k_y & k_x \end{pmatrix} \begin{pmatrix} \tilde{\Phi}^+ \\ \tilde{\Psi}_x^+ \\ \tilde{\Psi}_y^+ \end{pmatrix} \quad (2.111)$$

$$+ \frac{1}{\omega\rho} \begin{pmatrix} k_x & \frac{k_x k_y}{k_{z,s}} & \frac{(k_s^2 - k_x^2)}{k_{z,s}} \\ k_y & \frac{-(k_s^2 - k_y^2)}{k_{z,s}} & \frac{-k_x k_y}{k_{z,s}} \\ -k_{z,p} & -k_y & k_x \end{pmatrix} \begin{pmatrix} \tilde{\Phi}^- \\ \tilde{\Psi}_x^- \\ \tilde{\Psi}_y^- \end{pmatrix} \quad (2.112)$$

Using the definition $\tilde{\mathbf{Q}}^p = \tilde{\mathbf{L}}^p \tilde{\mathbf{D}}^p$

$$\begin{pmatrix} \tilde{V}_x(z) \\ \tilde{V}_y(z) \\ -\tilde{T}_{zz}(z) \\ -\tilde{T}_{xz}(z) \\ -\tilde{T}_{yz}(z) \\ \tilde{V}_z(z) \end{pmatrix} = \begin{pmatrix} \tilde{\mathbf{L}}_1^p & \tilde{\mathbf{L}}_1^p \\ \tilde{\mathbf{L}}_2^p & -\tilde{\mathbf{L}}_2^p \end{pmatrix} \begin{pmatrix} \tilde{\Phi}^+ \\ \tilde{\Psi}_x^+ \\ \tilde{\Psi}_y^+ \\ \tilde{\Phi}^- \\ -\tilde{\Psi}_x^- \\ -\tilde{\Psi}_y^- \end{pmatrix}, \quad (2.113)$$

and the expressions for $\tilde{\mathbf{L}}_1^p$ and $\tilde{\mathbf{L}}_2^p$ in equations (2.100) and (2.101), it can then be seen that

$$\ell_{1p} = \frac{k_x}{\omega \varrho}, \quad \eta_1 = \frac{-k_y(k_s^2 - k_y^2)}{k_x k_{z,s} \omega \varrho}, \quad \eta_2 = \frac{k_y k_{z,s}}{k_x \omega \varrho}, \quad (2.114)$$

$$\eta'_1 = \frac{-k_y^2}{k_{z,s} \omega \varrho}, \quad \eta'_2 = \frac{-k_{z,s}}{\omega \varrho}, \quad (2.115)$$

and

$$\tilde{\mathbf{L}}_1^p = \frac{\mu}{\omega^2 \varrho} \begin{pmatrix} \frac{\omega k_x}{\mu} & \frac{-\omega k_x k_y}{\mu k_{z,s}} & \frac{-\omega(k_s^2 - k_x^2)}{\mu k_{z,s}} \\ \frac{\omega k_y}{\mu} & \frac{\omega(k_s^2 - k_y^2)}{\mu k_{z,s}} & \frac{\omega k_x k_y}{\mu k_{z,s}} \\ (k_s^2 - 2k_x^2 - 2k_y^2) & -2k_y k_{z,s} & 2k_x k_{z,s} \end{pmatrix}. \quad (2.116)$$

And

$$\ell_{2p} = \frac{2\mu}{\omega^2 \varrho} k_x k_{z,p}, \quad \xi_2 = \frac{\mu k_y}{\omega^2 \varrho k_x} (k_s^2 - 2k_x^2 - 2k_y^2), \quad (2.117)$$

$$\xi'_2 = \frac{-\mu}{\omega^2 \varrho} (k_s^2 - 2k_x^2 - 2k_y^2). \quad (2.118)$$

To find normalization factors ξ_1 and ξ'_1 an equation additional to equation (2.112) is necessary; an expression for $-\tilde{T}_{yz}$ or $-\tilde{T}_{xz}$ expressed in terms of $\tilde{\Phi}^\pm$, $\tilde{\Psi}_x^\pm$ and $\tilde{\Psi}_y^\pm$. From equation (2.106) it can be seen that

$$\nabla \times \mathbf{V} = -\frac{1}{j\omega \rho} \nabla \times (\nabla \times \mathbf{\Psi}). \quad (2.119)$$

Together with the linear deformation equation:

$$\partial_t \tau_{ij} = \delta_{ij} \lambda \partial_k v_k + \mu (\partial_i v_j + \partial_j v_i), \quad (2.120)$$

and using equations (2.108) and (2.112):

$$-\tilde{T}_{yz} = \frac{\mu}{\omega^2 \varrho} [2k_y k_{z,p} (\tilde{\Phi}^+ - \tilde{\Phi}^-) + (k_s^2 - 2k_y^2) (\tilde{\Psi}_x^+ + \tilde{\Psi}_x^-) + 2k_x k_y (\tilde{\Psi}_y^+ + \tilde{\Psi}_y^-)] \quad (2.121)$$

The remaining normalization factors can now be obtained:

$$\xi_1 = \frac{-\mu k_y}{\omega^2 \varrho k_x} (k_s^2 - 2k_y^2), \quad \xi'_1 = \frac{-\mu}{\omega^2 \varrho} 2k_y^2, \quad (2.122)$$

and

$$\tilde{\mathbf{L}}_2^p = \frac{\mu}{\omega^2 \varrho} \begin{pmatrix} 2k_x k_{z,p} & -2k_x k_y & -(k_s^2 - 2k_x^2) \\ 2k_y k_{z,p} & (k_s^2 - 2k_y^2) & 2k_x k_y \\ \frac{\omega k_{z,p}}{\mu} & -\frac{\omega k_y}{\mu} & \frac{\omega k_x}{\mu} \end{pmatrix}, \quad (2.123)$$

Equation (2.113) can also be written as

$$\begin{pmatrix} \tilde{V}_x(z) \\ \tilde{V}_y(z) \\ -\tilde{T}_{zz}(z) \\ -\tilde{T}_{xz}(z) \\ -\tilde{T}_{yz}(z) \\ \tilde{V}_z(z) \end{pmatrix} = \begin{pmatrix} \tilde{\mathbf{L}}_1^{+,p} & \tilde{\mathbf{L}}_1^{-,p} \\ \tilde{\mathbf{L}}_2^{+,p} & \tilde{\mathbf{L}}_2^{-,p} \end{pmatrix} \begin{pmatrix} \tilde{\Phi}^+ \\ \tilde{\Psi}_x^+ \\ \tilde{\Psi}_y^+ \\ \tilde{\Phi}^- \\ \tilde{\Psi}_x^- \\ \tilde{\Psi}_y^- \end{pmatrix}, \quad (2.124)$$

where $\tilde{\mathbf{L}}_{1,2}^{+,p}$ are the “composition sub-matrices” for the downgoing part of the wavefield, and $\tilde{\mathbf{L}}_{1,2}^{-,p}$ are the “composition sub-matrices” for the upgoing part of the wavefield. The relation with $\tilde{\mathbf{L}}_{1,2}^p$ is

$$\tilde{\mathbf{L}}_1^{+,p} = \tilde{\mathbf{L}}_1^p, \quad (2.125)$$

$$\tilde{\mathbf{L}}_1^{-,p} = \tilde{\mathbf{L}}_1^p(-k_{z,s}), \quad (2.126)$$

$$\tilde{\mathbf{L}}_2^{+,p} = \tilde{\mathbf{L}}_2^p, \quad (2.127)$$

$$\tilde{\mathbf{L}}_2^{-,p} = \tilde{\mathbf{L}}_2^p(-k_{z,p}). \quad (2.128)$$

The sign change of the vertical wavenumber between down- and upgoing wavefields is explained in Figure (2.1).

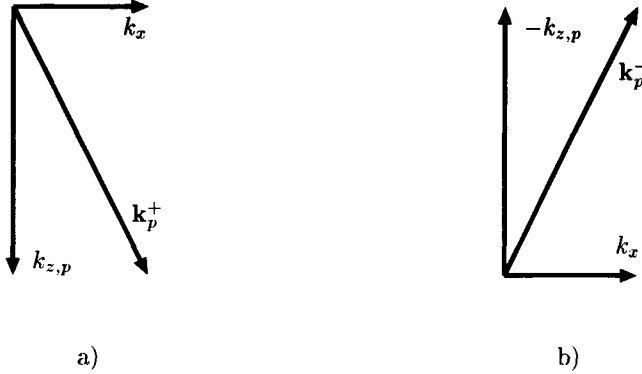


Fig. 2.1 Relation between a) the wavenumber corresponding with the downgoing plane P-wavefront (\mathbf{k}_P^+) and b) the upgoing P-wavefront (\mathbf{k}_P^-). The same relation exists for the S-waves.

For the remaining part of this thesis, $\tilde{\mathbf{Q}}^p$ is rearranged back to: $\tilde{\mathbf{Q}} = \tilde{\mathbf{L}}\tilde{\mathbf{D}}$ where

$$\tilde{\mathbf{Q}} = \begin{pmatrix} -\tilde{T}_z \\ \tilde{\mathbf{V}} \end{pmatrix} = \begin{pmatrix} \tilde{\mathbf{L}}_1^+ \\ \tilde{\mathbf{L}}_2^+ \end{pmatrix} \tilde{\mathbf{D}}^+ + \begin{pmatrix} \tilde{\mathbf{L}}_1^- \\ \tilde{\mathbf{L}}_2^- \end{pmatrix} \tilde{\mathbf{D}}^- = \begin{pmatrix} \tilde{\mathbf{L}}_1^+ & \tilde{\mathbf{L}}_1^- \\ \tilde{\mathbf{L}}_2^+ & \tilde{\mathbf{L}}_2^- \end{pmatrix} = \tilde{\mathbf{L}}\tilde{\mathbf{D}}, \quad (2.129)$$

and

$$\tilde{\mathbf{D}} = (\tilde{\Phi}^+, \tilde{\Psi}_x^+, \tilde{\Psi}_y^+, \tilde{\Phi}^-, \tilde{\Psi}_x^-, \tilde{\Psi}_y^-)^T. \quad (2.130)$$

The decomposition operator $\tilde{\mathbf{N}}$ is then the inverse of the composition operator $\tilde{\mathbf{L}}$. Or $\tilde{\mathbf{D}} = \tilde{\mathbf{L}}^{-1} \tilde{\mathbf{Q}} = \tilde{\mathbf{N}} \tilde{\mathbf{Q}}$, where

$$\tilde{\mathbf{N}} = \begin{pmatrix} \tilde{\mathbf{N}}_1^+ & \tilde{\mathbf{N}}_2^+ \\ \tilde{\mathbf{N}}_1^- & \tilde{\mathbf{N}}_2^- \end{pmatrix}. \quad (2.131)$$

The “composition sub-matrices” become:

$$\tilde{\mathbf{L}}_1^\pm = \frac{\mu}{\omega^2 \varrho} \begin{pmatrix} \pm 2k_x k_{z,p} & -2k_x k_y & -(k_s^2 - 2k_x^2) \\ \pm 2k_y k_{z,p} & k_s^2 - 2k_y^2 & 2k_x k_y \\ (k_s^2 - 2k_x^2 - 2k_y^2) & \mp 2k_y k_{z,s} & \pm 2k_x k_{z,s} \end{pmatrix}, \quad (2.132)$$

$$\tilde{\mathbf{L}}_2^\pm = \frac{1}{\omega \varrho} \begin{pmatrix} k_x & \mp \frac{k_x k_y}{k_{z,s}} & \mp \frac{(k_s^2 - k_x^2)}{k_{z,s}} \\ k_y & \pm \frac{(k_s^2 - k_y^2)}{k_{z,s}} & \pm \frac{k_x k_y}{k_{z,s}} \\ \pm k_{z,p} & -k_y & k_x \end{pmatrix} \quad (2.133)$$

and the “decomposition sub-matrices” become:

$$\tilde{\mathbf{N}}_1^\pm = \frac{1}{2} \begin{pmatrix} \pm \frac{k_x}{k_{z,p}} & \pm \frac{k_y}{k_{z,p}} & 1 \\ 0 & 1 & \mp \frac{k_y}{k_{z,s}} \\ -1 & 0 & \pm \frac{k_x}{k_{z,s}} \end{pmatrix}, \quad (2.134)$$

$$\tilde{\mathbf{N}}_2^\pm = \frac{\mu}{2\omega} \begin{pmatrix} 2k_x & 2k_y & \pm \frac{(k_s^2 - 2k_x^2 - 2k_y^2)}{k_{z,p}} \\ \mp \frac{k_x k_y}{k_{z,s}} & \pm \frac{(k_s^2 - k_x^2 - 2k_y^2)}{k_{z,s}} & -2k_y \\ \mp \frac{(k_s^2 - 2k_x^2 - k_y^2)}{k_{z,s}} & \pm \frac{k_x k_y}{k_{z,s}} & 2k_x \end{pmatrix}. \quad (2.135)$$

For laterally invariant media, derivations of the decomposition equations from the elastic wave equation have been given in various publications (Frasier, 1970; Aki and Richards, 1980; Kennett, 1983; Ursin, 1983).

As in the acoustic case, using the definition

$$\tilde{\mathbf{Q}}(z) = \tilde{\mathbf{L}}(z) \tilde{\mathbf{D}}(z), \quad (2.136)$$

and its inverse

$$\tilde{\mathbf{D}}(z) = \tilde{\mathbf{L}}^{-1}(z) \tilde{\mathbf{Q}}(z) \quad (2.137)$$

$$= \tilde{\mathbf{N}}(z) \tilde{\mathbf{Q}}(z), \quad (2.138)$$

the one-way wave equation can be written as

$$\partial_z \tilde{\mathbf{D}} = \tilde{\mathbf{B}} \tilde{\mathbf{D}}, \quad (2.139)$$

with

$$\tilde{\mathbf{B}} = \tilde{\mathbf{A}} - \tilde{\mathbf{N}}\partial_z \tilde{\mathbf{L}}. \quad (2.140)$$

This gives a coupled system of equations for the down- and upgoing P- and S-wavefields.

From equation (2.140) it can be seen that when the medium is homogeneous, the partial derivative of $\tilde{\mathbf{L}}$ becomes zero so $\tilde{\mathbf{B}}$ reduces to the diagonal matrix $\tilde{\mathbf{A}}$, hence the down- and upgoing P- and S-wavefields decouple. For z -dependent media the down- and upgoing P- and S-wavefields are coupled by the term $\tilde{\mathbf{N}}\partial_z \tilde{\mathbf{L}}$.

In a homogeneous layer, a solution of the two-way wave equation, $\partial_z \tilde{\mathbf{Q}} = \tilde{\mathbf{A}} \tilde{\mathbf{Q}}$, is given by

$$\tilde{\mathbf{Q}}(z) = \tilde{\mathbf{W}}(z, z_0) \tilde{\mathbf{Q}}(z_0), \quad (2.141)$$

where

$$\tilde{\mathbf{W}}(z, z_0) = \exp(\tilde{\mathbf{A}}\Delta z), \quad (2.142)$$

with $\Delta z = z - z_0$.

The operator $\tilde{\mathbf{W}}(z, z_0)$ describes two-way wavefield extrapolation from z_0 to z . The wavefield extrapolation can also be performed in three separate steps, using the one-way equation. This follows from

$$\tilde{\mathbf{W}}(z, z_0) = \exp(\tilde{\mathbf{L}}\tilde{\mathbf{A}}\tilde{\mathbf{L}}^{-1}\Delta z) = \tilde{\mathbf{L}}\exp(\tilde{\mathbf{A}}\Delta z)\tilde{\mathbf{L}}^{-1} = \tilde{\mathbf{L}}\tilde{\mathbf{V}}(z, z_0)\tilde{\mathbf{L}}^{-1}, \quad (2.143)$$

with

$$\tilde{\mathbf{V}}(z, z_0) = \exp(\tilde{\mathbf{A}}\Delta z). \quad (2.144)$$

Putting this expression for $\tilde{\mathbf{W}}$ into equation (2.141) results in

$$\tilde{\mathbf{Q}}(z) = \tilde{\mathbf{L}}\tilde{\mathbf{V}}(z, z_0)\tilde{\mathbf{L}}^{-1}\tilde{\mathbf{Q}}(z_0), \quad (2.145)$$

where, from right to left, $\tilde{\mathbf{L}}^{-1}\tilde{\mathbf{Q}}(z_0)$ describes decomposition of the total wavefield at z_0 into downgoing and upgoing waves, $\tilde{\mathbf{V}}(z, z_0)$ describes one-way extrapolation of downgoing and upgoing waves separately from z_0 to z , and $\tilde{\mathbf{L}}$ describes the composition of the downgoing and upgoing waves at z to the total wavefield again.

In this thesis we will be concentrating on the composition/decomposition operators $\tilde{\mathbf{L}}$ and $\tilde{\mathbf{N}}$ for the special case of ocean-bottom seismic data, with an emphasis on the implementation of the decomposition theory to field data.

2.1.3 Special case ($k_y = 0$)

For further insight, it is interesting to look at the special case of a wavefield propagating in the x, z -plane (i.e. $k_y = 0$). Substituting $k_y = 0$ in equation (2.70), two uncoupled systems are obtained.

One system, contains only particle motion in the y -direction while the wavefield is propagating in the x, z -plane:

$$\partial_z \begin{pmatrix} -\tilde{T}_{yz}(z) \\ \tilde{V}_y(z) \end{pmatrix} = \begin{pmatrix} 0 & -j\omega\varrho - \frac{1}{j\omega}\mu k_x^2 \\ -j\frac{\omega}{\mu} & 0 \end{pmatrix} \begin{pmatrix} -\tilde{T}_{yz}(z) \\ \tilde{V}_y(z) \end{pmatrix}. \quad (2.146)$$

Waves that behave in this way are also called SH waves.

The other system contains only particle motion in the x - and z -directions while the wavefield is, again, propagating in the x, z -plane:

$$\partial_z \begin{pmatrix} -\tilde{T}_{xz}(z) \\ -\tilde{T}_{zz}(z) \\ \tilde{V}_x(z) \\ \tilde{V}_z(z) \end{pmatrix} = \begin{pmatrix} 0 & jk_x \frac{\lambda}{\lambda+2\mu} & -j\omega\varrho - \frac{1}{j\omega}\alpha_1 k_x^2 & 0 \\ jk_x & 0 & 0 & -j\omega\varrho \\ -j\frac{\omega}{\mu} & 0 & 0 & jk_x \\ 0 & -j\frac{\omega}{\lambda+2\mu} & jk_x \frac{\lambda}{\lambda+2\mu} & 0 \end{pmatrix} \begin{pmatrix} -\tilde{T}_{xz}(z) \\ -\tilde{T}_{zz}(z) \\ \tilde{V}_x(z) \\ \tilde{V}_z(z) \end{pmatrix} \quad (2.147)$$

Waves that behave in this way are also called P-SV waves.

The “composition” and “decomposition sub-matrices” for this special case reduce to

$$\begin{pmatrix} -\tilde{T}_{yz} \\ \tilde{V}_y \end{pmatrix} = \tilde{\mathbf{L}}_{SH} \begin{pmatrix} \tilde{\Psi}_x^+ \\ \tilde{\Psi}_x^- \end{pmatrix}, \quad (2.148)$$

$$\tilde{\mathbf{L}}_{SH} = \frac{1}{\omega\varrho} \begin{pmatrix} \frac{\mu k_s^2}{\omega} & \frac{\mu k_s^2}{\omega} \\ \frac{k_s^2}{k_{z,s}} & \frac{k_s^2}{k_{z,s}} \end{pmatrix}, \quad (2.149)$$

$$\tilde{\mathbf{N}}_{SH} = \tilde{\mathbf{L}}_{SH}^{-1} = \frac{1}{2} \begin{pmatrix} 1 & \frac{\mu k_{z,s}}{\omega} \\ 1 & \frac{-\mu k_{z,s}}{\omega} \end{pmatrix}, \quad (2.150)$$

$$\begin{pmatrix} -\tilde{T}_{xz}(z) \\ -\tilde{T}_{zz}(z) \\ \tilde{V}_x(z) \\ \tilde{V}_z(z) \end{pmatrix} = \begin{pmatrix} \tilde{\mathbf{L}}_{1,P-SV}^+ & \tilde{\mathbf{L}}_{1,P-SV}^- \\ \tilde{\mathbf{L}}_{2,P-SV}^+ & \tilde{\mathbf{L}}_{2,P-SV}^- \end{pmatrix} \begin{pmatrix} \tilde{\Psi}_y^+ \\ \tilde{\Psi}_y^- \end{pmatrix}, \quad (2.151)$$

$$\tilde{\mathbf{L}}_{1,P-SV}^{\pm} = \frac{\mu}{\omega^2\varrho} \begin{pmatrix} \pm 2k_x k_{z,p} & -(k_s^2 - 2k_x^2) \\ k_s^2 - 2k_x^2 & \pm 2k_x k_{z,s} \end{pmatrix}, \quad (2.152)$$

$$\tilde{\mathbf{L}}_{2,P-SV}^{\pm} = \frac{1}{\omega\varrho} \begin{pmatrix} k_x & \mp k_{z,s} \\ \pm k_{z,p} & k_x \end{pmatrix}, \quad (2.153)$$

$$\tilde{\mathbf{N}}_{1,P-SV}^{\pm} = \frac{1}{2} \begin{pmatrix} \pm \frac{k_x}{k_{z,p}} & 1 \\ -1 & \pm \frac{k_x}{k_{z,s}} \end{pmatrix}, \quad (2.154)$$

$$\tilde{\mathbf{N}}_{2,P-SV}^{\pm} = \frac{\mu}{2\omega} \begin{pmatrix} 2k_x & \pm \frac{(k_s^2 - 2k_x^2)}{k_{z,p}} \\ \mp \frac{(k_s^2 - 2k_x^2)}{k_{z,s}} & 2k_x \end{pmatrix}. \quad (2.155)$$

For the special case of a wavefield propagating in the x, z -plane, $\tilde{\Psi}_x$ denotes the potential for S-waves polarized in the y -direction and $\tilde{\Psi}_y$ denotes the potential for S-waves polarized in the x, z -plane. Thus, $\tilde{\Psi}_x$ is equal to the potential for SH waves and $\tilde{\Psi}_y$ is equal to the potential for SV waves.

2.2 Wavefield decomposition for the special case of ocean-bottom data

The composition and decomposition equations derived in the previous sections can be respectively written as:

$$\tilde{\mathbf{Q}} = \tilde{\mathbf{L}} \tilde{\mathbf{D}}$$

or

$$\begin{pmatrix} -\tilde{\mathbf{T}}_z(z) \\ \tilde{\mathbf{V}}(z) \end{pmatrix} = \begin{pmatrix} \tilde{\mathbf{L}}_1^+(z) & \tilde{\mathbf{L}}_1^-(z) \\ \tilde{\mathbf{L}}_2^+(z) & \tilde{\mathbf{L}}_2^-(z) \end{pmatrix} \begin{pmatrix} \tilde{\mathbf{D}}^+(z) \\ \tilde{\mathbf{D}}^-(z) \end{pmatrix} \quad (2.156)$$

and

$$\tilde{\mathbf{D}} = \tilde{\mathbf{L}}^{-1} \tilde{\mathbf{Q}} = \tilde{\mathbf{N}} \tilde{\mathbf{Q}}$$

or

$$\begin{pmatrix} \tilde{\mathbf{D}}^+(z) \\ \tilde{\mathbf{D}}^-(z) \end{pmatrix} = \begin{pmatrix} \tilde{\mathbf{N}}_1^+(z) & \tilde{\mathbf{N}}_2^+(z) \\ \tilde{\mathbf{N}}_1^-(z) & \tilde{\mathbf{N}}_2^-(z) \end{pmatrix} \begin{pmatrix} -\tilde{\mathbf{T}}_z(z) \\ \tilde{\mathbf{V}}(z) \end{pmatrix}. \quad (2.157)$$

For the acoustic case $\tilde{\mathbf{Q}}$ is given by equation (2.25), $\tilde{\mathbf{L}}, \tilde{\mathbf{N}}$ by equation (2.35), and $\tilde{\mathbf{D}}$ by equation (2.42), (2.44) or (2.51). For the elastic case $\tilde{\mathbf{Q}}$ is given by equation (2.71), $\tilde{\mathbf{L}}$ by equations (2.132)-(2.133), $\tilde{\mathbf{N}}$ by equations (2.134)-(2.135) and $\tilde{\mathbf{D}}$ by equation (2.130). The above equations are rewritten for the ocean-bottom situation by applying the specific boundary conditions for a fluid-solid contact, i.e. vanishing shear-stress and normal-stress equal to minus the acoustic pressure.

In the application of the decomposition theory to ocean-bottom data, k_y will be taken equal to zero. A short summary of the assumptions and limitations within the decomposition theory as derived in this chapter, will be given in section 2.7. Limitations in application will also be discussed with the field data examples.

Furthermore, the composition/decomposition equations are transformed to the ray-parameter-frequency (p, ω) domain. In this domain the operators become frequency independent, thus avoiding divisions with low frequencies. Using the relationships

$$k_x = \omega p$$

and

$$k_z = \omega q,$$

where

$$q = \sqrt{\frac{1}{c^2} - p^2}$$

is the vertical slowness or vertical rayparameter, the vectors and matrices in equations (2.156) and (2.157) can be rewritten in the p, ω domain for the acoustic and elastic situation by writing $\tilde{\mathbf{U}}(k_x, z, \omega) \equiv \tilde{\mathbf{U}}(\omega p, z, \omega)$, and substituting the above expressions into the matrices $\tilde{\mathbf{L}}$ and $\tilde{\mathbf{N}}$. In the following $\tilde{\mathbf{U}}(z)$ will be used as short for $\tilde{\mathbf{U}}(\omega p, z, \omega)$.

2.2.1 Acoustic wavefield vectors and composition/decomposition operators

In the acoustic case, the traction and particle velocity vectors and the one-way wavefield vectors become scalars, according to

$$\tilde{\mathbf{T}}_z(z) = -\tilde{P}(z), \quad \tilde{\mathbf{V}}(z) = \tilde{V}_z(z) \quad (2.158)$$

and

$$\tilde{\mathbf{D}}^+(z) = \tilde{P}^+(z), \quad \tilde{\mathbf{D}}^-(z) = \tilde{P}^-(z), \quad (2.159)$$

where $\tilde{P}(z)$ is the acoustic pressure at depth level z , $\tilde{V}_z(z)$ the vertical component of the particle velocity and where $\tilde{P}^+(z)$ and $\tilde{P}^-(z)$ represent the pressure in the downgoing and upgoing wavefields¹, respectively.

The acoustic composition/decomposition sub-matrices also become scalars, given by

$$\tilde{\mathbf{L}}_1^\pm(z) = 1, \quad \tilde{\mathbf{L}}_2^\pm(z) = \pm \frac{q(z)}{\rho(z)} \quad (2.160)$$

and

$$\tilde{\mathbf{N}}_1^\pm(z) = \frac{1}{2}, \quad \tilde{\mathbf{N}}_2^\pm(z) = \pm \frac{\rho(z)}{2q(z)}. \quad (2.161)$$

¹In the remainder of this thesis the pressure normalization will be used for the acoustic one-way wavefields.

Note that the operators depend only on the velocity and density of the acoustic medium. Substitution of equations (2.158–2.161) into equation (2.157) yields

$$\tilde{P}^{\pm}(z) = \frac{1}{2}\tilde{P}(z) \pm \frac{\varrho(z)}{2q(z)}\tilde{V}_z(z). \quad (2.162)$$

The depth of the ocean-bottom will be defined as $z = z_1$. The density, velocity, and vertical rayparameter in the water layer will be denoted by ϱ_0 , c_0 and q_0 . Hence, decomposition just above the ocean-bottom is described by

$$\tilde{P}^{\pm}(z_1) = \frac{1}{2}\tilde{P}(z_1) \pm \frac{\varrho_0}{2q_0}\tilde{V}_z(z_1), \quad (2.163)$$

where $\tilde{P}(z_1)$ and $\tilde{V}_z(z_1)$ are the (Radon transformed) pressure and velocity measurements and $\tilde{P}^+(z_1)$ and $\tilde{P}^-(z_1)$ are the downgoing and upgoing wave fields just above the ocean-bottom (actually at $z_1 - \epsilon$, with $\epsilon \rightarrow 0$).

2.2.2 Synthetic data

The effect of the decomposition will be demonstrated on synthetic data from a simple horizontally layered model. In Table 2.2 the model parameters are given. The pressure and velocity components as a function of offset and time (at the interface between the first and second layer, i.e., the ocean-bottom) calculated for this model are displayed in Figure 2.2. The synthetic data were calculated with a dipole P-wave point source, located at the water surface at $z = 0$. The source wavelet is a zero-phase cosine wavelet within the frequency bandwidth of the data. The bandwidth of the synthetic data goes up to 60 Hz. The synthetic data were calculated using the reflectivity method (Müller, 1985).

Table 2.2 Model parameters used for the generation of synthetic data.

depth (m)	P-velocity (m/s)	S-velocity (m/s)	density (kg/m ³)
0 - 500	1500	0	1000
500 - 1000	2100	600	2000
1500 - 2000	2500	1700	2200
> 2500	3000	1900	2500

Application of the acoustic decomposition operators to the synthetic data involves:

- Applying a Radon transform to the data in Figure 2.2.

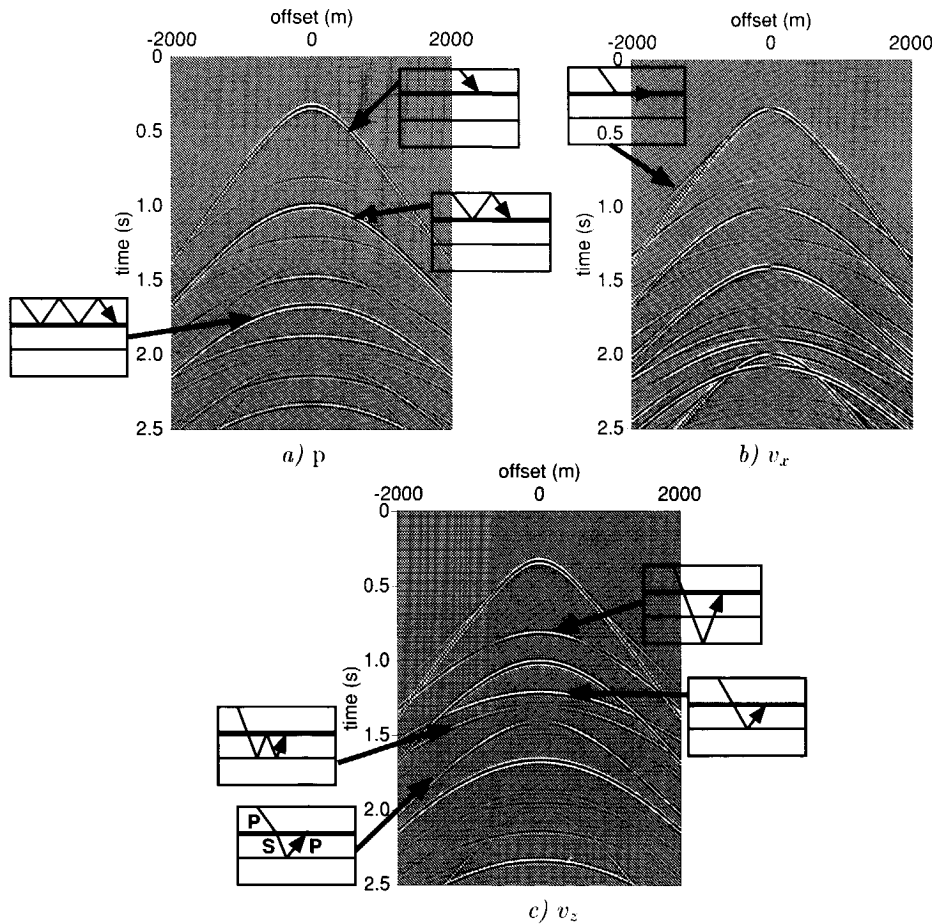


Fig. 2.2 Synthetic ocean-bottom data, (a) pressure component, (b) horizontal in-line velocity component, and (c) vertical velocity component.

- Applying equation (2.163) for each frequency component ω and each rayparameter p .
- Performing an inverse Radon transform.

The result of this procedure is displayed in Figure 2.3. Note the absence of primary reflections (upgoing) in the downgoing pressure wavefield just above the bottom, as expected.

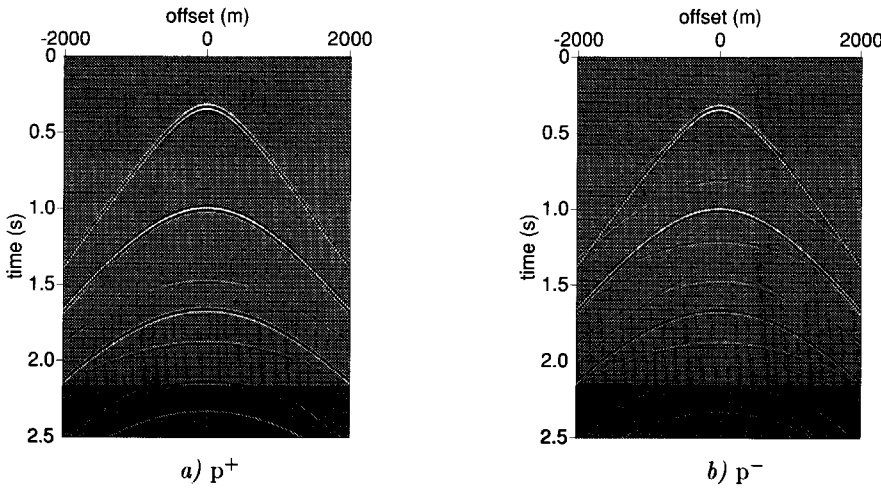


Fig. 2.3 Acoustic decomposition just above the bottom, (a) downgoing pressure wavefield, (b) upgoing pressure wavefield.

2.2.3 Elastic wavefield vectors and composition/decomposition operators

For the 2-D elastic case, the traction and particle velocity vectors and the one-way wavefield vectors become

$$\tilde{\mathbf{T}}_z(z) = \begin{pmatrix} \tilde{T}_{xz}(z) \\ \tilde{T}_{zz}(z) \end{pmatrix}, \quad \tilde{\mathbf{V}}(z) = \begin{pmatrix} \tilde{V}_x(z) \\ \tilde{V}_z(z) \end{pmatrix}, \quad (2.164)$$

and

$$\tilde{\mathbf{D}}^+(z) = \begin{pmatrix} \tilde{\Phi}^+(z) \\ \tilde{\Psi}^+(z) \end{pmatrix}, \quad \tilde{\mathbf{D}}^-(z) = \begin{pmatrix} \tilde{\Phi}^-(z) \\ \tilde{\Psi}^-(z) \end{pmatrix}, \quad (2.165)$$

where $\tilde{\Psi}$ is the SV-wave potential and is the same as $\tilde{\Psi}_y$ of equation (2.130)).

The elastic composition/decomposition operators are given by

$$\tilde{\mathbf{L}}_1^\pm(z) = c_S^2(z) \begin{pmatrix} \pm 2pq_P(z) & -(c_S^{-2}(z) - 2p^2) \\ c_S^{-2}(z) - 2p^2 & \pm 2pq_S(z) \end{pmatrix}, \quad (2.166)$$

$$\tilde{\mathbf{L}}_2^\pm(z) = \frac{1}{\varrho(z)} \begin{pmatrix} p & \mp q_S(z) \\ \mp q_P(z) & p \end{pmatrix}. \quad (2.167)$$

$$\tilde{\mathbf{N}}_1^\pm(z) = \frac{1}{2} \begin{pmatrix} \pm \frac{p}{q_P(z)} & 1 \\ -1 & \pm \frac{p}{q_S(z)} \end{pmatrix} \quad (2.168)$$

and

$$\tilde{\mathbf{N}}_2^\pm(z) = \frac{\varrho(z)c_S^2(z)}{2} \begin{pmatrix} 2p & \pm \frac{c_S^{-2}(z) - 2p^2}{q_P(z)} \\ \mp \frac{c_S^{-2}(z) - 2p^2}{q_S(z)} & 2p \end{pmatrix}, \quad (2.169)$$

where the vertical rayparameters are defined as

$$q_P(z) = \sqrt{c_P^{-2}(z) - p^2}, \quad q_S(z) = \sqrt{c_S^{-2}(z) - p^2}, \quad (2.170)$$

with c_P , c_S and ϱ , the compressional velocity, shear velocity and density of the elastic medium. At the ocean-bottom, the elastic operators, $\tilde{\mathbf{L}}_1^\pm(z_1)$, $\tilde{\mathbf{L}}_2^\pm(z_1)$, $\tilde{\mathbf{N}}_1^\pm(z_1)$ and $\tilde{\mathbf{N}}_2^\pm(z_1)$, depend solely on $c_{P,1}$, $c_{S,1}$ and ϱ_1 just below the ocean-bottom. Hence, using equation (2.157), decomposition just below the ocean-bottom is described by

$$\tilde{\mathbf{D}}^\pm(z_1) = -\tilde{\mathbf{N}}_1^\pm(z_1)\tilde{\mathbf{T}}_z(z_1) + \tilde{\mathbf{N}}_2^\pm(z_1)\tilde{\mathbf{V}}(z_1), \quad (2.171)$$

where $\tilde{\mathbf{T}}_z(z_1)$ and $\tilde{\mathbf{V}}(z_1)$ are the (Radon transformed) stress and velocity measurements and $\tilde{\mathbf{D}}^+(z_1)$ and $\tilde{\mathbf{D}}^-(z_1)$ are the downgoing and upgoing wavefields just below the ocean-bottom (actually at $z_1 + \epsilon$, with $\epsilon \rightarrow 0$). At the ocean-bottom the shear-stress vanishes, whereas the normal stress is equal to minus the acoustic pressure. Hence, in equation (2.171) we have

$$-\tilde{\mathbf{T}}_z(z_1) = \begin{pmatrix} 0 \\ \tilde{P}(z_1) \end{pmatrix}. \quad (2.172)$$

Application of the elastic decomposition operators to the synthetic data (Figure 2.2), following a similar procedure as described in section 2.2.2, gives the result displayed in Figure 2.4. Note the absence of the water multiples and the direct (transmitted) source wave in the upgoing P- and S-wavefields just below the bottom, as expected.

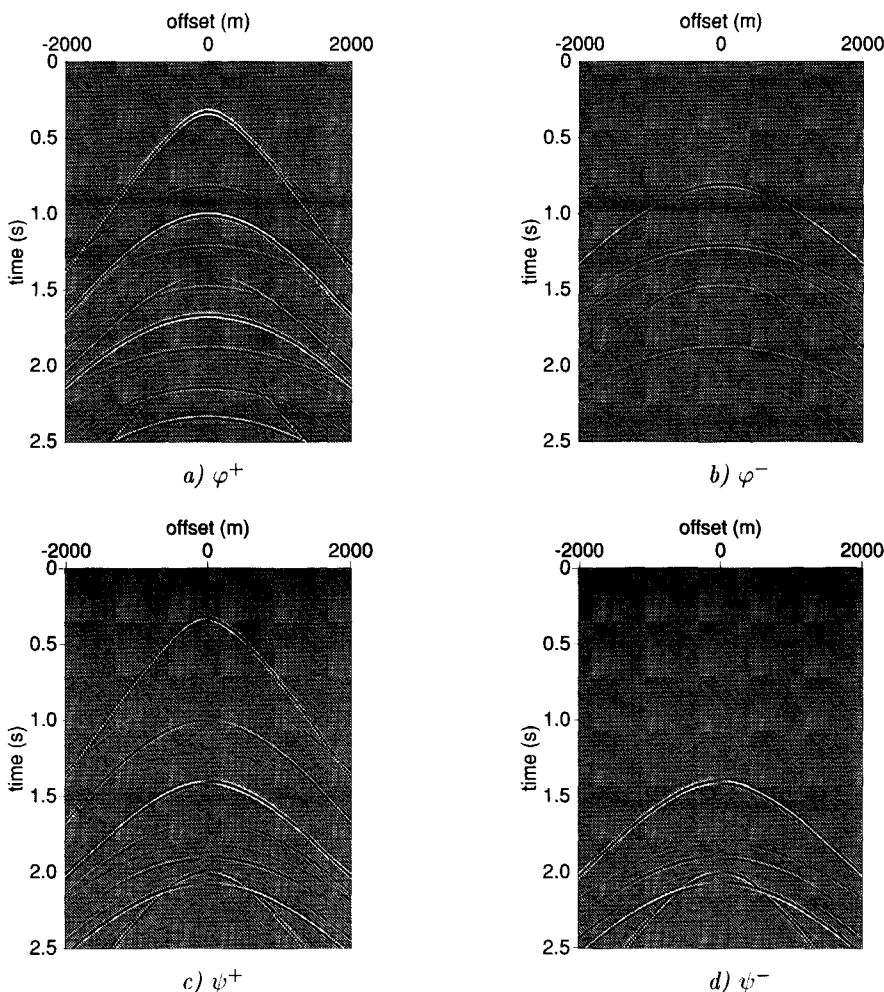


Fig. 2.4 Elastic decomposition just below the bottom, (a) downgoing P-waves, (b) upgoing P-waves, (c) downgoing S-waves, and (d) upgoing S-waves.

2.3 Wavefield decomposition in two steps

In the previously treated elastic decomposition procedure the down- and upgoing waves and the P- and S-waves were separated simultaneously. An alternative formulation is possible, where the same decomposition result is obtained in two steps. A derivation of the equations for multi-component surface data is given in Wapenaar and Haimé (1991). Here a similar derivation is presented for ocean-bottom data. In the two-step decomposition procedure the first decomposition step yields down- and upgoing fields expressed in terms of stresses. This choice is arbitrary; other wave field quantities could be chosen. However, with this choice the decomposition equations will appear to have a simple form. The second decomposition step separates the P- and S-waves. The derivation of the partial decomposition operators is as follows. From equation (2.156) we obtain

$$-\tilde{\mathbf{T}}_z(z_1) = \underbrace{\tilde{\mathbf{L}}_1^+(z_1)\tilde{\mathbf{D}}^+(z_1)}_{-\tilde{\mathbf{T}}_z^+(z_1)} + \underbrace{\tilde{\mathbf{L}}_1^-(z_1)\tilde{\mathbf{D}}^-(z_1)}_{-\tilde{\mathbf{T}}_z^-(z_1)}, \quad (2.173)$$

or

$$\begin{pmatrix} -\tilde{\mathbf{T}}_z^+(z_1) \\ -\tilde{\mathbf{T}}_z^-(z_1) \end{pmatrix} = \begin{pmatrix} \tilde{\mathbf{L}}_1^+(z_1) & \mathbf{O} \\ \mathbf{O} & \tilde{\mathbf{L}}_1^-(z_1) \end{pmatrix} \begin{pmatrix} \tilde{\mathbf{D}}^+(z_1) \\ \tilde{\mathbf{D}}^-(z_1) \end{pmatrix}, \quad (2.174)$$

or, upon substitution of equation (2.157)

$$\begin{pmatrix} -\tilde{\mathbf{T}}_z^+(z_1) \\ -\tilde{\mathbf{T}}_z^-(z_1) \end{pmatrix} = \begin{pmatrix} \tilde{\mathbf{M}}_1^+(z_1) & \tilde{\mathbf{M}}_2^+(z_1) \\ \tilde{\mathbf{M}}_1^-(z_1) & \tilde{\mathbf{M}}_2^-(z_1) \end{pmatrix} \begin{pmatrix} -\tilde{\mathbf{T}}_z(z_1) \\ \tilde{\mathbf{V}}(z_1) \end{pmatrix}, \quad (2.175)$$

where the partial decomposition operators are defined as

$$\tilde{\mathbf{M}}_1^\pm(z_1) = \tilde{\mathbf{L}}_1^\pm(z_1)\tilde{\mathbf{N}}_1^\pm(z_1), \quad (2.176)$$

$$\tilde{\mathbf{M}}_2^\pm(z_1) = \tilde{\mathbf{L}}_1^\pm(z_1)\tilde{\mathbf{N}}_2^\pm(z_1). \quad (2.177)$$

For the second decomposition step into P- and S-waves equation (2.174) is merely inverted, yielding

$$\begin{pmatrix} \tilde{\mathbf{D}}^+(z_1) \\ \tilde{\mathbf{D}}^-(z_1) \end{pmatrix} = \begin{pmatrix} \{\tilde{\mathbf{L}}_1^+(z_1)\}^{-1} & \mathbf{O} \\ \mathbf{O} & \{\tilde{\mathbf{L}}_1^-(z_1)\}^{-1} \end{pmatrix} \begin{pmatrix} -\tilde{\mathbf{T}}_z^+(z_1) \\ -\tilde{\mathbf{T}}_z^-(z_1) \end{pmatrix}. \quad (2.178)$$

Expressions for the two-step decomposition operators of the first step for the 2-D case can then be obtained by substituting equations (2.176),(2.177) and (2.166–2.169) into equation (2.175). We find

$$-\tilde{\mathbf{T}}_z^\pm(z_1) = -\tilde{\mathbf{M}}_1^\pm(z_1)\tilde{\mathbf{T}}_z(z_1) + \tilde{\mathbf{M}}_2^\pm(z_1)\tilde{\mathbf{V}}(z_1), \quad (2.179)$$

or

$$\begin{pmatrix} -\tilde{T}_{xz}^{\pm}(z_1) \\ -\tilde{T}_{zz}^{\pm}(z_1) \end{pmatrix} = \frac{1}{2} \begin{pmatrix} 1 & \pm \frac{\gamma_1 p}{q_{S,1}} \\ \mp \frac{\gamma_1 p}{q_{P,1}} & 1 \end{pmatrix} \begin{pmatrix} 0 \\ \tilde{P}(z_1) \end{pmatrix} + \frac{\varrho_1}{2} \begin{pmatrix} \pm \frac{\beta_1}{q_{S,1}} & 0 \\ 0 & \pm \frac{\beta_1}{q_{P,1}} \end{pmatrix} \begin{pmatrix} \tilde{V}_x(z_1) \\ \tilde{V}_z(z_1) \end{pmatrix}, \quad (2.180)$$

or

$$-\tilde{T}_{xz}^{\pm}(z_1) = \pm \frac{\gamma_1 p}{2q_{S,1}} \tilde{P}(z_1) \pm \frac{\varrho_1 \beta_1}{2q_{S,1}} \tilde{V}_x(z_1), \quad (2.181)$$

$$-\tilde{T}_{zz}^{\pm}(z_1) = \frac{1}{2} \tilde{P}(z_1) \pm \frac{\varrho_1 \beta_1}{2q_{P,1}} \tilde{V}_z(z_1), \quad (2.182)$$

where

$$\beta_1 = c_{S,1}^4 [4p^2 q_{P,1} q_{S,1} + (c_{S,1}^{-2} - 2p^2)^2], \quad (2.183)$$

$$\gamma_1 = c_{S,1}^2 [2q_{P,1} q_{S,1} - (c_{S,1}^{-2} - 2p^2)], \quad (2.184)$$

$$q_{P,1} = \sqrt{c_{P,1}^{-2} - p^2}, \quad (2.185)$$

$$q_{S,1} = \sqrt{c_{S,1}^{-2} - p^2}. \quad (2.186)$$

Note the simple structure of equations (2.181) and (2.182): only two data-components are required simultaneously. Also note that equation (2.182) has the same form as the acoustic decomposition equation (2.162), apart from the factor β_1 (this factor approaches unity when $c_{S,1}$ approaches zero). Application of equations (2.181) and (2.182) to the synthetic data of Figure 2.2, following a similar procedure as described in section 2.2.2, gives the results displayed in Figure 2.5. Note the direct (transmitted) source wave is absent in both the downgoing and upgoing shear stressfields² and the water multiples and the direct (transmitted) source wave are absent in the upgoing normal stressfield just below the bottom, as expected.

For the P- and S-wave decomposition step, equation (2.166) is substituted into equation (2.178) to obtain

$$-\tilde{\mathbf{D}}^{\pm}(z_1) = \{\tilde{\mathbf{L}}_1^{\pm}(z_1)\}^{-1} \tilde{\mathbf{T}}_z^{\pm}(z_1), \quad (2.187)$$

or

$$\begin{pmatrix} \tilde{\Phi}^{\pm}(z_1) \\ \tilde{\Psi}^{\pm}(z_1) \end{pmatrix} = \frac{c_{S,1}^2}{\beta_1} \begin{pmatrix} \pm 2pq_{S,1} & c_{S,1}^{-2} - 2p^2 \\ -(c_{S,1}^{-2} - 2p^2) & \pm 2pq_{P,1} \end{pmatrix} \begin{pmatrix} -\tilde{T}_{xz}^{\pm}(z_1) \\ -\tilde{T}_{zz}^{\pm}(z_1) \end{pmatrix}. \quad (2.188)$$

The results of this step are similar to Figure (2.4), therefore they are not displayed again.

²Due to the boundary condition $\tau_{xz} = 0$ at the ocean-bottom and the fact that the upgoing wavefield should not contain the direct source wave, the downgoing wavefield cannot contain a direct source wave either without violating the boundary condition.

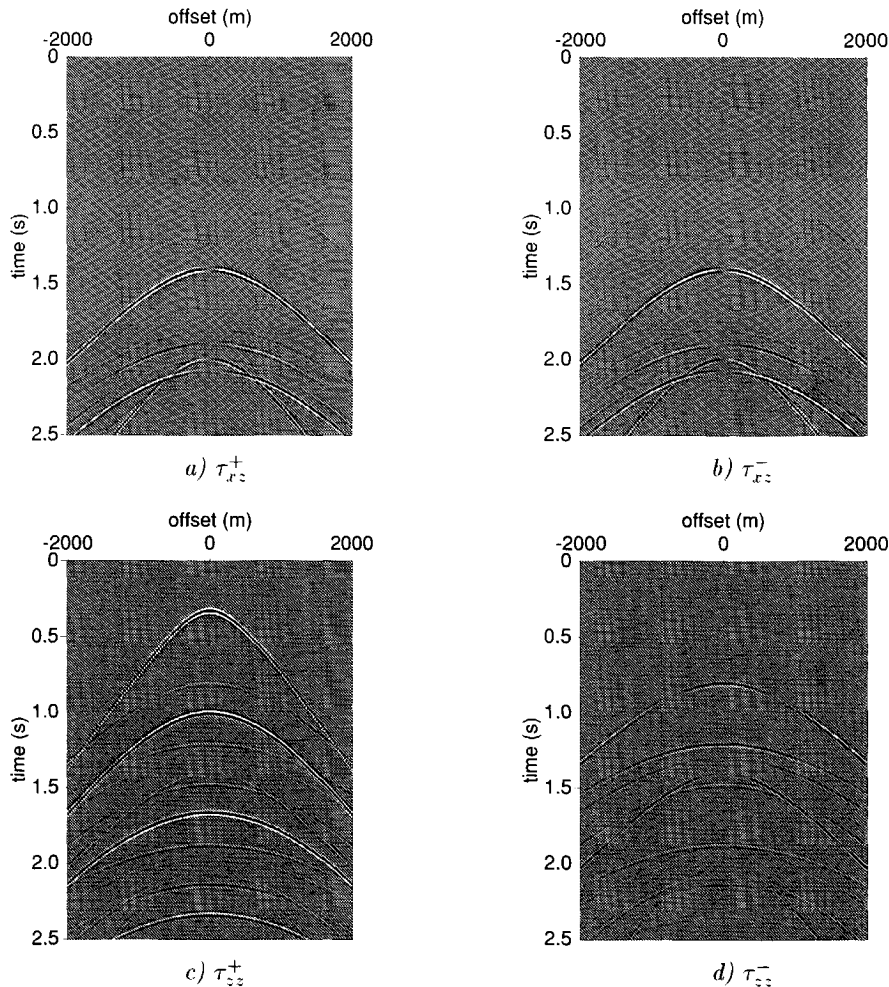


Fig. 2.5 Step 1 of elastic two-step decomposition just below the bottom, (a) downgoing shear stressfield, (b) upgoing shear stressfield, (c) downgoing normal stressfield, (d) upgoing normal stressfield.

2.4 An adaptive decomposition scheme

The two-step decomposition procedure makes it possible to apply an adaptive decomposition to ocean-bottom data without any a priori knowledge of the medium parameters just below the ocean-bottom and the calibration factors between the measurements of the different components. The proposed adaptive decomposition scheme consists of five stages. It makes use of three intermediate decomposition results from the acoustic decomposition and the elastic two-step decomposition. In the last stage the down- and upgoing P- and S-waves are obtained. The model parametrization is shown in Figure 2.6.

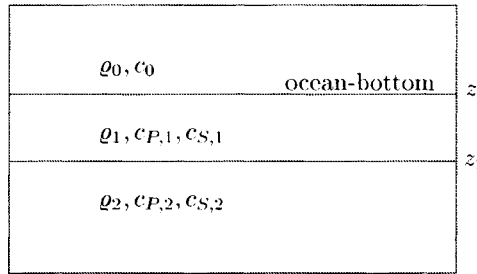


Fig. 2.6 Model parametrization.

Figure 2.7 gives an overview of the equations involved in the decomposition scheme. Figure 2.8 shows how the scheme is implemented in practice. The y -component of the particle velocity is not taken into account, which simplifies the application. In the following, each stage in the adaptive decomposition scheme will be treated separately.

Stage 1: Corrections for cross-coupling

In this first stage the measurement of the vertical velocity component (denoted by v_z') is corrected for imperfections in the acquisition that are not addressed further on in the scheme. Often when the pressure and vertical velocity components of field data are compared, strong events with a low moveout velocity are observed on the vertical velocity component that are not present on the pressure component. These events (presumably converted waves) will not be compensated for when the components are combined in the decomposition procedure and therefore they will deteriorate the decomposition result if they are not removed.

When v_z' would truly be that part of the wavefield with its displacement perpendic-

Ideal

1. rotation:

$$v_z = \cos \phi \cos \theta v_z' - \sin \phi v_x' - \cos \phi \sin \theta v_y'$$

$$v_x = \sin \phi \cos \theta v_z' + \cos \phi v_x' - \sin \phi \sin \theta v_y'$$

2. above bottom:

$$\tilde{P}^\pm = \frac{1}{2} \tilde{P} \pm \frac{\varrho_0}{2q_0} \tilde{V}_z$$

3. below bottom:

$$-\tilde{T}_{zz}^\pm = \frac{1}{2} \tilde{P} \pm \frac{\varrho_1 \beta_1}{2q_{P,1}} \tilde{V}_z$$

4. below bottom:

$$-\tilde{T}_{xz}^\pm = \pm \frac{\gamma_1 p}{2q_{S,1}} \tilde{P} \pm \frac{\varrho_1 \beta_1}{2q_{S,1}} \tilde{V}_x$$

5. below bottom:

$$\tilde{\Phi}^\pm = \frac{c_{S,1}^2}{\beta_1} \{ \mp 2pq_{S,1} \tilde{T}_{xz}^\pm - (c_{S,1}^{-2} - 2p^2) \tilde{T}_{zz}^\pm \}$$

$$\tilde{\Psi}^\pm = \frac{c_{S,1}^2}{\beta_1} \{ (c_{S,1}^{-2} - 2p^2) \tilde{T}_{xz}^\pm \mp 2pq_{P,1} \tilde{T}_{zz}^\pm \}$$

Fig. 2.7 Overview of the equations involved in the adaptive decomposition scheme. All decomposition equations are formulated in the rayparameter-frequency domain.

Practical

1. rotation and cross-coupling:

$$v_z = v_z' - r_1(t) * v_x' - r_2(t) * v_y'$$

$$v_x = v_x'$$

Criterion: similar events on p and v :

2. above bottom:

$$\tilde{P}^\pm = \frac{1}{2} \tilde{P} \pm A(\omega) \frac{\varrho_0}{2q_0} \tilde{V}_z$$

Criterion: no primaries in p^+

$$\Rightarrow a(t) \Rightarrow A(\omega)$$

3. below bottom:

$$-\tilde{T}_{zz}^\pm = \frac{1}{2} \tilde{P} \pm A(\omega) \tilde{F}(p) \tilde{V}_z$$

Criteria: no direct wave and no waterbottom multiples in τ_{zz}^-

$\Rightarrow \tilde{F}(p)$; inversion \Rightarrow estimates of $\varrho_1, c_{P,1}, c_{S,1}$

4. below bottom:

$$-\tilde{T}_{xz}^\pm = \pm \frac{\gamma_1 p}{2q_{S,1}} \tilde{P} \pm B(\omega) \frac{\varrho_1 \beta_1}{2q_{S,1}} \tilde{V}_x$$

Criterion: no direct wave in τ_{xz}^\pm

$$\Rightarrow b(t) \Rightarrow B(\omega)$$

5. below bottom:

$$\begin{aligned} \tilde{\Phi}^\pm &= \frac{c_{S,1}^2}{\beta_1} \{ \mp 2pq_{S,1} \tilde{T}_{xz}^\pm - (c_{S,1}^{-2} - 2p^2) \tilde{T}_{zz}^\pm \} \\ \tilde{\Psi}^\pm &= \frac{c_{S,1}^2}{\beta_1} \{ (c_{S,1}^{-2} - 2p^2) \tilde{T}_{xz}^\pm \mp 2pq_{P,1} \tilde{T}_{zz}^\pm \} \end{aligned}$$

Fig. 2.8 Overview of the adaptive decomposition scheme as it is applied in practice.

ular to the ocean-bottom, it should be expected that the same events are recorded as on the pressure component (although with different amplitudes)³. In the ideal case (perfect geophones, perfect coupling) the only deviation from v_z' compared to

³Due to the opposite sign of the reflection coefficients for pressure and vertical velocity, and the interference of different events, it is possible, though, to have situations where different events are seen on the two components.

the ‘true’ vertical particle velocity component could be a rotation caused by e.g. topography of the ocean-bottom. In Figure 2.7 only the rotational corrections to the vertical geophone component and the horizontal x -component are shown, as only these components are used in the further stages of the adaptive decomposition scheme. The full rotation operator for all three velocity components is given by:

$$\begin{pmatrix} v_x \\ v_y \\ v_z \end{pmatrix} = \begin{pmatrix} \cos \phi & -\sin \phi \sin \theta & \sin \phi \cos \theta \\ 0 & \cos \theta & \sin \theta \\ -\sin \theta & -\cos \phi \sin \theta & \cos \phi \cos \theta \end{pmatrix} \begin{pmatrix} v_x' \\ v_y' \\ v_z' \end{pmatrix}, \quad (2.189)$$

where ϕ is the in-line rotation angle and θ is the cross-line rotation angle (see Figure 2.9). Here it is assumed that only two angles are required to define the rotation, because the x -component is already oriented in the correct direction (i.e. the direction of the cable).

In practice (Figure 2.8), the vertical component is corrected by adaptively subtracting the horizontal components from it, in this way removing the unwanted horizontal motion from this component. For gimballed geophones the leaking of energy is mostly caused by so called ‘mechanical cross-coupling’ (Maxwell, 1998), meaning that the vertical geophone is also sensitive to horizontal motions, and the horizontal geophones to vertical motions. Conversely, the horizontal components can be contaminated with vertical motion, and need to be corrected for cross-coupling too. However, these components cannot be treated in the same way as the vertical component, as there is no similar calibration criterion. An additional correction in the horizontal plane was discussed in (Gaiser, 1998; Li and Yuan, 1999). Here, the horizontal components have been correctly orientated in the cable direction by minimization of the energy in the direct arrival on the crossline component. This correctly orients the horizontal components - assuming a roughly horizontally layered medium - but does not remove cross-contamination of vertical motion. However, the problem of cross-coupling might be solved in the future by more advanced measuring systems.

Stage 2: Acoustic decomposition just above the bottom

The acoustic decomposition just above the ocean-bottom is used to resolve the calibration filter $A(\omega)$ between the pressure and vertical velocity component. Modifying equation (2.163), gives in the p, ω -domain

$$\tilde{P}^\pm = \frac{1}{2} \tilde{P} \pm A(\omega) \frac{\varrho_0}{2q_0} \tilde{V}_z, \quad (2.190)$$

where ϱ_0 and q_0 are the density and vertical slowness of the water-layer. The calibration filter is supposed to include all differences between the hydrophone and the

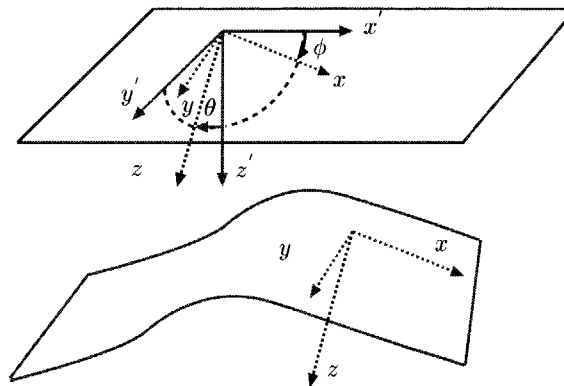


Fig. 2.9 The coordinate system x', y', z' is measured by a gimballed geophone system (the z -axis is vertical with respect to the water surface). Coordinate system x, y, z is rotated so that z is locally normal to the ocean-bottom, where ϕ is the rotation angle in the x, z plane and θ is the rotation angle in the y, z plane.

vertical geophone component that are not related to the actual wavefield propagation, such as differences in coupling and impulse response of the measuring devices. The acoustic decomposition operators in equation (2.190), $1/2$ and $\varrho_0/(2q_0)$, are already known (as they depend solely on the velocity and density of the water). This leaves $A(\omega)$ as the only unknown factor. To resolve $A(\omega)$ the extra condition is imposed that there should be no primary reflections present in the decomposed *downgoing* wavefield *above* the bottom (\tilde{P}^+). A least-squares optimization procedure on this criterion is performed in the time domain, within a window containing mainly primary reflections. As a result the convolution filter $a(t)$ is obtained, which is then transformed to the frequency domain. The procedure is shown schematically in Figure 2.8. Filter $A(\omega)$ is used as input to the next stage of the scheme. In Figure 2.10, the optimization result for the synthetic dataset is displayed. The window in between the gray lines in Figure 2.10a and b contains only primary reflections and should be empty after optimal subtraction of the \tilde{p} and \tilde{v}_z components (Figure 2.10c). As there are no coupling issues with synthetic data the coupling filter (Figure 2.10d) should be 1.

Stage 3: Elastic decomposition into τ_{zz}^\pm just below the bottom

The next stage is an elastic decomposition *below* the bottom, into up- and downgoing normal stressfields. As in the previous stage we are dealing again with the pressure and vertical velocity components. Modifying equation (2.182), gives in the p, ω -

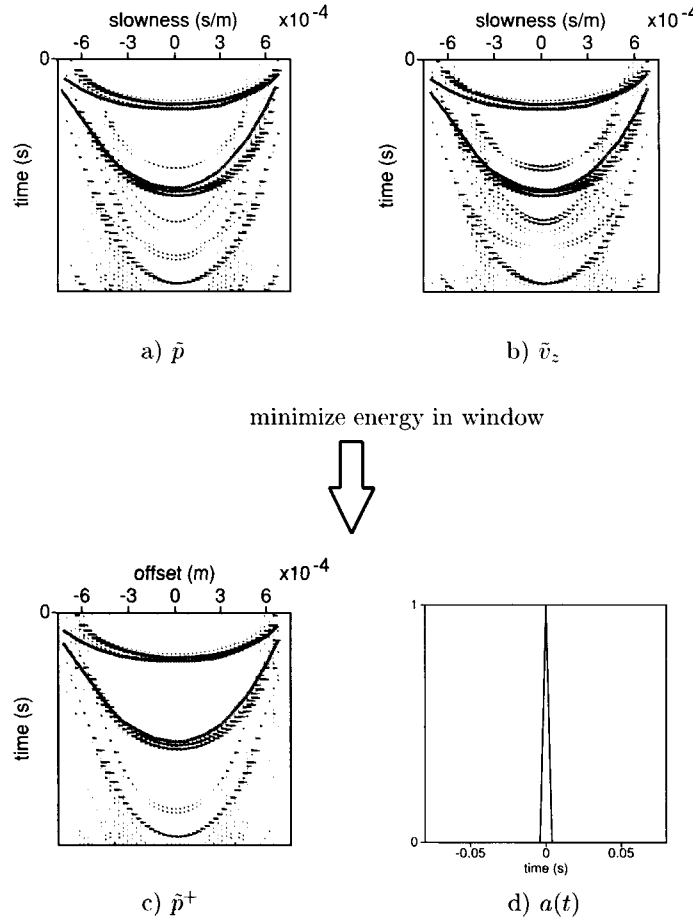


Fig. 2.10 Demonstration of the optimization procedure in stage 2 applied to the synthetic data. After multiplication of (a) with $\frac{1}{2}$ and (b) with $\frac{q}{2q}$ in the p, ω -domain, the gathers are subtracted from each other so that the energy in the window between the curved gray lines becomes minimal. The subtraction result is displayed in (c). The calibration filter (d) is approximately 1 for the synthetic data.

domain

$$-\tilde{T}_{zz}^{\pm} = \frac{1}{2}\tilde{P} \pm A(\omega) \frac{\varrho_1 \beta_1}{2q_{P,1}} \tilde{V}_z, \quad (2.191)$$

where ϱ_1 and $q_{P,1}$ are the density and vertical P-wave slowness of the medium just below the bottom.

The calibration filter $A(\omega)$ is already known from stage 2. This time the unknown factor is the operator in front of the \tilde{V}_z component, as it depends on the (unknown) medium parameters just below the bottom. To find the operator, the expression is replaced by a general rayparameter dependent filter $\tilde{F}(p)$:

$$-\tilde{T}_{zz}^{\pm} = \frac{1}{2}\tilde{P} \pm A(\omega)\tilde{F}(p)\tilde{V}_z. \quad (2.192)$$

The condition imposed on the decomposition result is that there should be no direct wave or water bottom multiples in the *upgoing* normal stressfield *below* the bottom. A least-squares optimization procedure on this criterion is implemented in the time domain within a window containing at least the direct arrival (see Figure 2.11). As a result a convolution filter $\hat{f}(p)$ is obtained which is then transformed to the frequency domain to obtain $\tilde{F}(p)$ ⁴ (Figure 2.11d). Note the absence of the water multiples and the direct (transmitted) source wave in the upgoing normal stress wavefield just below the bottom (Figure 2.11c), after subtraction.

An estimate of the medium parameters is obtained by inverting the filter $\tilde{F}(p) = (\varrho_1 \beta_1)/(2q_{P,1})$. The amplitude of the decomposition operator has the value of half the P-wave impedance for normal incidence, therefore an estimate of the impedance can be obtained from the amplitude of $\tilde{F}(p)$ at $p = 0$. The amplitude of $\tilde{F}(p)$ becomes very large when the rayparameter corresponds to the critical angle (i.e., when $p = \pm 1/c_{P,1}$), thus giving an estimate for $c_{P,1}$. A more detailed description of the inversion for the medium parameters is given in section 2.4.1. The estimates that were used for stage 4 and 5 are $c_{P,1} = 2083$ m/s, $c_{S,1} = 557$ m/s and $\varrho_1 = 2037$ kg/m³ (the actual values are in Table 2.2), and were obtained with the more robust inversion method (section 2.4.1).

Stage 4: Elastic decomposition into τ_{xz}^{\pm} just below the bottom

The fourth decomposition stage involves the pressure and horizontal inline velocity components, making it possible to resolve the calibration filter $B(\omega)$ between them.

⁴Theory predicts that the filter $\tilde{F}(p)$ is frequency independent. Due to the fact that the filter $\hat{f}(p)$ is obtained in the time-domain and the bandlimited nature of seismic data, some frequency dependency is always induced by the temporal Fourier transformation. However, within the bandwidth of the data the frequency dependency is negligible.

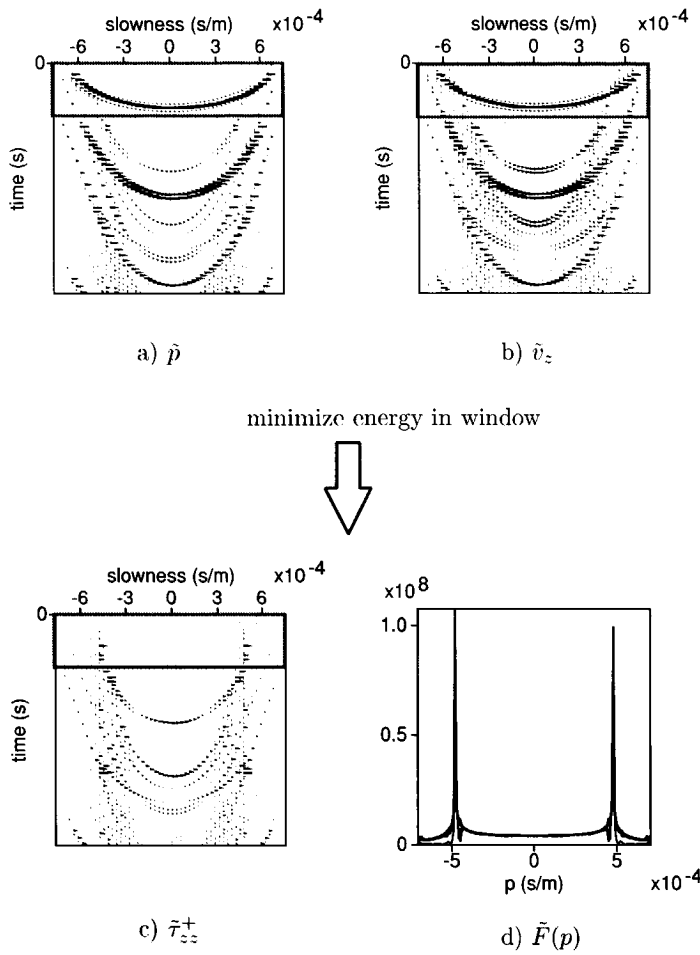


Fig. 2.11 Demonstration of the optimization procedure in stage 3 applied to the synthetic data. After multiplication of (a) with $\frac{1}{2}$ and (b) with $\frac{q\beta}{2q}$ in the p, ω -domain, the gathers are subtracted from each other so that the energy in the rectangular window becomes minimal. The subtraction result is displayed in (c). The decomposition operator $\tilde{F}(p)$ obtained after the optimization procedure is displayed in (d).

Modifying equation (2.181), gives in the p, ω -domain

$$-\tilde{T}_{xz}^{\pm} = \pm \frac{\gamma_1 p}{2q_{S,1}} \tilde{P} \pm B(\omega) \frac{\varrho_1 \beta_1}{2q_{S,1}} \tilde{V}_x. \quad (2.193)$$

From equation (2.193) it can be seen that first the decomposition operators, $(\gamma_1 p)/(2q_{S,1})$ and $(\varrho_1 \beta_1)/(2q_{S,1})$, must be calculated with the medium parameters just below the ocean-bottom found in stage 3, before $B(\omega)$ can be determined.

The condition for an optimal decomposition result is that there should be no direct wave in either the up- or downgoing shear stressfields (as discussed in section 2.3). Again the optimization procedure is implemented in the time domain in a window containing the direct arrival (Figure 2.12), and a convolution filter $b(t)$ is obtained (Figure 2.12d). After optimal subtraction of the components the direct wave is almost completely removed (Figure 2.12c). A small amount of energy remains due to the small differences between the inverted parameters and the model parameters.

Stage 5: Elastic decomposition into P- and S-wave potentials just below the bottom

In the last stage of the adaptive decomposition scheme the estimated parameters just below the ocean-bottom (stage 3) and the results of the elastic decomposition into down- and upgoing stressfields (stage 3 and stage 4) are simply combined to obtain the down- and upgoing P- and S-waves in the p, ω -domain. According to equation (2.188)

$$\tilde{\Phi}^{\pm} = \frac{c_{S,1}^2}{\beta_1} \{ \mp 2pq_{S,1} \tilde{T}_{xz}^{\pm} - (c_{S,1}^{-2} - 2p^2) \tilde{T}_{zz}^{\pm} \}, \quad (2.194)$$

$$\tilde{\Psi}^{\pm} = \frac{c_{S,1}^2}{\beta_1} \{ (c_{S,1}^{-2} - 2p^2) \tilde{T}_{xz}^{\pm} \mp 2pq_{P,1} \tilde{T}_{zz}^{\pm} \}. \quad (2.195)$$

The final decomposition results are displayed in Figure 2.13. Note that the direct wave has not been completely removed from the upgoing S-wavefield in Figure 2.13d. This is caused again by the small difference between the inverted parameters and the model parameters.

An alternative option would be to use the total (i.e. one-step) elastic decomposition (equations (2.157),(2.168),(2.169)) and the estimations of $A(\omega), c_{P,1}, c_{S,1}, \rho_1$, and $B(\omega)$. In Figure 2.14 the difference between the final decomposition result obtained with the adaptive decomposition scheme, and the decomposition results obtained with equations (2.157),(2.168),(2.169) and the model parameters is displayed. The small differences remaining can be attributed to numerical errors in the adaptive scheme and the small errors in the inversion for the parameters.

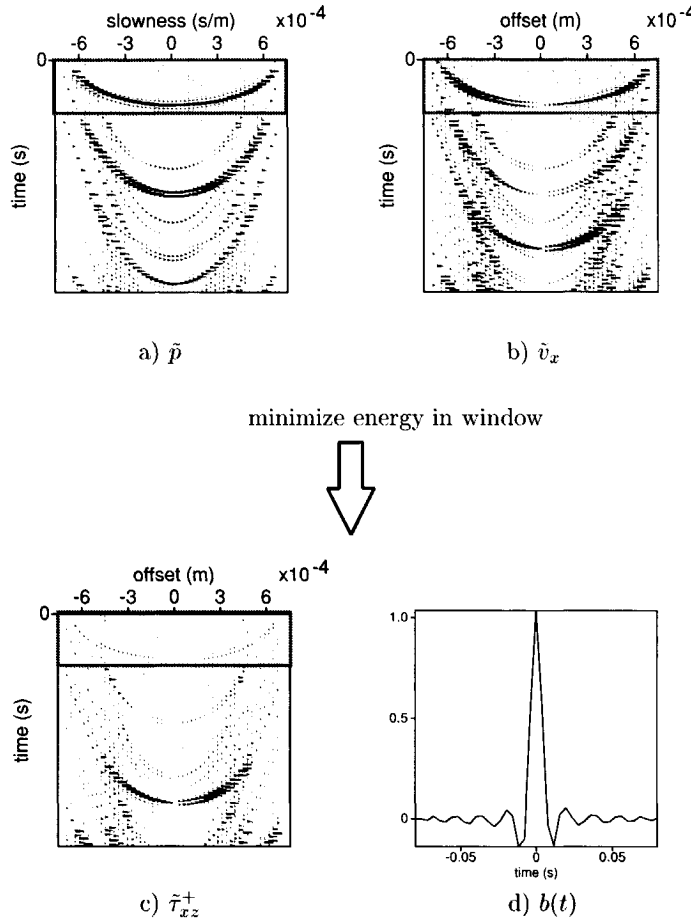


Fig. 2.12 Demonstration of the optimization procedure of stage 4 applied to the synthetic data. After multiplication of (a) with $\frac{\gamma_1 p}{2q_{S,1}}$ and (b) with $\frac{\rho_1 \beta_1}{2q_{S,1}}$ in the p, ω -domain, the gathers are subtracted from each other so that the energy in the rectangular window becomes minimal. The subtraction result is displayed in (c). The calibration filter (d) is approximately 1 for the synthetic data.

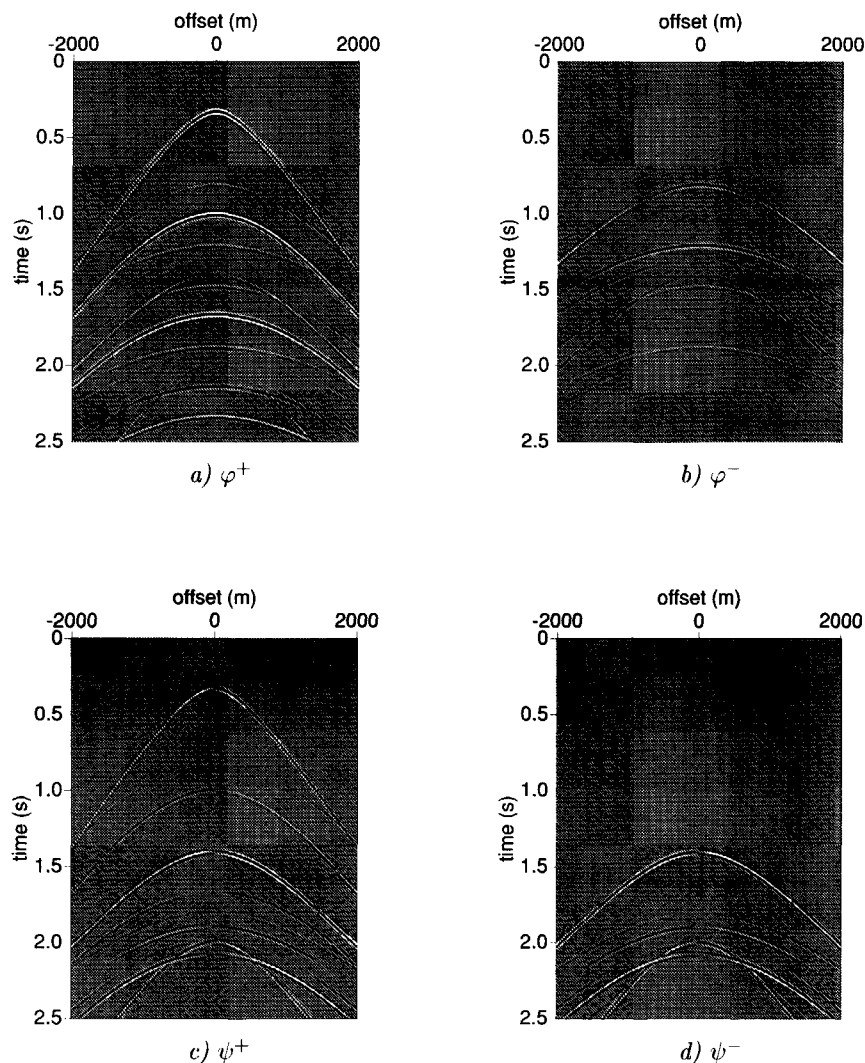


Fig. 2.13 Elastic decomposition results just below the bottom obtained with the adaptive decomposition scheme, (a) downgoing P-waves, (b) upgoing P-waves, (c) downgoing S-waves, and (d) upgoing S-waves.

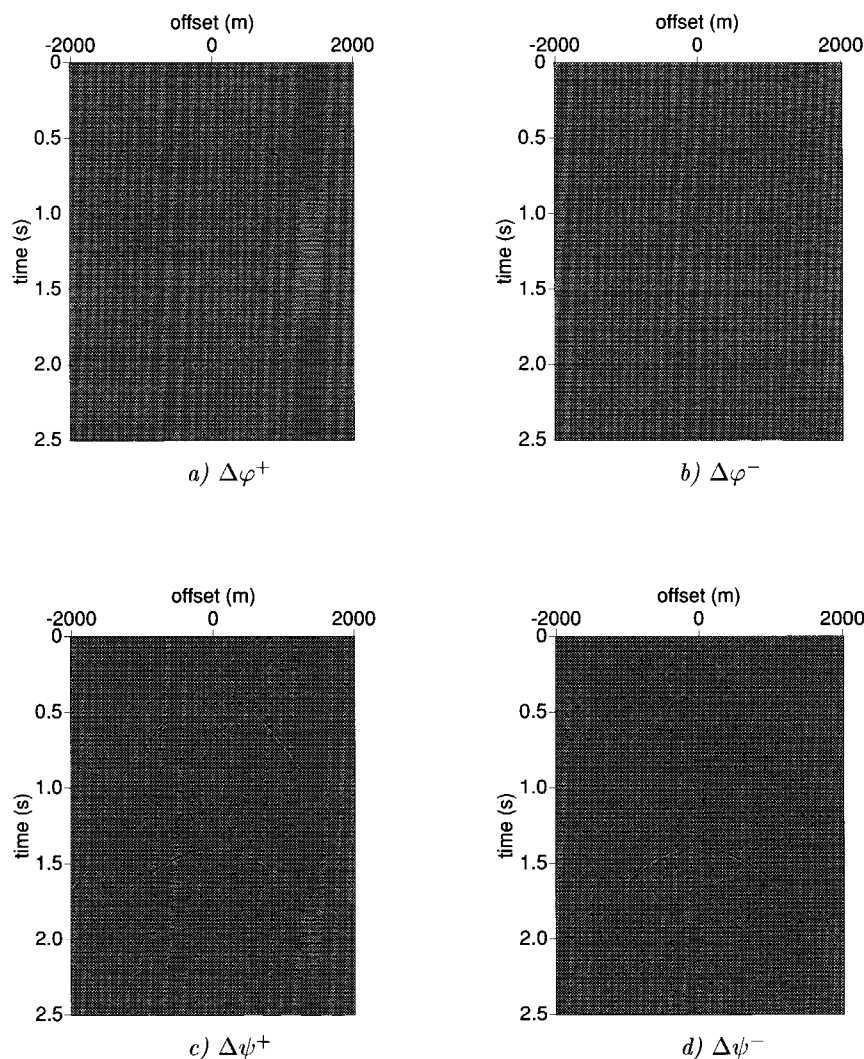


Fig. 2.14 Difference between elastic decomposition just below the bottom using equations (2.157), (2.168), (2.169) and the model parameters directly, and using the adaptive decomposition scheme, (a) downgoing P-waves, (b) upgoing P-waves, (c) downgoing S-waves, and (d) upgoing S-waves.

2.4.1 Frequency independent inversion of $\tilde{F}(p)$

An essential part in the adaptive decomposition scheme described above is the inversion for the medium parameters. Without the medium parameters the P- and S-wave decomposition cannot be accomplished. The decomposition operator $\frac{\varrho_1\beta_1}{2q_{P,1}}$ is fitted to the filter $\tilde{F}(p)$ estimated in stage 3 of the adaptive decomposition by a least-squares optimization procedure, to obtain values for the density, P- and S-velocity. The least-squares error is defined as

$$\epsilon(\mathbf{u}) = \sum_i \frac{1}{2} |\mathcal{F}(\mathbf{u}; p_i) - \tilde{F}(p_i)|^2, \quad (2.196)$$

$$\text{where } \mathcal{F}(\mathbf{u}; p) = \frac{\varrho_1\beta_1}{2q_{P,1}}, \quad \text{and } \mathbf{u} = (c_{P,1}, c_{S,1}, \varrho_1).$$

In the optimization procedure, $\epsilon(\mathbf{u})$ is minimized. An initial estimate of the medium parameters is obtained from the location of the singularities of $\tilde{F}(p)$ (giving $c_{P,1}$). From the amplitude of $\tilde{F}(p)$ at $p = 0$ (which is equal to half the P-wave impedance) an estimate of ϱ_1 is obtained. An initial estimate for $c_{S,1}$ is obtained by assuming a realistic velocity ratio ($c_{P,1}/c_{S,1}$). For the synthetic example a ratio of 4 was chosen. Once an initial estimate for \mathbf{u} has been obtained the actual curve fitting is done in the pre-critical rayparameter domain, in this case the rayparameter interval $[-4 \cdot 10^{-4}, 4 \cdot 10^{-4}]$ s/m was used. Otherwise the large amplitudes of the singularities influence the curve fitting too much. This is demonstrated in Figure 2.15, where the mismatch between $\tilde{F}(p)$ and the best fit, $\hat{F}(p)$, is displayed, using the whole rayparameter range. The error is displayed as a function of the discretization step dp with which $\tilde{F}(p)$ is sampled. The discretization step must be very small for the error to remain consistent.

In Figure 2.16 the filter $\tilde{F}(p)$, obtained from the synthetic data is displayed. The synthetic data belong to the horizontally layered model (Table 2.2) with parameters $c_{P,1} = 2100$ m/s, $c_{S,1} = 600$ m/s and $\varrho_1 = 2000$ kg/m³ just below the ocean-bottom. In the same figure the best fitting decomposition operator (line with dots) is given, which corresponds to the values $c_{P,1} = 2100.2$ m/s, $c_{S,1} = 599.2$ m/s and $\varrho_1 = 1984.6$ kg/m³. In Table 2.3 the medium parameter values for the initial estimate and the final estimate are compared to the model parameters. As can be seen the estimates are close to the true model. Only the density estimate has not improved compared to the initial estimate.

The inversion, using only the pre-critical rayparameter domain for the fitting of $\tilde{F}(p)$, is not robust enough when there is noise present in the data. In Figure 2.17, the sensitivity of $\tilde{F}(p)$ to the parameters c_P and c_S is investigated by calculating $\tilde{F}(p)$ for slightly different values and looking at the difference. From these figures it can be seen that the information on c_P is contained mainly in the singularity

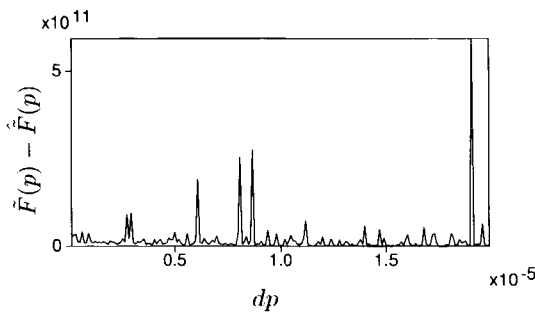


Fig. 2.15 Sensitivity of error (mismatch between $\hat{F}(p)$ and $\tilde{F}(p)$) to the discretization (stepsize of dp), including the singularities.

Table 2.3 Model parameters compared with inversion result.

model	P-velocity (m/s)	S-velocity (m/s)	density (kg/m ³)
initial estimate	2100	600	2000
final estimate (pre-critical)	2083.3	520.8	2001.7
modified inversion	2100.2	599.2	1984.6
	2083.3	557	2037

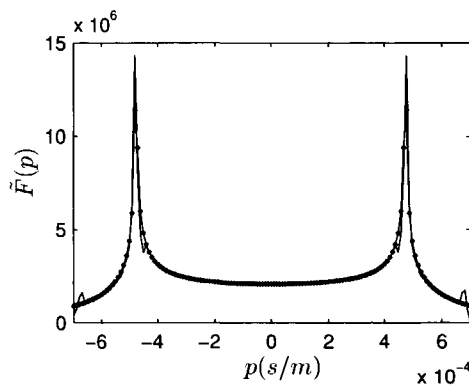


Fig. 2.16 The least-squares optimization filter together with the best-fitting decomposition operator (thick line) obtained from inversion.

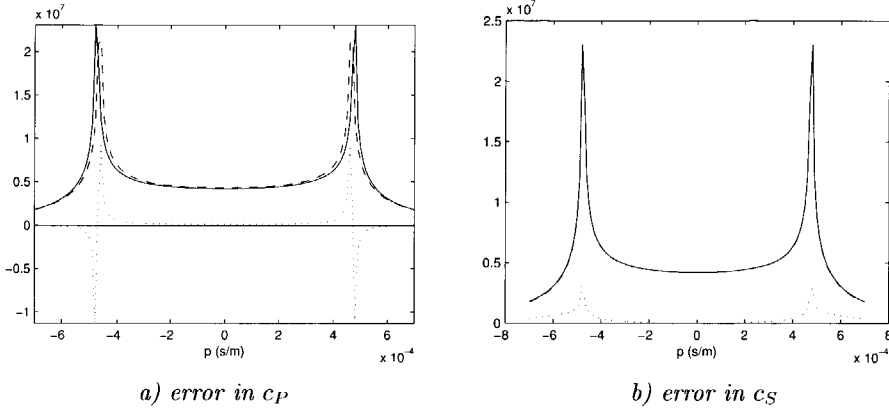


Fig. 2.17 Sensitivity of $\tilde{F}(p)$ to variations in, (a) c_P , and (b) c_S . The dotted line is the difference between (a) $\tilde{F}(p)$ for $c_P = 2100$ m/s and $c_P = 2150$ m/s, and (b) between $\tilde{F}(p)$ for $c_S = 600$ m/s and $c_S = 610$ m/s. The difference in (b) has been multiplied by 10 for display purposes.

location. The function $\tilde{F}(p)$ is most sensitive to c_S in the neighbourhood of the singularities. Because the singularities are not included in the curve-fitting, c_P is not well constrained in the optimization procedure. This may lead to c_P values far from the initial values, which is not desired. A second problem, in the presence of noise, is that the part of $\tilde{F}(p)$ that contains the information on c_S , is near the critical angle. Using only the rayparameter interval $[-4 \cdot 10^{-4}, 4 \cdot 10^{-4}]$ s/m, does not leave enough information to obtain reliable c_S estimates.

To obtain a more robust inversion, a modified inversion was used:

- First estimate c_P from singularity location.
- Keep c_P fixed, choose realistic c_S and estimate ϱ from a rayparameter interval around 0.
- Keep c_P and ϱ fixed, and estimate c_S from a larger rayparameter interval, but not including the singularities.

This inversion is more robust in the presence of noise. The parameters for the synthetic example estimated in this way are $c_{P,1} = 2083$ m/s, $c_{S,1} = 557$ m/s and $\varrho_1 = 2037$ kg/m³. For the synthetic data these estimates are a bit less accurate than with the previous inversion procedure (Table 2.3), but still acceptable.

2.5 Combined extrapolation/decomposition operators

In the adaptive decomposition scheme, discussed in the previous sections, it was implicitly assumed that the medium below the ocean-bottom was homogeneous at least up to a certain depth, so that the wavefield that is reflected from interfaces below the ocean-bottom is well separated in time from the wavefield that travels directly from source to ocean-bottom receiver. In this case, the decomposition operator $\tilde{F}(p)$, found by optimization, is indeed frequency-independent in the rayparameter-frequency domain (at least within the data bandwidth).

Let us consider the situation where there is a only a thin homogeneous layer present just below the ocean-bottom. The layer is thin enough for reverberations within the layer to interfere with the wave that travels directly from source to receiver. The optimization procedure that removes the ‘direct wave’, will now produce a frequency dependent operator $\tilde{F}(p, \omega)$ in the rayparameter-frequency domain (within the data bandwidth). The frequency dependency is explained by the fact that the operator $\tilde{F}(p, \omega)$ is not a pure decomposition operator anymore, but a combination of an extrapolation and a decomposition operator. The principle is illustrated by Figure 2.18. Figure 2.18a shows the situation where $\Delta z = z_2 - z_1$ is large enough to distinguish between the first reflection from below and the direct arrival from above. In this case, the optimization in stage 3 gives the upgoing wavefield just below z_1 and $\tilde{F}(p)$ is frequency independent within the bandwidth. In Figure 2.18b the situation is shown schematically where Δz is not large enough to distinguish between the direct and reflected arrivals. The optimization in stage 3, by removing not only the direct arrival but also the reverberations within the thin layer, now gives the upgoing wavefield just below the thin layer (i.e. just below z_2) and $\tilde{F}(p, \omega)$ is frequency dependent within the bandwidth. Of course there are other possible ocean-bottom models that would produce frequency dependent operators, another example would be ocean-bottoms with a velocity gradient in top.

For the simple case where the ocean-bottom model consists of a thin homogeneous layer on top of a half-space, an analytical expression for the operator $\tilde{F}(p, \omega)$ can be derived. This will be done first assuming an acoustic medium below the ocean-bottom, and then for an elastic medium below the ocean-bottom. With the latter expression it is then, in theory, possible to invert for all model-parameters in a thin-layer scenario, and use these parameters to obtain the upgoing P- and S-wave potentials just below z_2 .

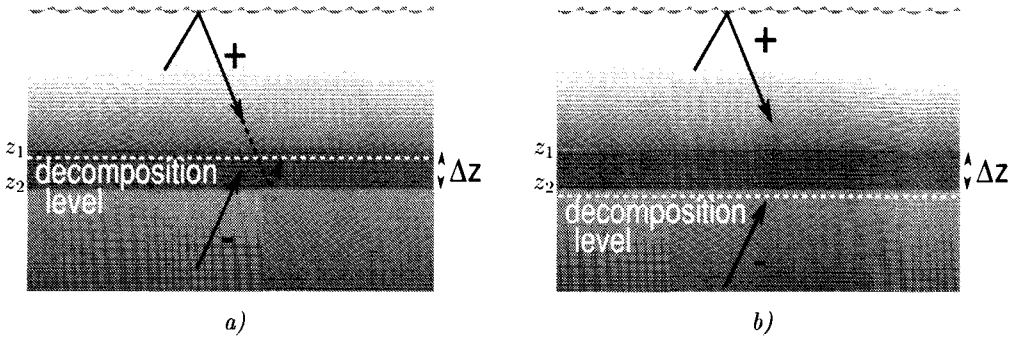


Fig. 2.18 Upgoing wavefield obtained after stage 3 of the adaptive decomposition scheme
a) with Δz large enough to distinguish between the direct arrival from above and first reflection from below, b) with Δz small enough to cause interference between the direct arrival and the first reflection from below.

2.5.1 Analytic expression for $\tilde{F}(p, \omega)$: forward model with thin layer

Acoustic case

As $\tilde{F}(p, \omega)$ removes the energy from the direct source arrival as well as the reverberations within the thin layer, this is similar to obtaining the upgoing field just below depth level z_2 (see Figure 2.18 b). A decomposition at z_2 is given by

$$\begin{pmatrix} \tilde{P}^+(z_2) \\ \tilde{P}^-(z_2) \end{pmatrix} = \frac{1}{2} \begin{pmatrix} 1 & \frac{\varrho_2}{q_2} \\ 1 & -\frac{\varrho_2}{q_2} \end{pmatrix} \begin{pmatrix} \tilde{P}(z_2) \\ \tilde{V}_z(z_2) \end{pmatrix}, \quad (2.197)$$

and $[\tilde{P}(z_2), \tilde{V}_z(z_2)]^T$ is related to the wavefield at the ocean-bottom (z_1) by the two-way wavefield extrapolation matrix (Wapenaar and Berkhouwt, 1989)

$$\begin{pmatrix} \tilde{P}(z_2) \\ \tilde{V}_z(z_2) \end{pmatrix} = \begin{pmatrix} \cos(\omega q_1 \Delta z) & -\frac{i\varrho_1}{q_1} \sin(\omega q_1 \Delta z) \\ \frac{q_1}{j\varrho_1} \sin(\omega q_1 \Delta z) & \cos(\omega q_1 \Delta z) \end{pmatrix} \begin{pmatrix} \tilde{P}(z_1) \\ \tilde{V}_z(z_1) \end{pmatrix}, \quad (2.198)$$

with $\Delta z = z_2 - z_1$.

Substituting equation (2.198) into equation (2.197) gives

$$\begin{pmatrix} \tilde{P}^+(z_2) \\ \tilde{P}^-(z_2) \end{pmatrix} = \frac{1}{2} \begin{pmatrix} \tilde{A} & -\frac{\varrho_1}{q_1} \tilde{B} \\ \tilde{C} & -\frac{\varrho_1}{q_1} \tilde{D} \end{pmatrix} \begin{pmatrix} \tilde{P}(z_1) \\ \tilde{V}_z(z_1) \end{pmatrix}, \quad (2.199)$$

where

$$\tilde{A} = \cos(\omega q_1 \Delta z) - \frac{j \varrho_2 q_1}{\varrho_1 q_2} \sin(\omega q_1 \Delta z), \quad (2.200)$$

$$\tilde{B} = j \sin(\omega q_1 \Delta z) - \frac{\varrho_2 q_1}{\varrho_1 q_2} \cos(\omega q_1 \Delta z), \quad (2.201)$$

$$\tilde{C} = \cos(\omega q_1 \Delta z) + \frac{j \varrho_2 q_1}{\varrho_1 q_2} \sin(\omega q_1 \Delta z), \quad (2.202)$$

$$\tilde{D} = j \sin(\omega q_1 \Delta z) + \frac{\varrho_2 q_1}{\varrho_1 q_2} \cos(\omega q_1 \Delta z). \quad (2.203)$$

The acoustic decomposition equation for the situation without the thin layer reads

$$\tilde{P}^-(z_1) = \frac{1}{2} \tilde{P}(z_1) - \tilde{F}(p) \tilde{V}_z(z_1), \quad (2.204)$$

where

$$\tilde{F}(p) = \frac{\varrho_1}{2q_1}. \quad (2.205)$$

For the situation with the thin layer, the upgoing wavefield below the layer is obtained with

$$\tilde{P}^-(z_2) = \frac{1}{2} \tilde{C} \tilde{P}(z_1) - \frac{\varrho_1}{2q_1} \tilde{D} \tilde{V}_z(z_1), \quad (2.206)$$

see equation (2.199). In practice the parameters of the thin layer and the layer underneath are unknown and therefore the operators \tilde{C} and \tilde{D} are unknown. When both sides of equation (2.206) are divided by \tilde{C} to obtain

$$\frac{\tilde{P}^-(z_2)}{\tilde{C}} = \frac{1}{2} \tilde{P}(z_1) - \tilde{F}(p, \omega) \tilde{V}_z(z_1), \quad (2.207)$$

with

$$\tilde{F}(p, \omega) = \frac{\varrho_1 \tilde{D}}{2q_1 \tilde{C}}. \quad (2.208)$$

And $\tilde{F}(p, \omega)$ can be obtained in the same way as $\tilde{F}(p)$ in equation (2.204). Note that in the case of a thin layer the upgoing wavefield obtained by matching \tilde{P} and \tilde{V}_z is a scaled version of the upgoing pressure wavefield just below the thin layer.

Elastic case

In the elastic case a decomposition just below z_2 into down- and upgoing normal stress wavefields is given by

$$\begin{pmatrix} -\tilde{T}_{zz}^+(z_2) \\ -\tilde{T}_{zz}^-(z_2) \end{pmatrix} = \frac{1}{2} \begin{pmatrix} -\frac{\gamma_2 p}{q_{P,2}} & 1 & 0 & \frac{\varrho_2 \beta_2}{q_{P,2}} \\ \frac{\gamma_2 p}{q_{P,2}} & 1 & 0 & -\frac{\varrho_2 \beta_2}{q_{P,2}} \end{pmatrix} \begin{pmatrix} -\tilde{T}_{xz}(z_2) \\ -\tilde{T}_{zz}(z_2) \\ \tilde{V}_x(z_2) \\ \tilde{V}_z(z_2) \end{pmatrix}, \quad (2.209)$$

see equation (2.180). Furthermore, $[-\tilde{T}_{xz}(z_2), -\tilde{T}_{zz}(z_2), \tilde{V}_x(z_2), \tilde{V}_z(z_2)]^T$ is related to the wavefield at the ocean-bottom (z_1) by the two-way elastic wavefield extrapolation matrix (Wapenaar et al., 1987)

$$\begin{pmatrix} -\tilde{T}_{xz}(z_2) \\ -\tilde{T}_{zz}(z_2) \\ \tilde{V}_x(z_2) \\ \tilde{V}_z(z_2) \end{pmatrix} = \begin{pmatrix} \tilde{W}_{11} & \tilde{W}_{12} & \tilde{W}_{13} & \tilde{W}_{14} \\ \tilde{W}_{21} & \tilde{W}_{22} & \tilde{W}_{23} & \tilde{W}_{24} \\ \tilde{W}_{31} & \tilde{W}_{32} & \tilde{W}_{33} & \tilde{W}_{34} \\ \tilde{W}_{41} & \tilde{W}_{42} & \tilde{W}_{43} & \tilde{W}_{44} \end{pmatrix} \begin{pmatrix} 0 \\ \tilde{P}(z_1) \\ \tilde{V}_x(z_1) \\ \tilde{V}_z(z_1) \end{pmatrix}. \quad (2.210)$$

The elements of the two-way elastic extrapolation matrix are dependent on the frequency, medium parameters and thickness of layer 1 and are given in (Appendix A, Wapenaar et al. (1987)). Substituting equation (2.210) into equation (2.209) gives

$$\begin{pmatrix} -\tilde{T}_{zz}^+(z_2) \\ -\tilde{T}_{zz}^-(z_2) \end{pmatrix} = \frac{1}{2} \begin{pmatrix} -\frac{\gamma_2 p}{q_{P,2}} & 1 & 0 & \frac{\varrho_2 \beta_2}{q_{P,2}} \\ \frac{\gamma_2 p}{q_{P,2}} & 1 & 0 & -\frac{\varrho_2 \beta_2}{q_{P,2}} \end{pmatrix} \begin{pmatrix} \tilde{W}_{11} & \tilde{W}_{12} & \tilde{W}_{13} & \tilde{W}_{14} \\ \tilde{W}_{21} & \tilde{W}_{22} & \tilde{W}_{23} & \tilde{W}_{24} \\ \tilde{W}_{31} & \tilde{W}_{32} & \tilde{W}_{33} & \tilde{W}_{34} \\ \tilde{W}_{41} & \tilde{W}_{42} & \tilde{W}_{43} & \tilde{W}_{44} \end{pmatrix} \begin{pmatrix} 0 \\ \tilde{P}(z_1) \\ \tilde{V}_x(z_1) \\ \tilde{V}_z(z_1) \end{pmatrix}, \quad (2.211)$$

or

$$-\tilde{T}_{zz}^-(z_2) = \frac{1}{2} \tilde{A} \tilde{P}(z_1) - \tilde{B} \tilde{V}_z(z_1) - \tilde{C} \tilde{V}_x(z_1), \quad (2.212)$$

where

$$\tilde{A} = \frac{\gamma_2 p}{q_{P,2}} \tilde{W}_{12} + \tilde{W}_{22} - \frac{\varrho_2 \beta_2}{q_{P,2}} \tilde{W}_{42}, \quad (2.213)$$

$$\tilde{B} = -\frac{\gamma_2 p}{2q_{P,2}} \tilde{W}_{14} - \frac{1}{2} \tilde{W}_{24} + \frac{\varrho_2 \beta_2}{2q_{P,2}} \tilde{W}_{44}, \quad (2.214)$$

$$\tilde{C} = -\frac{\gamma_2 p}{2q_{P,2}} \tilde{W}_{13} - \frac{1}{2} \tilde{W}_{23} + \frac{\varrho_2 \beta_2}{2q_{P,2}} \tilde{W}_{43}. \quad (2.215)$$

The elastic decomposition equation for the situation without the thin layer reads

$$-\tilde{T}_{zz}^-(z_1) = \frac{1}{2} \tilde{P}(z_1) - \tilde{F}(p) \tilde{V}_z(z_1) \quad (2.216)$$

where

$$\tilde{F}(p) = \frac{\varrho_1 \beta_1}{2q_{P,1}}. \quad (2.217)$$

For the situation with the thin layer the upgoing wavefield is given by equation (2.212). In practice the parameters of the thin layer and the layer underneath are

unknown and therefore the operator \hat{A} is unknown. Dividing both sides of equation (2.212) by \hat{A} gives

$$-\frac{\hat{T}_{zz}^-(z_2)}{\hat{A}} = \frac{1}{2}\hat{P}(z_1) - \hat{F}_1(p, \omega)\hat{V}_z(z_1) - \hat{F}_2(p, \omega)\hat{V}_x(z_1), \quad (2.218)$$

with $\hat{F}_1(p, \omega) = \frac{\hat{B}}{\hat{A}}$ and $\hat{F}_2(p, \omega) = \frac{\hat{C}}{\hat{A}}$. Now $\hat{F}_1(p, \omega)$ can be obtained in the same way as $\hat{F}(p)$ in equation (2.216), provided the contribution of the horizontal particle velocity component can be neglected. Note that in the case of a thin layer the upgoing wavefield obtained by matching \hat{P} and \hat{V}_z is a scaled version of the upgoing normal stressfield just below the thin layer. Inverting the expression for $\hat{F}_1(p, \omega)$ results in seven medium parameters - the velocities and densities of the thin layer and the medium beneath, and the thickness of the thin layer.

2.5.2 Frequency-dependent inversion

The extrapolation/decomposition operator B/A is fitted to the filter $\hat{F}_1(p, \omega)$ by a least-squares optimization procedure to obtain values for the density and P- and S-velocity of layer 1 and 2 and the thickness of layer 1. The least-squares error is defined as

$$\epsilon(\mathbf{u}) = \sum_i \sum_j \frac{1}{2} |\mathcal{F}(\mathbf{u}; p_j, \omega_i) - \hat{F}_1(p_j, \omega_i)|^2, \quad (2.219)$$

where $\mathcal{F}(\mathbf{u}; p, \omega) = \frac{B(\mathbf{u}; p, \omega)}{A(\mathbf{u}; p, \omega)}$,

and $\mathbf{u} = (c_{P,1}, c_{S,1}, \varrho_1, c_{P,2}, c_{S,2}, \varrho_2, \Delta z)$.

In the optimization procedure, $\epsilon(\mathbf{u})$ is minimized.

To obtain synthetic data for the thin-layer scenario, a layer with a thickness of 20 meters is added to the model used in the previous examples (see Table 2.4). The optimization criterion used to determine the operator $\hat{F}_1(p, \omega)$ is the removal of the direct arrival. As the removal of the direct arrival is easiest determined in the time-domain, the least-squares optimization procedure is implemented in the $\tau - p$ domain, and the obtained operator is actually $\hat{f}_1(p, \tau)$. The optimization operator is displayed in the $\tau - p$ domain in Figure 2.19a. For comparison, an example of an optimization filter obtained from field data is also shown (Figure 2.19b). If the optimization operator would be frequency-independent, it would be represented by a delta function in the time domain - or because of the limited bandwidth of the data, a sinc function. This is obviously not the case in Figure 2.19a. A physical interpretation of this operator in the time domain can be given. The first event aligning at $\tau = 0$ removes the direct arrival, the later events take care of the removal of the reverberations inside the thin layer. The time-difference (denoted by $\Delta\tau$

in Figure 2.19a) at $p = 0$ (i.e. at normal incidence of the wavefield) between the successive events is the two-way traveltime within the thin layer.

Table 2.4 Model parameters used for the generation of synthetic data with a thin layer.

depth (m)	P-velocity (m/s)	S-velocity (m/s)	density (kg/m ³)
0 - 480	1500	0	1000
480 - 500	1700	100	1470
500 - 1000	2100	600	2000
1500 - 2000	2500	1700	2200
> 2500	3000	1900	2500

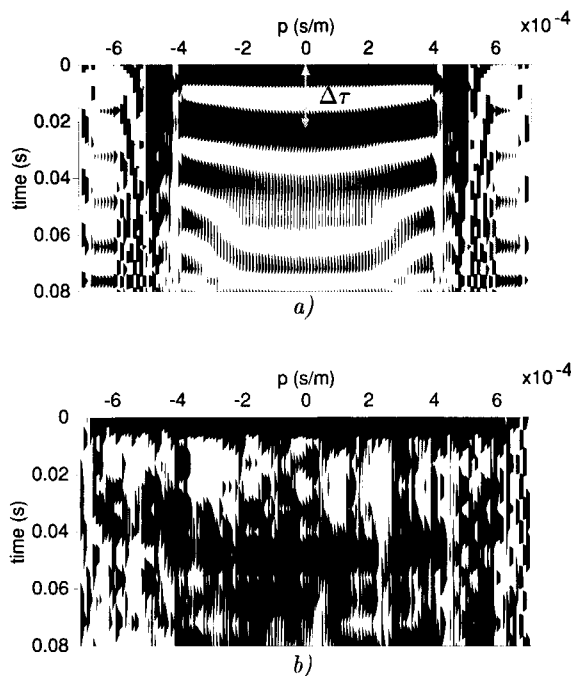


Fig. 2.19 The filter $\hat{f}_1(p, \tau)$ in the rayparameter-time domain, (a) filter for the synthetic data and (b) filter obtained from a field dataset.

The initial estimates of c_P for the first and second layer are taken from the values of the rayparameter p at the location of the singularities of $\tilde{F}_1(p, \omega)$. The densities are initially given the same value as the P-velocities. An initial estimate for c_S is obtained by assuming a velocity ratio (c_P/c_S) of 10 in the first layer and a ratio of 4 in the second layer. The thickness of layer 1 is estimated by using the time difference in $\hat{f}_1(p, \tau)$ at $p = 0$ between $\tau = 0$ and the first reverberation in the $\tau - p$ domain (see Figure 2.19a) as the two-way vertical traveltime in the first layer ($\Delta z = \frac{1}{2}c_{P,1}\Delta\tau$). The initial estimates are given in Table 2.5.

Once an initial estimate for \mathbf{u} has been obtained, the actual curve fitting is done in the pre-critical rayparameter domain $[-4 \cdot 10^{-4}, 4 \cdot 10^{-4}]$ s/m in the frequency range up to 60 Hz (see Figure 2.20). Also some boundary conditions are used to restrict the optimization procedure:

- The lower boundaries for the medium parameters of layer 1 are put at $c_P = 1400$ m/s, $c_S = 0$ m/s and $\varrho = 1000$ kg/m³.
- The minimum layer thickness is 1 m and the maximum is 100 m.
- The upper boundaries for the P-wave velocities c_P of both layers are not allowed to lie too far from the singularity positions.
- The upper boundaries for the S-wave velocities c_S of both layers are not allowed to be larger than $\sqrt{\frac{3}{4}}c_{P,\max}$ ⁵.

In Table 2.5 the medium parameter values for the initial estimate and the final estimate are compared to the true values. In Figure 2.20 the filter $\tilde{F}_1(p, \omega)$ is displayed obtained from the synthetic data belonging to a horizontally layered model with the parameters given in Table 2.5. In the same figure the best fitting decomposition operator (thick line) is given, which corresponds to the values of the final estimate (Table 2.5). The obtained fit is good (the filter and the decomposition operator overlap almost completely), and the final estimate for the medium parameters is reasonably close to the true model parameters.

2.6 Incorporation of a thin layer in the adaptive decomposition scheme

After the inversion for the seven parameters that describe the thin layer model, the end result - down- and upgoing P- and S-waves just below z_2 - still has to be obtained. To incorporate the previously discussed theory into the adaptive decomposition scheme discussed in section 2.4, it is necessary to calculate the down- and

⁵Using the definitions $c_P = \sqrt{(K + \frac{4}{3}\mu)\varrho^{-1}}$ and $c_S = \sqrt{\mu\varrho^{-1}}$, and taking $K \geq 0$, it follows that $c_S \leq \sqrt{\frac{3}{4}}c_P$.

Table 2.5 Model parameters compared with inversion result.

	P-velocity (m/s)	S-velocity (m/s)	density (kg/m3)	Δz (m)
model (layer 1)	1700	100	1470	20
initial estimate	1655.1	166	1655.1	19
final estimate	1711.3	112.8	1440.6	20.4
model (layer 2)	2100	600	2000	-
initial estimate	2155.1	538.8	2155.1	-
final estimate	2081.9	627.5	1968.2	-

upgoing normal and shear stressfields just below z_2 . These stressfields are input to stage 5 that gives the down- and upgoing P- and S-waves just below z_2 . For stage 5 the old equations (2.194) and (2.195) are used, except this time with the medium parameters just below z_2 . The extension of the adaptive decomposition scheme is displayed schematically in Figure 2.21.

In Figure 2.22a,b the synthetic data are displayed that belong to the configuration without the thin layer (Table 2.2), after a decomposition into down- and upgoing normal stressfields just below z_1 (see Figure 2.18a). In Figure 2.22c,d the synthetic data are displayed that belong to the configuration with the thin layer (Table 2.4), after a decomposition into down- and upgoing normal stressfields just below z_2 (see Figure 2.18b), using extrapolation and decomposition operators according to equation (2.211). Note that Figures 2.22c,d are almost the same as 2.22a,b except for a lengthening of the wavelet in the downgoing normal stressfield due to the reverberations within the thin layer.

In Figure 2.23a,b the synthetic data are displayed that belong to the configuration without the thin layer (Table 2.2), after a decomposition into down- and upgoing shear stressfields just below z_1 . In Figure 2.23c,d the synthetic data are displayed that belong to the configuration with the thin layer (Table 2.4), after a decomposition into down- and upgoing shear stressfields just below z_2 , using extrapolation and

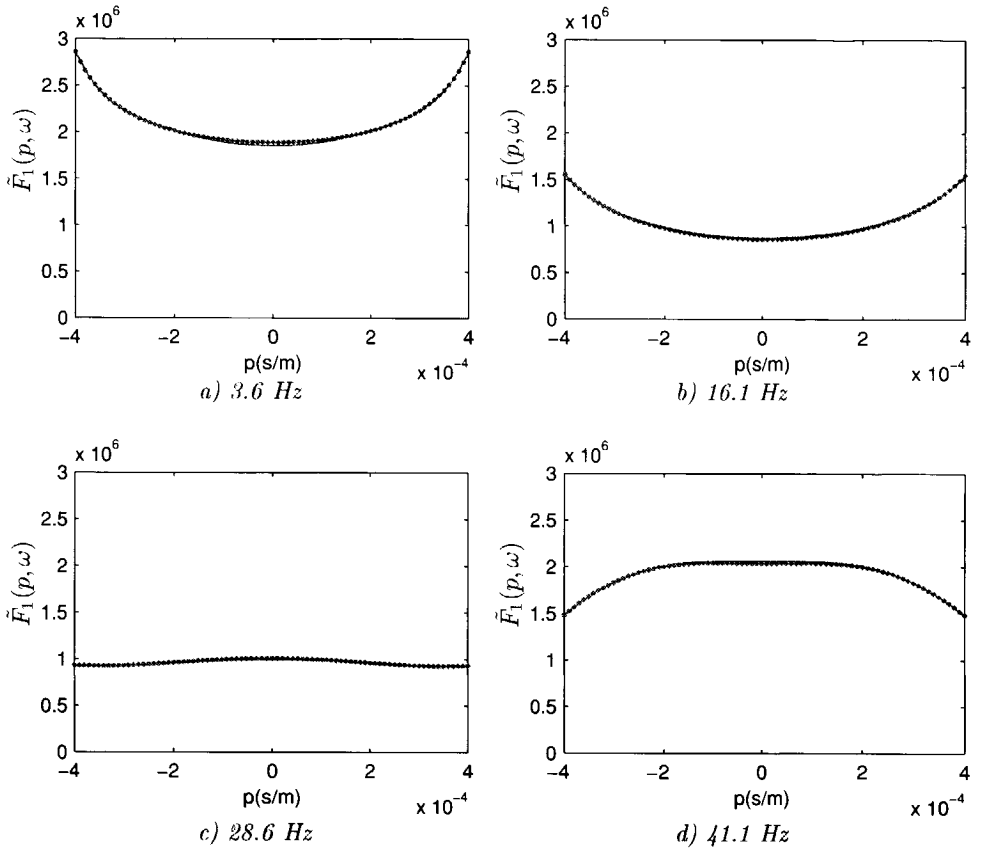


Fig. 2.20 Comparison of least-squares filter with analytic filter (thick line) calculated with the estimated parameters in Table 2.5 for four different frequencies ($\omega/2\pi$).

decomposition operators according to:

$$\begin{pmatrix} -\tilde{T}_{xz}^+(z_2) \\ -\tilde{T}_{xz}^-(z_2) \end{pmatrix} = \frac{1}{2} \begin{pmatrix} 1 & \frac{\gamma_2 p}{q_{S,2}} & \frac{\varrho_2 \beta_2}{q_{S,2}} & 0 \\ 1 & -\frac{\gamma_2 p}{q_{S,2}} & -\frac{\varrho_2 \beta_2}{q_{S,2}} & 0 \end{pmatrix} \begin{pmatrix} \tilde{W}_{11} & \tilde{W}_{12} & \tilde{W}_{13} & \tilde{W}_{14} \\ \tilde{W}_{21} & \tilde{W}_{22} & \tilde{W}_{23} & \tilde{W}_{24} \\ \tilde{W}_{31} & \tilde{W}_{32} & \tilde{W}_{33} & \tilde{W}_{34} \\ \tilde{W}_{41} & \tilde{W}_{42} & \tilde{W}_{43} & \tilde{W}_{44} \end{pmatrix} \begin{pmatrix} 0 \\ \tilde{P}(z_1) \\ \tilde{V}_x(z_1) \\ \tilde{V}_z(z_1) \end{pmatrix}. \quad (2.220)$$

In this case the upgoing shear stressfield (Figure 2.23d) looks almost identical to Figure (2.23b), but the downgoing shear stressfields below z_1 (Figure 2.23a) and

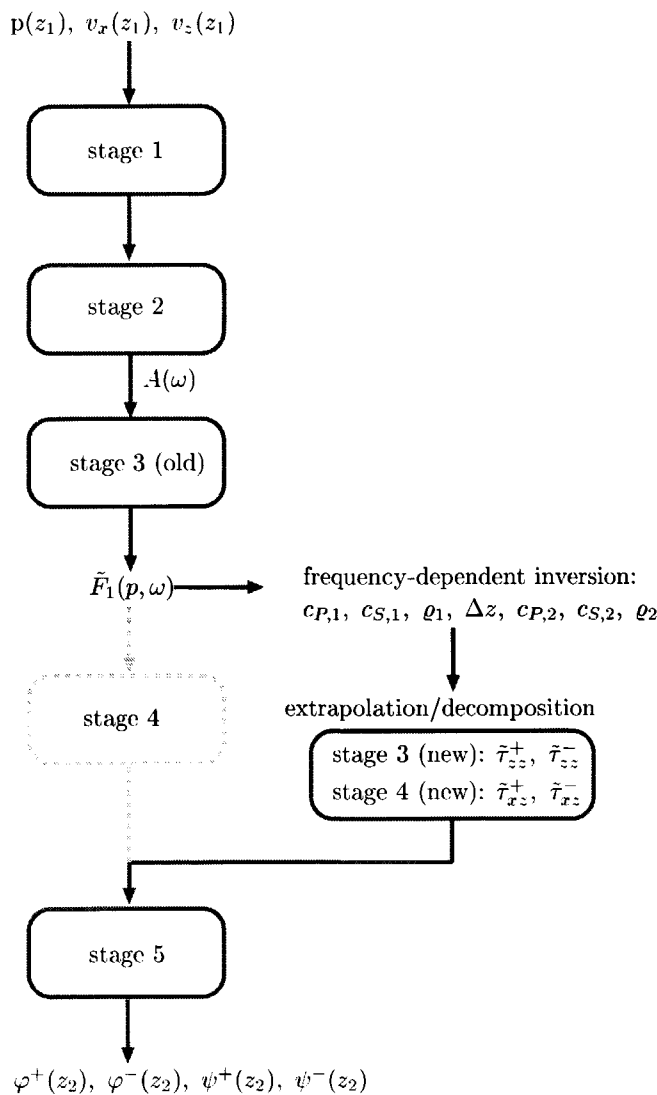


Fig. 2.21 Adaptive decomposition scheme for an ocean-bottom model with a thin layer just below the ocean-bottom.

below z_2 (Figure 2.23c) look different due to the reverberations within the thin layer. Also note that at the ocean-bottom one of the boundary conditions is that $\tau_{xz}(z_1) = 0$, and therefore it follows that the down- and upgoing shear stressfields just below the ocean-bottom are equal except for opposite polarity, $\tau_{xz}^+(z_1) = -\tau_{xz}^-(z_1)$. At z_2 this boundary condition is not valid: $\tau_{xz}^+(z_2) \neq -\tau_{xz}^-(z_2)$. This explains why the downgoing and upgoing shear stressfields at z_2 do not look alike.

2.7 Limitations in the application of the decomposition operators.

The acoustic and elastic composition and decomposition operators, were derived in section 2.1 in the wavenumber-frequency domain, for the situation of a laterally homogeneous medium (only variations with respect to the depth coordinate are present). However, the derived composition/decomposition relations

$$\begin{aligned}\tilde{\mathbf{Q}}(z) &= \tilde{\mathbf{L}}(z)\tilde{\mathbf{D}}(z), \\ \tilde{\mathbf{D}}(z) &= \tilde{\mathbf{L}}^{-1}(z)\tilde{\mathbf{Q}}(z),\end{aligned}$$

(equations 2.137, 2.138) have a wider applicability than solely laterally homogeneous media. The composition/decomposition operators are applied locally at a fixed depth level (e.g. the ocean-bottom) and therefore only require lateral homogeneity around the considered depth level z . Hence, for OBC applications, the medium below the ocean-bottom can be arbitrarily complex, except at the level directly below the ocean-bottom where the decomposition takes place.

The OBC data that are considered in sections 2.2-2.6, are recorded along a line-profile. For this situation, only a 2-D image of the subsurface (in the x, z -plane) can be obtained, and the medium has to be assumed invariant in the y direction. Invariancy in the y direction corresponds to a line-source parallel to the y -axis, and therefore the recorded wavefield is only a function of the x and z coordinates. When the subsurface as well as the wavefield are assumed independent of the y coordinate, we speak of a 2-D assumption. Moreover, with 2-D OBC data the source emits only P-waves in the x, z -plane, and therefore v_y will be zero. The assumption for the 2-D adaptive decomposition scheme of section 2.4 is a laterally homogeneous medium directly below the ocean-bottom, again the medium below can be arbitrarily complex. If there is strong lateral variation present just below the ocean-bottom, instead of matrix multiplications in the wavenumber-frequency domain, the decomposition operators will have to be applied in the space-frequency domain as short local convolution operators (Herrmann, 1992). This makes it possible to take space dependency within the receiver aperture into account, and in addition allows for irregularly spaced detectors. This approach will not be applied in this thesis.

When applying the decomposition procedure to real OBC data (Chapters 3 and 4),

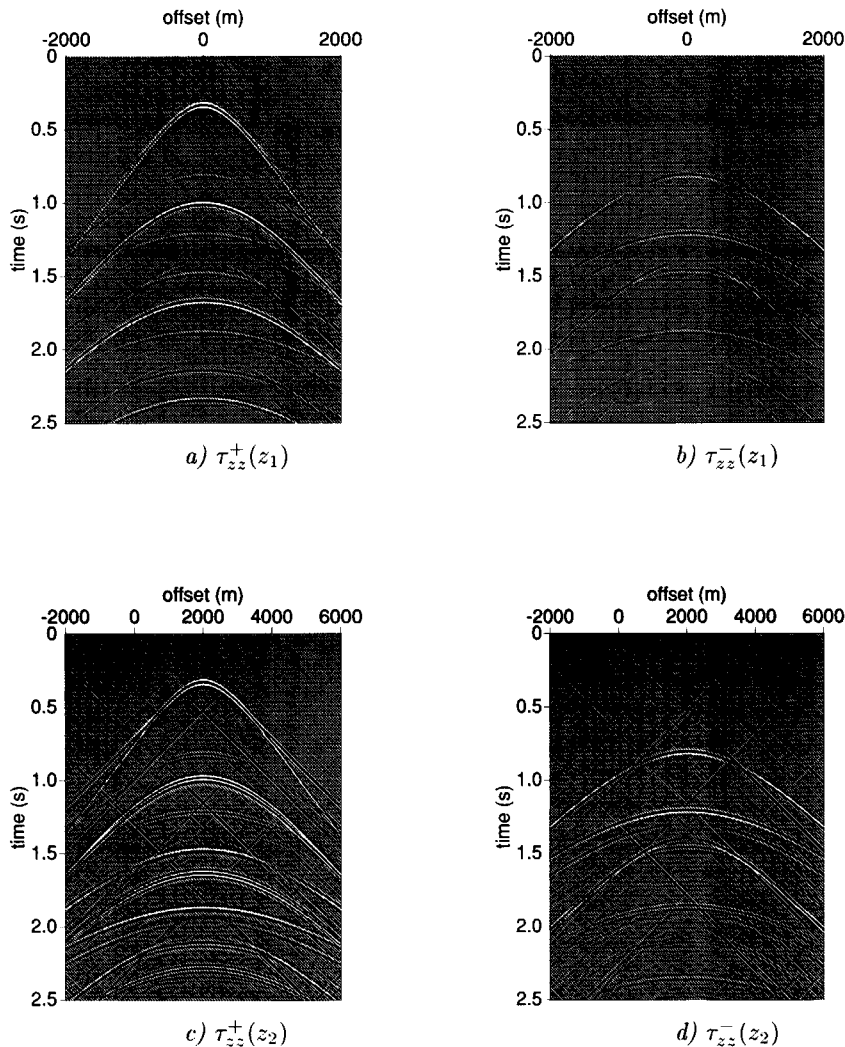


Fig. 2.22 Comparison of decomposition results for τ_{zz}^{\pm} for the synthetic dataset of the ocean-bottom model without thin layer (a,b) and with thin layer (c,d).

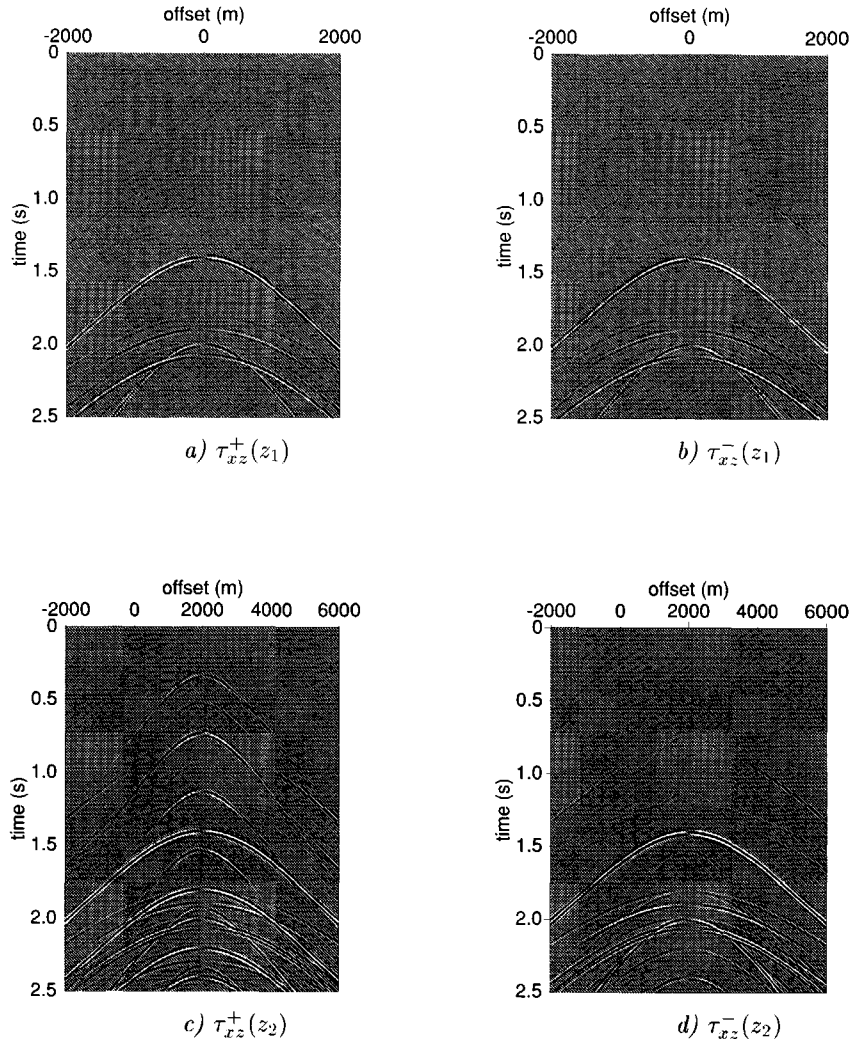


Fig. 2.23 Comparison of decomposition results for τ_{xz}^{\pm} for the synthetic dataset of the ocean-bottom model without thin layer (a,b) and with thin layer (c,d).

there are two additional issues. The data are acquired with point sources instead of with line sources, and secondly, the coupling of the receivers to the ocean-bottom can vary per receiver component.

To treat the amplitudes correctly (as the decomposition theory expects line sources instead of point sources) a geometric spreading correction should be applied. One could correct the wavefield from 3D-spreading to 2D-spreading by transformation from a point-source to a line-source (Wapenaar et al., 1992), or, equivalently, use cylindrical wave decomposition operators (Herrmann, 1992). The transformation from 3-D to 2-D spreading assumes a 1-D medium. This assumption can be relaxed somewhat by applying the transformation to common-midpoint gathers. For the datasets in Chapters 3,4 and 5 of this thesis a simple geometric spreading correction of \sqrt{t} has been applied, which assumes a homogeneous macro model. Although this is not fully correct in terms of amplitudes, the composition/decomposition equations are robust to errors made in the spreading correction, as was also found by Osen (1998).

Furthermore, in the application of wavefield decomposition to field datasets, coupling issues of the geophones have to be dealt with. It is often more practical to work with common-receiver gathers than with common-shot gathers (the latter should be done in accordance to theory), so that one coupling factor can be estimated per receiver gather. Moreover, other practical considerations, like aperture of common-receiver gathers vs. common-shot gathers and static correction, can make it preferable to work with common-receiver gathers. For laterally homogeneous media, common-shot gathers are equivalent to common-receiver gathers and this is not an issue. In the case of only locally laterally homogeneous media, common-shot gathers and common-receiver gathers are generally not identical. Depending on the degree of structure, this could cause events to be mapped onto (slightly) wrong p -values in the rayparameter domain. Although the assumption of a 1-D medium has to be made to substitute common-shot gathers by common-receiver gathers, in practice, wavefield decomposition applied in this way, still works quite well for mildly laterally inhomogeneous media. Limitations imposed by the theory will be further discussed with the field data examples.

Chapter 3

Wavefield decomposition: practical aspects for the deep to medium-depth ocean-bottom

The wavefield decomposition procedure is illustrated on two field data examples of the North Sea. The first example is for a deep ocean-bottom (~ 1200 m) dataset from the Vøring field, where the effects of the decomposition procedure can be clearly seen. However, from this dataset only one receiver gather was available. The second example is for a water depth of ~ 300 m from the Snorre field from which a 2D dataset was available. Both examples have relatively deep water bottoms. This simplifies the application of the adaptive decomposition scheme in a number of ways, as there is less interference between events. Therefore, these datasets are appropriate for a first evaluation of the performance of the adaptive decomposition scheme.

3.1 A deep ocean-bottom example: Vøring

The deep ocean-bottom field dataset (~ 1200 m), provided by Saga Petroleum A.S.A., has been acquired in the Vøring area, offshore Norway and is described in Brink et al. (1996). From this dataset one receiver position at the ocean-bottom was available where both the pressure and the particle velocity were measured. This receiver position has a full coverage of 401 shots at the sea-surface, with a shot interval of approximately 25 meters, resulting for each component in a common-receiver gather of 401 traces with 25 meters spacing (Figure 3.1). The frequency content of the data lies in the range of 1-60 Hz.

The decomposition theory treated in the previous chapter describes the decomposition operators to perform a decomposition at the receiver side and should therefore be applied to common-shot gathers. As there is only a common-receiver gather available, it will therefore be treated as if it were a common-shot gather. Strictly

speaking, this assumption necessitates a 1-D medium, as was discussed in section 2.7. The common-receiver gathers in Figure 3.1 for the four raw data components, exhibit a fairly symmetric behaviour around zero-offset and therefore indicate that the medium is approximately horizontally layered. If this is indeed the case, the amplitudes can be transformed from point-sources to line-sources using a 3-D to 2-D amplitude transformation (Wapenaar et al., 1992). However, the transformation resulted in a discontinuity at zero-offset on the receiver gathers. Apparently, the data are not symmetric enough across zero-offset to use the 3-D/2-D transformation. There is also no possibility to form CMP-gathers for this particular dataset, so the data have instead been corrected by multiplication of the amplitudes with the square-root of time. Even with this simple correction, the 2-D decomposition scheme still seems to work reasonably well (Schalkwijk et al., 1999).

Stage 1: Corrections for cross-coupling

In this first stage the v_z measurement is corrected for cross-coupling. This dataset shows a very clear example of cross-coupling. If the pressure and vertical velocity components of the field data are compared (Figures 3.1a and b), strong events with a low moveout velocity are observed on the v_z component, e.g. in the window marked **B**, that are not present on the p component. These events (presumably converted waves) will not be compensated for when the components are combined in the decomposition procedure and therefore they will deteriorate the decomposition result if they are not removed.

To remove the unwanted events from the v_z component, two temporal convolution filters, $r_1(t)$ and $r_2(t)$ were determined in the space-time domain by optimization:

$$v_z(x, t) = v_z'(x, t) - r_1(t) * v_x'(x, t) - r_2(t) * v_y'(x, t), \quad (3.1)$$

where $v_i'(x, t)$ for $i = x, y, z$ are the measured velocity components. As in the window **B** (Figure 3.1) almost no energy is present on the p component, the convolution filters were calculated to minimize the energy over this window on the v_z component. The resulting v_z component is shown in Figure 3.2. In the following stages of the decomposition scheme the corrected v_z component will be used.

Stage 2: Acoustic decomposition just above the bottom

This stage is used to set the relative strengths of the pressure and vertical velocity components correctly. In the field data a window **A** is chosen that contains mainly primary reflections (see Figures 3.1 a and b). The calibration filter $A(\omega)$ is calculated that best minimizes the energy in window **A** in the decomposed *downgoing* wavefield. The acoustic decomposition result is shown in Figure 3.3. All primary

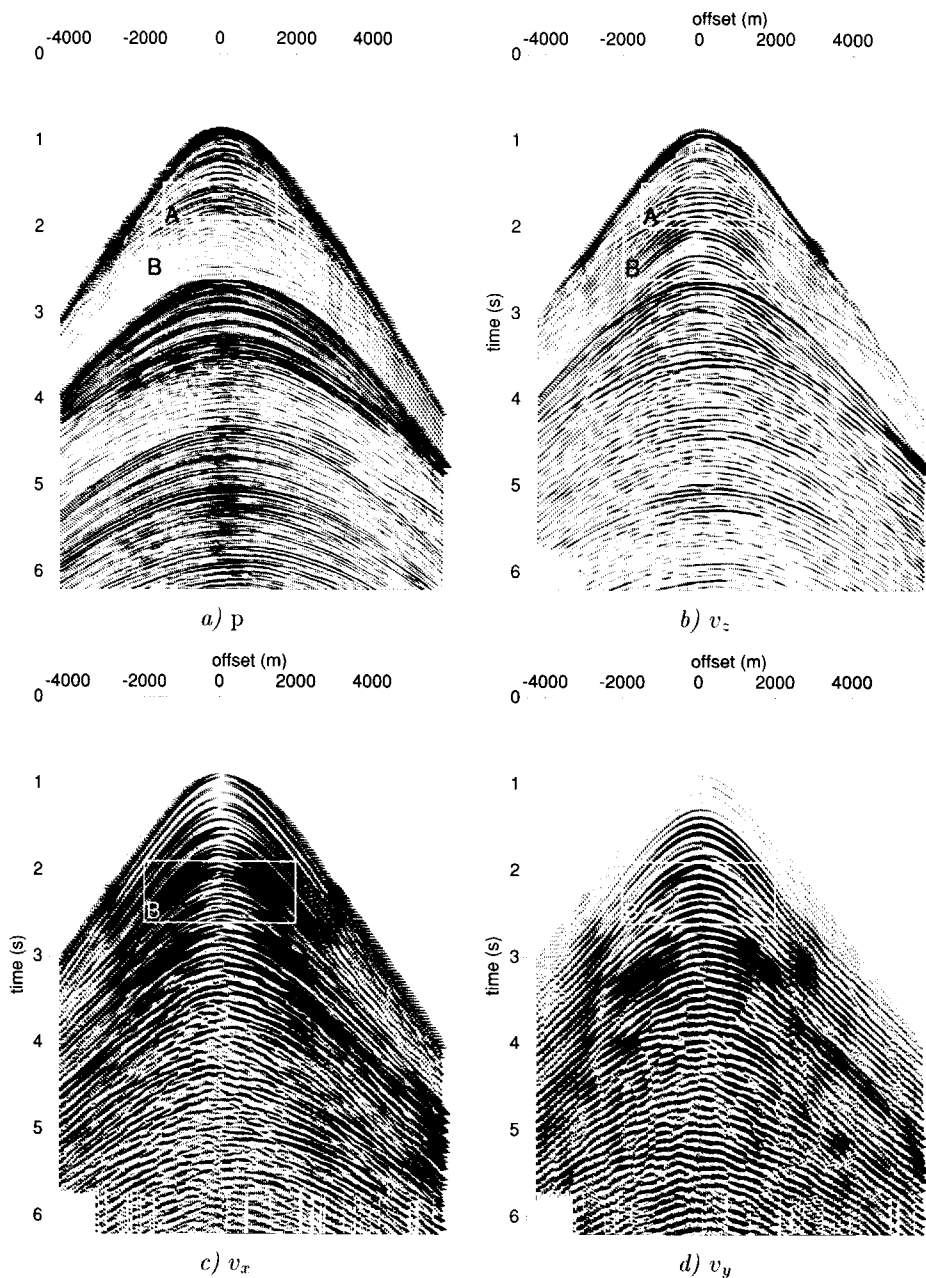


Fig. 3.1 Ocean bottom measurements of the Vørting dataset, provided by Saga Petroleum A.S.A., Norway. a) Pressure just above the bottom. b) Vertical component of the multi-component geophone. c) Horizontal inline component. d) Horizontal crossline component. The windows A and B are related to the second and first stage of the adaptive decomposition scheme respectively.

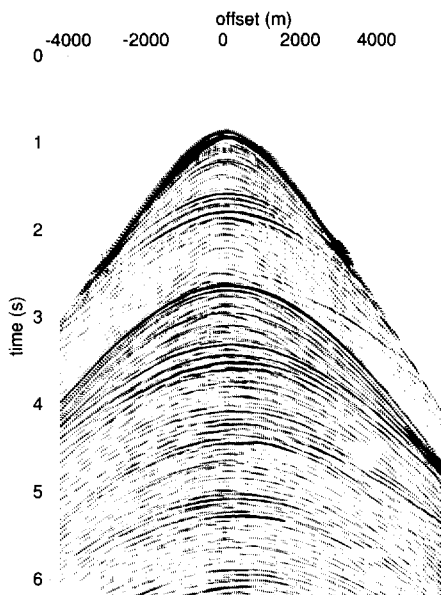


Fig. 3.2 Output of stage 1 of the adaptive decomposition scheme; v_z after correcting for 'cross-coupling'.

reflection energy has been moved to the upgoing wavefield. Note that the energy of the multiples (arriving at the zero-offset channel from approximately 2.6 seconds) has been decreased in the upgoing wavefield. The summation of the two decomposed wavefields will yield again the total pressure of Figure 3.1a ($p = p^+ + p^-$).

Stage 3: Elastic decomposition into τ_{zz}^\pm just below the bottom

Besides giving an elastic decomposition result *below* the bottom in down- and up-going normal stressfields, this stage yields an optimization filter, $\tilde{F}(p)$, from which the medium parameters just below the bottom can be inverted.

The decomposition results of the third stage are displayed in Figures 3.4 a and b. The energy minimization was done in two curved windows over the direct wave and the first order multiple in $\tilde{\tau}_{zz}^-$ in the $\tau - p$ domain. The direct arrival has been well removed, as well as the first order water multiple. In fact all surface-related

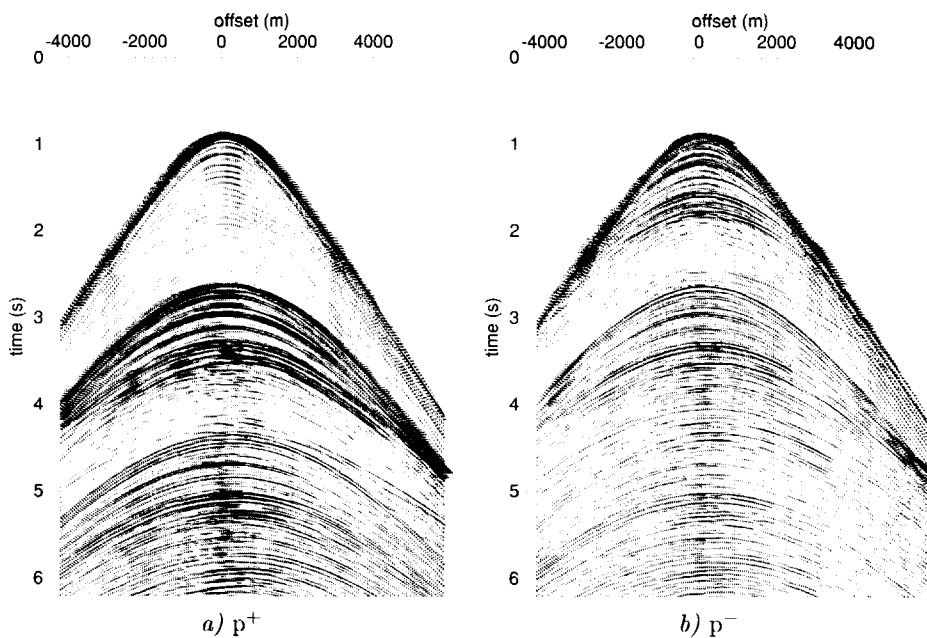


Fig. 3.3 Output of stage 2 of the adaptive decomposition scheme. a) Downgoing pressure wavefield just above the bottom. b) Upgoing pressure wavefield just below the bottom.

multiples should be removed from the upgoing stressfield, except the source-side peg-leg multiples¹.

An estimate of the medium parameters is obtained by inverting the filter $\tilde{F}(p) = \frac{\rho_2 \beta_2}{2q_{P,2}}$. Although in theory the operator $\tilde{F}(p)$ is frequency independent, better results are obtained by admitting a frequency dependent filter $\tilde{F}(p, \omega)$. In Figure 3.5, the filter $\tilde{F}(p, \omega)$ obtained from the data is displayed for frequencies between 13 and 53 Hz (from dark to light). The modulus of the best-fitting² theoretical decomposition operator is plotted in the same figure (dotted line). Note that the frequency-dependency of the filter $\tilde{F}(p, \omega)$ can not be explained by the theoretical operator. The average value for the impedance from Figure 3.5 is $2.5 \cdot 10^6 \text{ kg/m}^2\text{s}$, c_P was estimated from the peaks at $p = \pm 1/1670 \text{ s/m}$, giving a density estimate of 1497 kg/m^3 . A value for c_S could not be obtained from $\tilde{F}(p, \omega)$ as the higher

¹To remove these multiples as well, an additional surface-related multiple elimination procedure should be applied. However, then a full receiver coverage at the bottom is necessary; this is discussed in Chapter 5.

²Best fit in this case was obtained by visual inspection.

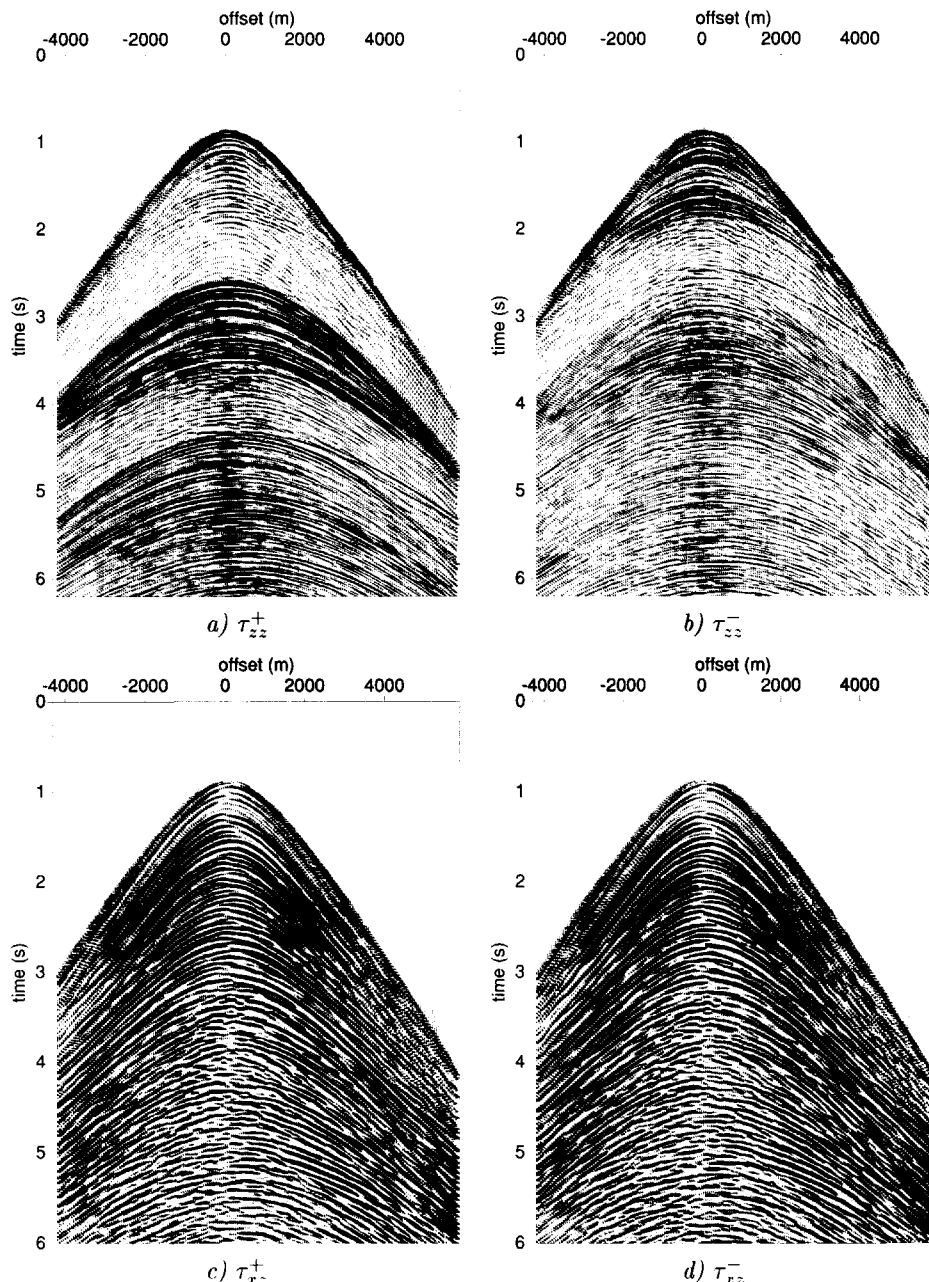


Fig. 3.4 Top: Output of stage 3 of the adaptive decomposition scheme. a) Downgoing normal stressfield just below the bottom. b) Upgoing normal stressfield just below the bottom. Bottom: Output of stage 4 of the adaptive decomposition scheme. c) Downgoing shear stressfield just below the bottom. d) Upgoing shear stressfield just below the bottom.

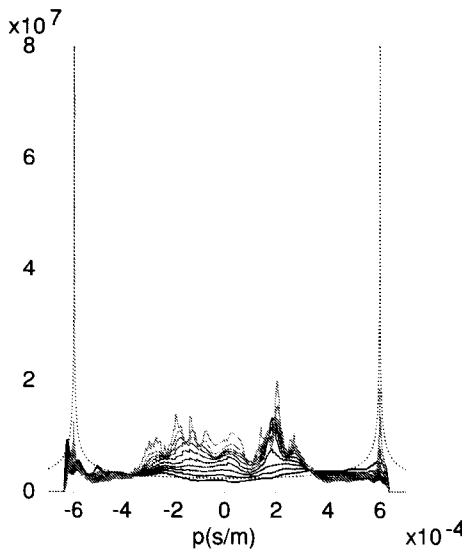


Fig. 3.5 The filter $\hat{F}(p, \omega)$ for frequencies between 13 and 53 Hz (black to grey lines) and the modulus of the theoretical decomposition operator $\varrho_2 \beta_2 / 2q_{P,2}$ (dashed line) for $c_{P,2} = 1670$ m/s, $c_{S,2} = 100$ m/s and $\varrho_2 = 1497$ kg/m³.

angles, containing this information, were not well recorded in these data. Therefore the value for c_S was estimated in stage 4.

Stage 4: Elastic decomposition into τ_{xz}^{\pm} just below the bottom

In the fourth decomposition stage, the relative strengths of the pressure and horizontal (in-line) velocity components are set correctly. From equation (2.193) it follows that first the decomposition operators need to be calculated with the medium parameters just below the ocean-bottom, before the calibration filter $B(\omega)$ can be obtained. For several values of c_S within a realistic velocity interval, the calibration filter $B(\omega)$ was estimated. The optimization was performed in a curved window containing the direct wave, in the $\tau - p$ domain. The value for c_S at which the direct wave was best removed was 100 m/s. The final result for the up- and downgoing shear stressfields is shown in Figures 3.4 c and d. Note that the direct wave has been attenuated but could not be completely removed. Note also that $\tau_{xz}^+ = -\tau_{xz}^-$, which follows from equation (2.193).

Stage 5: Elastic decomposition into P- and S-wave potentials just below the bottom

In the last stage the estimated parameters just below the ocean-bottom and the results of the elastic decomposition into up- and downgoing stressfields are simply combined to obtain the up- and downgoing P- and S-waves. The results for the up- and downgoing P- and S-wave potentials are displayed in Figure 3.6. The results can be judged on the condition that there should not be any direct wave or water bottom multiples in the upgoing P- and S-waves (Figures 3.6 b and d), but cannot be changed anymore in this stage. The condition applies quite nicely to the up- and downgoing P-waves (Figures 3.6 a and b). The decomposition into S-waves (Figures 3.6 c and d) is less satisfying - little difference is seen between the upgoing and downgoing wavefields (except for a sign change). Also, the direct wave does not seem to be much attenuated in the upgoing wavefield. The P- and (converted) S-waves appear well separated from each other.

3.2 Comparison before and after decomposition

To see the effect of decomposition more clearly, in Figure 3.7 the upgoing P- and S-waves are displayed next to the vertical and horizontal geophone components. When both the P- and S-wave velocity contrasts between the upper layer and the layers underneath are large, the wavefields bend to the vertical and therefore the vertical geophone component will record mostly P-waves and the horizontal component will record mostly S-waves already. In this data example the S-wave velocity is low just below the bottom. Therefore, the vertical velocity component (and also τ_{zz}) will contain mainly P-waves. Depending on the P-wave velocity contrast, P-waves can be recorded on the vertical as well as the horizontal geophone components. There is not much evidence of events present in Figure 3.7d that are suppressed in Figure 3.7c. Therefore, it is concluded that v_x (and also τ_{xz}) contains mainly S-wave energy already. The decomposition operators perform a separation into up- and downgoing wavefields; the P/S separation has been performed already by the subsurface in this case. The main difference between Figure 3.7a and b, and between c and d is an attenuation of the direct wave and the waterlayer-related multiples.

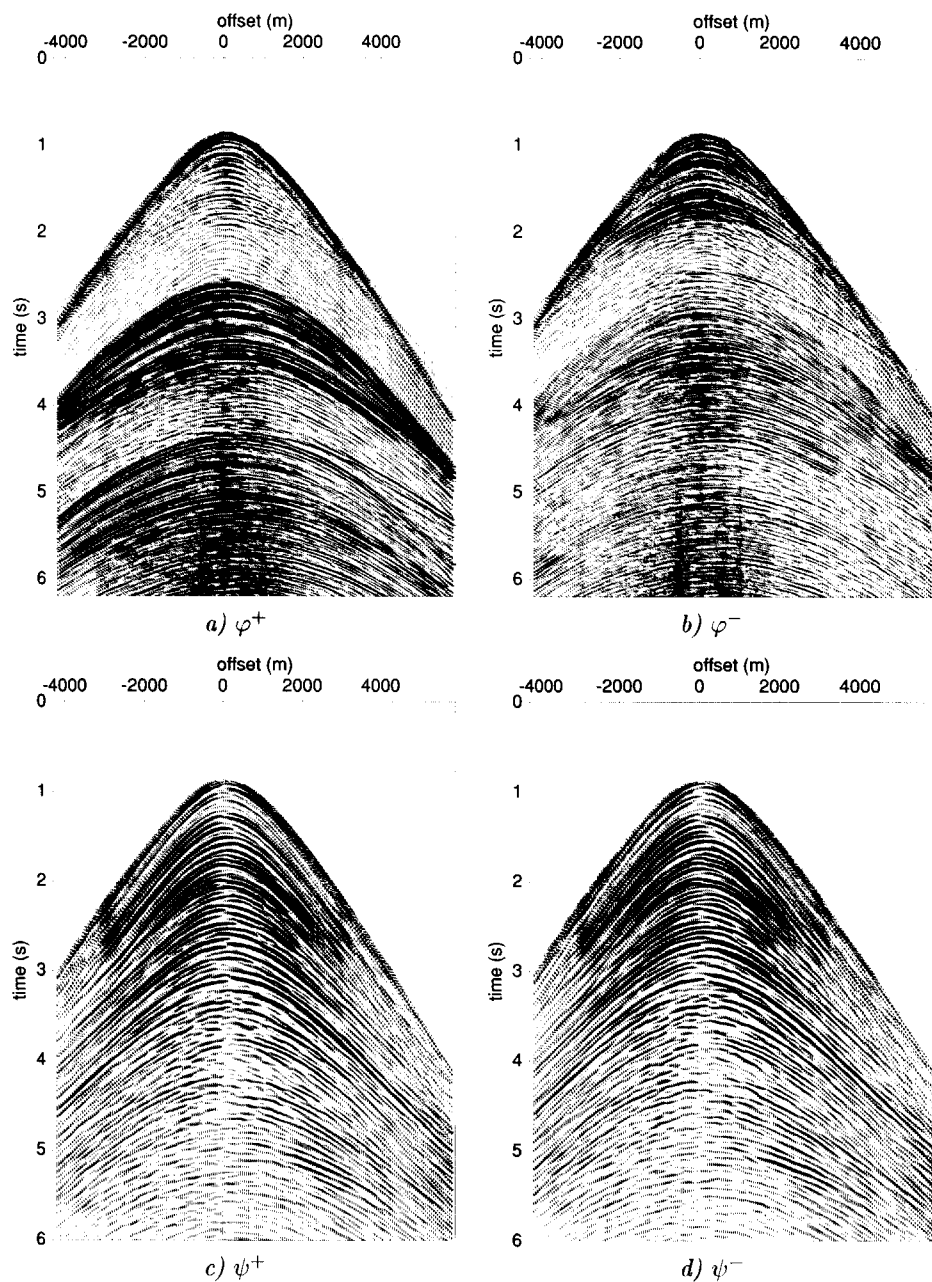


Fig. 3.6 Output of stage 5 of the adaptive decomposition scheme. a) Downgoing P-wave potential just below the bottom. b) Upgoing P-wave potential just below the bottom. c) Downgoing S-wave potential just below the bottom. d) Upgoing S-wave potential just below the bottom.

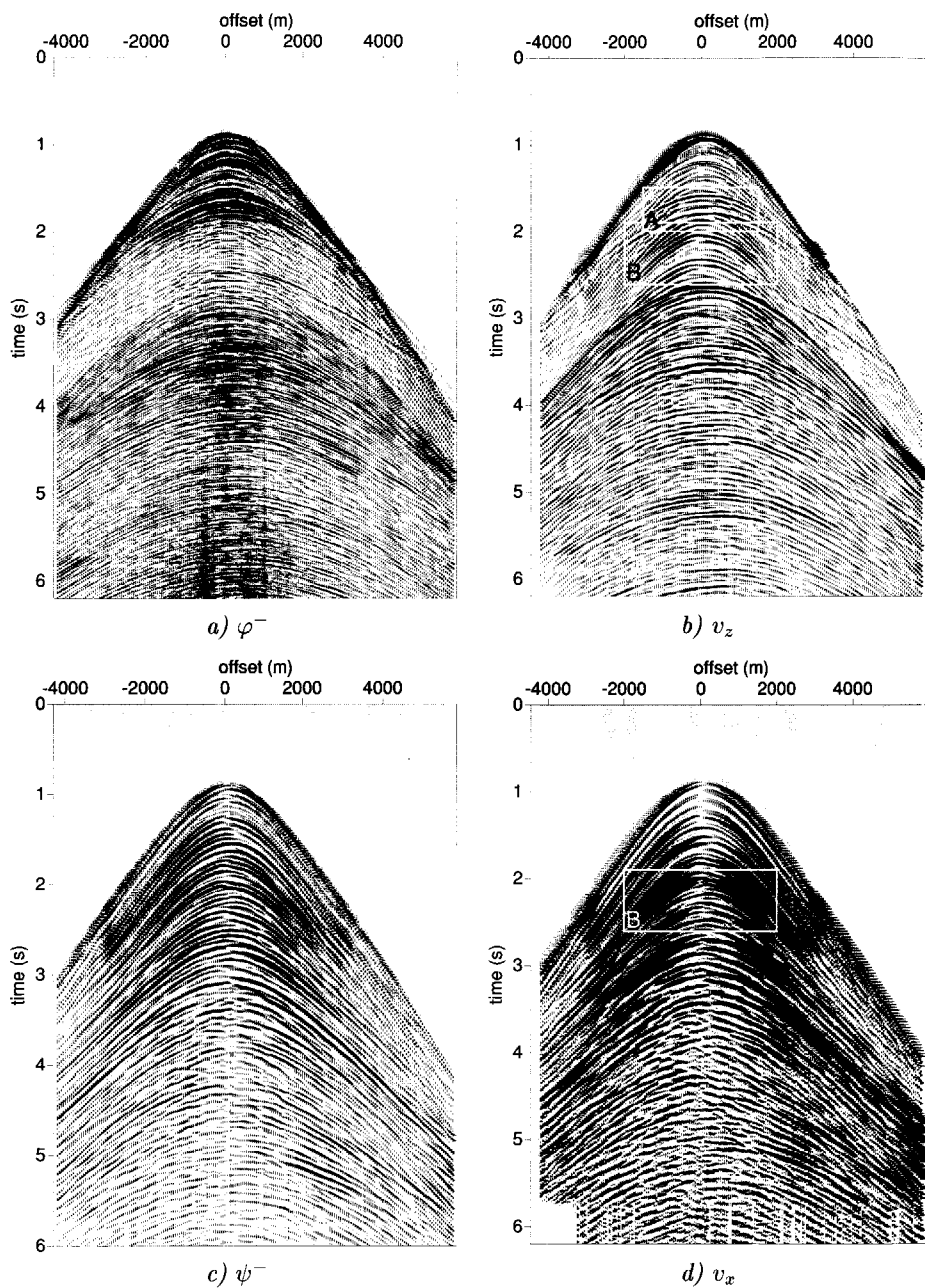


Fig. 3.7 Top: a) Upgoing P-wave potential just below the bottom, compared to b) vertical geophone component after deconvolution. Bottom: c) Upgoing S-wave potential just below the bottom, compared to d) horizontal inline component.

3.3 A medium-depth ocean-bottom example: Snorre

The adaptive decomposition scheme will now be applied to a medium-depth ocean-bottom field dataset, with a water depth of approximately 300 meters³. The dataset, provided by SAGA Petroleum A.S.A., has been acquired over the Snorre field, offshore Norway. The data consist of 447 shots at the surface and 127 multicomponent receiver groups on a cable at the ocean-bottom. The source line lies over the receiver line. Both the receiver spacing and the shot interval are 25 meters. The water depth is approximately 300 meters. The measured signal contains frequencies up to 120 Hz. The average frequency spectra of the signal (for one common-receiver gather) recorded by the pressure, vertical component and horizontal inline component is displayed in Figure 3.8. In order to avoid spatial aliasing within the data bandwidth when transforming the data to the p, ω -domain to apply adaptive decomposition, the data needed to be interpolated to a trace spacing of 6.25 meters.

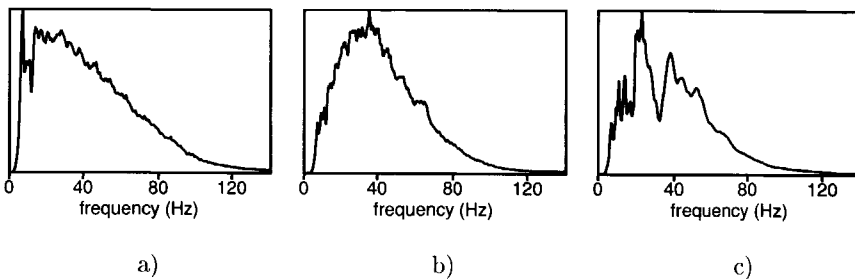


Fig. 3.8 The average frequency spectra of the different components of the ocean-bottom seismic data. a) Spectrum of the pressure component, b) spectrum of the vertical velocity component, c) spectrum of the horizontal inline velocity component.

Some selected raw data are shown in Figures 3.9 and 3.10. In Figure 3.9 one common-receiver gather has been selected from the dataset for a receiver position in the middle of the receiver line. Figure 3.10 displays the common-shot gathers of the four data components belonging to one source in the middle of the shot line. As explained earlier in this chapter, the decomposition at the ocean-bottom should be applied to common shot gathers. Although compared to the previous example there are more receiver positions available, it is not practical to work with common-shot gathers here either. In the acquisition of the dataset under consideration, the receiver line (3 km) is much shorter than the source line (11 km), causing the shot gathers to

³The data example of Snorre has been submitted to Geophysics; Adaptive decomposition of multi-component ocean-bottom seismic data into down- and upgoing P- and S-waves, K. M. Schalkwijk, C. P. A. Wapenaar, and D. J. Verschuur

have less aperture than the receiver gathers. Furthermore, the shot gathers close to the ends of the line do not contain small offsets. Therefore, the involved Radon transforms will produce unacceptable artifacts, and it becomes more complicated to identify crucial events in the decomposition for gathers containing only larger offsets.

Although in this dataset some structures are present deeper below the bottom, for the first package of reflectors the situation is practically 1-D, which justifies the use of common receiver gathers. As an additional test, the adaptive decomposition procedure was also performed on common-shot gather 323 (Figure 3.10), resulting in no big differences with common-receiver gather 63 and especially with the filter $\tilde{F}(p, \omega)$. In the following, the adaptive decomposition scheme will be demonstrated on one selected common-receiver gather of the Snorre dataset.

Stage 1: Corrections for cross-coupling

If the pressure and vertical velocity components for the Snorre dataset are compared (Figures 3.9a and b) there does not seem to be much ‘cross-coupling’ present (i.e. events with low moveout on the v_z component that are not present on the p component). Therefore, this dataset was taken directly to stage 2.

Stage 2: Acoustic decomposition just above the bottom

In the field data under consideration a window has to be chosen that contains mainly primary reflections. Compared with the previous example, a rectangular window (Figure 3.1) is less appropriate. If the water depth is not too shallow (i.e. if there are primary reflections arriving before the first water multiple), a curved window can be taken between the direct source arrival and the first water multiple (window in between dashed lines in Figure 3.11). The calibration filter $A(\omega)$ is calculated that best minimizes the energy in the chosen window in the decomposed *downgoing* wavefield (Figure 3.11a). The acoustic decomposition result is shown in Figure 3.11 for the first 1.5 seconds of data of the same common receiver gather as displayed in Figure 3.9 (number 63). Most primary reflection energy has been moved to the upgoing wavefield, and the energy of the multiples has also been decreased in the upgoing wavefield (Figure 3.11b).

Stage 3: Elastic decomposition into τ_{zz}^{\pm} just below the bottom

To obtain the down- and upgoing normal stressfields *below* the bottom, the optimization procedure was applied to a rectangular window in the upgoing wavefield extending to 0.27 seconds in the τ, p domain. This window lies roughly over the direct wave. It was found that it is not essential to make a tight fitting window as was

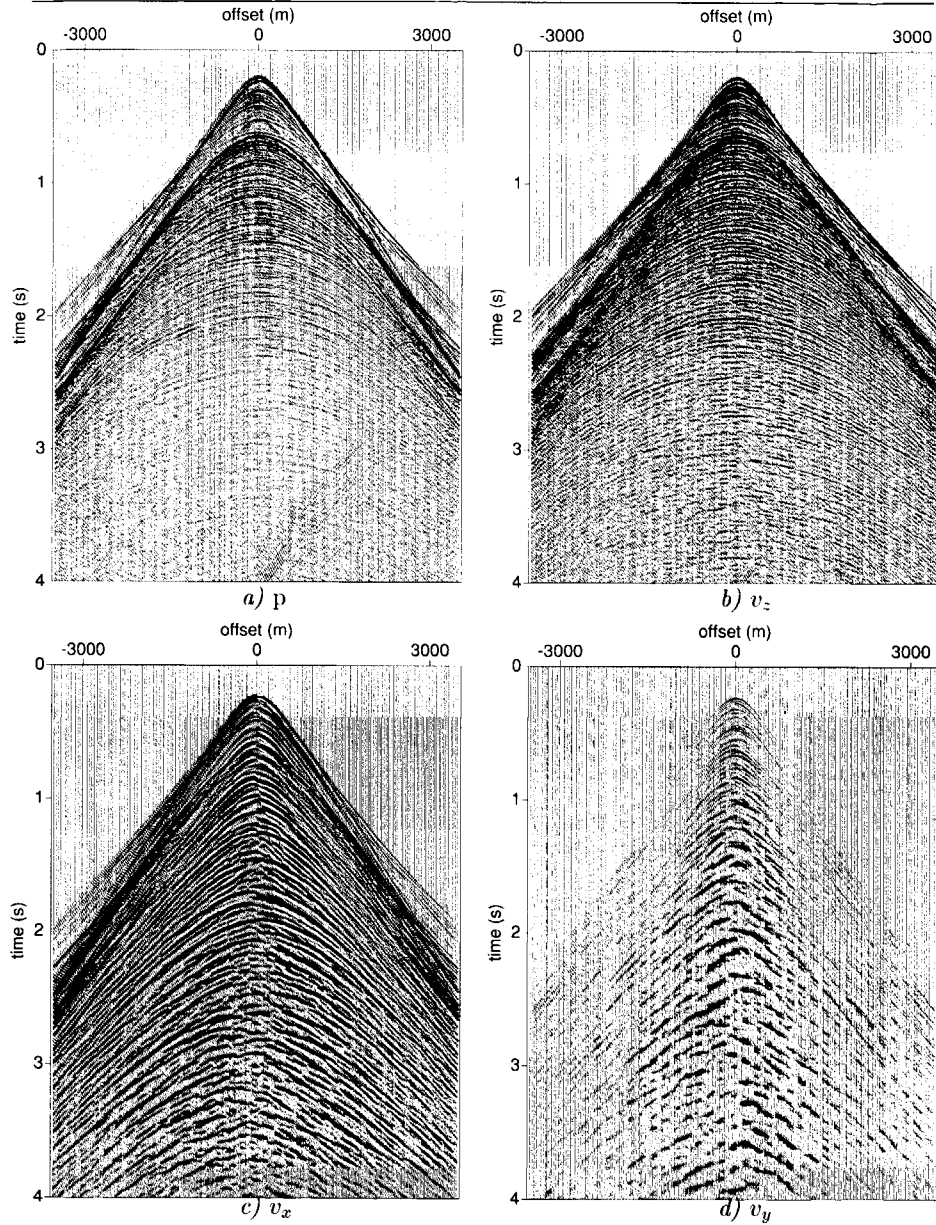


Fig. 3.9 Ocean bottom measurements of one common-receiver gather (number 63) from the Snorre 2-D line, provided by Saga Petroleum A.S.A., Norway. a) Pressure just above the bottom (bandpass filtered to reduce the airgun bubble effect for display purpose). b) Vertical component of the multi-component geophone. c) Horizontal inline component. d) Horizontal crossline component.

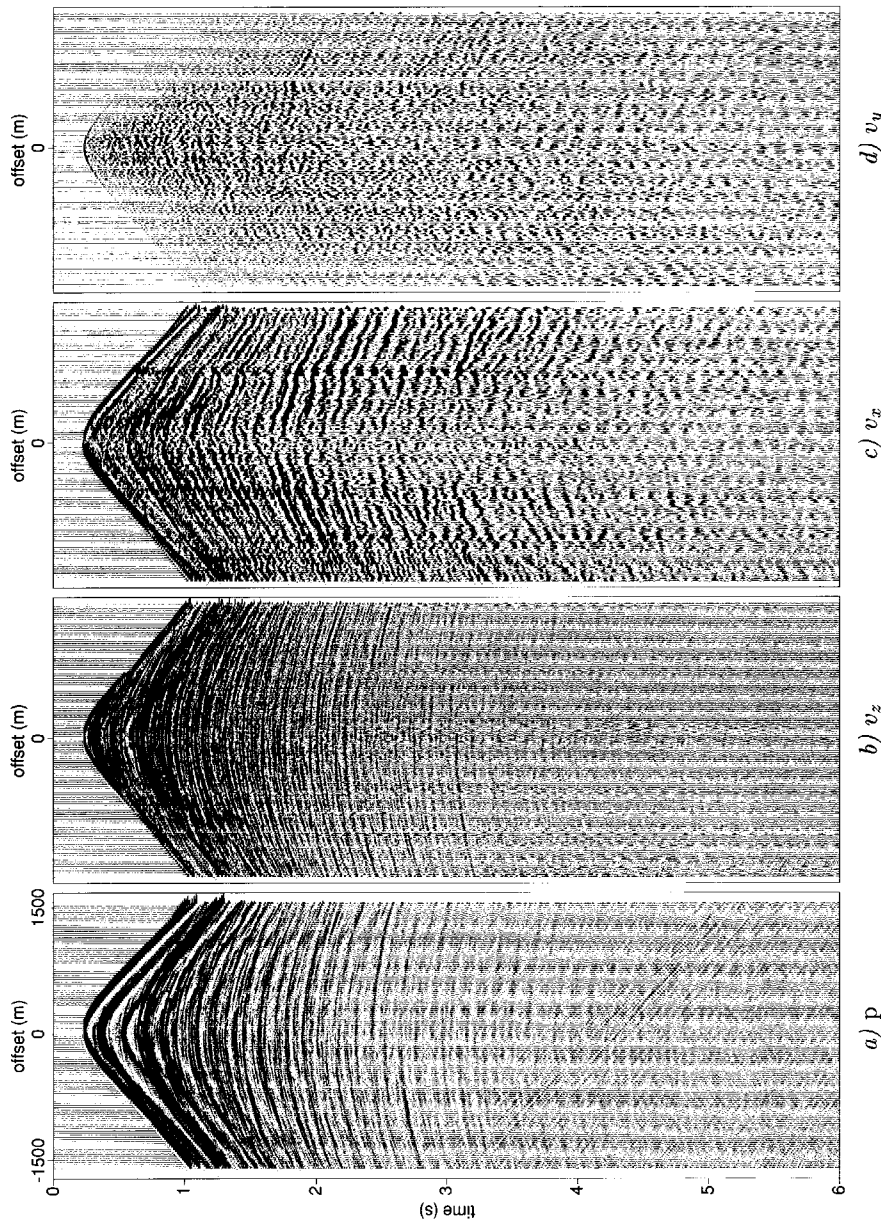


Fig. 3.10 Ocean-bottom measurements of one common-shot gather (number 323) from the Snorre 2-D line, provided by Saga Petroleum A.S.A., Norway. (a) Pressure just above the bottom. (b) Vertical component of the multi-component geophone. (c) Horizontal inline component. (d) Horizontal crossline component.

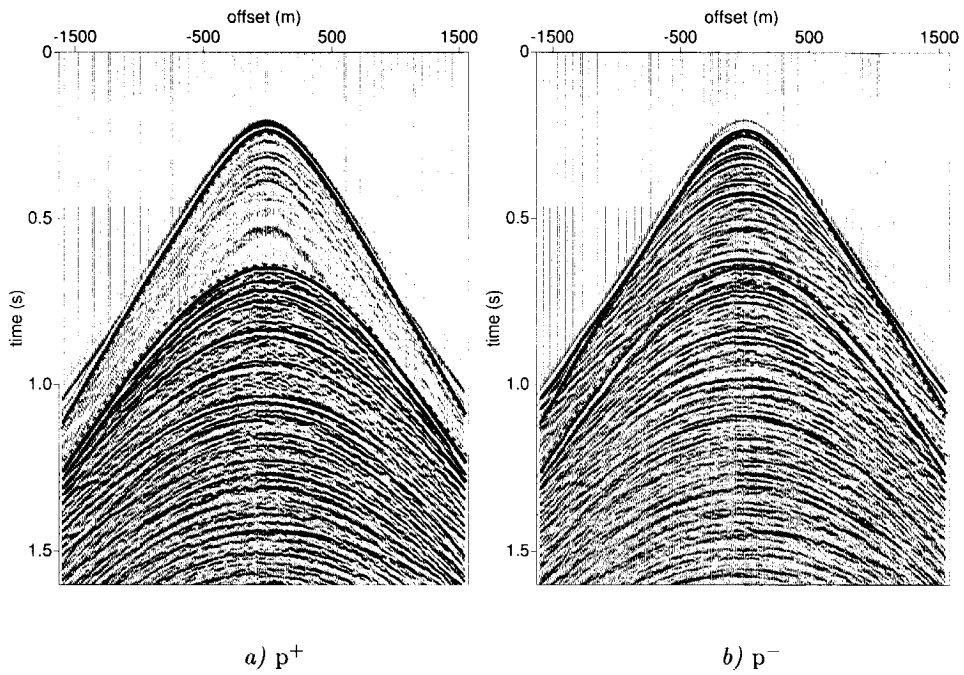


Fig. 3.11 Output of stage 2 of the adaptive decomposition scheme. a) Downgoing pressure wavefield just above the bottom. b) Upgoing pressure wavefield just above the bottom. The dashed line indicates the optimization window used in this stage of the adaptive decomposition scheme.

done in the previous example, as the direct wave has much more energy compared to other events in the window. The decomposition results of this third stage are displayed in Figure 3.12. The direct arrival has been well removed in Figure 3.12b, as well as the first order water multiple.

In Figure 3.13, the filter $\hat{F}(p, \omega)$ obtained from the data is shown for frequencies between 30 and 100 Hz. The modulus of the best-fitting⁴ theoretical decomposition operator is plotted in the same figure (line with dots). The parameter values that were obtained are $c_{P,2} = 1870$ m/s, $c_{S,2} = 450$ m/s and $\varrho_2 = 1698$ kg/m³. In this example a reasonably reliable estimate for c_S could be obtained.

⁴In this case the best fit was obtained using the frequency independent inversion method explained in Chapter 2. A discussion on the reliability of these parameters is given with the data example in Chapter 4.

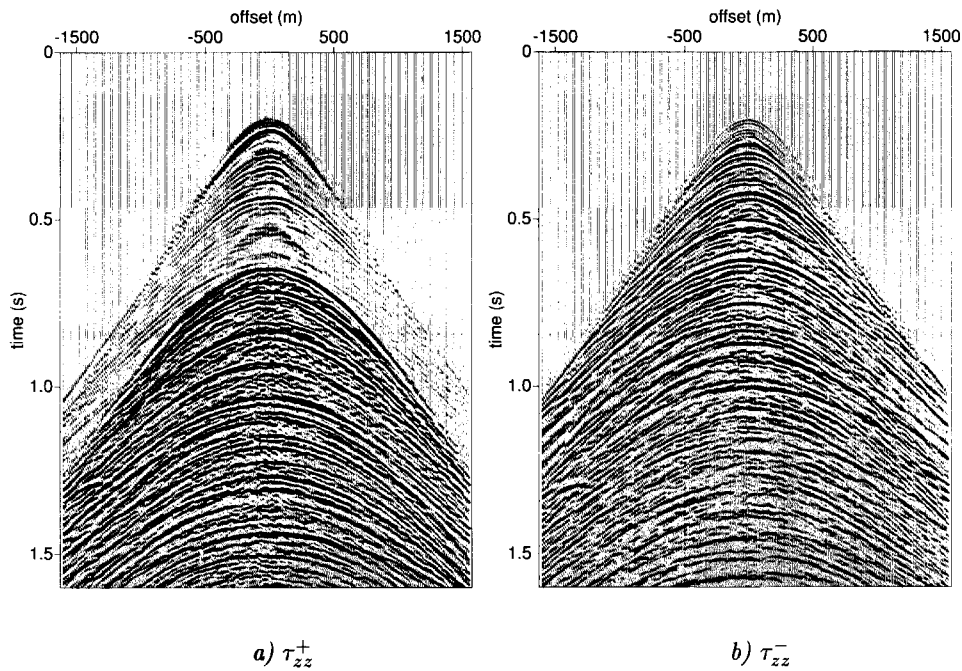


Fig. 3.12 Output of stage 3 of the adaptive decomposition scheme, where the decomposition result was obtained by adaptively estimating the decomposition operator $\tilde{F}(p)$. a) Downgoing normal stressfield just below the bottom. b) Upgoing normal stressfield just below the bottom.

Stage 4: Elastic decomposition into τ_{xz}^{\pm} just below the bottom

The optimization procedure to remove the direct wave from the downgoing as well as from the upgoing wavefield, was done in the τ, p domain, using the same window as in the previous stage. The results for the down- and upgoing shear stressfields are shown in Figure 3.14. Note that the direct wave has been more evidently attenuated than with the previous field data example (Figure 3.4).

Stage 5: Elastic decomposition into P- and S-wave potentials just below the bottom

After combination of all the previously obtained results, the obtained results for the down- and upgoing P- and S-wave potentials are displayed in Figures 3.15 and 3.16. The results can be judged on the condition that there should not be any direct wave

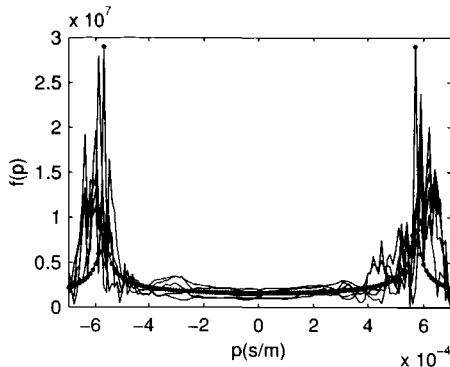


Fig. 3.13 Least-squares operator $\tilde{F}(p, \omega)$ from a field dataset. The solid lines are different frequencies in the interval between 30-100 Hz.

or water bottom multiples in the upgoing P- and S-waves (Figures 3.15b and 3.16b), although these results cannot be changed anymore in this stage. The condition applies quite nicely to the upgoing P-waves (Figure 3.15b). The decomposition into S-waves (Figures 3.16a and b) also looks good - although the direct wave is not totally removed from the upgoing S-wavefield. The S decomposition result contains events with lower and higher frequency content; the higher frequency events correspond with waves that mostly traveled as P-waves and have converted to S just before detection.

3.4 Comparison before and after decomposition

In Figure 3.17 the upgoing P- and S-waves after decomposition are compared to the v_z and the v_x components. The main difference between the upgoing P-waves below the bottom and the v_z component (Figure 3.17a and b) is a removal/attenuation of the water multiples, as with the previous example.

The upgoing S-waves below the bottom (Figure 3.17c) show a lower frequency content than the original v_x component (Figure 3.17d). This is caused by stage 4 of the adaptive decomposition procedure, where the coupling filter $B(\omega)$ matches the source wavelet of the p component to the wavelet of the v_x component. In addition, the high frequency events mentioned in the previous section can be distinguished only on the decomposed S-waves, and not on the v_x component which may be evidence for separation of P- and S-waves between components. Also the direct arrival is clearly better removed in the upgoing S-wavefield than in the previous example.

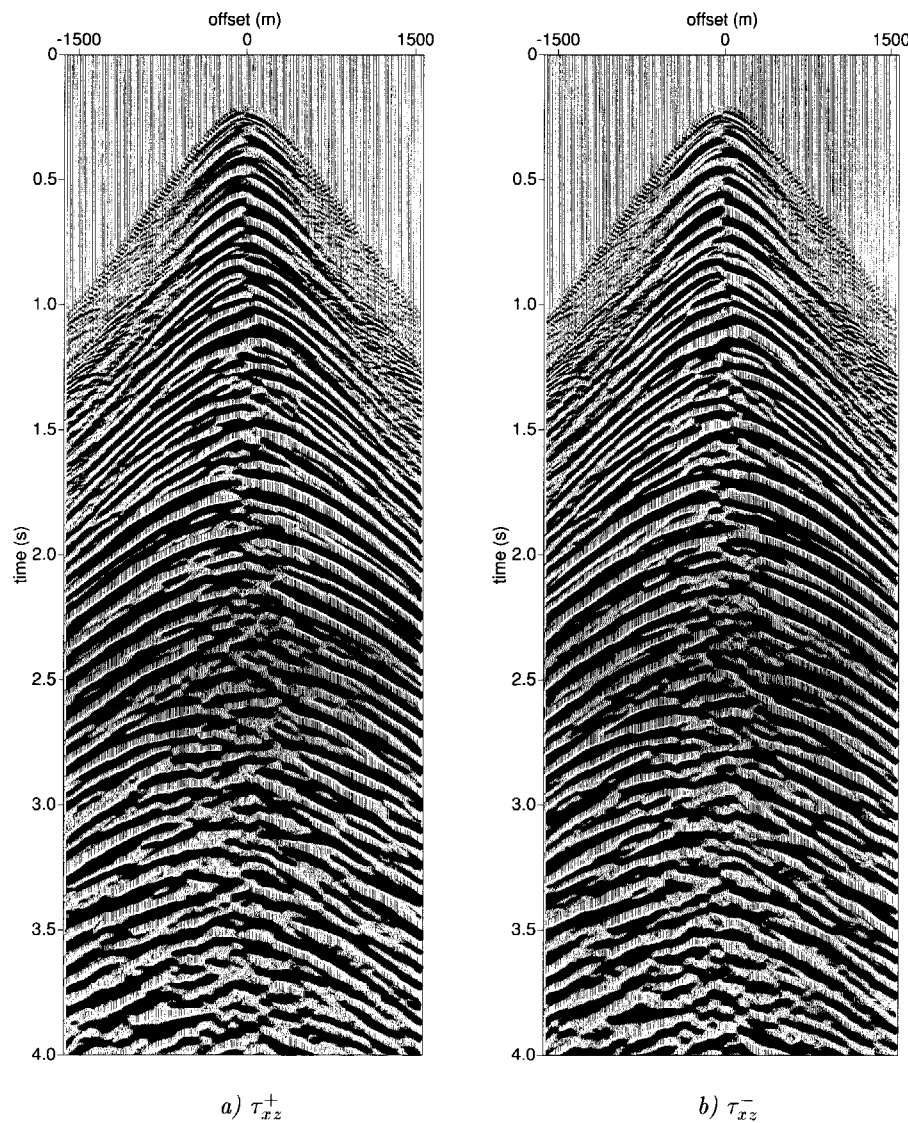


Fig. 3.14 Output of stage 4 of the adaptive decomposition scheme. a) Downgoing shear stressfield just below the bottom. b) Upgoing shear stressfield just below the bottom.

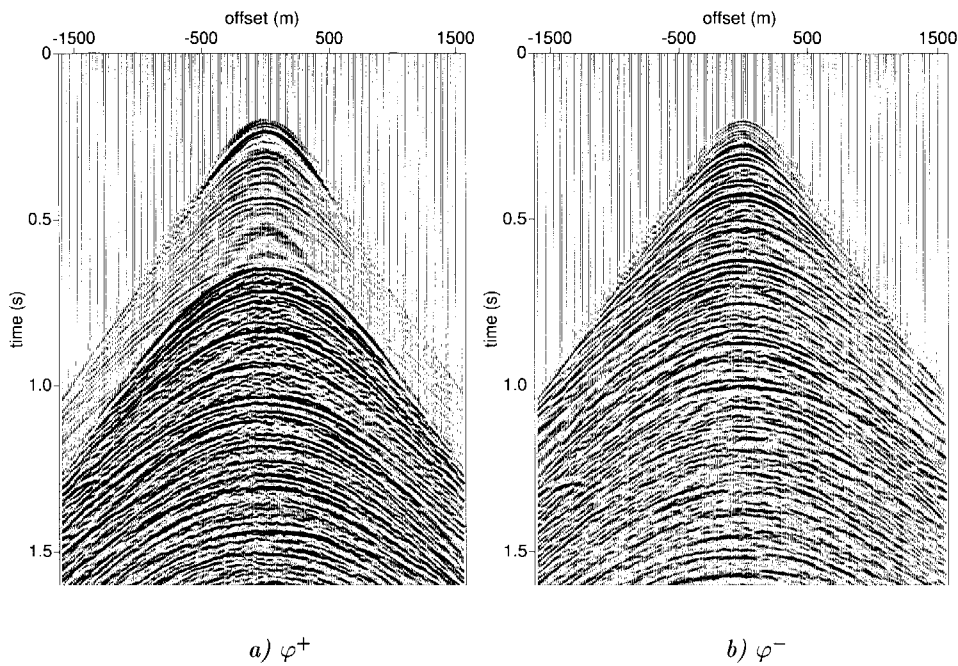


Fig. 3.15 Output of stage 5 of the adaptive decomposition scheme. (a) Downgoing P-wave potential just below the bottom. (b) Upgoing P-wave potential just below the bottom.

3.5 Application of the adaptive decomposition scheme to the 2-D line

In order to apply the adaptive decomposition scheme to the whole line, the data were sorted into common receiver gathers. As was discussed in the beginning of the section 3.3 this is not totally correct, but was necessary due to acquisition geometry. For each common receiver gather an identical offset window is selected and therefore the optimization windows are constant over the line. To keep things simple the medium parameters are kept constant over the line and equal to the values of the previous example (i.e. the middle ocean-bottom receiver); only the calibration filters $A(\omega)$ and $B(\omega)$ are allowed to vary and are estimated per ocean-bottom receiver.

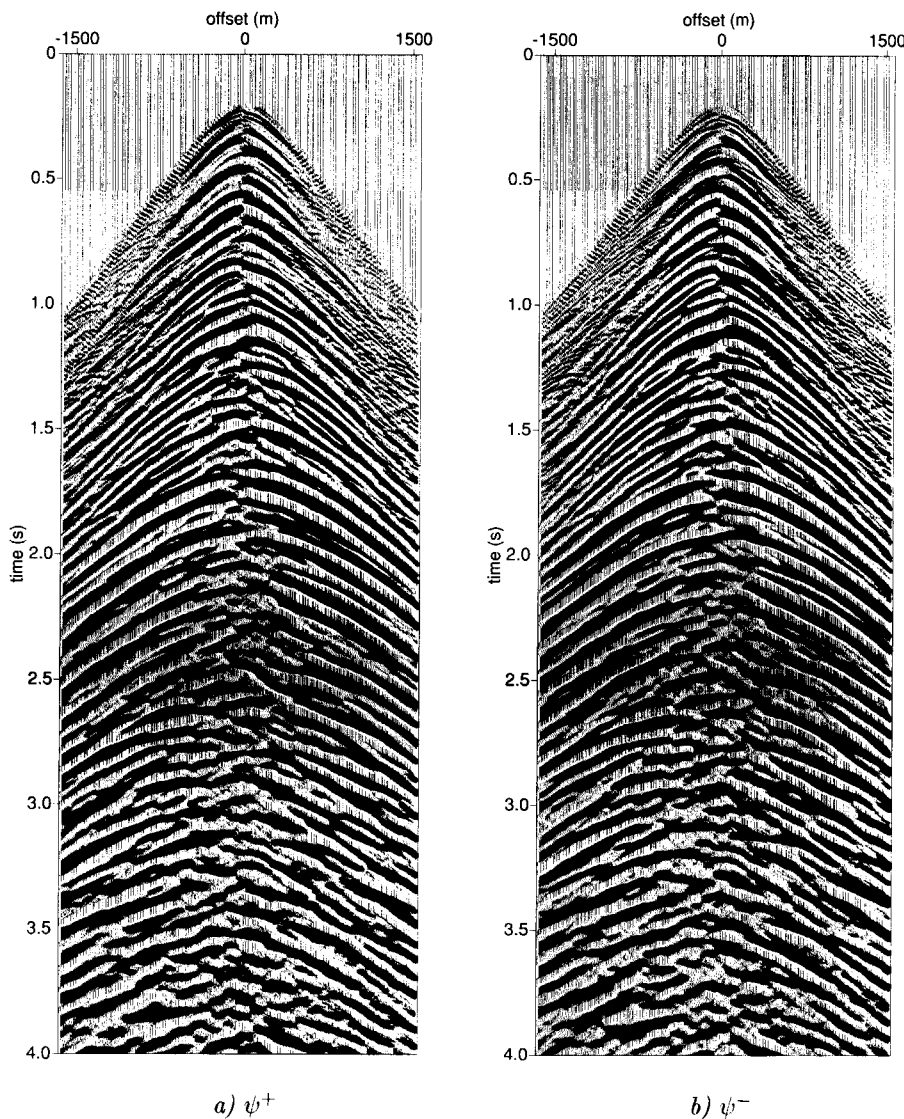


Fig. 3.16 Output of stage 5 of the adaptive decomposition scheme. a) Downgoing S-wave potential just below the bottom. b) Upgoing S-wave potential just below the bottom.

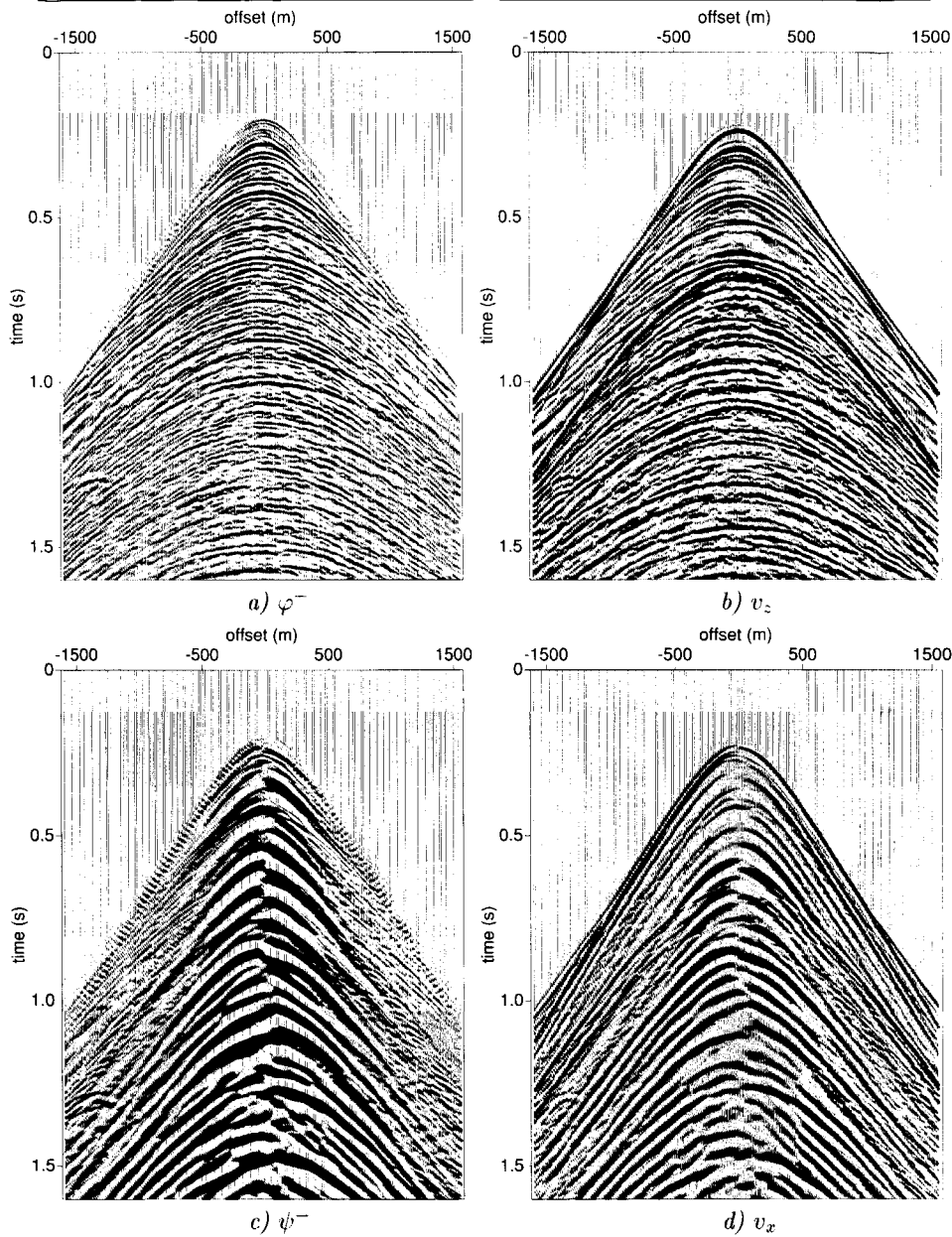


Fig. 3.17 Top: a) Upgoing P-wave potential just below the bottom, compared to b) vertical geophone component after deconvolution. Bottom: c) Upgoing S-wave potential just below the bottom, compared to d) horizontal inline component.

3.5.1 Choosing optimization windows

To apply the adaptive decomposition scheme, two optimization windows are used. One window that contains only primary reflections (stage 2) and one window that contains the direct arrival and optionally one or more water bottom multiples (stages 3 and 4).

Filter $a(t)$ is obtained in stage 2 by adding the pressure and vertical velocity components in the time domain, after each has been multiplied with the appropriate decomposition operator, such that the energy over a window containing only up-going waves becomes minimal. The (curved) window is chosen between the direct arrival and the first water bottom multiple. Here the window is determined once. This could be made automatic by using a tracking program to locate the first arrival and the first water bottom multiple and taking the area in between as the window. This window choice would not apply for very shallow water depths as primary and multiples would not be clearly separated in time (see also Chapter 4).

Filter $b(t)$ is obtained by adding the pressure and horizontal inline velocity components in the time domain (stage 4), after each has been multiplied with the appropriate decomposition operator, such that the energy over a chosen window containing the direct arrival becomes minimal. In this case the window was chosen as a simple rectangle in the $\tau - p$ domain over the direct wavefield. Other events present in the window did not noticeably influence the optimization result, as the energy of the direct wave is large in comparison to other events.

In Figure 3.18 the coupling filters $A(\omega)$ and $B(\omega)$ obtained in stage 2 and stage 4 of the adaptive decomposition scheme are displayed for all 127 common receiver gathers. The filters are shown in the time domain and were bandpass filtered to represent the same frequency band as the data. Note the correlation between $a(t)$ and $b(t)$: where $a(t)$ is stronger (less energy on v_z component), $b(t)$ seems to be weaker (more energy on v_x component). Note that this (assumed) coupling effect is also noticeable on the raw data (Figure 3.10b,c).

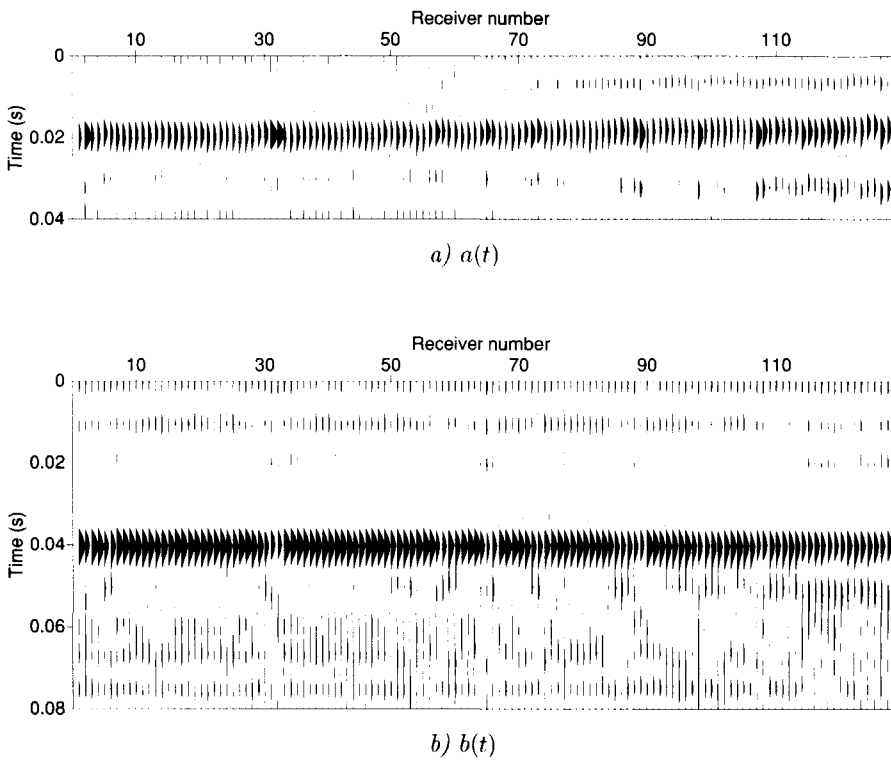


Fig. 3.18 Calibration filters for all 127 common receiver gathers (a) between pressure and vertical velocity component and (b) between pressure and horizontal inline velocity component.

3.5.2 Decomposition results for all common receiver gathers

For each common receiver gather the same aperture window was selected (-1500 to 1500 m offset), on which the decomposition was applied. The medium parameters were assumed constant over the line (i.e. estimated only once for common-receiver gather 63 at $c_{P,2} = 1870$ m/s, $c_{S,2} = 450$ m/s, $\rho_2 = 1698$ kg/m³). For every 10th common receiver gather the quality of the decomposition results from stage 2 to 5 was checked. To compare the decomposed result to the raw data, in Figure 3.19 the zero-offset sections for the pressure and vertical velocity are displayed. The pressure component has been bandpass filtered to reduce the low-frequency airgun bubble

effect. For the down- and upgoing P-waves, the zero-offset sections are displayed (Figure 3.20). The down- and upgoing S-waves are displayed in common-offset gathers (500 m) in Figure 3.21. The dipping primary event that partly interferes with the first water multiple in Figure 3.19 (at about 0.65 seconds) has been completely recovered in Figure 3.20b after the decomposition process. The downgoing P-waves in Figure 3.20a contain almost no energy between the first arrival and the first water multiple (in theory there should be no energy at all). The major differences between the down- and upgoing S-waves (Figure 3.21a and b) is the absence of the direct wave from the upgoing wavefield and the difference in polarity between the down- and upgoing wavefields (the low S-velocity at the ocean-bottom makes the reflection coefficients for converted waves impinging on the ocean-bottom from below almost equal to minus one).

3.6 Conclusions

Two datasets with relatively deep ocean-bottoms were used to (successfully) verify the adaptive decomposition procedure (see Chapter 2) on field data. The wavefield decomposition was applied per common-receiver gather. In the first example of the Vørung dataset, just one common-receiver gather was available. In the second example of the Snorre dataset, it was found more practical to work with common-receiver gathers for the extension of the decomposition to the entire 2-D dataset (due to coupling issues and aperture). Decomposition was repeated for all receiver gathers in the Snorre dataset using fixed medium parameters across the receiver line. The variability of receiver coupling found over the line, is reflected in the raw data.

In the adaptive decomposition scheme, the desired (kinematic) result is obtained by estimating optimal filters. The filters are then inverted for the medium parameters, which are necessary to obtain the final P- and S-wave separation. The inversion of the medium parameters just below the bottom for the Vørung and Snorre datasets was made more complicated because:

- The shape of the filters differed from the theoretical decomposition operator in the pre-critical rayparameter interval.
- The filters exhibited considerable frequency dependency within the data bandwidth.

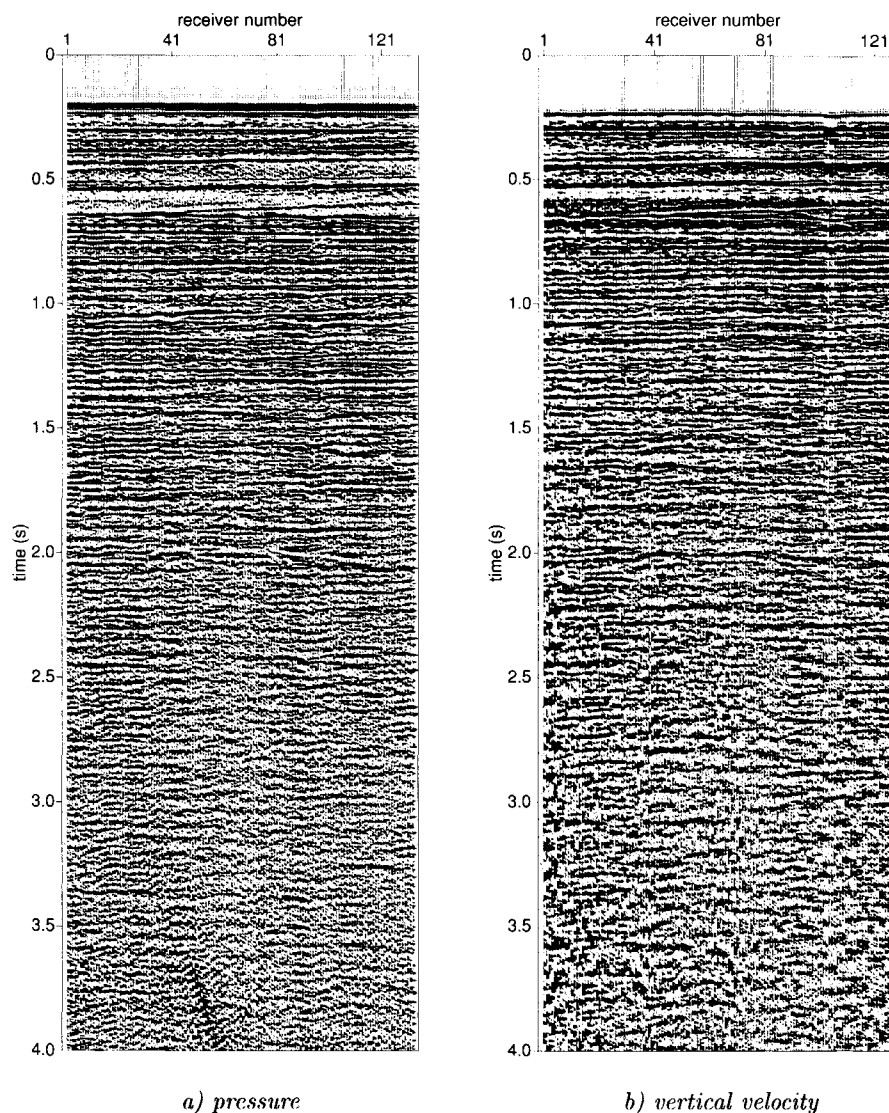


Fig. 3.19 Zero-offset sections of raw data.

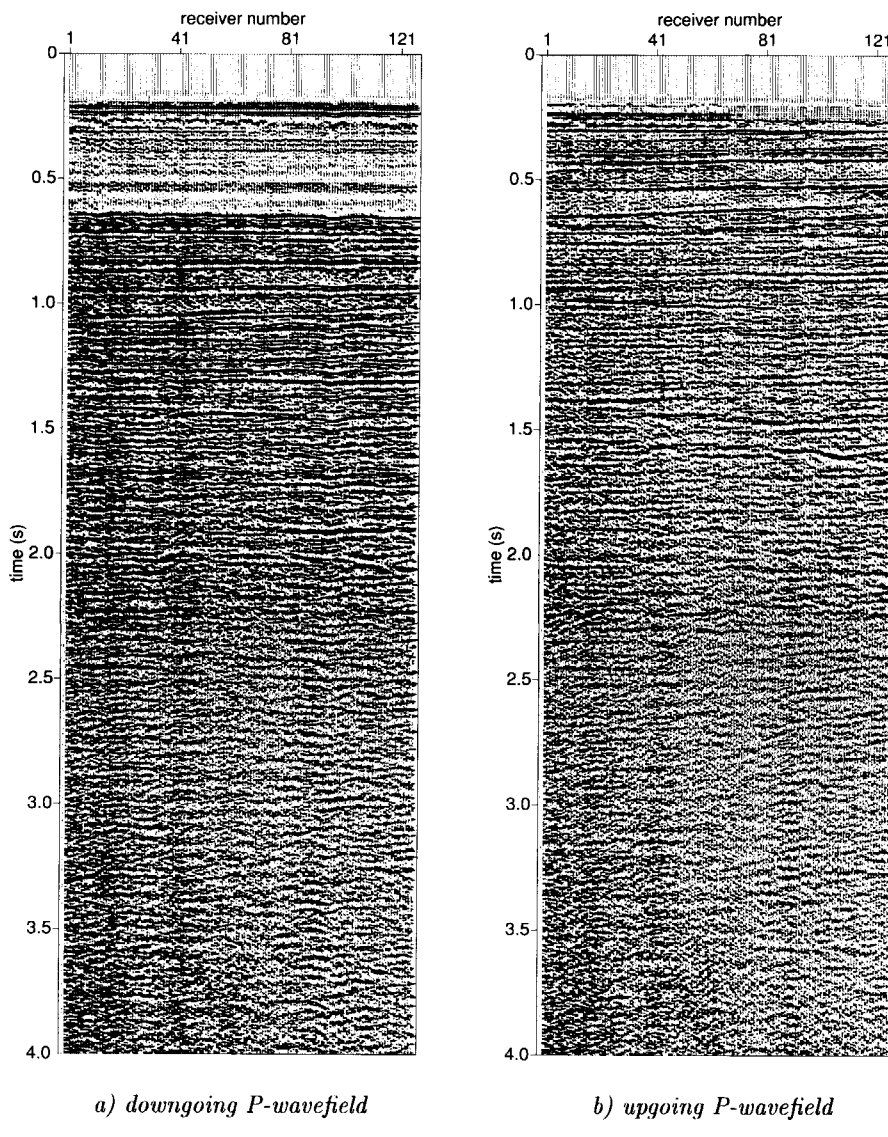


Fig. 3.20 Zero-offset sections of the P-wave decomposition result below the bottom.

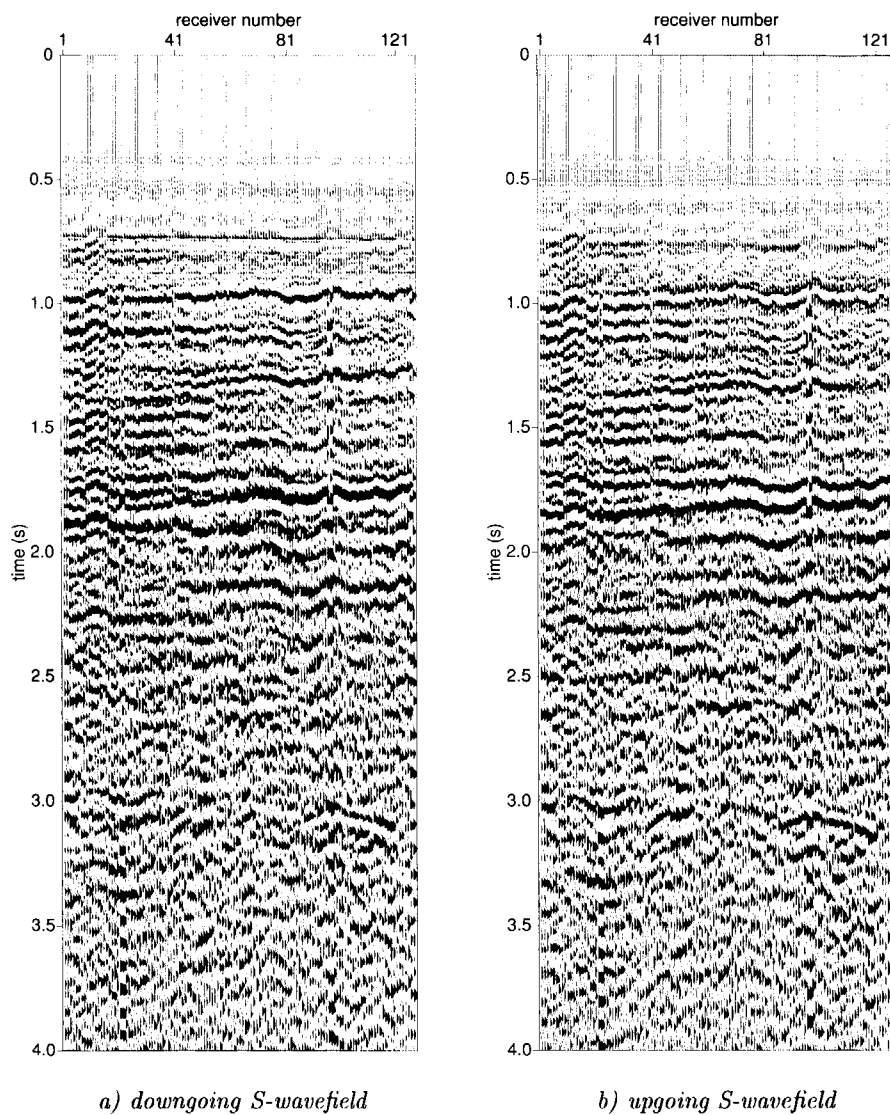


Fig. 3.21 Common-offset sections (500 m) of the S-wave decomposition result below the bottom.

Chapter 4

Wavefield decomposition: practical aspects for the shallow ocean-bottom

Aspects of ocean-bottom measurements not covered by the wavefield decomposition theory are phenomena like air gun bubbles (to which the hydrophone seems especially sensitive compared to the three-component geophone) and mechanical “cross-coupling”. In the application of the adaptive decomposition procedure to field data with a shallow ocean-bottom such phenomena will have a more pronounced effect, due to interference between events. In this chapter, the wavefield decomposition procedure, applied to a shallow (~ 120 m) ocean-bottom dataset from the Mahogany Field in the Gulf of Mexico, will be treated.

4.1 A shallow ocean-bottom example: Mahogany

The Mahogany Field is located in the subsalt play of the Gulf of Mexico, offshore Louisiana (Figure 4.1, taken from Camp and McGuire, 1997). The subsalt play is an area extending over 300 miles (500 km), characterized by tabular salt bodies, migrated upwards from a deeper salt layer below the sediments. The sediment accumulations between the deeper salt layer and the allochthonous (removed from its depositional location) salt sheets are the target of subsalt hydrocarbon exploration in this region (Figure 4.2), see for example Gras et al. (1998). The challenge for seismic acquisition/processing in this case is to obtain an image of the sediment structure in between the salts. The anomalous properties of the salt cause abrupt lateral variations in the velocity and density that may distort the seismic reflections.

The 4-C ocean-bottom dataset, provided by BP, that is used here for the demonstra-

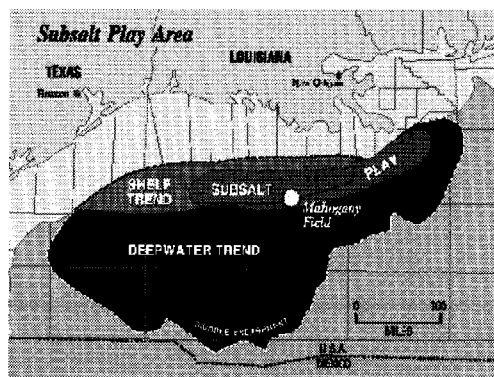


Fig. 4.1 Location of the Mahogany Field.

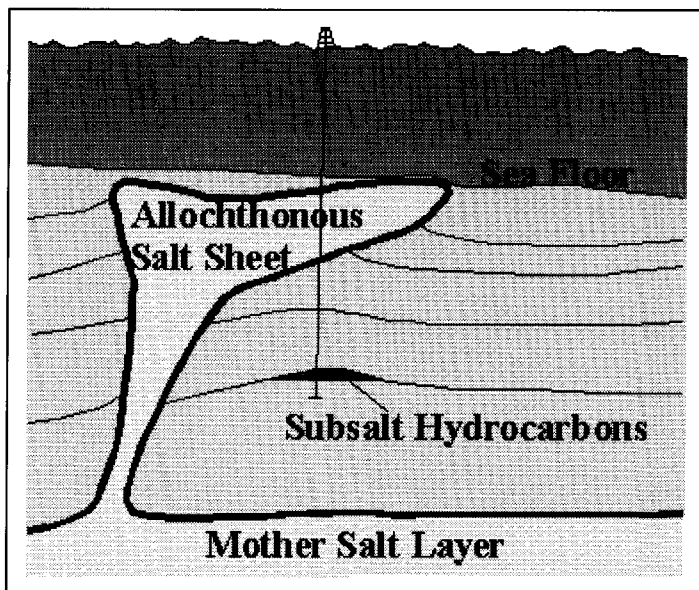


Fig. 4.2 Geology in the subsalt play, Gulf of Mexico area.

tion of the decomposition procedure was acquired in 1997 in the Mahogany Field by Geco-Prakla, using the Nessie 4C cable. There were 60 ocean-bottom receivers with a spacing of 25 m on a cable of 1500 m. The depth of the ocean-bottom is about 120 m. The airgun source was just below the water surface at a depth of 6 m. The interval between the shots was also 25 m. The ocean-bottom cable was moved 7 times. Each time the source covers the cable with a maximum offset of 10000 m. In this way a very long receiver line (7×1500 m) is obtained. The acquisition configuration is displayed in Figure 4.3. The data are recorded up to 10

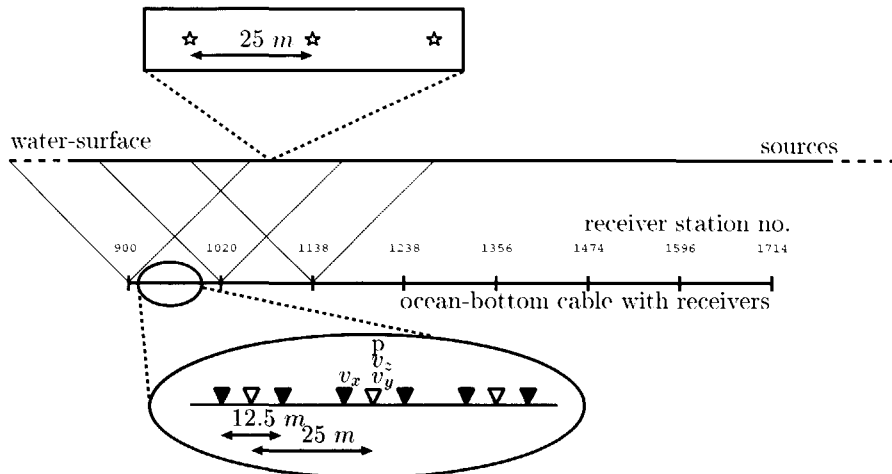


Fig. 4.3 Acquisition of the Mahogany ocean-bottom data.

seconds with a time sampling of 4 ms. In Figure 4.5 an example is shown of the first 8 seconds of the measured data on the pressure component. The data displayed are seven common-receiver gathers selected from the line, with offsets ranging from -700 m up to 700 m. The receiver number is given above each gather in Figure 4.5. From deeper reflection events, some idea of the sediment structure can be obtained. In Figures 4.6 and 4.7, the data of common-receiver gather 1321 are displayed for all four components for the total offset and time range. The pressure component in Figure 4.6a shows strong reverberations of the direct wave, these are caused by reverberations of the airgun source (airgun bubble). The airgun bubble in this case has approximately the same periodicity as the reverberations within the water layer. On the vertical velocity component (Figure 4.6 b) the airgun bubble can also be observed, but it is much weaker than on the pressure component, due to the higher sensitivity of the hydrophone for low frequencies. In addition the vertical component displays "cross-coupling" with the horizontal components (the events with low moveout velocity at near offsets). The horizontal (v_x) and crossline (v_y) velocity

components are displayed in Figures 4.7a and b (at the same scaling). Up to about 3 seconds the energy on the v_y component is small compared to the v_x component, after that the two components are about the same strength. This is an indication for the complex deeper structure where 3D effects come into play, for the shallower portion the situation is more or less 2D - resulting in less energy on the v_y component compared to the v_x component. Note the similarity between the near offset low moveout events in Figure 4.7 and the "cross-coupling" in Figure 4.6 b.

Before decomposition, the p , v_x and v_z data are deconvolved to remove the strong airbubble effect (Figures 4.8 and 4.9). The airbubble is assumed to stay constant over the spread, whereas the primary events may slightly change location. To find a predictive deconvolution filter that does not affect other events interfering with the airbubble, all components to be deconvolved (pressure, in-line velocity and vertical velocity) are combined to estimate an average angle-independent deconvolution filter (average over 3 components and the 7 common-receiver gathers displayed in Figure 4.5). After application of the estimated average deconvolution filter to all components (p , v_x and v_z), much of the airbubble has been removed; in Figure 4.8a only one "extra" reverberation was not removed. The average spectra of the deconvolved gathers are displayed in Figure 4.4.

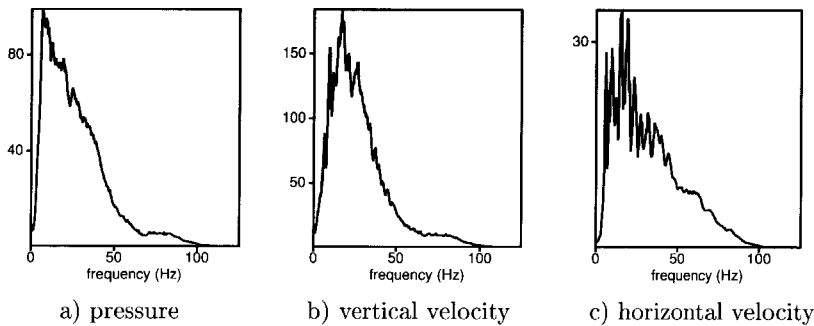


Fig. 4.4 Average frequency spectra of the data after deconvolution.

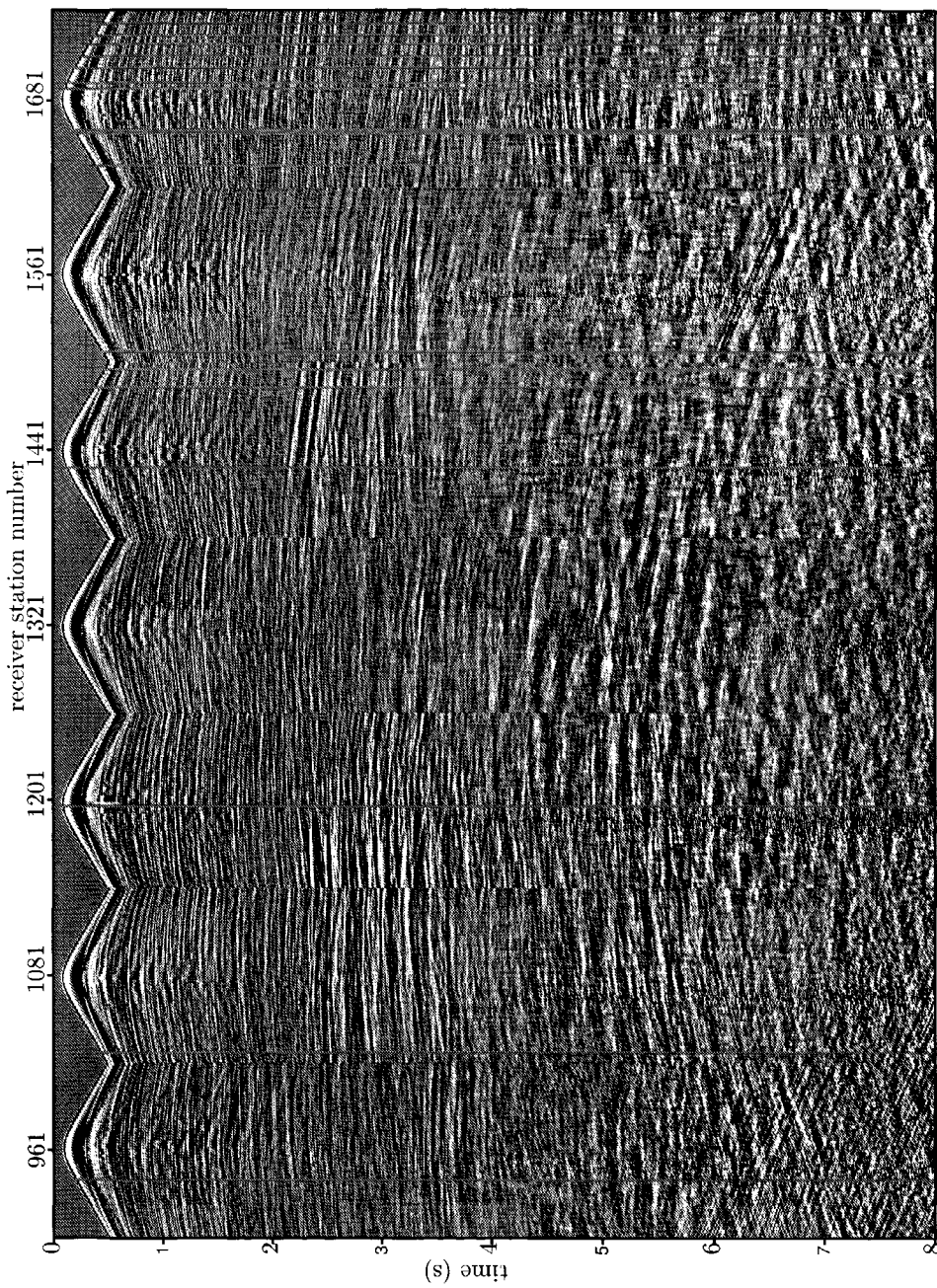


Fig. 4.5 Seven selected common-receiver gathers of the Mahogany ocean-bottom data.

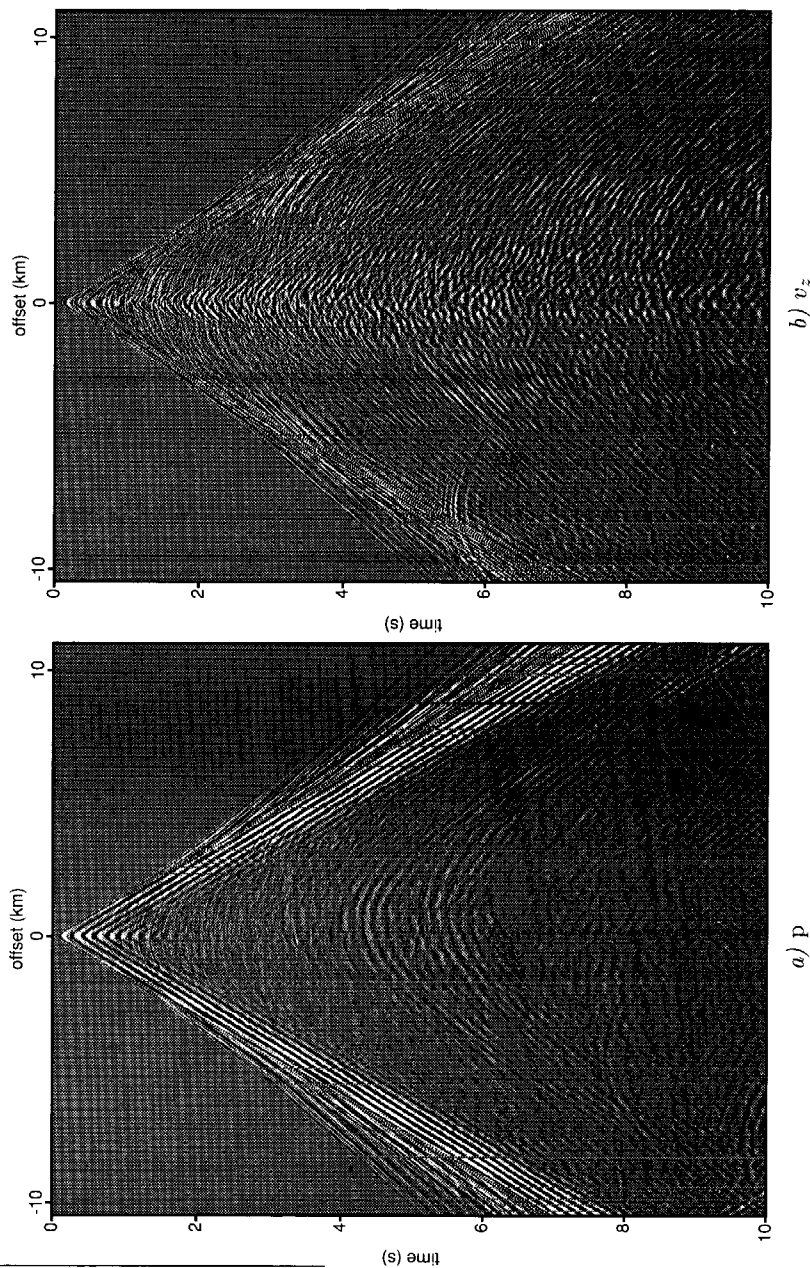


Fig. 4.6 Ocean bottom measurements of one common-receiver gather (number 1321) displayed with a gain factor of $t^{1.5}$, a) Pressure just above the bottom. b) Vertical velocity component.

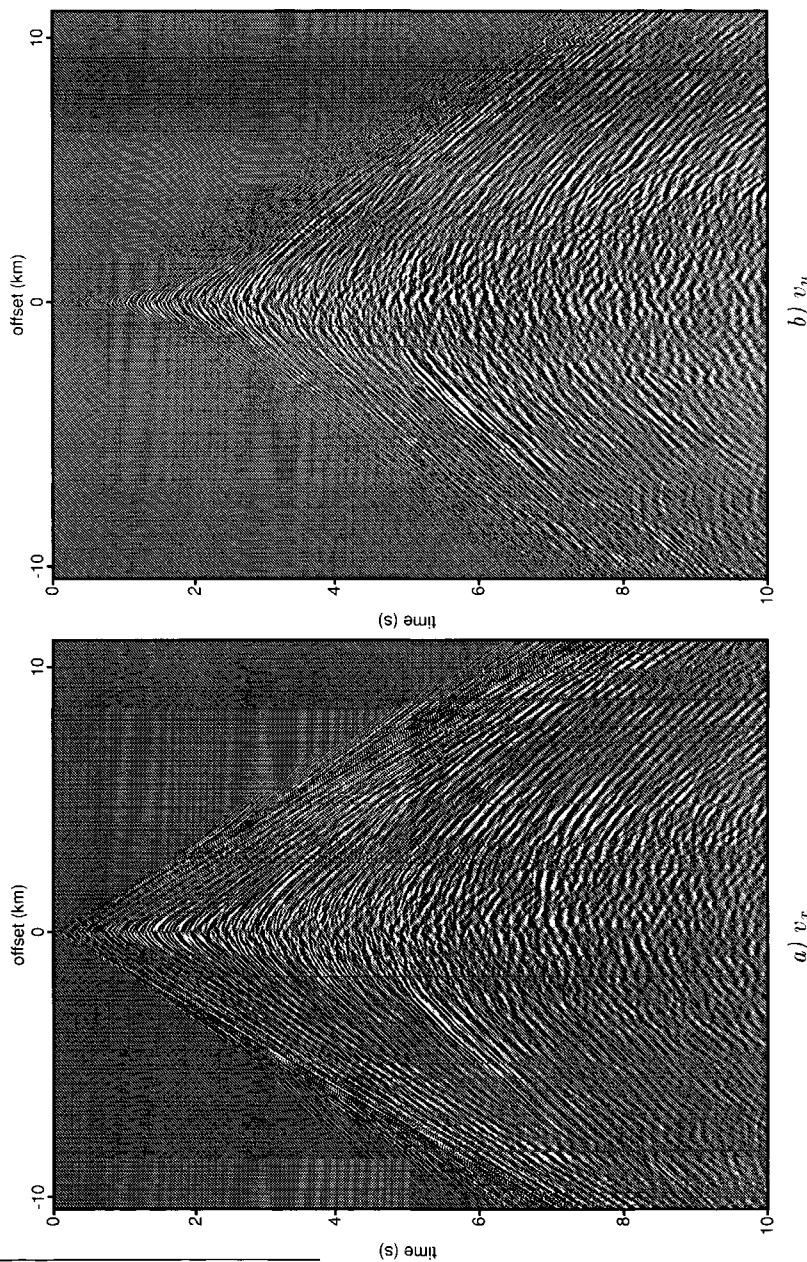


Fig. 4.7 Ocean bottom measurements of one common-receiver gather (number 1321) displayed with a gain factor of $t^{1.5}$. a) Horizontal inline component. b) Horizontal crossline component.

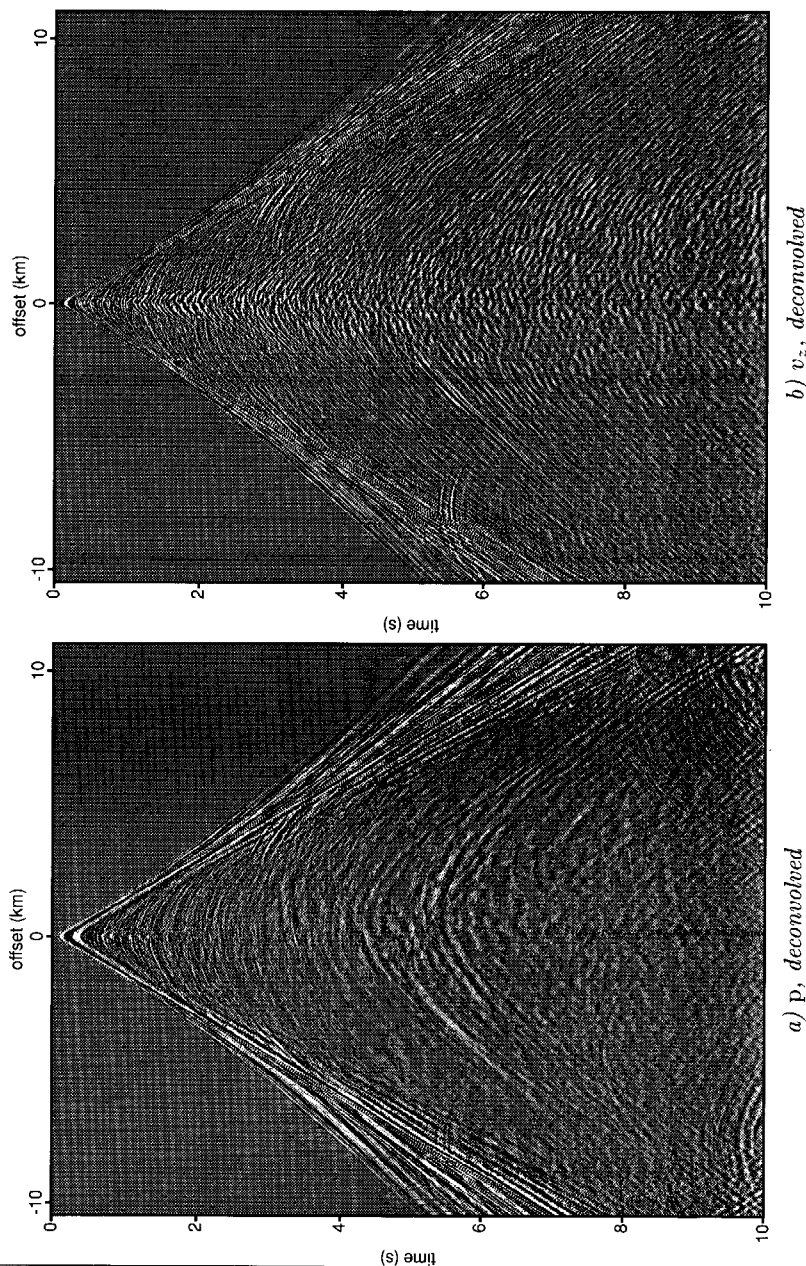


Fig. 4.8 Ocean bottom measurements of one common-receiver gather (number 1321) displayed with a gain factor of $t^{1.5}$ after deconvolution, a) Pressure just above the bottom. b) Vertical velocity component.

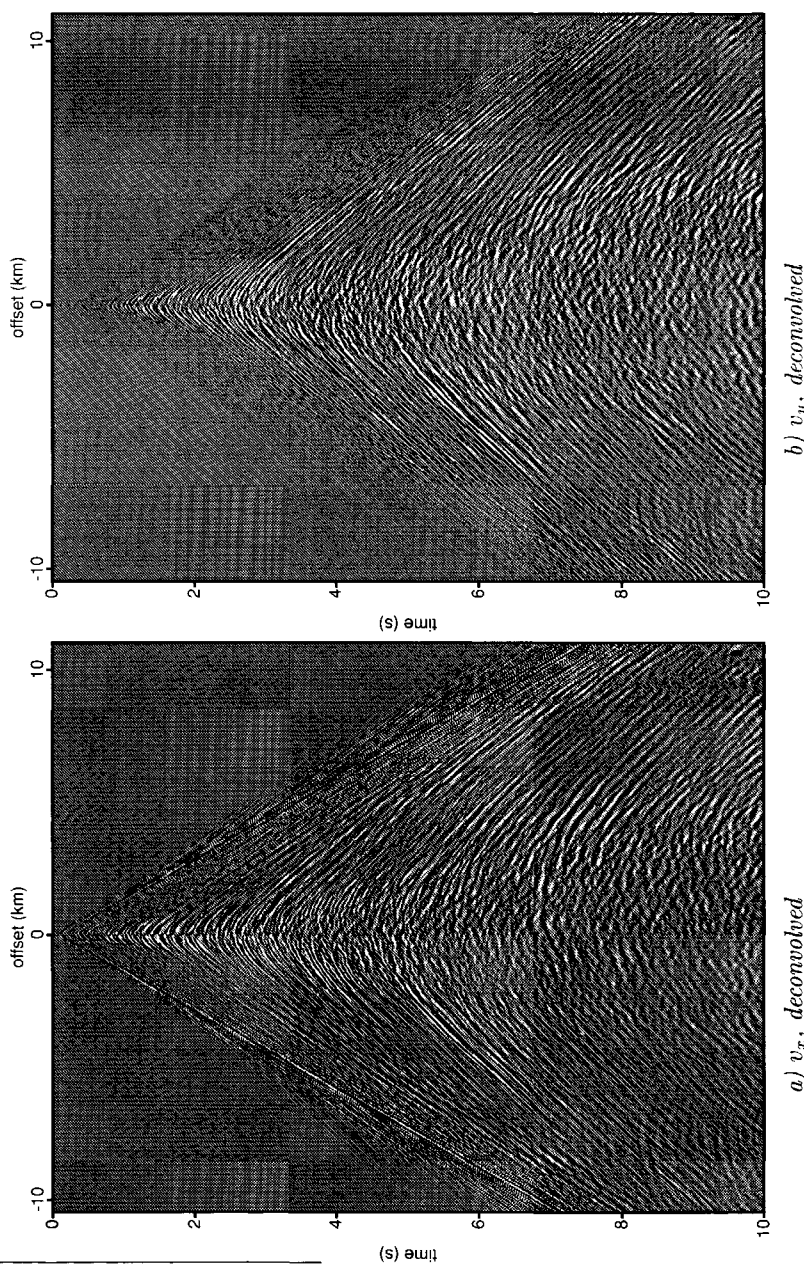


Fig. 4.9 Ocean bottom measurements of one common-receiver gather (number 1321) displayed with a gain factor of $t^{1.5}$ after deconvolution, a) Horizontal inline component. b) Horizontal crossline component.

4.2 Decomposition of one common-receiver gather

The performance of the 5-stage adaptive decomposition procedure, as described in Chapter 2, is tested on common-receiver gather 1321 after predictive deconvolution (Figures 4.8 and 4.9). Before decomposition was applied, the receiver gather was interpolated to a shot-interval of 12.5 meters to avoid aliasing within the frequency bandwidth in the Fourier and Radon transformations.

Stage 1: Corrections for cross-coupling

A correction to the vertical particle velocity, in the way discussed in the previous chapter, will not remove cross-coupling well in this case. The interference of the cross-coupling with other events is the reason that the minimum energy criterion does not apply. Therefore, stage 1 was not applied.

Stage 2: Acoustic decomposition just above the bottom

To apply stage 2 of the adaptive decomposition scheme, a window must be found that contains mostly primary energy. Choosing the window to lie between the direct arrival and the first multiple, as in Chapter 3, does not work in this case. Therefore, a primary window has to be chosen somewhere else in the data. This window is displayed in Figure 4.10a in the x, t domain, as the optimization will be performed in this domain. In Figures 4.10c and d the results after acoustic decomposition just above the ocean-bottom are displayed in the x, t domain. The arrows around 1.3 seconds highlight the primary event that was focussed on in the optimization procedure. Most energy in this event is moved to the upgoing wavefield. This result was obtained with a scalar scaling factor a between p and v_z (i.e. setting the length of the time filter $a(t)$ to one time sample, Figure 4.10b). Allowing $a(t)$ to be longer did not give better results. It is therefore better to simply keep a as a scalar and not introduce any frequency-dependency in further stages. In Figure 4.11 the down- and upgoing pressure fields just above the ocean-bottom are displayed in a larger window with offsets ranging from -5000 to 5000 m.

Stage 3: Elastic decomposition into τ_{zz}^\pm just below the bottom

It is not difficult to determine the window for stage 3, a window containing the direct wave only, as this does not have to be a very tight window. In Figure 4.12a this window is displayed in the τ, p domain, as the optimization will be performed in this domain. The down- and upgoing normal stress-fields are displayed in the

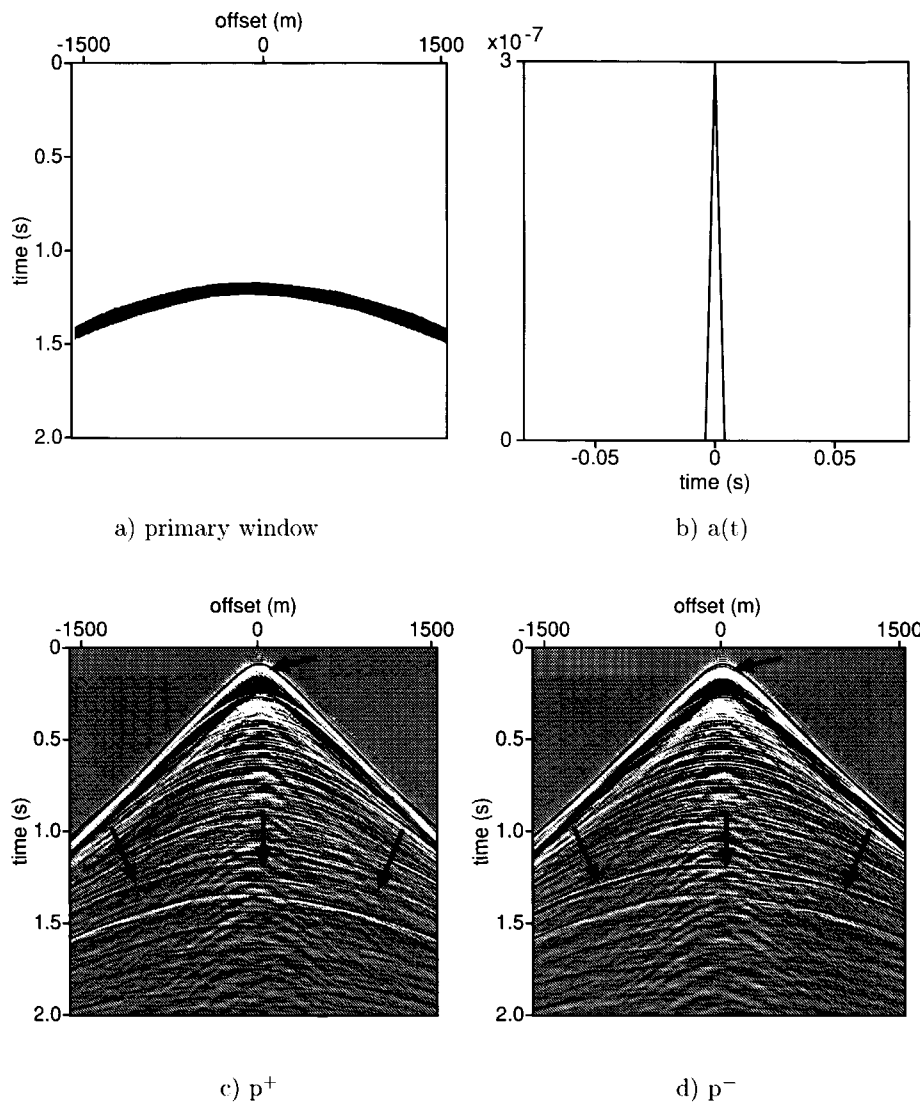


Fig. 4.10 Demonstration of the optimization procedure in decomposition stage 2 applied to receiver gather 1321: a) the black area defines the window over which the minimum energy criterion is applied, b) is the resulting (scalar) optimization filter and c) and d) show the acoustic decomposition result just above the ocean-bottom, in which the events that should have been suppressed in the downgoing wavefield are highlighted by arrows, note the small primary event just after the first arrival.

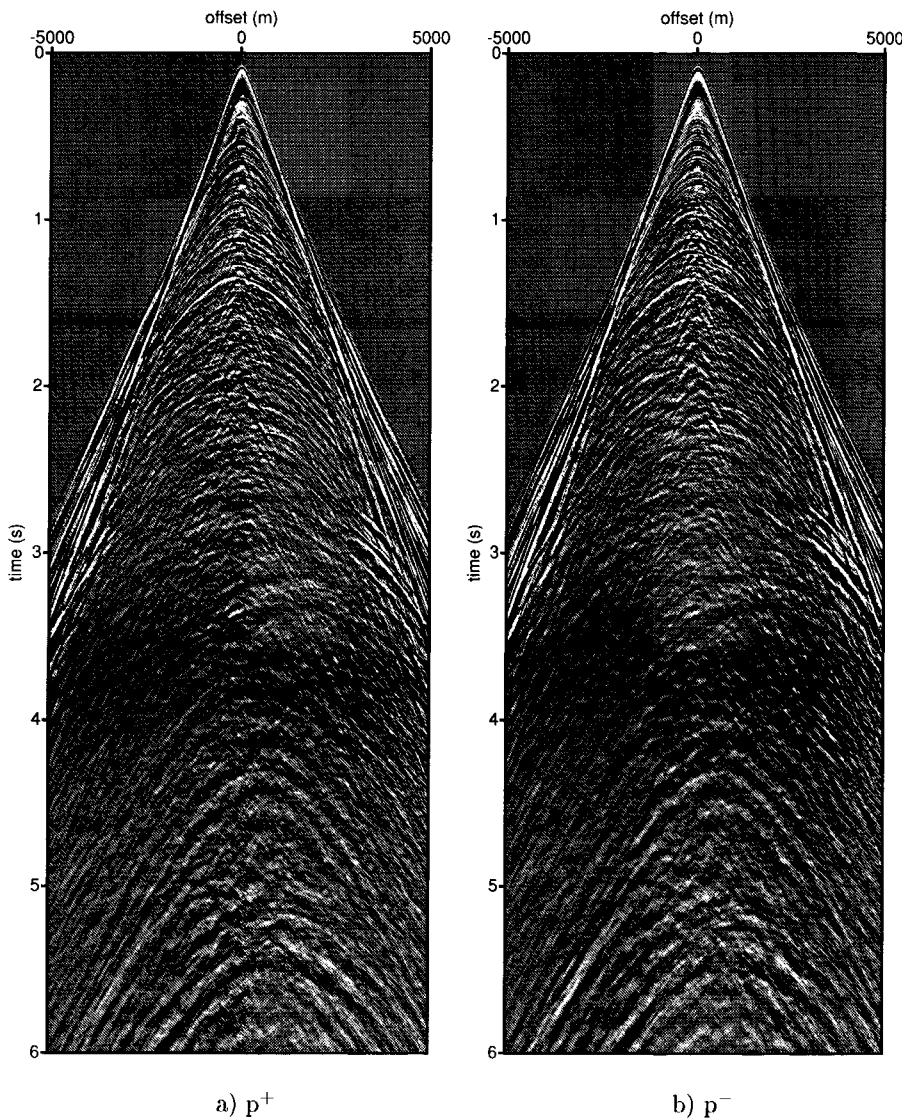


Fig. 4.11 Decomposition result of stage 2 applied to receiver gather 1321, a) is the down-going pressure wavefield just above the ocean-bottom and b) is the upgoing pressure wavefield.

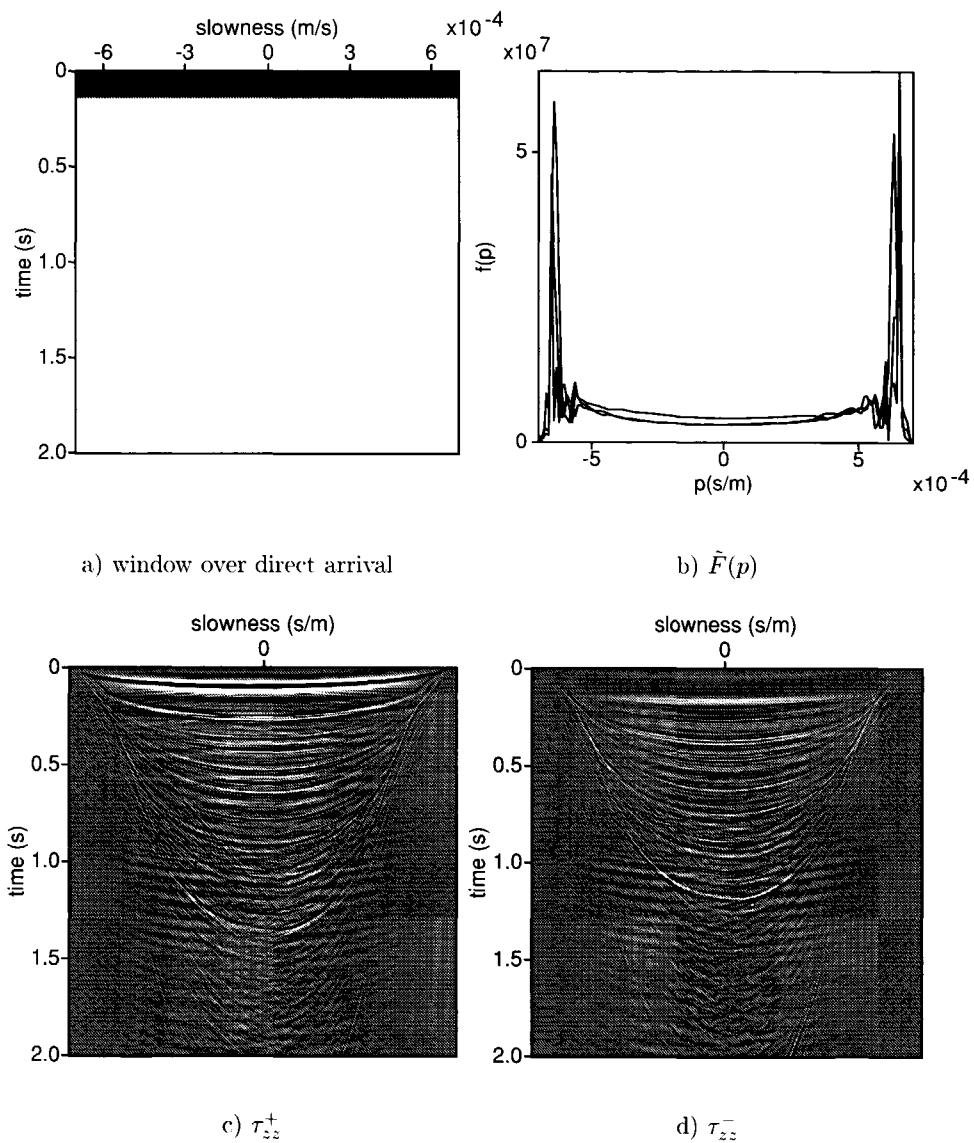


Fig. 4.12 Demonstration of the optimization procedure in stage 3 applied to receiver gather 1321: a) the black area defines the window over which the minimum energy criterion is applied, b) is the resulting optimal decomposition operator and c) and d) show the elastic decomposition result into down- and upgoing normal stressfields just below the ocean-bottom in the τ, p domain.

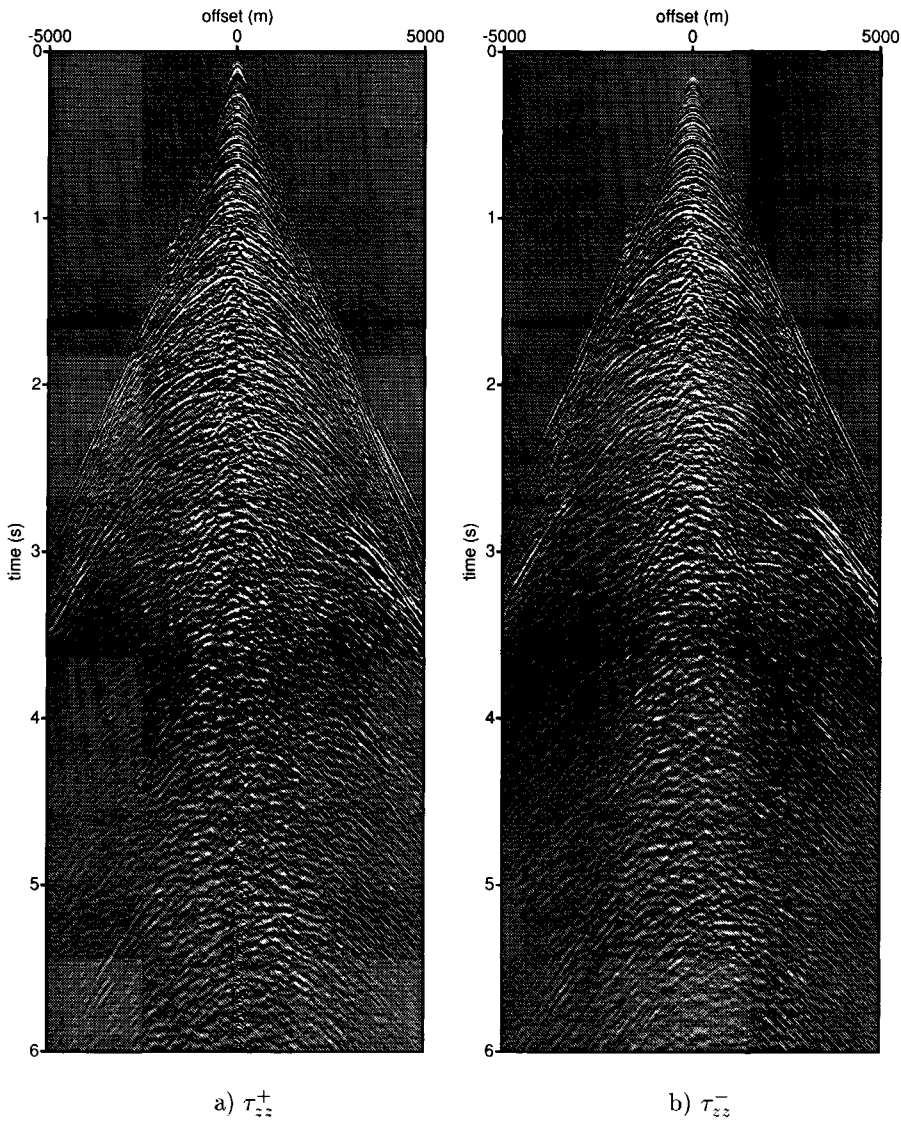


Fig. 4.13 Decomposition result of stage 3 applied to receiver gather 1321: a) the down-going normal stressfield just below the ocean-bottom and b) the upgoing normal stressfield.

τ, p domain in Figures 4.12c and d¹. Figure 4.12b shows the resulting optimization filter $\tilde{F}(p)$ for gather 1321. The different lines in the plot of $\tilde{F}(p)$ denote different frequencies within the frequency bandwidth. The frequency-dependency is small, so a frequency independent inversion of $\tilde{F}(p)$ should give good estimates of the medium parameters just below the ocean-bottom. The medium parameters obtained from the inversion are $c_P = 1538$ m/s $c_S = 128$ m/s and $\varrho = 1129$ kg/m³. In Figure 4.13 the down- and upgoing normal stress-fields just below the ocean-bottom are displayed in the x, t domain in a window with offsets ranging from -5000 to 5000 m.

Stage 4: Elastic decomposition into τ_{xz}^{\pm} just below the bottom

In this stage, the p and v_x components are combined to obtain the down- and upgoing shear stressfields just below the ocean-bottom, and a relative coupling filter, $b(t)$, is estimated for the v_x component.

The window used in stage 4 (Figure 4.14a), is the same as in stage 3. Using the medium parameters found in stage 3, the appropriate decomposition operators are applied to the p and v_x components. The scaling filter, $b(t)$, is displayed in Figure 4.14b. The down- and upgoing shear stressfields are shown in the τ, p domain in Figure 4.14c and d. The direct wave has been attenuated but not completely removed.

Because the direct arrival has a high signal-to-noise ratio, the length of the scaling filter $b(t)$ is not so critical as in stage 2. However, making the scaling filter $b(t)$ longer in time has another effect in this case. This is illustrated in Figures 4.15. In Figure 4.15a and b the \hat{p} and \hat{v}_x components are displayed in the τ, p domain after deconvolution. As mentioned earlier, one low-frequency reverberation of the airgun bubble is not removed from the pressure component after deconvolution (see Figure 4.15a). This low-frequency event is not present on the v_x component (Figure 4.15b). Because the frequency spectra are not the same, a long filter $b(t)$ is required to match the different signatures, resulting in a cross-talk with primaries that are located closely to the direct arrival. As a result resolution will be lost in the decomposition result of stage 4. Figures 4.15c and d show the down- and upgoing shear stressfields that were obtained using Figures 4.15a and b as input. The decomposition result has less resolution than the measured v_x component. The down- and upgoing shear stressfields in Figures 4.14c and d were obtained after a bandpass filter was applied to the pressure component p to remove the remaining low frequency reverberation. This decomposition result has similar resolution as the original v_x component. In Figure 4.16 the down- and upgoing shear stressfields of Figure 4.14 are displayed in the x, t domain for a window ranging from offsets of -5000 m to 5000 m.

¹The upgoing normal stressfield determined in stage 3 can help identify primary reflection events. If necessary, stage 2 could then be repeated with a better primary window choice.

Stage 5: Elastic decomposition into P- and S-wave potentials just below the bottom

The results of stages 3 and 4 were combined to obtain the down- and upgoing P- and S-wave potentials (φ^\pm and ψ^\pm). The final decomposition result for receiver gather 1321 is displayed in Figures 4.17 and 4.18 in the x, t domain. As c_S was quite low, the decomposition for the main part performed a separation of downgoing and upgoing wavefields and not so much of P- and S-waves, as the latter was already accomplished by the low S-velocity.

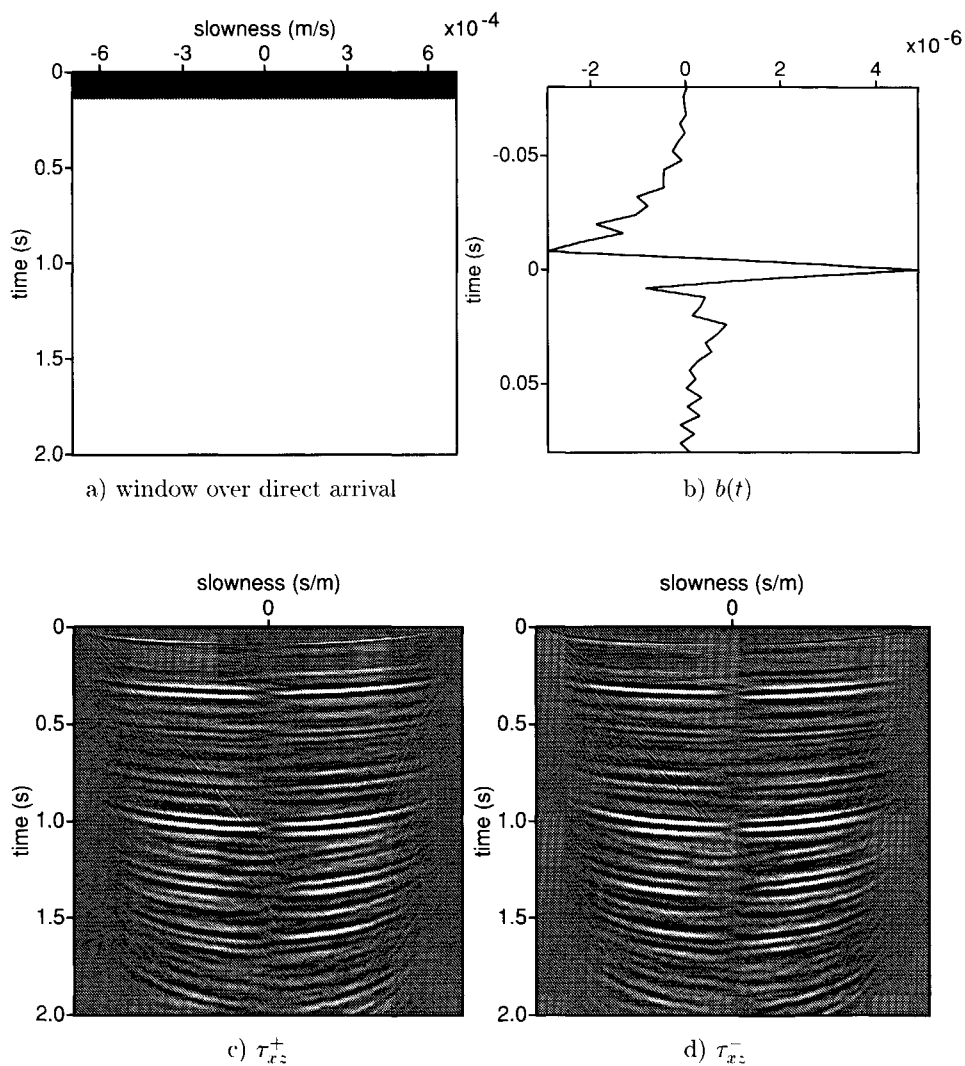


Fig. 4.14 Demonstration of the optimization procedure in stage 4 applied to receiver gather 1321: a) the black area defines the window over which the minimum energy criterion is applied, b) the resulting calibration filter and c) and d) show the elastic decomposition result into down- and upgoing shear stressfields just below the ocean-bottom in the τ, p domain.

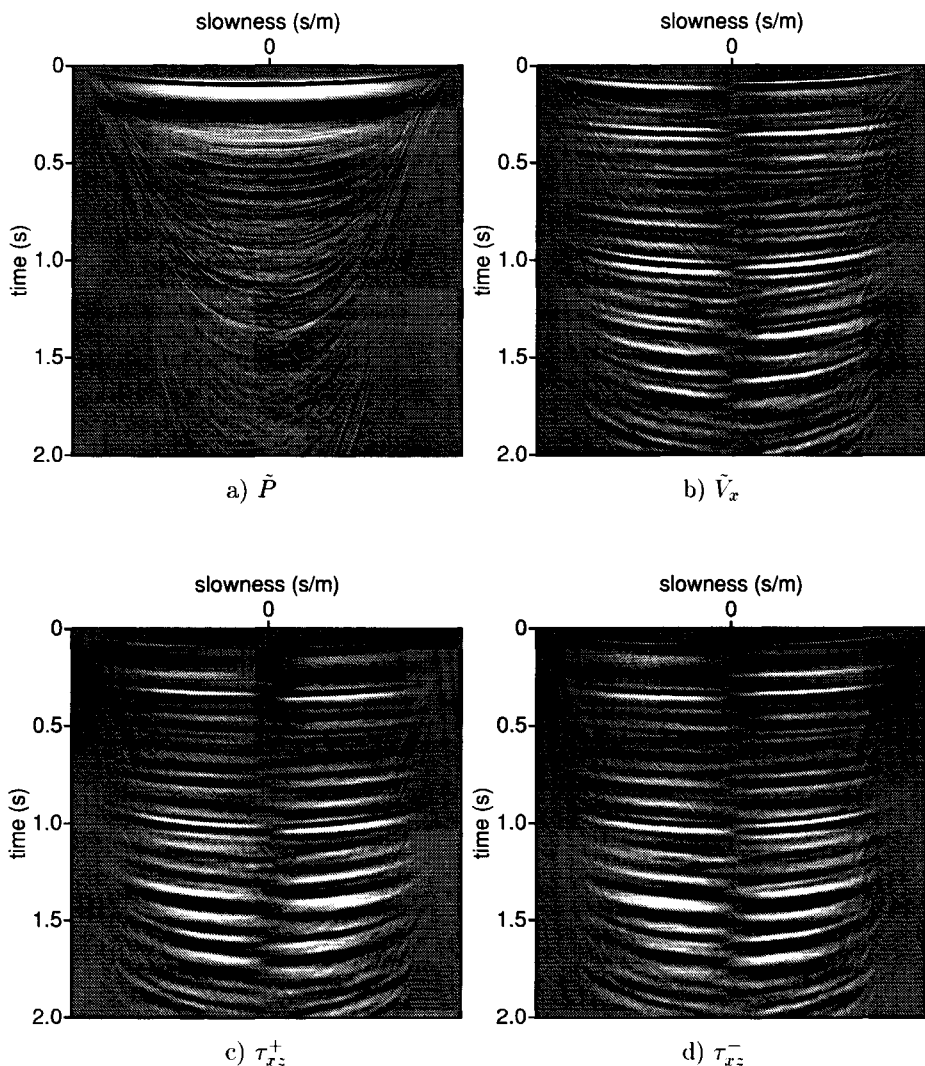


Fig. 4.15 Repeating the optimization procedure of stage 4, as shown in the previous figure, but without the application of a bandpass filter ($f=0,25,75,100$), a) \hat{P} component after deconvolution, interpolation and $\tau - p$ transform, b) \hat{v}_x component after deconvolution and $\tau - p$ transform c) and d) show the elastic decomposition result into down- and upgoing shear stressfields just below the ocean-bottom in the τ, p domain.

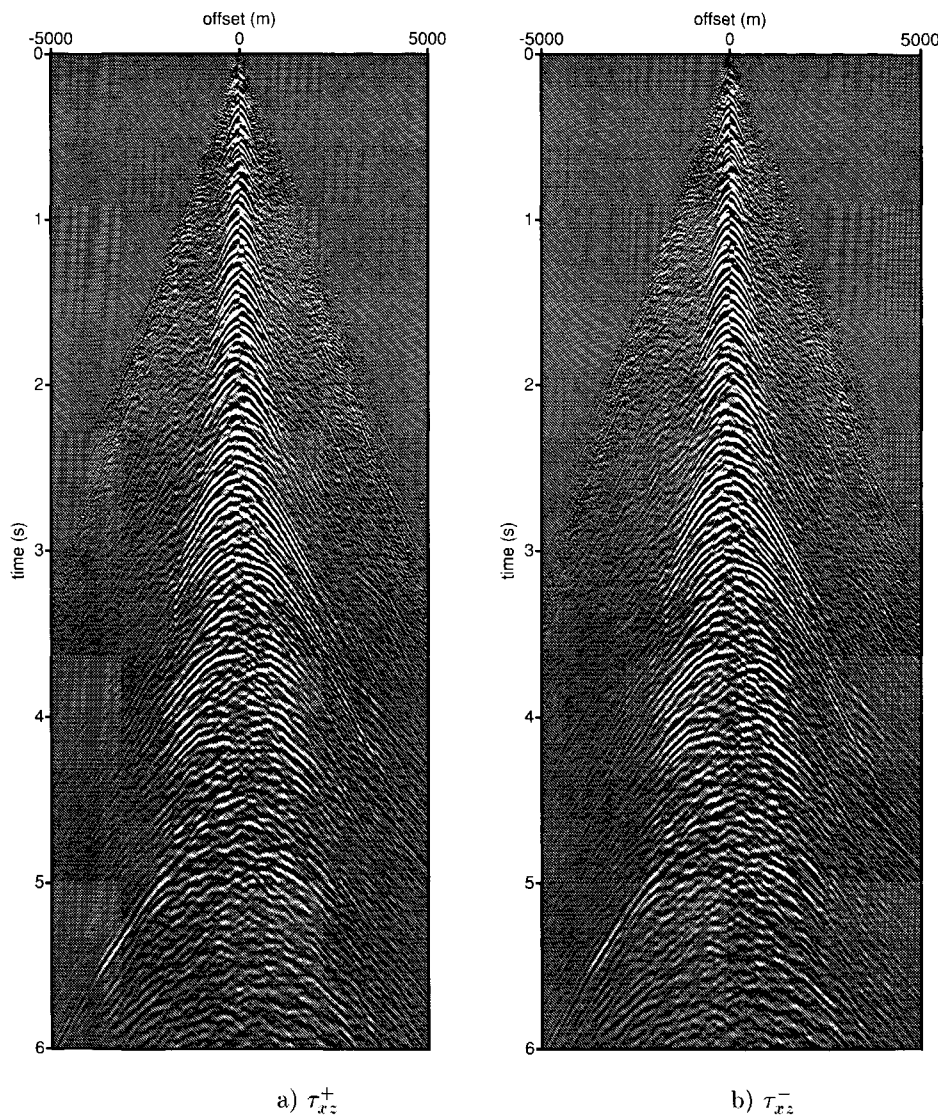


Fig. 4.16 Decomposition result of stage 4 applied to receiver gather 1321: a) the down-going shear stressfield just below the ocean-bottom and b) the upgoing shear stressfield.

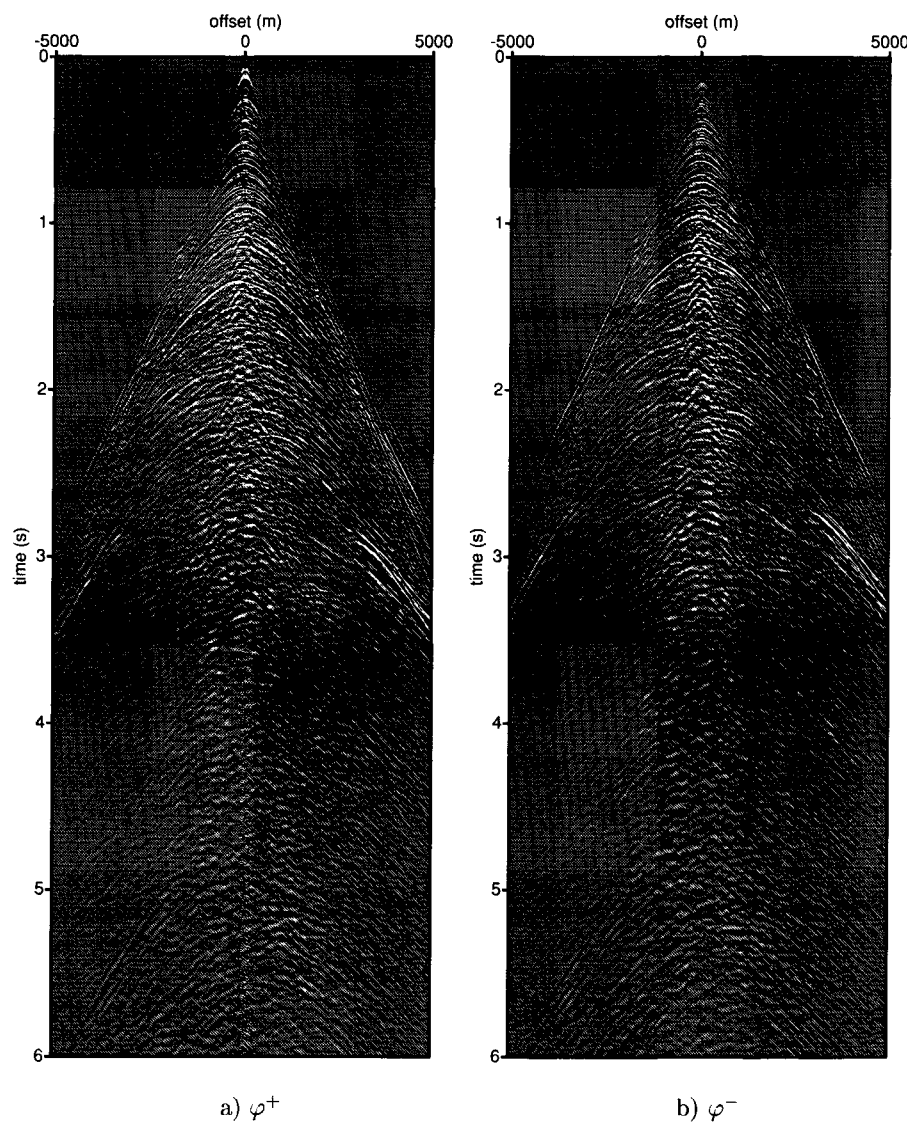


Fig. 4.17 Decomposition result of stage 5 applied to receiver gather 1321: a) the down-going P-potential just below the ocean-bottom and b) the upgoing P-potential.

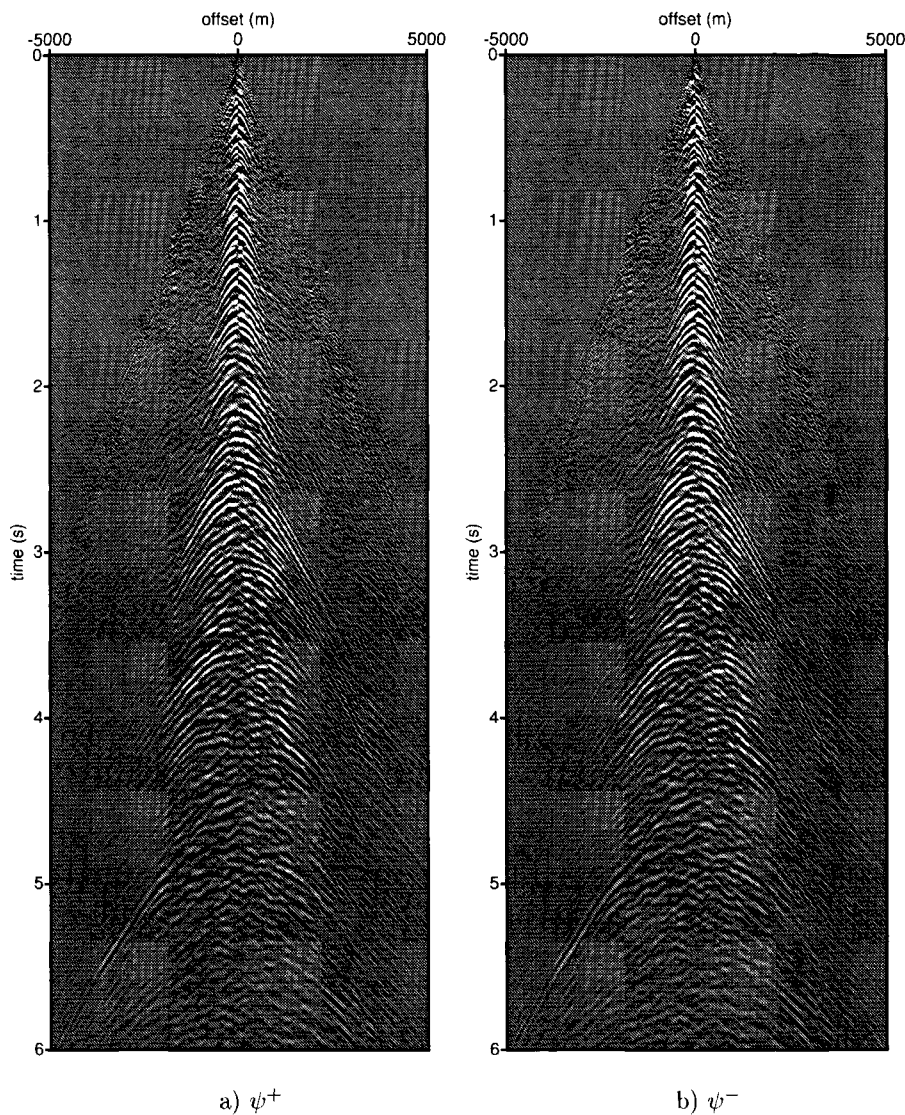


Fig. 4.18 Decomposition result of stage 5 applied to receiver gather 1321: a) the down-going S-potential just below the ocean-bottom and b) the upgoing S-potential.

4.3 Application to part of the 2-D data

The decomposition procedure was repeatedly applied to successive common-receiver gathers to decompose the full 2-D dataset. In this section examples will be shown from the fourth receiver line (Figure 4.3). This subselection of data consists of common-receiver gathers 1239-1355. In a later section inversion results for line three and line five will also be given.

Preprocessing (deconvolution and interpolation) of the data was done as discussed in section 4.1. The deconvolution was performed on six gathers at a time until all 59 gathers in the line have been deconvolved, according to the deconvolution strategy explained in section 4.1. The 6 common-receiver gathers are separated from each other as far as possible over the line.

Stage 1 is not applied to this dataset - as was discussed in the previous section. To apply stage 2 of the adaptive decomposition scheme, a window must be chosen that contains mostly primary energy. The window of Figure 4.10a could not be used for all receiver gathers in the line, as the primary event at 1.2 seconds is not equally strong over the whole line. Therefore, an additional primary event at 0.8 seconds is chosen to aid optimization for parts of the line where one primary becomes weaker. By using a mask that combines both events, a constant primary window can be used over the line and the picking of the window has to be performed only once. This window is displayed in Figure 4.19a. The results of stage 2 for gather 1305 obtained with this mask window, are shown in Figure 4.19. In Figures 4.19c and d the results after acoustic decomposition just above the ocean-bottom are displayed. The arrows between 1.0 seconds and 1.5 seconds highlight one of the primary events that should be removed from the downgoing wavefield just above the bottom by the optimization procedure. Most energy in this event has indeed moved to the upgoing wavefield. Note that in addition a small primary event just after the direct wave has been suppressed in the downgoing wavefield (uppermost arrow in Figures 4.19c and d). This result was obtained with a scalar scaling factor a between the p and v_z components (i.e. setting the length of the time filter $a(t)$ to one sample, Figure 4.19b), as in the previous section. Each common-receiver gather gives one scaling factor a (Figure 4.20). The scaling factor a is not very constant over line 4, this indicates a variable coupling of the v_z component over the receiver line.

It is much more difficult to find an appropriate primary window for a relatively shallow ocean-bottom because there is much more interference between events. This gives greater inaccuracy in the estimation of the filter $a(t)$. The effect of inaccurate estimates of $a(t)$ on the further stages of the adaptive decomposition scheme will be investigated in section 4.4.

It is not difficult to determine the window for stage 3 - a window containing the direct wave only, as this does not have to be a very tight window. The window displayed in Figure 4.12a can be used over the whole line. For each receiver gather in the line a decomposition filter $\tilde{F}(p)$ is determined. The inversion result of the medium parameters from all filters $\tilde{F}(p)$ obtained from line 4 is displayed in Figure 4.22. The c_P estimates remain quite constant over the line at a value around 1600 m/s. The ϱ estimates show more fluctuations from values in the order of 1500 kg/m³ up to 2500 kg/m³ and even two outliers above 2500 kg/m³. The estimates for c_S lie around an average value of 300 m/s with two inversion results giving an S-velocity of zero. A further discussion of the inversion results is given in the next section.

4.4 Estimation of the medium parameters

In this section, the inversion of the medium parameters for the Mahogany dataset from the optimal filters $\tilde{F}(p)$ will be investigated in more detail. The filter $\tilde{F}(p)$ is determined in the time-domain and then transformed to the frequency-domain. In Figure 4.23, the filter $\tilde{F}(p)$ of receiver gather 1317 is displayed as a function of (positive) rayparameter and frequency. The source spectrum is plotted in the background. As can be seen the filter $\tilde{F}(p)$ is not frequency independent over the whole frequency range, but it is approximately frequency independent within the main data bandwidth (considering only the precritical part of the filter). For the inversion, three frequency components of the filter $\tilde{F}(p)$ in the strongest part of the source spectrum were selected (see Figure 4.31), and an average inversion result, weighted with the relative strengths of the particular frequencies in the source spectrum, is obtained.

If the filter $\tilde{F}(p)$ is frequency independent within the data bandwidth, the question arises whether it would suffice to estimate an optimization filter $\hat{f}(p, \tau)$ with only one time sample. In theory, this would be possible only for pre-critical angles, as for higher angles the imaginary part of the decomposition operator is not zero anymore (Figure 4.24). To represent the operator in the time domain for post critical angles, longer filters are therefore necessary.

In Figure 4.25 the decomposition result of stage 3, calculated with a filter length of 1 time sample (i.e. a frequency independent filter), and a filter length of 21 time samples, are displayed in the τ, p -domain. For a longer filter the direct arrival has been better removed from the upgoing normal stressfield (Figure 4.25b) than for a filter of length one. For the later arrival times the sections look quite similar. The filters $\tilde{F}(p)$ obtained with filter lengths of 1 and 21 are compared in Figure 4.26. In Figure 4.26a the filter obtained for receiver gather 1237 is displayed. The three thin lines are 3 frequencies within the data bandwidth (filterlength is 21 samples in

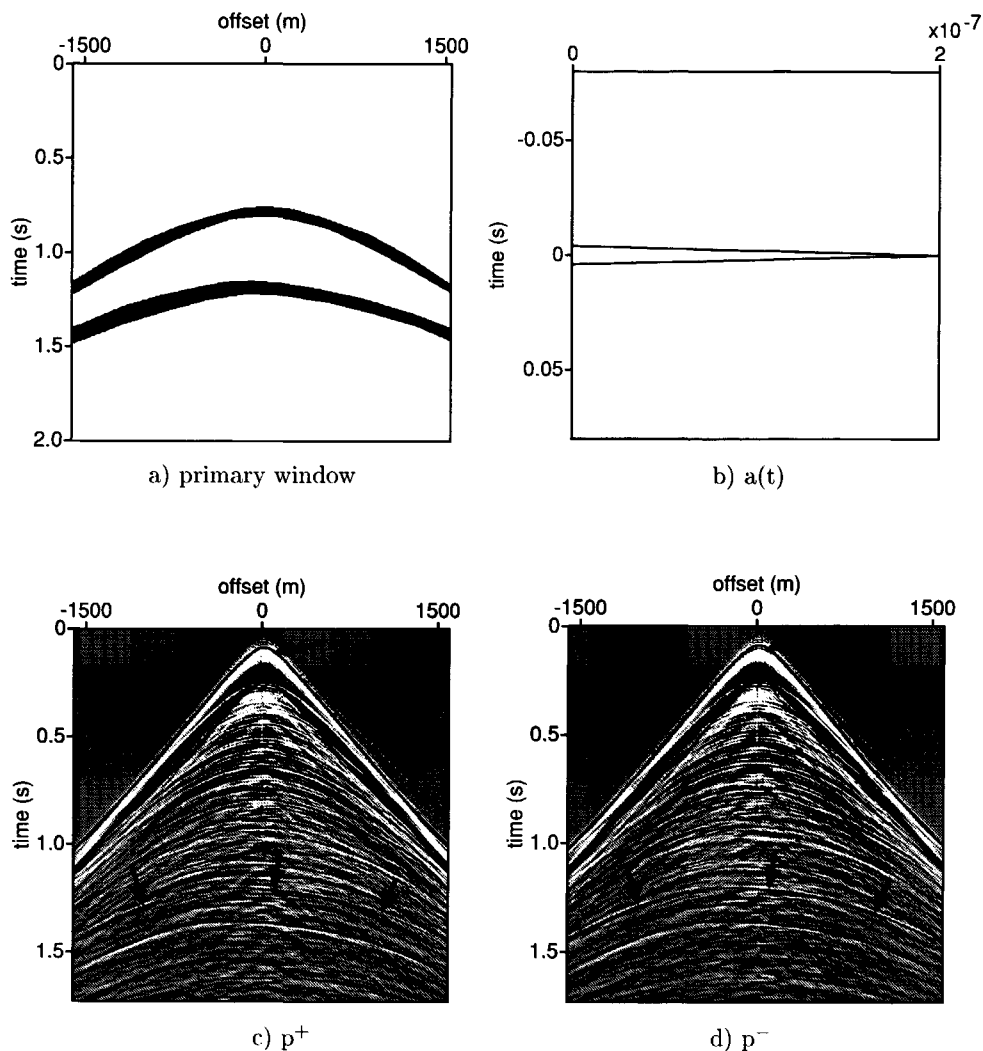


Fig. 4.19 Demonstration of the optimization procedure in stage 2 applied to receiver gather 1305: a) the black area depicts the window over which the minimum energy criterion is applied, b) is the resulting (scalar) optimization filter and c) and d) show the acoustic decomposition result just above the ocean-bottom, in which two primary events that should have been suppressed in the downgoing wavefield are highlighted by arrows, note the small primary event close after the direct arrival.

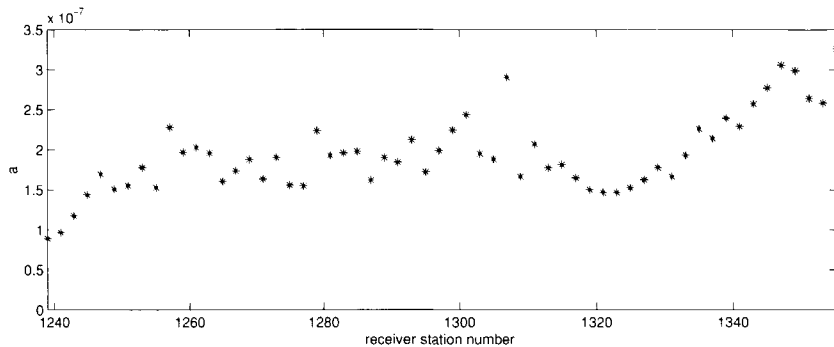


Fig. 4.20 Estimations of the (scalar) calibration filters between p and v_z over line 4 displayed as a function of receiver station number, using the optimization window in Figure 4.19a.

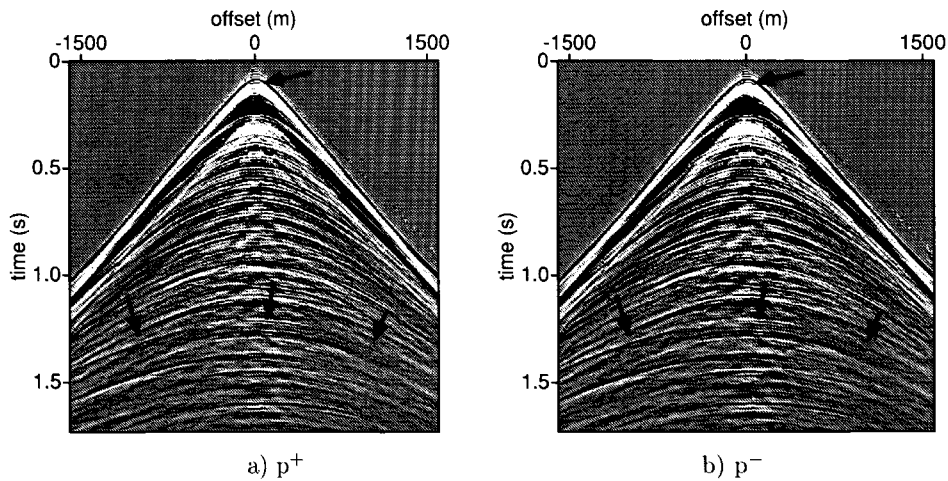


Fig. 4.21 Decomposition result of stage 2 applied to receiver gather 1239.

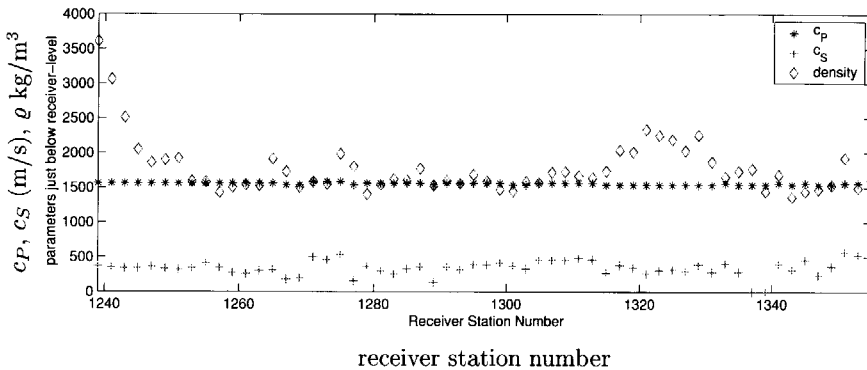


Fig. 4.22 Inversion results for the medium parameters just below the ocean-bottom for line 4 displayed as a function of receiver station number. Diamonds denote the density estimates, stars the c_P estimates and plusses the c_S estimates.

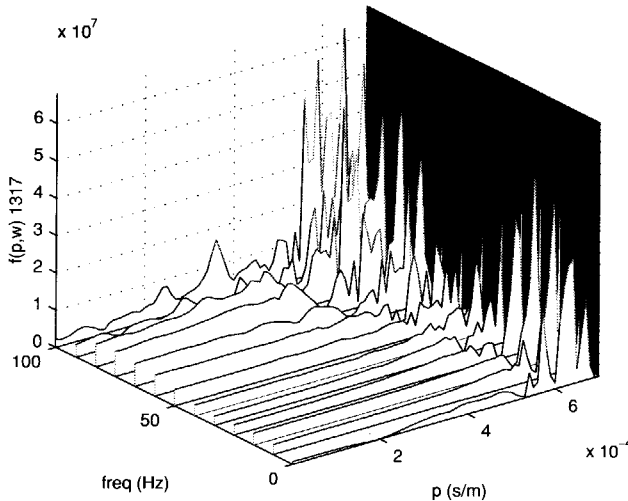


Fig. 4.23 The filter $\tilde{F}(p)$, obtained from common-receiver gather 1317 after transformation from the τ, p -domain to the ω, p -domain. Only the result for positive p -values has been displayed. On the plane in the background the average frequency spectrum of the data is displayed.

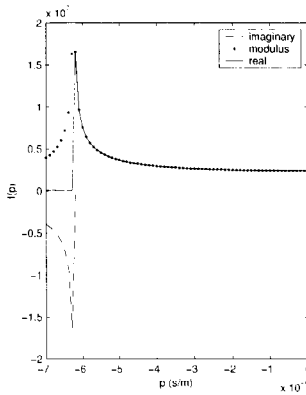


Fig. 4.24 The theoretical decomposition operator $\tilde{F}(p)$. The dotted line is the modulus, the positive valued solid line is the real part of the operator, and the remaining line is the imaginary part of the operator.

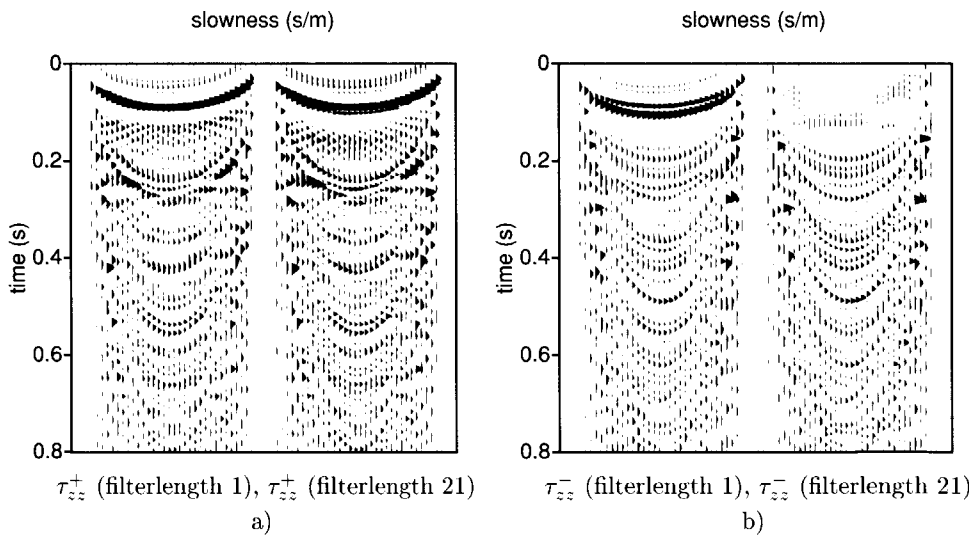


Fig. 4.25 Demonstration of effect of filter length of $f(p, \tau)$ in the optimization procedure in stage 3 applied to receiver gather 1237, in a) the downgoing normal stress-field in the τ, p -domain is displayed, obtained respectively with filterlength 1 and filterlength 21, in b) the upgoing normal stressfield is displayed, obtained respectively with a filterlength of 1 time sample and of 21 time samples.

the time domain). The thick solid line denotes the operator obtained using only one time sample. The latter lies slightly under the curves for the frequencies of 25 and 33 Hz in the rayparameter interval $[-6 \cdot 10^{-4}, -4 \cdot 10^{-4}]$ in the precritical rayparameter interval. In Figure 4.26b the light gray lines are all operators obtained over line 3 with filter length 1, the black lines are all operators over the line of filter length 21, plotted together (only the frequency component of 33 Hz is displayed). The smear off the operators gives an indication of variations in medium parameters over the line. The peak positions remain quite stable, the curvatures for higher rayparameter values change gradually.

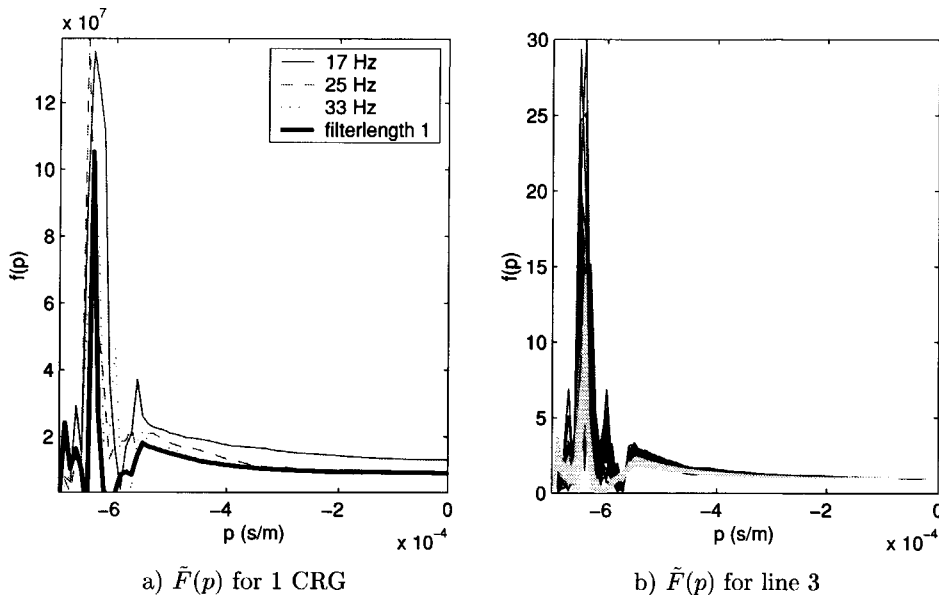


Fig. 4.26 Filter $\tilde{F}(p)$; a) for receiver gather 1237 the difference is shown between a filter of 21 samples (frequencies of 17, 25 and 33 Hz are displayed), and a filter of 1 time sample (thick solid line); in b) the variability of the filter is displayed by plotting the filters of all receiver gathers in line 3 together (the light-gray lines are filters of 1 time sample, the dark lines are the frequency of 33 Hz selected from the filter of 21 samples). All filters are normalized to the filter value at $p = 0$.

Determination of compressional velocity

The P-velocity is determined by locating the maxima of $\tilde{F}(p)$. In this way for each $\tilde{F}(p)$ 3 values for the maxima location are obtained (one for each frequency). From

these 3 values the median is taken to obtain one P-velocity per receiver gather. The P-velocities as a function of receiver number are displayed in Figure 4.27. Three levels for the velocity can be distinguished. This appearance is due to the discrete rayparameter values at which the singularities are sampled. The difference between the upper- and lower level is taken as the uncertainty in the P-velocity estimate (where it is assumed that the ocean-bottom has a constant P-velocity over the receiver line).

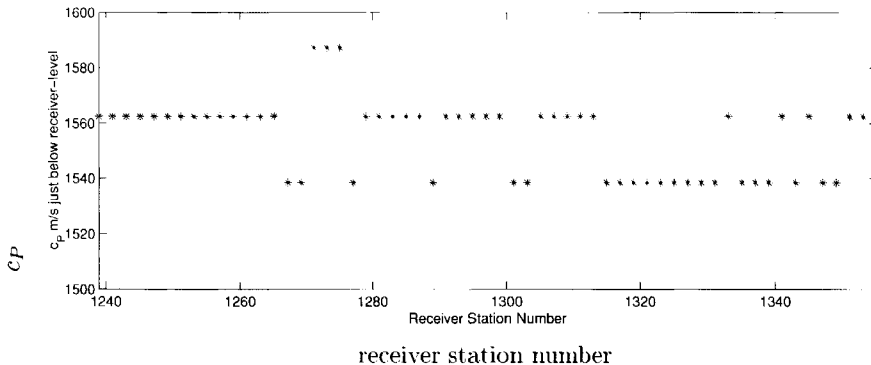


Fig. 4.27 Inversion results for the P-velocity just below the ocean-bottom over line 4 displayed as a function of receiver station number.

Determination of density

From Figure 4.22 it can be seen that the density estimates fluctuate strongly across the line, even obtaining unrealistic values. The density appears as a constant in the decomposition operator $\frac{\varrho_3}{2q_P}$. The average value of the 3 frequency components at small ray parameter values is taken as the density estimate. This means that if the coupling filter $A(\omega)$ that is estimated in stage 2 is not correct, the optimization procedure in stage 3 will compensate for this error. If the filter A is just a scaling factor (i.e. frequency independent) it follows that an erroneous determination of the filter A results in a (rayparameter independent) amplitude change in the filter $\tilde{F}(p)$:

$$\tilde{P}^{\pm} = \frac{1}{2} \tilde{P} \pm A_{err} \frac{\varrho_0}{2q_0} \tilde{V}_z, \quad (4.1)$$

where $A_{err} = A \cdot d$ with d a scale factor, and A the true scaling filter,

$$-\tilde{T}_{zz}^{\pm} = \frac{1}{2}\tilde{P} \pm A_{err}\tilde{F}(p)\tilde{V}_z, \quad (4.2)$$

$$= \frac{1}{2}\tilde{P} \pm Ad\tilde{F}(p)\tilde{V}_z, \quad (4.3)$$

$$= \frac{1}{2}\tilde{P} \pm A\tilde{F}_{err}(p)\tilde{V}_z, \quad (4.4)$$

where $\tilde{F}_{err} = d\tilde{F}(p)$ is the filter that is actually estimated in the least squares optimization of stage 3. Neither the singularity location nor the shape of filter $\tilde{F}(p)$ are influenced by the error in scaling filter A when the latter is frequency independent. Only the amplitude of the filter $\tilde{F}(p)$ is changed. In fact, an inversion is carried out for $(d\rho)/2$, where d is the error made in the estimation of scaling filter A after stage 2. Therefore the behaviour of the density estimates in Figure 4.22 does not reflect the variability of the density over the line, but rather is an indication that the scaling filter has not been well determined in stage 2. The c_P and c_S estimates remain unaffected by this error. The fluctuations of the density estimates over the line reflect the accuracy with which the scaling factor a has been determined. For a shallow ocean-bottom the events are closer together and it is difficult to isolate a window with only primary energy - resulting in a less well determined scaling factor.

It can be verified that an unrealistic density estimate is coupled to an unsatisfying decomposition result in stage 2. In Figure 4.21 the decomposition result of stage 2 for receiver gather 1239 is displayed. For this gather an abnormally high density estimate was found. Compared to the decomposition result at receiver 1305 (Figure 4.19c and d), where a density estimate close to 1500 kg/m^3 was obtained, there is still considerable primary energy present in the downgoing wavefield in Figure 4.21a. Note the small primary event coming just after the direct arrival: in Figure 4.19 this event has been moved to the upgoing wavefield, in Figure 4.21 this event is still present in both the down- and upgoing pressure field. The fixed primary window that is used over the line, is not optimal for this receiver gather. Although the decomposition result of stage 2 is not so good, this does not influence the quality of the decomposition result of stage 3, as an error in the coupling filter $a(t)$ is compensated by $\tilde{F}(p)$ (or by the density estimate, after inversion).

Determination of shear velocity

The S-velocity is estimated by least-square fitting of the theoretical decomposition operator to the curvature of the filter $\tilde{F}(p)$ in the pre-critical rayparameter range. In Figure 4.22 the inversion results for c_S over the line are displayed. At some receiver locations the inversion for c_S is not stable and becomes zero. In Figure 4.28 an explanation for the low c_S estimates is given. In the inversion procedure

the locations denoted with a star are already fixed. These fixed points are the locations of the singularities (and therefore the rayparameter at these locations is the inverse of c_P), and the value of the filter $\tilde{F}(p)$ at $p = 0$. Therefore, there is one variable left (c_S) to adjust the curvature between these fixed points. In Figure 4.28 the arrows denote in which direction the curve goes when c_S gets slower or faster. A c_S velocity around zero therefore indicates that the curve could not be fitted with the one remaining variable. Another way to change the curvature is to vary c_P slightly. In Figure 4.29 c_P is varied between its uncertainty bounds (Figure 4.27). The effects on the inversion for c_S are displayed by the solid lines. The lines were obtained by fixing c_P at its lowest and highest possible value, respectively, and performing the inversion for c_S (using a constant c_P over the line). The inter-dependency of c_P and c_S is further illustrated in Figure 4.30, where the inversion results for c_S are displayed for several receiver locations as a function of fixed c_P . In

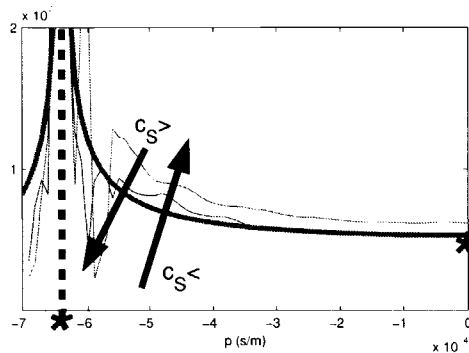


Fig. 4.28 Inversion procedure for c_S from the filter $\tilde{F}(p)$, the thick dark line is the initial fit, the stars denote the positions of the filter that are fixed, i.e. the location of the peaks and the amplitude at $p = 0$. The remaining variable, c_S , controls the curvature between the fixed points.

Figure 4.30a, a receiver location is chosen that remains stable for the c_S inversion. In this case, there is an almost linear relationship between c_S and c_P . In Figure 4.30b, the inversion results for c_S as a function of c_P are displayed for some other receiver locations, including receiver locations that were unstable in the inversion for c_S . It can be seen that at these unstable locations the curves are not linear anymore, and give c_S results of zero for several c_P values. In Figure 4.31 six of the filters $\tilde{F}(p)$ are displayed for receiver gathers 1265, 1267, 1269, 1271, 1273 and 1275. From the bottom row realistic c_S estimates were obtained, the top row resulted in c_S estimates close to zero. The differences between the filters $\tilde{F}(p)$ that gave an

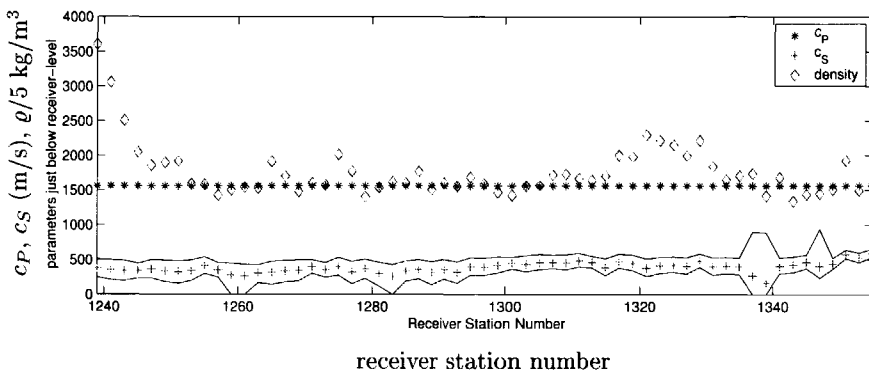


Fig. 4.29 Inversion results for the medium parameters just below the ocean-bottom for line 4 displayed as a function of receiver station number. Diamonds denote the density estimates, stars the c_P estimates and pluses the c_S estimates. The solid lines around the c_S estimates denote the c_S estimates made with the lowest and highest possible c_P within the error margins, respectively (where c_P was taken constant over the line).

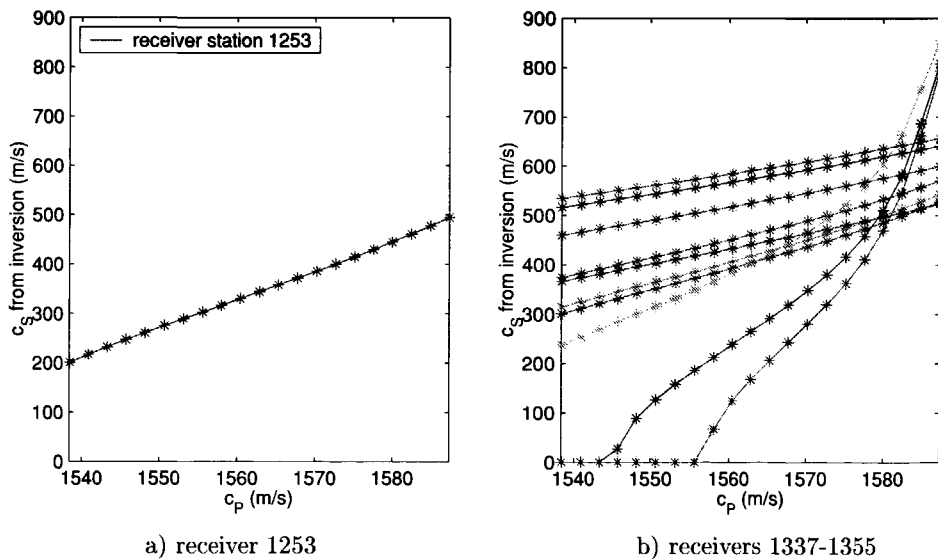


Fig. 4.30 Inversion result of c_S as a function of c_P , a) for receiver 1253, b) for receivers 1337-1355.

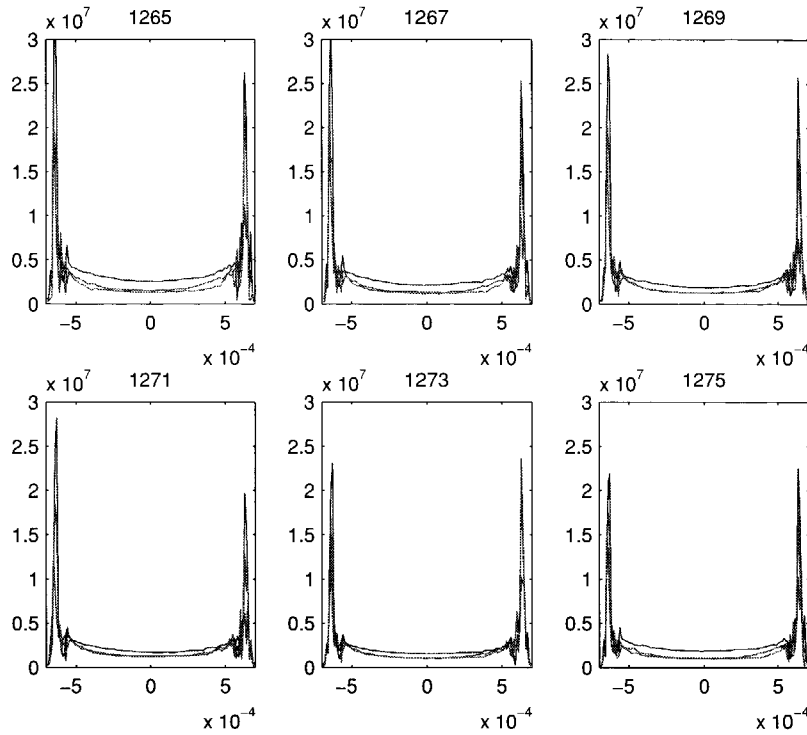


Fig. 4.31 Estimated filters $\tilde{F}(p)$ for six different receiver stations, given by the number above each filter $\tilde{F}(p)$. The different lines in the plots of the filters $\tilde{F}(p)$ denote different frequency components within the source spectrum. The filters in the top row resulted in c_S inversion estimates around zero, the filters in the bottom row gave realistic c_S estimates.

acceptable inversion result and those that did not, are not evident. The reason for the unstable behavior is therefore not clear. Nevertheless, the c_S inversion procedure remains quite sensitive to noise (field data). When a different means of estimating the shear velocity is present this could be utilized to quantify the reliability of the c_S estimates.

4.4.1 Importance of medium parameters in total decomposition scheme

From the previous discussion on the inversion for the medium parameters it can be summarized that:

- the c_P estimate is well determined;
- the c_S estimate is sensitive to small errors in c_P as well as the noise level near the critical angle, and the inversion can easily become unstable;
- the ϱ estimate is contaminated with residual coupling errors on the vertical geophone component. With the inversion it is not possible to distinguish between the density and the coupling corrections.

However, not all parameters are equally important in the next stages (stage 4 and 5) of the decomposition scheme. The equation that is used in stage 4,

$$-\tilde{T}_{xz}^{\pm} = \pm \frac{\gamma_1 p}{2q_{S,1}} \tilde{P} \pm B(\omega) \frac{\varrho_1 \beta_1}{2q_{S,1}} \tilde{V}_z, \quad (4.5)$$

does contain the density in the nominator. But at the same time it contains the coupling factor $B(\omega)$. Errors in ϱ are therefore not important as they can be compensated for by $B(\omega)$. The correct c_P/c_S ratio is important in this stage for optimal direct wave removal.

The equations used in stage 5,

$$\tilde{\Phi}^{\pm} = \frac{c_{S,1}^2}{\beta_1} \{ \mp 2pq_{S,1} \tilde{T}_{xz}^{\pm} - (c_{S,1}^{-2} - 2p^2) \tilde{T}_{zz}^{\pm} \}, \quad (4.6)$$

$$\tilde{\Psi}^{\pm} = \frac{c_{S,1}^2}{\beta_1} \{ (c_{S,1}^{-2} - 2p^2) \tilde{T}_{xz}^{\pm} \mp 2pq_{P,1} \tilde{T}_{zz}^{\pm} \}, \quad (4.7)$$

do not contain the density. They use the decomposition results of stage 3 and stage 4. The decomposition results of stage 3, \tilde{T}_{zz}^{\pm} , are obtained without medium parameters. The decomposition results of stage 4, \tilde{T}_{xz}^{\pm} , and the equations of stage 5 are dependent on the correct c_P and c_S estimates again.

4.4.2 Inversion strategy for Mahogany

The inversion for the Mahogany dataset was performed per receiver line. First, the inversion was run with a variable c_P over the line (determined by the location of the maxima at each receiver location). This typically resulted in a couple of c_S estimates of zero. The variation of c_P over the line was then used to give minimum and maximum values of c_P . In a next inversion run, c_P was given a constant value over the line in the middle of the possible c_P -range. If this still gave zero c_S estimate, c_P was chosen progressively higher until all c_S estimates were larger than zero. The inversion results for line 3, 4 and 5 are displayed in Figures 4.32, 4.33, and 4.34. For line 3 the c_P was fixed at 1577 m/s, for line 4 at 1563 m/s and for line 5 at 1577 m/s.

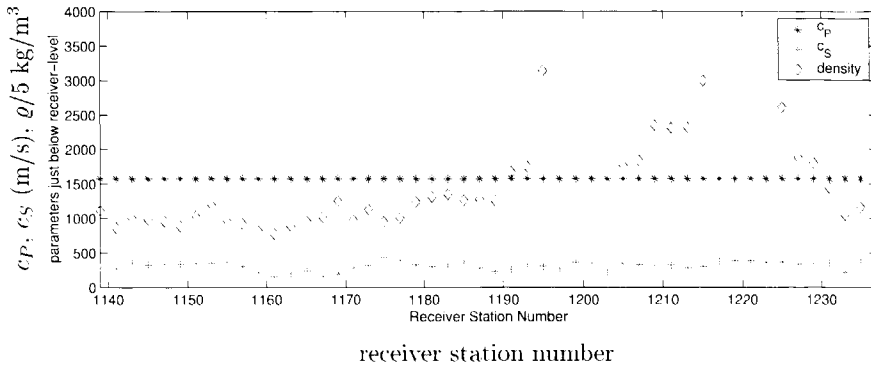


Fig. 4.32 Inversion results for the medium parameters just below the ocean-bottom for line 3 displayed as a function of receiver station number. Diamonds denote the density estimates, stars the c_P estimates and plusses the c_S estimates.

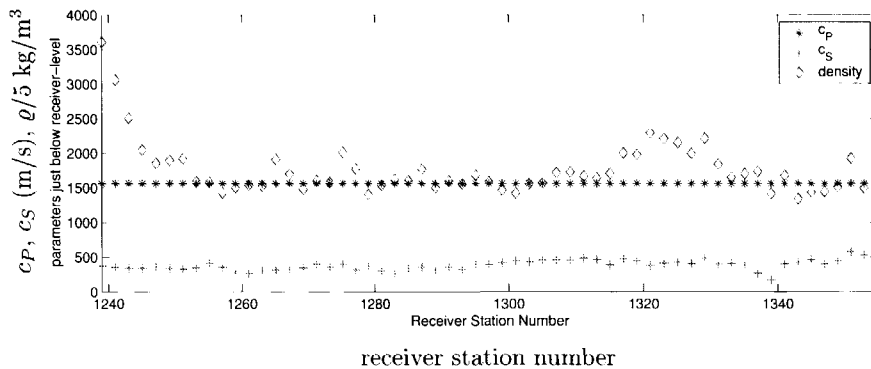


Fig. 4.33 Inversion results for the medium parameters just below the ocean-bottom for line 4 displayed as a function of receiver station number. Diamonds denote the density estimates, stars the c_P estimates and plusses the c_S estimates.

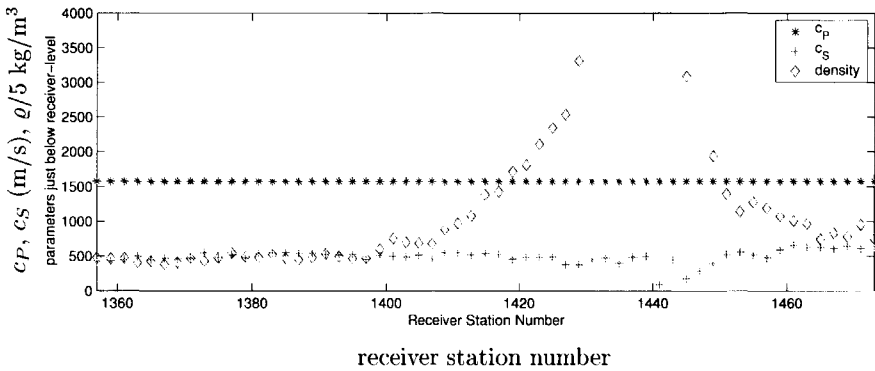


Fig. 4.34 Inversion results for the medium parameters just below the ocean-bottom for line 5 displayed as a function of receiver station number. Diamonds denote the density estimates, stars the c_P estimates and plusses the c_S estimates.

Stages 4 and 5 were implemented on the common-receiver gathers of line 4, using the medium parameters of Figure 4.33. The decomposition results of stage 5 are (partly) displayed in Figures 4.35, 4.36, 4.37, and 4.38 for seven selected gathers (displayed on near offset sections), and in Figures 4.39 and 4.40 as common-offset sections. Because the quality of the common-offset sections is poor, the decomposition results for the P-waves are also displayed after poststack time migration (Figures 4.41 and 4.42). The S-wave decomposition results were only stacked, using the common-conversion point method as discussed in (Tessmer and Behle, 1988; Harrison and Stewart, 1993) (Figure 4.44). In the time migrated sections a salt layer can be distinguished with the base of the salt roughly between 2.5 and 3 seconds. The downgoing P-wave section shows roughly the same structure, only with a time delay caused by the extra bounce inside the water layer. In the stack of the upgoing S-waves the top of the salt can be seen between roughly 4 and 6 seconds. The base cannot be distinguished.

4.5 Comparison before and after decomposition

To evaluate the benefit of the wavefield decomposition on the image quality of the subsurface, a poststack time migration was also performed on the measured data components. The time migrated section for the v_z component is displayed in Figure 4.43. Compared to the upgoing P-wave section in Figure 4.42 again the effect of a lot of multiple attenuation/removal is evident. To evaluate the effect of P- and

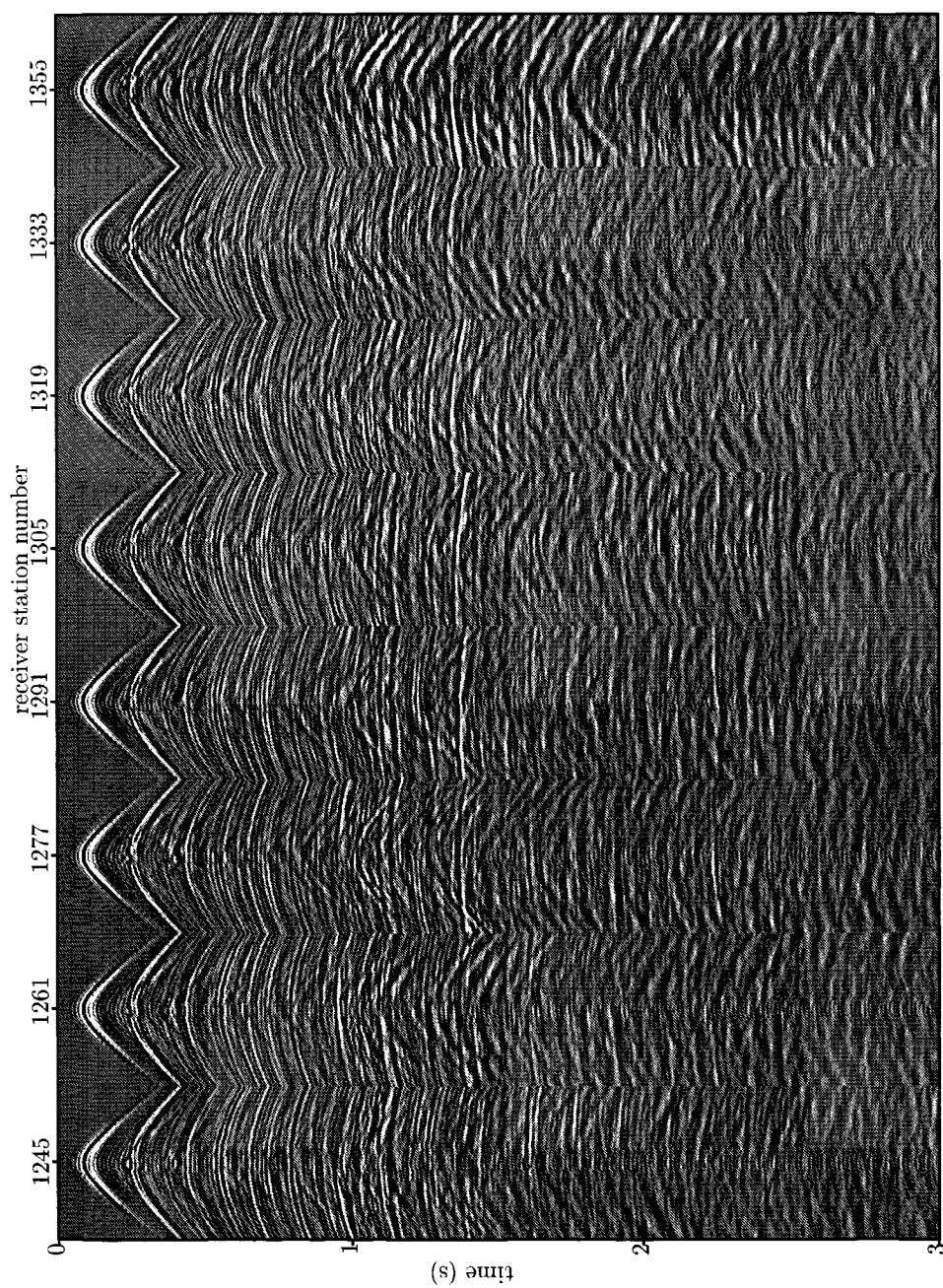


Fig. 4.35 Seven selected common-receiver gathers of the final decomposition result of line 4: downgoing P-wave potential.

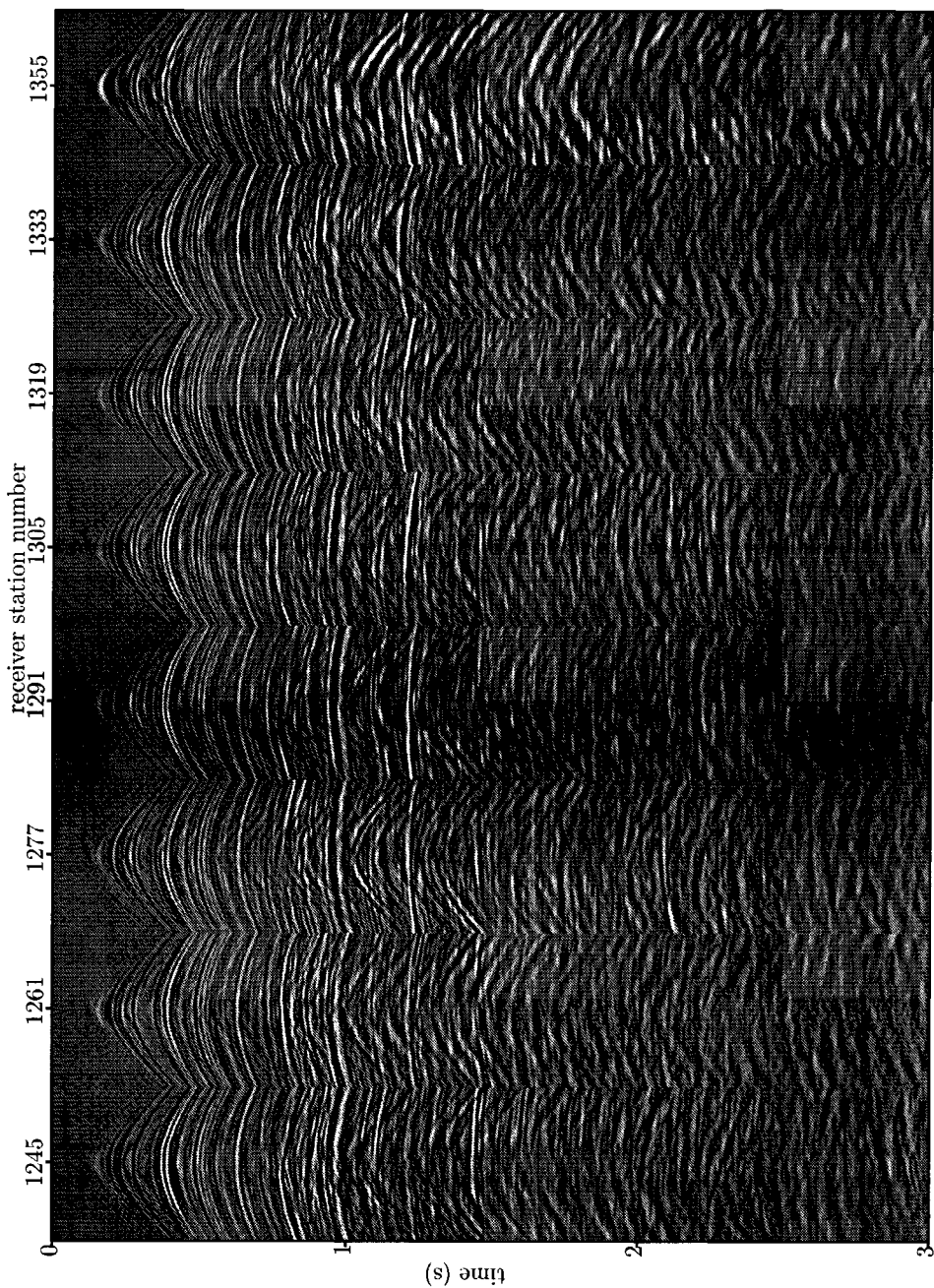


Fig. 4.36 Seven selected common-receiver gathers of the final decomposition result of line 4: upgoing P-wave potential.

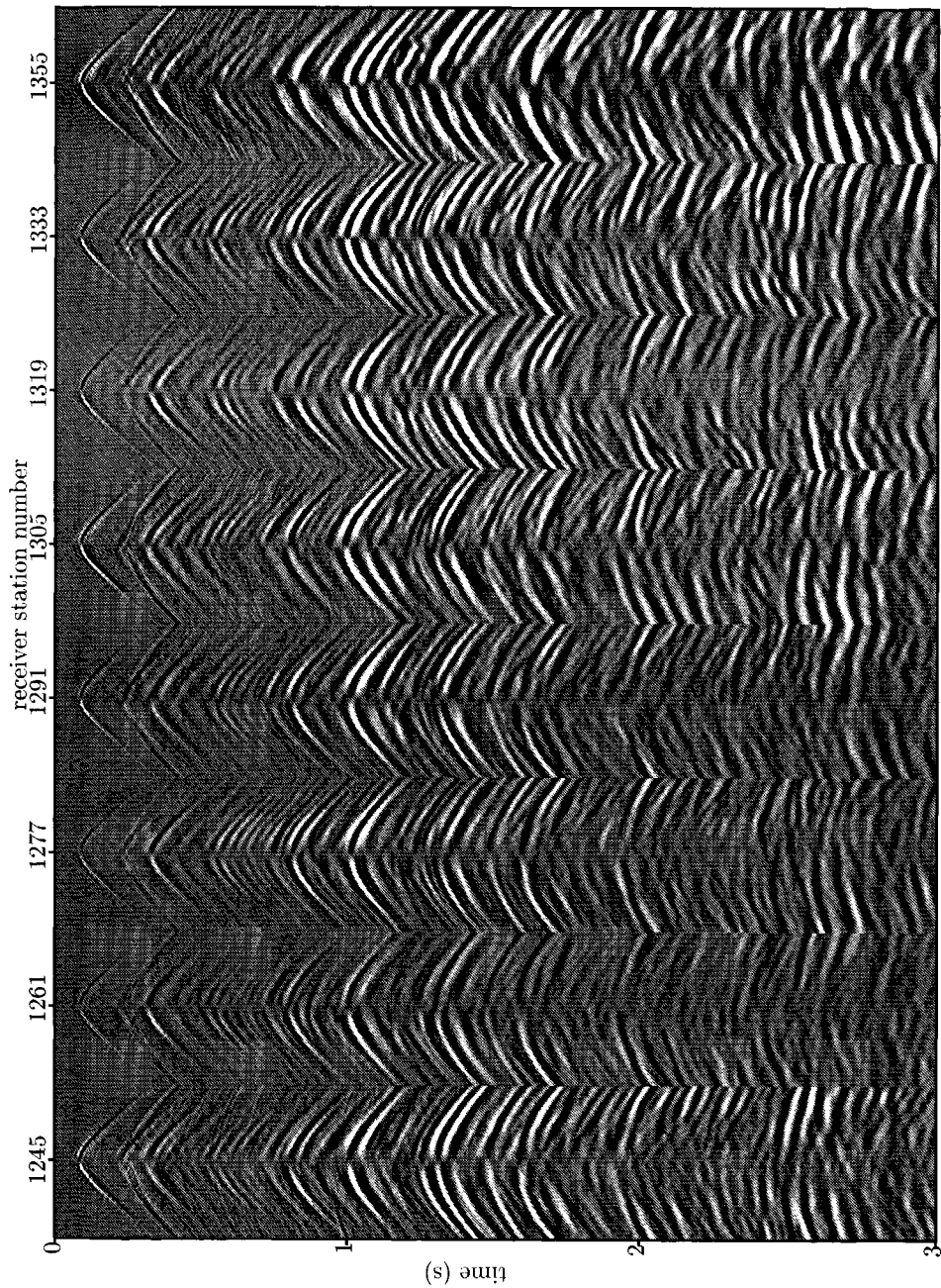


Fig. 4.37 Seven selected common-receiver gathers of the final decomposition result of line 4: downgoing S-wave potential.

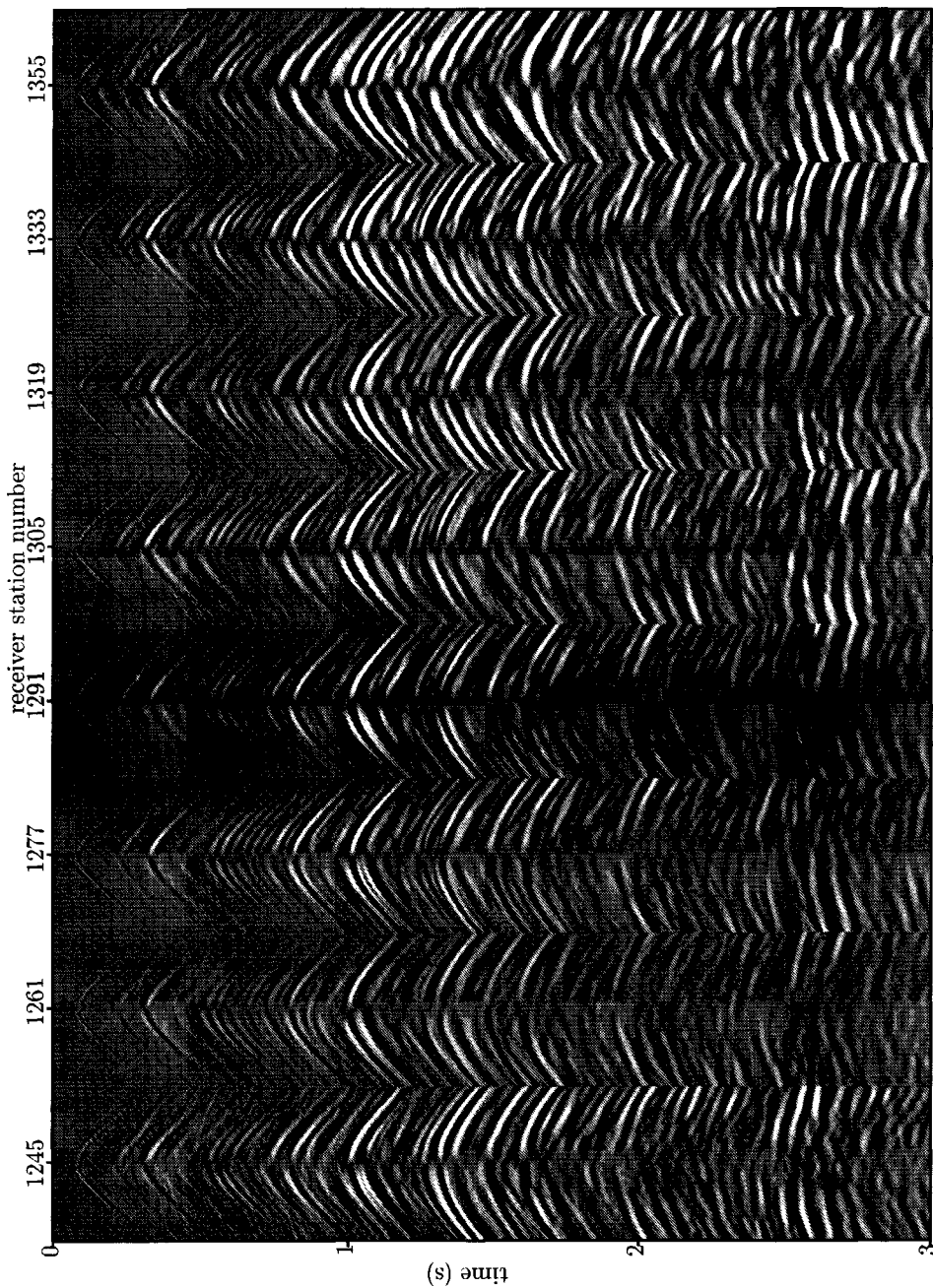


Fig. 4.38 Seven selected common-receiver gathers of the final decomposition result of line 4: upgoing S-wave potential.

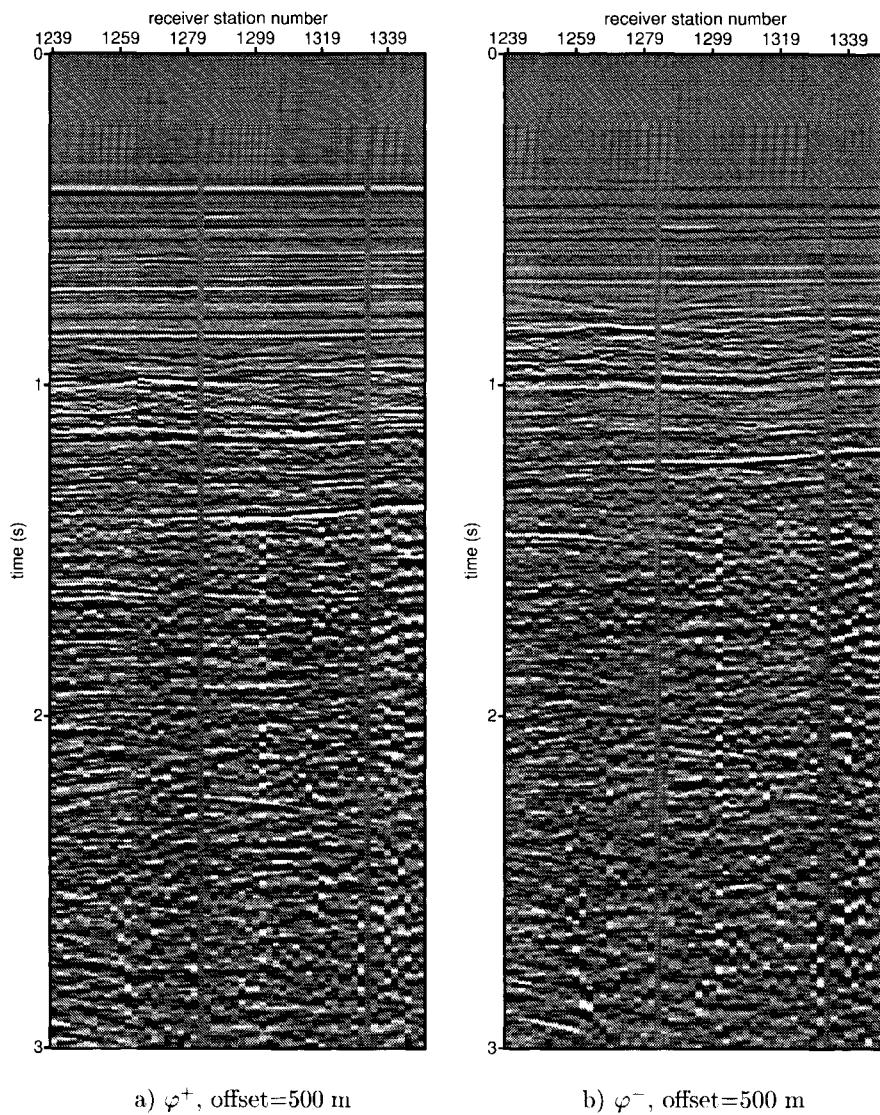


Fig. 4.39 Common offset sections of line 4 at 500 meter offset for a) the downgoing P-potential just below the ocean-bottom and b) the upgoing P-potential.

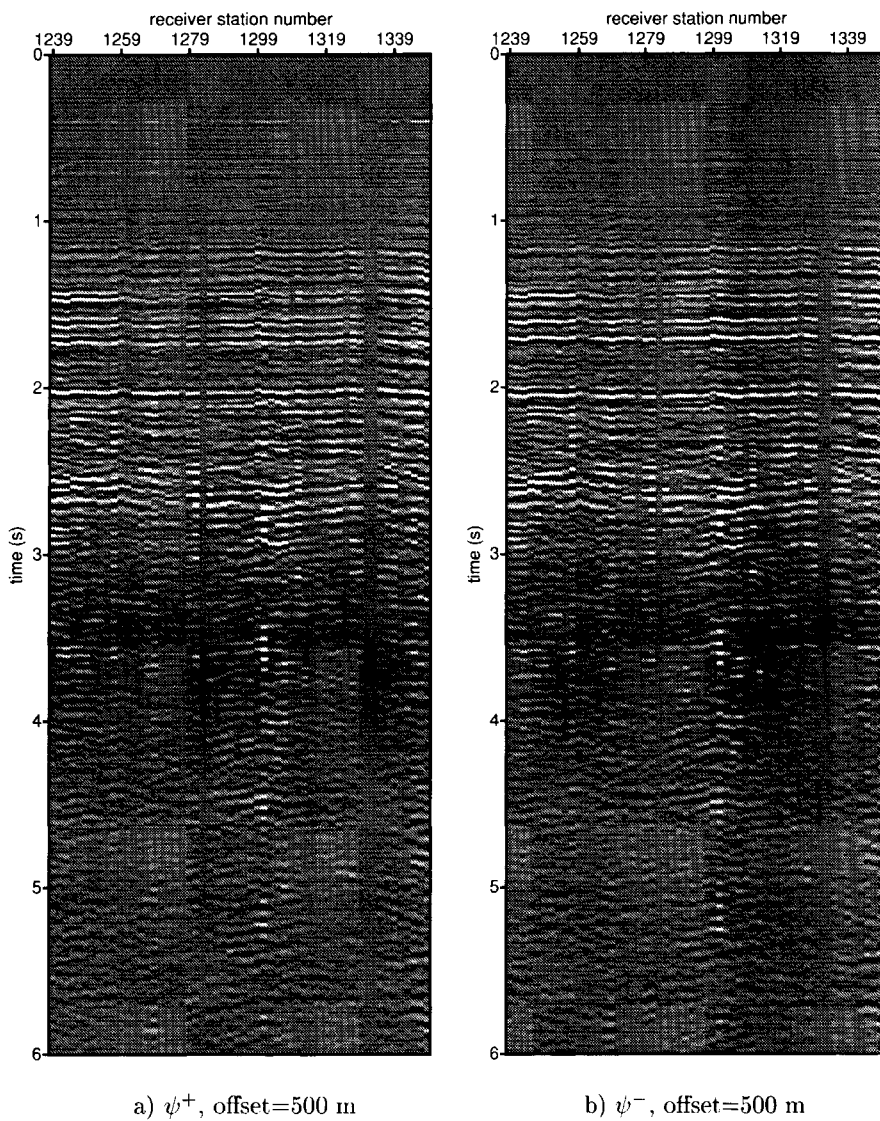


Fig. 4.40 Common offset sections of line 4 at 500 meter offset for a) the downgoing S-potential just below the ocean-bottom and b) the upgoing S-potential.

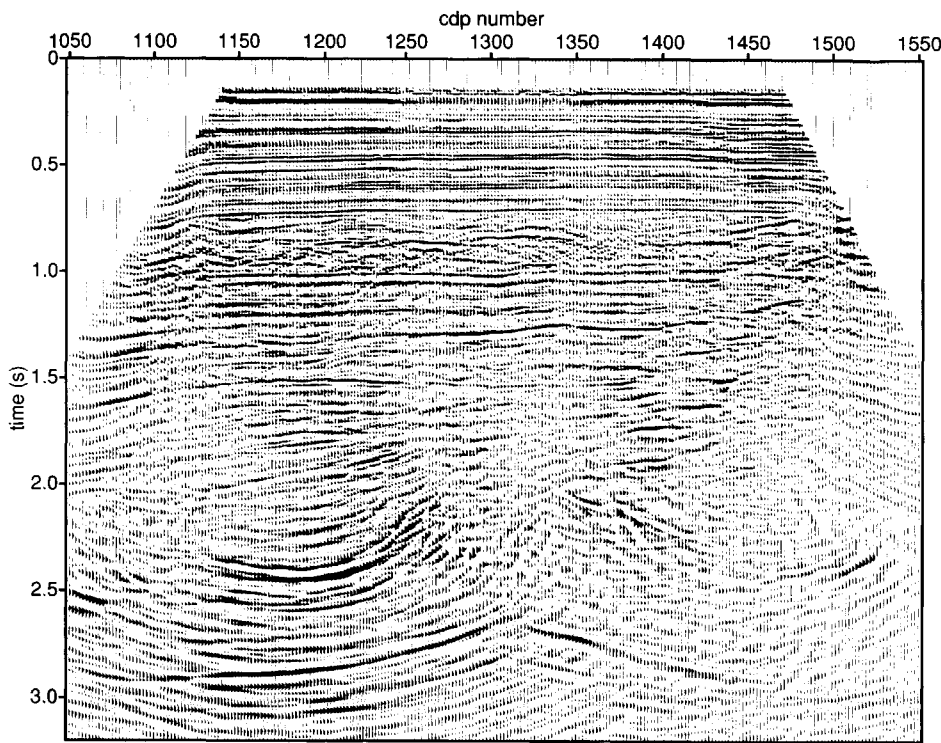


Fig. 4.41 Poststack time migrated section of the downgoing P-potential just below the ocean-bottom.

S-wave separation is more difficult - as with the examples in the previous chapter. Actually, converted primary reflections have to be identified in the v_z component that are removed from the upgoing P-wavefield.

In Figures 4.45 and 4.44 the stacks obtained by using the v_x component and the upgoing S-wavefield, respectively, can be compared. Some difference can be seen between the two stacked sections. Especially in the stack of the v_x component, the difference in coupling between the three ocean-bottom cables is apparent. In the decomposition result events appear more continuous over the three cables, which can probably be attributed to the estimation of coupling filters in stage 4 of the decomposition scheme.

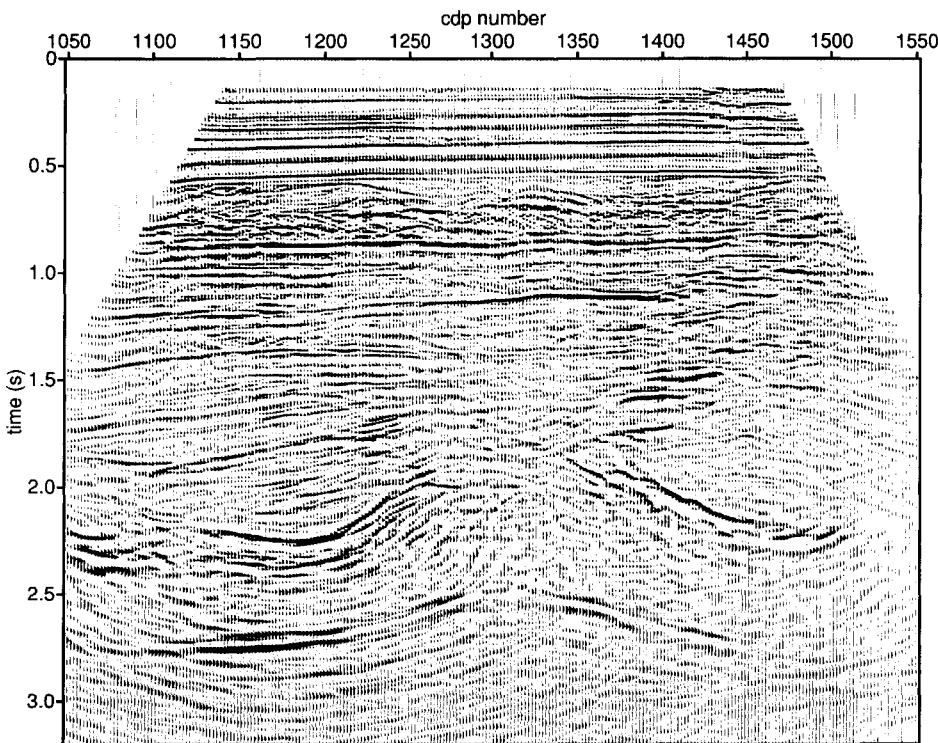


Fig. 4.42 Poststack time migrated section of the upgoing P-potential just below the ocean-bottom.

4.6 Conclusions

The adaptive decomposition procedure was tested on a field dataset with a shallower ocean-bottom (Mahogany). This was more challenging because of the greater interference between events. Deconvolution of the data, to remove the air bubble effect, must be done carefully, as not to affect the events interfering with it. Especially the determination of a window containing only primary events (stage 2 of the adaptive decomposition scheme) can be tricky for shallower data. The optimal filters resulting from stage 3, quite nicely resemble the theoretical decomposition operators, compared to the examples in the previous chapter. Therefore, it was possible to better analyse the inversion results. It can be concluded that

- The accuracy of the estimate of the density just below the ocean-bottom is dependent on the accuracy of the estimation of the calibration filter $a(t)$.

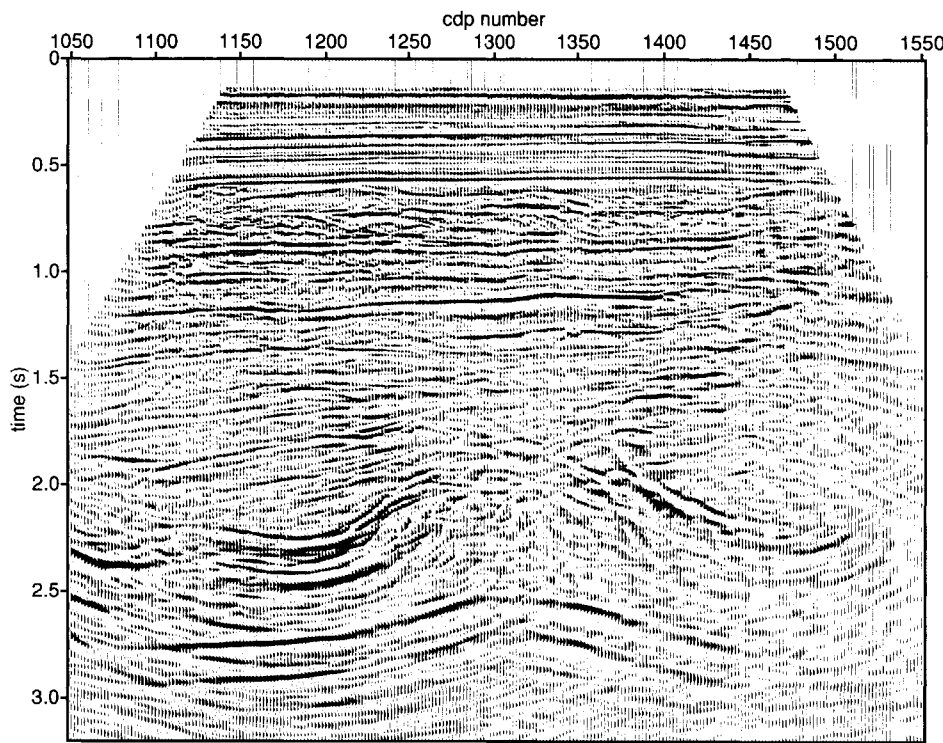


Fig. 4.43 Poststack time migrated section of the vertical velocity component.

- The estimate of the S-velocity is sensitive to small errors in the P-velocity estimate, and to the signal-to-noise ratio at higher angles. It does not always converge to a realistic solution for field data.
- The P-velocity can be accurately determined using the singularities location, also with field data.

Decomposition was repeated for all receiver gathers in the dataset using variable medium parameters across the receiver line. If the S-waves in the final decomposition result exhibit a lower resolution compared to the original v_x data, this is due to stage 4 of the decomposition scheme. It can be solved by better matching the frequency spectra of the pressure and horizontal inline velocity components beforehand.

Poststack time migrated images were made of the data before and after decomposition. The decomposed data resulted in clearer images for both the P- and S-wave sections.

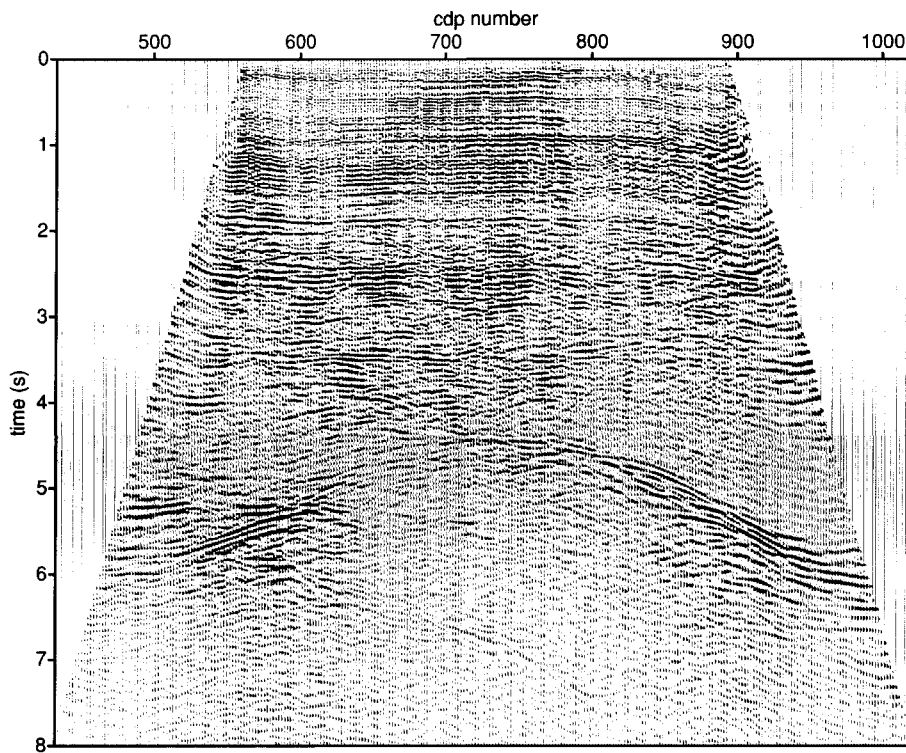


Fig. 4.44 Common conversion point stacked section of the upgoing S-potential just below the ocean-bottom, using $c_P/c_S = 3.5$.

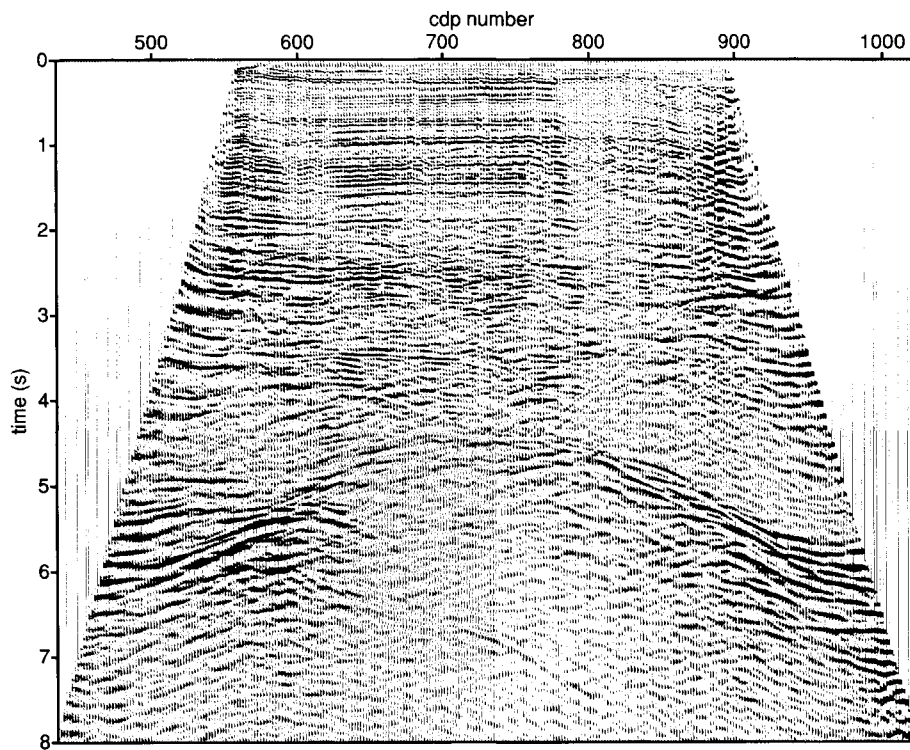


Fig. 4.45 Common conversion point stacked section of the horizontal inline velocity component v_x , using $c_P/c_S = 3.5$.

Chapter 5

Multiple elimination for ocean-bottom data

By performing a wavefield decomposition on multicomponent seismic ocean-bottom data, the upgoing P- and S-waves just below the ocean-bottom are obtained. After the wavefield decomposition, as described in the previous chapters, surface-related and internal multiples that arrive at the receiver from above will have been removed from the data. However, all multiples that end with a reflection from a reflector below the ocean-bottom will still be present in the decomposed upgoing data (Figure 5.1). In Figure 5.1a the surface-related multiple reflections that remain in the upgoing wavefield just below the bottom after decomposition are displayed. These type of reflections are also called source-side peg-legs, as the extra reverberation is on the side of the source. To remove the remaining surface-related multiples, the multiple elimination method described by Verschuur et al. (1992) and Berkhout and Verschuur (1997) is used (the removal of remaining internal multiples from the decomposed upgoing wavefield will not be addressed here). To apply this method to the decomposed dataset, it has to be extended to accomodate ocean-bottom ac-

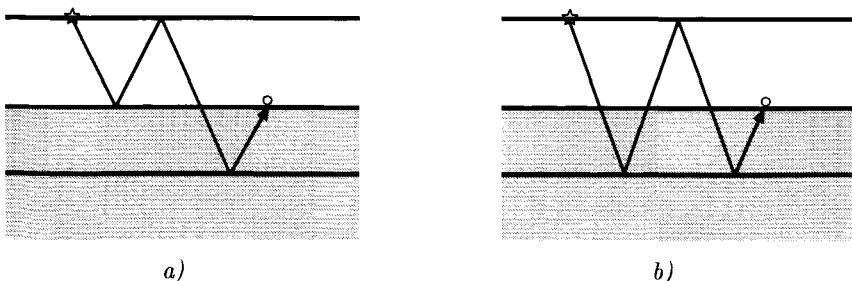


Fig. 5.1 Examples of events that are “upgoing” at the receiver, but still contain a surface reflection, (a) source-side peg-leg multiple, and (b) another source-side multiple.

quisition geometry (Verschuur and Neumann, 1999; Soellner and Widmaier, 2000). The multiple removal method can be used on any ocean-bottom receiver type (i.e. pressure, velocity, P-waves, S-waves). The relative importance of additional multiple elimination will be illustrated with examples of the synthetic data example and of the Mahogany field dataset. After multiple elimination the remaining events in the data are all supposed to be primary reflections coming from below the ocean-bottom (if internal multiples can be neglected), and the data can be migrated (i.e. putting the reflection events at the right positions in depth).

5.1 Theory of multiple elimination for OBS data

A lot of surface-related multiples have been removed by the decomposition, but events as in Figure 5.1 remain. To remove the remaining surface-related multiples from the data after decomposition, the multiple elimination method developed by Verschuur et al. (1992), reformulated as an iterative procedure by Berkhou and Verschuur (1997), is used. As this method is designed for data acquisition with both sources and receivers behind a boat at the sea surface (these type of data are often called streamer data or surface data), it has to be adapted to accommodate ocean-bottom acquisition geometry where the source is still behind the boat, but the receivers are now arranged at the ocean-bottom (data acquired this way are often called ocean-bottom cable data or OBC data). Multiple elimination for ocean-bottom data has been discussed in Verschuur and Neumann (1999) and Ikelle (1999) for the situation where streamer data are available alongside OBC data. The procedure discussed here is similar, except that in this case the streamer data are simulated from the OBC data. Field data examples of such a multiple elimination approach on "undecomposed" OBC data have been shown in Soellner and Widmaier (2000). First a short review of multiple elimination for surface data will be given which will then be extended to OBC data.

5.1.1 Matrix notation for discretized wavefields

To predict multiple contributions within a certain aperture, many sources and receiver positions are required simultaneously. Therefore, the data are organized in a data matrix, after transformation to the frequency-domain (see Berkhou, 1982). Note that the data matrix notation that is used in this chapter does not correspond to the matrix notation of earlier chapters. To distinguish the data matrices from the other matrices they will be written in the sens serif font, i.e. \mathbf{X} instead of \mathbf{X} . One column of the data matrix contains one shot record for one frequency component ω_i . Thus a matrix is obtained with the shot locations along the rows of the matrix and the receiver locations along the columns. Such a data matrix can then be

constructed for each frequency component. This data organization is well suited for processing steps in which each frequency component can be treated independently. Spatial convolutions can then be described by matrix multiplications. In practice the data matrices are often only partly filled (band matrices).

5.1.2 Forward model for surface data

In the case the surface at z_0 is a nonreflecting surface, the upgoing wavefield just below z_0 is given by

$$\mathbf{P}_0^-(z_0) = \mathbf{X}_0(z_0, z_0) \mathbf{S}^+(z_0), \quad (5.1)$$

with $\mathbf{X}_0(z_0, z_0)$ containing the spatial impulse responses of the medium, where the first variable denotes the receiver depth and the second variable the source depth. The source matrix $\mathbf{S}^+(z_0)$ contains the effective downgoing source wavefields at surface level z_0 . The matrix $\mathbf{P}_0^-(z_0)$ contains the upgoing wavefield at depth level z_0 for one frequency and all sources and receivers without surface multiples. One vector \vec{P}^- (i.e., one column of \mathbf{P}_0^-), contains a wavefield for one frequency and one source and all receivers. One vector $\vec{P}^{-\dagger}$ (i.e., one row of \mathbf{P}_0^-) contains a wavefield for one frequency and one receiver and all sources.

In the case the surface at z_0 is a reflecting surface, the total downgoing wavefield at z_0 is the illuminating source wavefield $\mathbf{S}^+(z_0)$ plus the downward reflected upgoing wavefield (see Figure 5.2):

$$\mathbf{P}^-(z_0) = \mathbf{X}_0(z_0, z_0) [\mathbf{S}^+(z_0) + \mathbf{R}^-(z_0) \mathbf{P}^-(z_0)], \quad (5.2)$$

or written explicitly

$$\mathbf{P}^-(z_0) = [\mathbf{I} - \mathbf{X}_0(z_0, z_0) \mathbf{R}^-(z_0)]^{-1} \mathbf{X}_0(z_0, z_0) \mathbf{S}^+(z_0). \quad (5.3)$$

Defining $\mathbf{X}(z_0, z_0)$ as the subsurface response with reflecting surface at z_0 , the total upgoing wavefield at z_0 can be written as

$$\mathbf{P}^-(z_0) = \mathbf{X}(z_0, z_0) \mathbf{S}^+(z_0). \quad (5.4)$$

Combining equations (5.3) and (5.4), it follows that

$$\mathbf{X}(z_0, z_0) = [\mathbf{I} - \mathbf{X}_0(z_0, z_0) \mathbf{R}^-(z_0)]^{-1} \mathbf{X}_0(z_0, z_0). \quad (5.5)$$

The total upgoing wavefield $\mathbf{P}^-(z_0)$ can also be written in a series expansion:

$$\begin{aligned} \mathbf{P}^-(z_0) = & [\mathbf{I} + \{\mathbf{X}_0(z_0, z_0) \mathbf{R}^-(z_0)\} + \{\mathbf{X}_0(z_0, z_0) \mathbf{R}^-(z_0)\}^2 \\ & + \{\mathbf{X}_0(z_0, z_0) \mathbf{R}^-(z_0)\}^3 + \dots] \mathbf{X}_0(z_0, z_0) \mathbf{S}^+(z_0). \end{aligned} \quad (5.6)$$

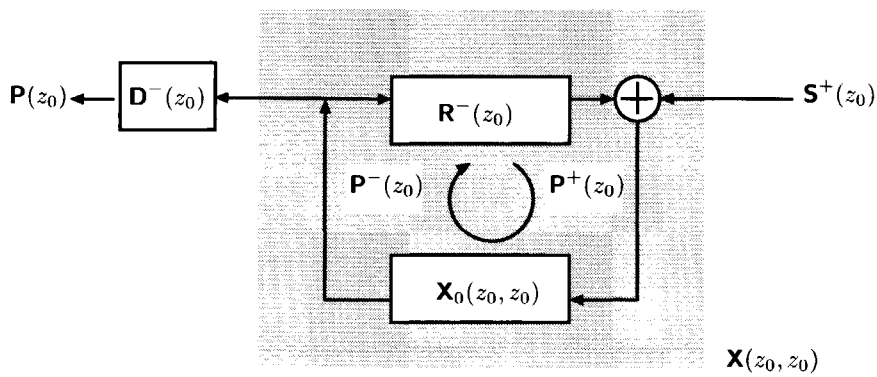


Fig. 5.2 The model of seismic reflections at the surface ($z = z_0$). The downgoing wavefield consists of source wavefield $\mathbf{S}^+(z_0)$ and the reflected upgoing wavefield $\mathbf{R}^-(z_0)\mathbf{P}^-(z_0)$. Operator $\mathbf{D}^-(z_0)$ adds the receiver directivity to the recorded data: $\mathbf{P}(z_0) = \mathbf{D}^-(z_0)\mathbf{P}^-(z_0)$ (Berkhout and Verschuur, 1997).

5.1.3 Multiple elimination for surface data

To find the “surface reflection-free” response of the medium, $\mathbf{X}_0(z_0, z_0)$, equation (5.5) has to be inverted

$$\mathbf{X}_0(z_0, z_0) = \mathbf{X}(z_0, z_0)[\mathbf{I} + \mathbf{R}^-(z_0)\mathbf{X}(z_0, z_0)]^{-1}, \quad (5.7)$$

and can then be written in a series expansion again¹:

$$\begin{aligned} \mathbf{X}_0(z_0, z_0) = & \mathbf{X}(z_0, z_0)[\mathbf{I} - \{\mathbf{R}^-(z_0)\mathbf{X}(z_0, z_0)\} + \{\mathbf{R}^-(z_0)\mathbf{X}(z_0, z_0)\}^2 \\ & - \{\mathbf{R}^-(z_0)\mathbf{X}(z_0, z_0)\}^3 + \dots]. \end{aligned} \quad (5.8)$$

Writing for $\mathbf{R}^-(z_0) = r_0\mathbf{I}$, an average free-surface reflection coefficient r_0 , equation (5.8) becomes

$$\begin{aligned} \mathbf{X}_0(z_0, z_0) = & \mathbf{X}(z_0, z_0) - r_0\mathbf{X}(z_0, z_0)^2 + r_0^2\mathbf{X}(z_0, z_0)^3 \\ & - r_0^3\mathbf{X}(z_0, z_0)^4 + \dots \end{aligned} \quad (5.9)$$

As in practice the unit impulse response of the medium is not measured, equations (5.1) and (5.4) are substituted into equation (5.9) to obtain the following series:

$$\begin{aligned} \mathbf{P}_0^-(z_0) = & \mathbf{P}^-(z_0) - \mathcal{A}(\omega)[\mathbf{P}^-(z_0)]^2 + \mathcal{A}^2(\omega)[\mathbf{P}^-(z_0)]^3 \\ & - \mathcal{A}^3(\omega)[\mathbf{P}^-(z_0)]^4 + \dots, \end{aligned} \quad (5.10)$$

¹This series does not necessarily converge. However, by assuming that there is always a nonzero traveltime until the first arrival, and assuming limited registration time (after inverse temporal FT of $\mathbf{X}_0(z_0, z_0)$), a finite number of terms is needed to create a multiple free output.

where the function $\mathcal{A}(\omega)$ contains the average free-surface reflection coefficient r_0 and the inverse source signature $S^{-1}(\omega)$:

$$\mathcal{A}(\omega) = r_0 S^{-1}(\omega), \quad (5.11)$$

\mathbf{P}^- and \mathbf{P}_0^- are the data with and without surface multiples. By writing the series this way, it is assumed that the source directivity can be neglected (or is already corrected for), i.e. $\mathbf{S}^+(z_0) = S(\omega)\mathbf{I}$. The first term on the right-hand side of equation (5.10) denotes the (deghosted) data itself, the second term contains the multiples once reflected from the surface, and so on.

5.1.4 Adaptive iterative multiple elimination for ocean-bottom data

The iterative version of the multiple elimination procedure consists of a repeated application of the following two steps (Berkhout and Verschuur, 1997):

- Prediction of the “unscaled” multiples by auto-convolution of the data:

$$\mathbf{M}(z_0) = \mathbf{P}_0^-(z_0)\mathbf{P}^-(z_0), \quad (5.12)$$

where z_0 denotes the water surface,

- Adaptive subtraction of the predicted multiples from the input data:

$$\mathbf{P}_0^-(z_0) = \mathbf{P}^-(z_0) - \mathcal{A}(\omega)\mathbf{M}(z_0). \quad (5.13)$$

The matrix $\mathbf{P}^-(z_0)$ is the multiple prediction operator and contains the upgoing pressure wavefield at the free surface (deghosted data) for one frequency and all sources. The matrix $\mathbf{P}_0^-(z_0)$ is the input data. In the first iteration $\mathbf{P}_0^-(z_0)$ is normally taken as the deghosted data itself ($\mathbf{P}^-(z_0)$).

In Berkhout and Verschuur (1997) it is also shown that the same multiple elimination procedure can be applied to a CFP gather (on the source or receiver side), using the original surface shot records as the multiple prediction operator. As the decomposed OBC data can be considered as a CFP gather, using focusing in detection with the focus point at the ocean-bottom, application of multiple elimination when streamer data is available is straightforward (see Verschuur and Neumann, 1999). When streamer data are not available, they can be simulated from the OBC data. Using the output of the acoustic decomposition of stage 2 of the adaptive decomposition scheme (*upgoing* pressure wavefield just *above* the ocean-bottom) and extrapolating this to the surface, simulated “receiver-ghost free” streamer data are obtained. The propagation operator is easily constructed using the water depth and velocity. Equation (5.12) modifies to

$$\tilde{M}^{-\dagger}(z_1^+, z_0) = \tilde{P}_0^{-\dagger}(z_1^+, z_0)\mathbf{W}^-(z_0, z_1)\mathbf{P}^-(z_1^-, z_0), \quad (5.14)$$

where z_1 is the depth of the ocean-bottom, z_1^- is just above the ocean-bottom and z_1^+ is just below the ocean-bottom. The dagger (\dagger) symbol indicates a row vector. The multiple prediction operator is

$$\mathbf{W}^-(z_0, z_1) \mathbf{P}^-(z_1^-, z_0),$$

which is the upgoing wavefield just above the bottom, forward extrapolated to the surface, thus simulating receiver ghost-free streamer data. $\vec{P}_0^{-\dagger}(z_1^+, z_0)$ contains the input data for one frequency and all shots, i.e. it corresponds to one (decomposed) common-receiver gather just below the bottom. The multiple prediction procedure as it is applied to OBC data is illustrated by Figure 5.3. The upgoing pressure wavefield just above the ocean-bottom is resorted from common-receiver gathers to common-shot gathers and then extrapolated to the surface. One-common shot gather of the simulated streamer data is shown in Figure 5.3. To predict the multiples this shot gather is convolved with a decomposed common-receiver gather. This can either be the upgoing P-waves or the upgoing S-waves just below the ocean-bottom (in fact the method will work on any ocean-bottom receiver type). The convolution results in curved events, with the apex at the spatial position of the reflection point of the multiple at the surface. These multiple contribution events are summed in the horizontal direction to obtain the multiples for one source-receiver pair. If this procedure is repeated for all common-shot records of the simulated streamer data, the multiple prediction for one complete common-receiver gather is obtained.

After prediction, these multiples can be adaptively subtracted from the input OBC data, similarly to equation 5.13:

$$\vec{P}_0^{\pm}(z_1, z_0) = \vec{P}^{\pm}(z_1, z_0) - \mathcal{A}(\omega) \vec{M}^{\pm}(z_1, z_0), \quad (5.15)$$

where $\vec{P}_0^{\pm}(z_1, z_0)$ can be the wavefield measurement at any receiver component as well as any of the wavefields after wavefield decomposition. Note that the same receiver component $\vec{P}_0^{\pm}(z_1, z_0)$ needs to be used in the prediction (equation 5.14)

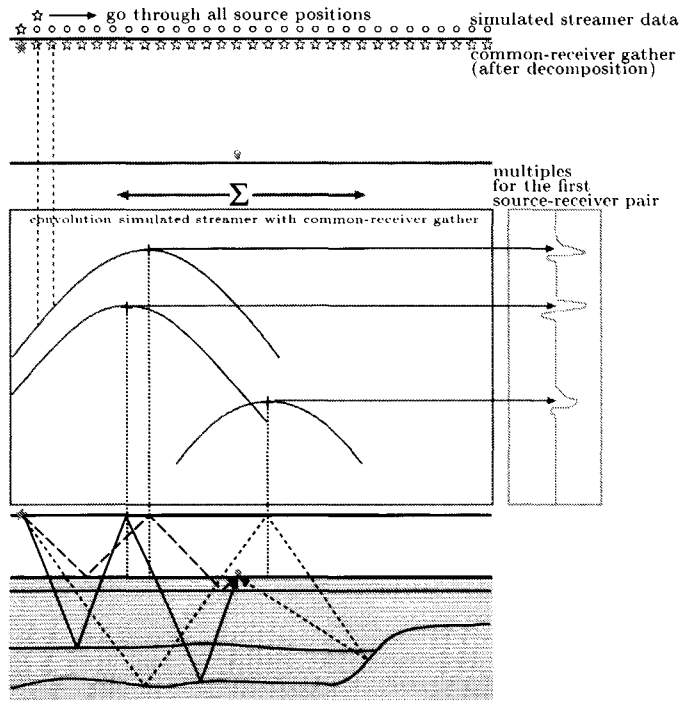


Fig. 5.3 Multiple prediction for OBS data: the decomposed common-receiver gather is convolved with the acoustic decomposition result after extrapolation to the water surface to simulate streamer data.

5.2 Multiple elimination: synthetic data example

The effect of multiple removal will be demonstrated on synthetic data from the simple horizontally layered model introduced in Chapter 2. The model parameters were given in Table 2.2, and the pressure and velocity components (at the interface between the first and second layer, i.e., the ocean-bottom) calculated for this model were shown in Figure 2.2.

There are two possible multiple removal operators for OBC data. In Figure 5.4a the operator is the upgoing pressure wavefield obtained from acoustic decomposition just above the ocean-bottom, extrapolated to the sea surface. For comparison, in Figure 5.4b the operator is obtained by modeling the synthetic pressure data with the source as well as the receivers at the sea-surface (i.e. streamer data). As can be seen the operators are equivalent for synthetic data. In the following multiple

elimination results, the operator in Figure 5.4a will be used, but obviously the results will not change when the modeled streamer data is used.

The adaptive surface-related multiple removal scheme is applied to various (receiver type) components, before or after wavefield decomposition at the ocean bottom. Each time the same operator data (Figure 5.4a) is used. The iterative procedure is applied. For the multiple removal results shown here four iterations have been used.

First, the OBS multiple removal algorithm is demonstrated on the measured pressure in the water layer with the hydrophone (Figure 5.5a). In Figure 5.5b the result of the adaptive multiple removal scheme is displayed and compared with the result of modeling the pressure component without surface multiples (Figure 5.5c). Only minor differences are visible between the multiple attenuated and the multiple-free result.

Next, the approach is tested for the vertical velocity component. The results are displayed in Figure 5.6. Again, the result is convincing.

As mentioned in the previous section, the type of ocean bottom component is not important, as long as the correct multiple prediction operator is used. Therefore, the procedure works equally well for the horizontal component, as can be observed in Figure 5.7.

If wavefield decomposition has been applied to the ocean bottom dataset, the same procedure can be used to remove the remaining source-side water layer peg-leg multiples from the decomposed data. This is demonstrated in Figure 5.8 for the upgoing P-waves just *below* the ocean bottom and in Figure 5.9 for the upgoing S-waves just below the ocean-bottom. For the latter situation, multiples that are removed by this method can for example be events that first bounce in the water layer, then propagate below the ocean bottom and are converted somewhere into S-waves, and then arrive at the ocean bottom as an upgoing S-wave. Note that the conversion could have taken place either during transmission or during reflection. On close inspection of Figure 5.9 it appears that indeed pretty strong events with approximately 2.1 and 2.8 seconds zero offset traveltimes are removed after the process.

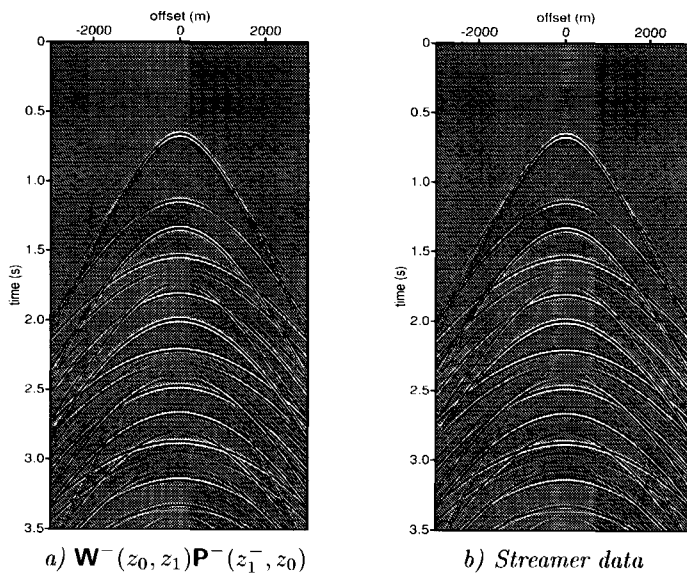


Fig. 5.4 Operators for surface-related multiple removal (a) Operator obtained by extrapolating the upgoing pressure wavefield just above the bottom to the sea surface. (b) Operator obtained by modeling synthetic streamer data at the sea surface.

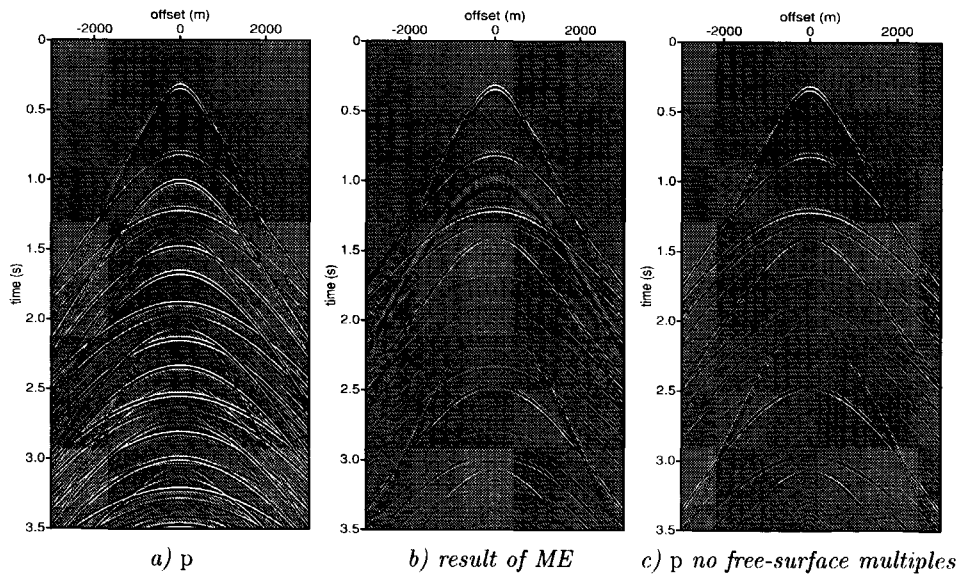


Fig. 5.5 Demultiple on OBC data: (a) pressure component, (b) pressure component after demultiple and (c) pressure component modeled without free-surface multiples.

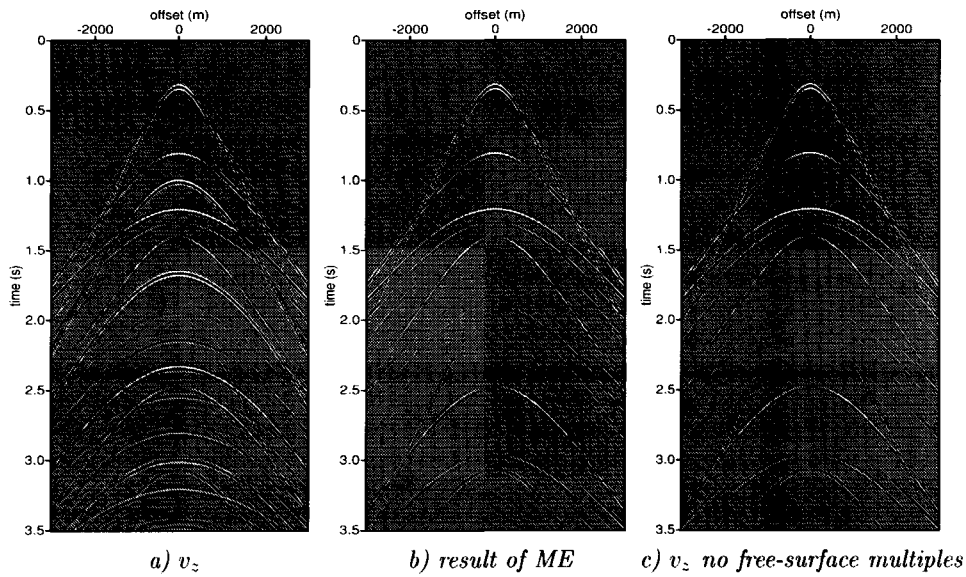


Fig. 5.6 Demultiple on OBC data: (a) vertical velocity component with multiples, (b) vertical velocity component after demultiple and (c) vertical velocity component modeled without free-surface multiples.

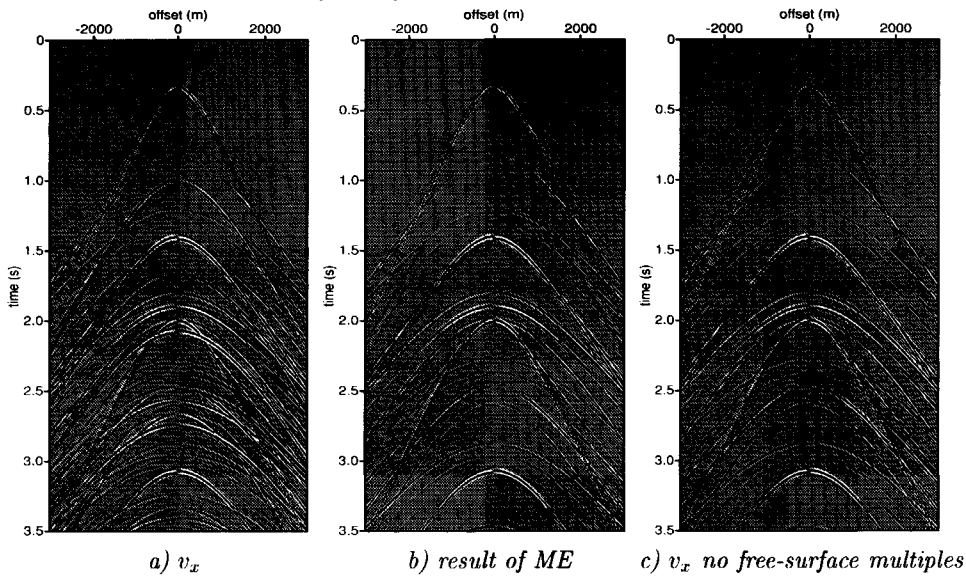


Fig. 5.7 Demultiple on OBC data: (a) horizontal inline velocity component with multiples, (b) after demultiple and (c) horizontal velocity component modeled without free-surface multiples.

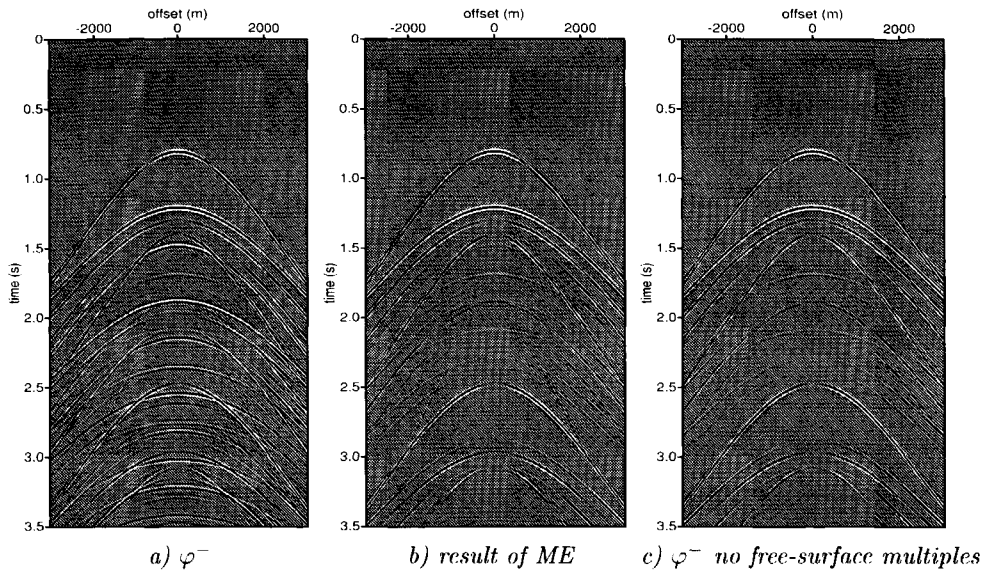


Fig. 5.8 Demultiple on OBC data: (a) upgoing P-waves obtained from decomposition, (b) upgoing P-waves after demultiple and (c) modeled upgoing P-waves without free-surface multiples.

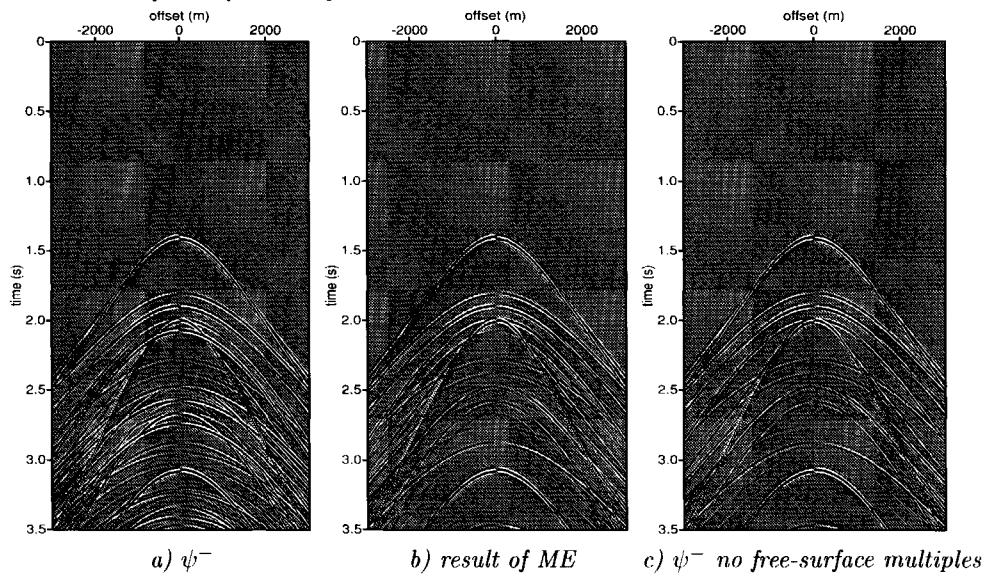


Fig. 5.9 Demultiple on OBC data: (a) upgoing S-waves obtained from decomposition, (b) upgoing S-waves after demultiple and (c) modeled upgoing S-waves without free-surface multiples.

5.3 Multiple elimination: Mahogany field dataset

The data example shown here to illustrate the multiple elimination procedure comes from the Mahogany dataset which was discussed in Chapter 4. In Figure 4.3 the acquisition geometry for this dataset is displayed. The acoustic decomposition result (obtained in stage 2 of the adaptive decomposition scheme) is used as the multiple prediction operator, after resorting into common-shot gathers and extrapolation of the receivers to the sea surface (to simulate streamer data). Because the receiver aperture is limited (compared to the source aperture), the aperture over which surface multiples can be predicted is restricted. A wavefield decomposition was performed on the data within the receiver station number range of 1020 to 1474 (see Figure 4.3). This aperture allows for a good surface multiple prediction within the receiver station number range of 1138 to 1356.

In Figure 5.10 the pressure data for common-receiver gather 1323 is displayed on the left, the upgoing P-wave potential after wavefield decomposition just below the bottom is displayed in the middle, and the predicted multiples for the upgoing P-waves are displayed on the right. A strong primary reflection can be seen at about 1.2 s zero-offset, from which at least two peg-leg multiples can be identified. After decomposition the multiples arising from this strong primary are already strongly attenuated, but the source-side peg-leg multiple can still be seen. This peg-leg multiple is also predicted in the right gather. In Figure 5.11 the predicted multiples have been subtracted from the decomposed upgoing P-wave gather. In the first gather the data is displayed after decomposition only, the middle gather displays the decomposed data after additional multiple elimination. The gather on the right contains the predicted multiples. The peg-leg multiple at about 1.35 s zero-offset has been removed. The arrow at 0.55 s zero-offset points at another multiple that has been removed by the multiple elimination process.

In Figure 5.12 the multiple elimination results at receiver location 1175 are displayed, where a strong reflection from the salt layer is present. The strong peg-leg multiple from this reflection is removed. The same multiple prediction operator can be used on the S-waves (Figure 5.13, where again the prediction and removal of the peg-leg multiple of the salt reflection can be clearly observed).

In Figure 5.14, the poststack time migrated sections for the upgoing P-wavefield before and after surface multiple elimination are displayed. The first stack displays the the upgoing P-wave potential without surface related multiple elimination. Compared with the second stack on the right, where additional multiple elimination has been applied, it can be seen that some remaining multiple energy has been attenuated. However, the removal of multiples is less evident in the stacked sections than in the common-receiver gathers.

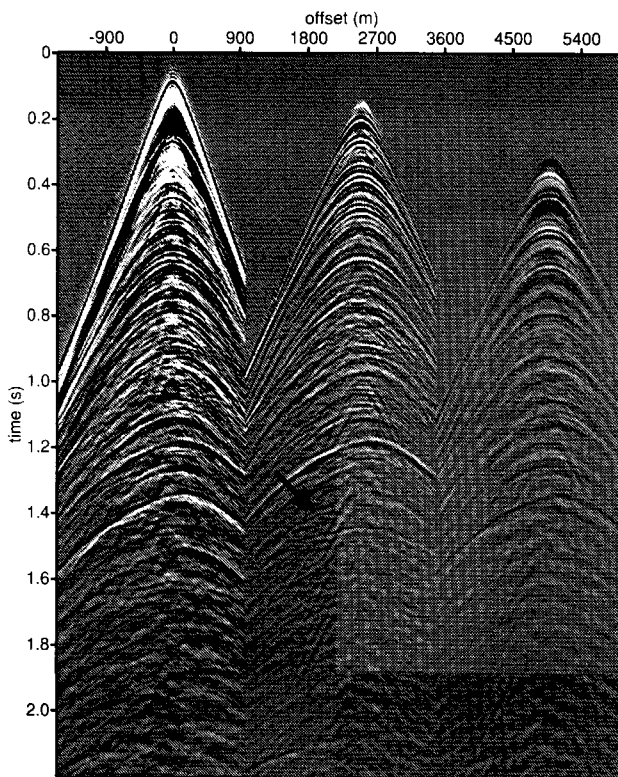


Fig. 5.10 Multiple prediction on one common-receiver gather at receiver location 1323. The first gather is the pressure component after deconvolution, the second gather is the upgoing P-wave potential just below the ocean-bottom obtained after elastic decomposition, and the third gather contains the predicted multiples for the decomposed P-wave gather. The arrow points at a remaining source-side pegleg multiple in the decomposition result.

5.4 Conclusions

To remove remaining surface-related multiples from the OBC data after decomposition, the acoustic decomposition result of stage 2 (i.e. the upgoing pressure wavefield just above the ocean-bottom) is used as the multiple prediction operator (after extrapolation to the sea surface). The same prediction operator can be used on all wave-types. After verification of the OBC surface-related multiple removal on the synthetic data introduced in Chapter 2, the method was applied to the de-

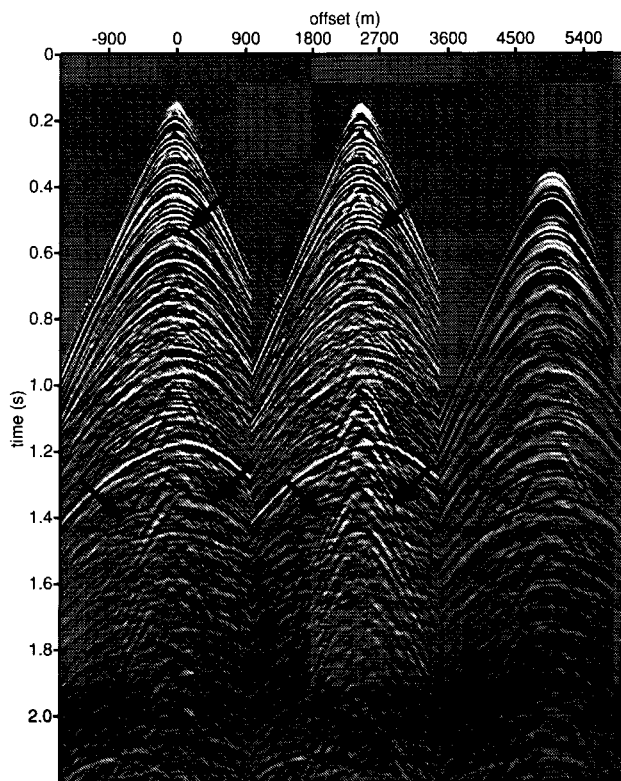


Fig. 5.11 Multiple removal result on the common-receiver gather at location 1323. The first gather is the upgoing P-wave potential just below the ocean-bottom obtained after elastic decomposition, the second gather is the upgoing P-wave potential after additional surface related multiple elimination, and the third gather contains the predicted multiples again, that were subtracted from the first gather. The arrows point at multiple events that were removed.

composed 2-D Mahogany dataset. The surface-related multiple removal procedure correctly predicted the remaining multiples in the decomposed data. The effect of the removal of remaining multiple energy is more evident on the individual receiver gathers than on the poststack time migrated section. Multiple removal in combination with wavefield decomposition can have additional value in the further processing of field data, as source-side pegleg multiples are left in the decomposition result that can have about the same strength as weaker primaries present in the data.

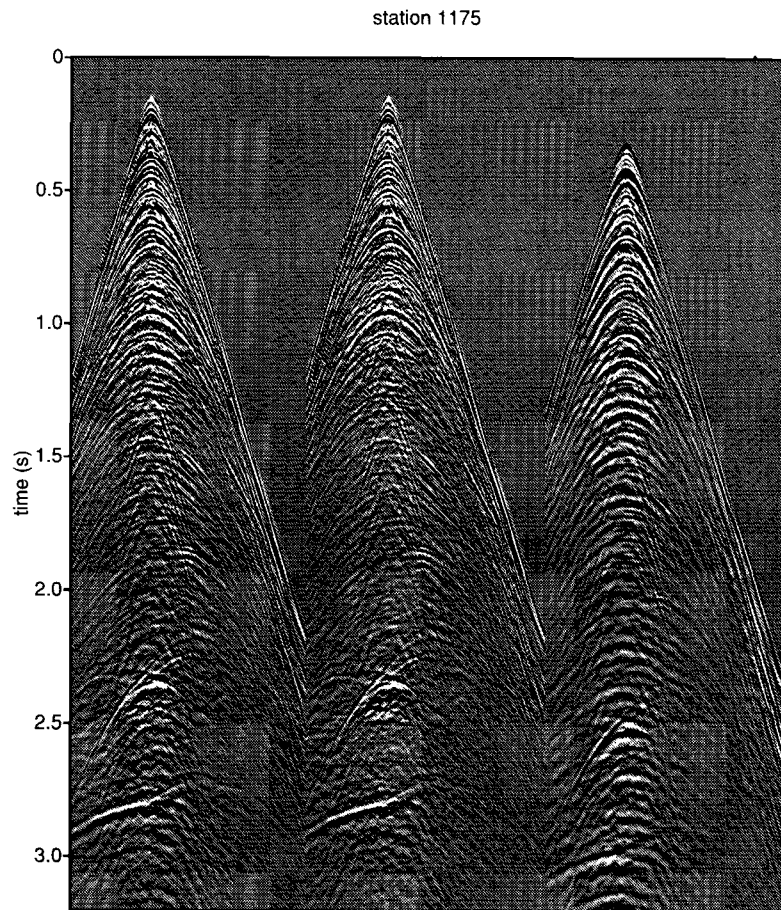


Fig. 5.12 Multiple removal result on the common-receiver gather at location 1175. The first gather is the upgoing P-wave potential just below the ocean-bottom obtained after elastic decomposition, the second gather is the upgoing P-wave potential after additional surface related multiple elimination, and the third gather contains the predicted multiples, that were subtracted from the first gather.

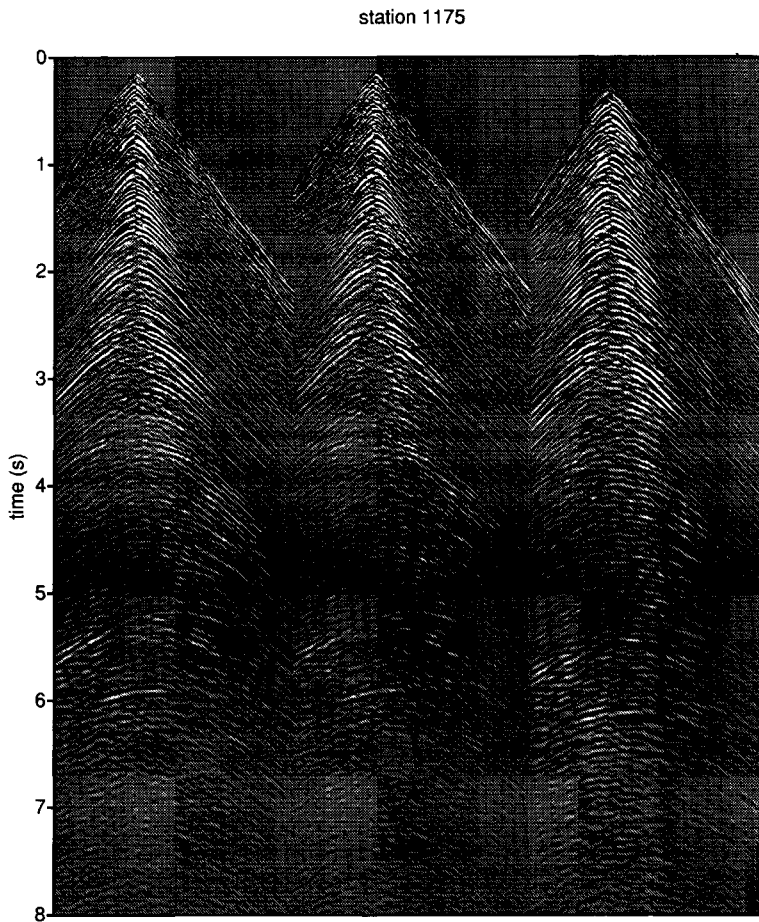


Fig. 5.13 Multiple removal result on the S-waves common-receiver gather at location 1175. The first gather is the upgoing S-wave potential just below the ocean-bottom obtained after elastic decomposition, the second gather is the upgoing S-wave potential after additional surface related multiple elimination, and the third gather contains the predicted multiples, that were subtracted from the first gather.

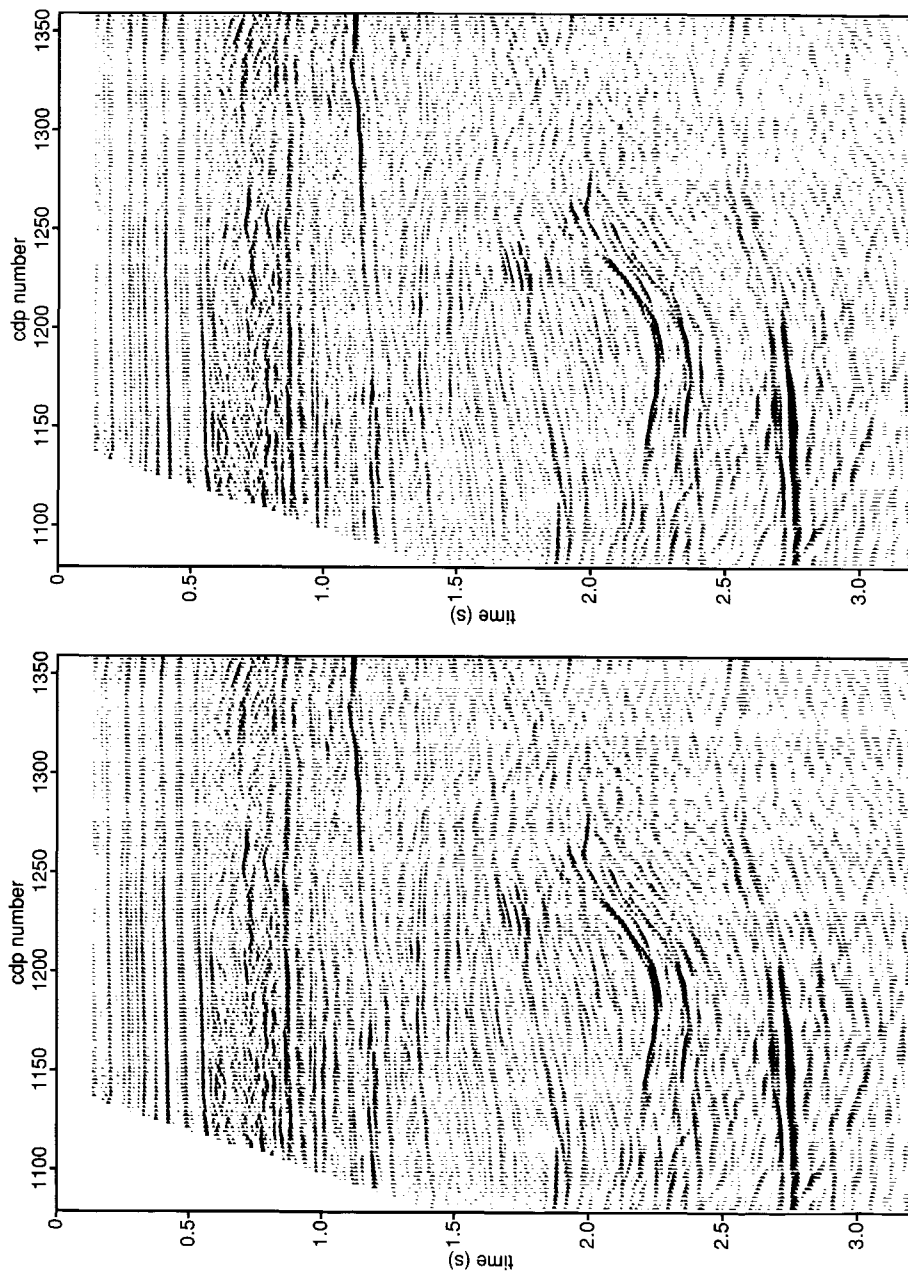


Fig. 5.14 Poststack time migrated sections of the upgoing P-wave potential (obtained after decomposition) and the upgoing P-wave potential after additional surface related multiple elimination.

Chapter 6

Conclusions and discussion

6.1 Conclusions

In this thesis wavefield decomposition has been studied specifically in the application to ocean-bottom seismic data. For this special case, wavefield decomposition reduces to a decomposition at the receiver side. For a decomposition at the ocean-bottom it is our task to separate the measured wavefields just above the bottom (i.e. in the water layer), and just below the bottom (a decomposition exactly at the bottom is undefined). To calculate the appropriate decomposition operators, the water parameters or the medium parameters just below the bottom need to be known. A review has been given of the decomposition theory, adapted for the case of multicomponent ocean-bottom data (Chapter 2). The process separates the P- and S-waves from each other, as well as the down- and upgoing wavefields (thus removing most surface-related multiples from the upgoing wavefield). In practice the decomposition equations are difficult to apply to field data, because of unknown medium parameters, coupling effects, etc.

To facilitate the application, the decomposition equations have been rewritten in a simpler form, leading to a scheme that requires less data components at a time. This result has been obtained by splitting the down- and upgoing wavefield decomposition and the P- and S-wave decomposition into two separate steps (Chapter 2).

Based on this two-step approach, a 5-stage adaptive decomposition scheme for 2-D data (see section 2.7) has been proposed, consisting of three intermediate decomposition results before obtaining the final result: down- and upgoing P- and S-waves (Chapter 2). Each intermediate result allows for the estimation of some unknown parameters. In addition the quality of these results can be checked, and if necessary, improved. The scheme allows for some imperfections of the measurements (imperfect coupling of the geophones, energy leaking between the geophone components)

and for unknown medium parameters just below the ocean-bottom. In stage 1 the vertical velocity component is corrected for energy leaking between the horizontal velocity components and the vertical component. Stage 2 then estimates a (relative) coupling filter for the vertical velocity component by means of an acoustic decomposition just above the ocean-bottom. Stage 3, an elastic decomposition into down- and upgoing normal stressfields just below the ocean-bottom, allows for the estimation of the medium parameters just below the receivers. Stage 4 estimates a (relative) coupling filter for the horizontal inline velocity component by means of an elastic decomposition just below the ocean-bottom into down- and upgoing shear stressfields. And finally, in stage 5 the down- and upgoing P- and S-waves are obtained by combining the down- and upgoing stressfields and using the estimates of the medium parameters just below the receivers.

For the case where the adaptive decomposition scheme would not perform very well, i.e. a thin sub-bottom layer, the analytic expressions of a combined extrapolation and decomposition operation have been derived (Chapter 2). On modeled synthetic data for a thin layer, a better decomposition result was obtained when using the appropriate decomposition operators. The combined extrapolation/decomposition operators have not been tested on field data.

Application of the wavefield decomposition equations could be successfully demonstrated on three field OBC datasets of different water depths (Chapters 3 and 4): Vøring (~ 1200 m), Snorre (~ 300 m) and Mahogany (~ 120 m). First the decomposition result was evaluated on one common-receiver gather. This also gives an initial estimate of the windows for the adaptive decomposition procedure to be used for an entire line of ocean-bottom data. The medium parameters just below the ocean-bottom were estimated by inversion of the optimization filter obtained in stage 3 of the adaptive decomposition scheme (in a frequency-independent way). Depending on the quality of the optimization filters, an inversion was performed at each receiver location (Mahogany), or a fixed average estimate was used for all receivers (Snorre). Although the decomposition theory requires application to common-shot gathers, it is in practice often only possible to use common-receiver gathers (due to statics, coupling, aperture). Strictly speaking it is only correct to substitute common-shot gathers by common-receiver gathers when the medium is laterally invariant. Experiences with field data show that it is still allowed to do so with mild lateral medium variations present.

The experience with various datasets has led to insight into the issues of decomposition theory when applied to field data. More specifically, window determination for the adaptive decomposition procedure was easier for the Snorre and Vøring data examples, than for the shallower Mahogany dataset. The decomposition into S-waves for the Vøring dataset did not give a very good removal of the direct arrival, and

the estimated S-velocity is very low (~ 100 m/s). This is not so surprising, considering the acquisition circumstances for Voring, where the geophones sunk into a very unconsolidated mud layer lying on the ocean-bottom. This situation does not correspond very well with the step-like contrasts for which the adaptive decomposition procedure works best. The Snorre and Mahogany datasets show a better direct wave removal for the upgoing S-wave section and also have somewhat higher S-velocity inversion results within the range of 200-500 m/s. Furthermore, it was possible to investigate the decomposition procedure on a full 2D-line (with the shooting parallel to the receiver line) for the Snorre and Mahogany datasets. In practice, this was just a repeated application of the adaptive decomposition procedure to each common-receiver gather. Only the window over the primary event (in stage 2 of the adaptive decomposition scheme) sometimes had to change gradually over the line.

The “cross-coupling” issue of “impure” vertical velocity components was present in both the Voring and Mahogany datasets. The corrections for “cross-coupling” as applied in this study worked adequately for the deeper Voring data but not for the Mahogany dataset. No further study was made towards a more robust method, as it is believed that this acquisition-related issue will eventually be solved by better OBC acquisition methods. The Snorre dataset - acquired with newer acquisition tools - does not show much evidence of cross-coupling. Differences between the measured p and v_z components, that would not be expected in theory, can probably be attributed to the differences in measuring between hydrophones and geophones. The hydrophone is insensitive to direction whereas the geophone should very precisely measure in a specific direction. Small discrepancies with respect to this direction can easily give discrepancies with the theoretical v_z component. However, it was found that a simple rotational correction would not remove the cross-coupling. It is assumed that part of this cross-coupling is attributed to mechanical coupling within the geophone. Therefore, the horizontal velocity components were subtracted from the vertical component using optimization filters, in such a way that the cross-coupling was optimally removed from the vertical component.

Knowing the medium parameters just below the receiver level is necessary for the separation of P- and S-waves. The separation of down- and upgoing wavefields alone can be performed without knowledge of the medium parameters below the bottom. Two possibilities for a parameter estimation from the data itself were investigated. First, estimates of the medium parameters can be obtained by direct inversion of the expression for the decomposition operator, by minimizing an error function. Or, estimates of the medium parameters can be obtained by first estimating an optimal filter and then matching this filter to the expression for the decomposition operator. Both optimization procedures aim to minimize the energy of the direct arrival in the upgoing wavefield just below the bottom. However, the latter method works better for field data. The error function in the first method does not have a well defined

minimum for field data. Direct inversion of the medium parameters was possible on synthetic data but did not work for field data.

In the adaptive decomposition scheme the desired (kinematic) result was obtained by estimating optimal filters. The filters are then inverted to the medium parameters. The accuracy of the inversion procedure on synthetic filters was good when only the pre-critical rayparameter interval was used (the large amplitudes at the critical angle do not influence the result). For field data, the inversion procedure was stabilized by fixing the rayparameter of the critical angle. The P-velocity is well determined by the inversion. A realistic density estimate for field data was not always possible, because the density is interrelated with the coupling factor of the vertical velocity component. The reliability of the density estimate therefore depends on how well the coupling could be estimated (stage 2 of the adaptive decomposition scheme). Conversely, if the density estimates are way off the mark, this is an indication that the coupling determination in stage 2 was not accurate enough. This is demonstrated by the density estimates in the shallower Mahogany example, that are often unrealistic (Chapter 4). An estimate of the S-velocity is difficult to obtain from the filter as it is very sensitive to the signal-to-noise ratio and depends on high(er) angles. Moreover, it is also sensitive to (small) errors in the P-velocity estimate. From inversion of filters from synthetic data, the S-velocity could be retrieved with a good accuracy. With field data the inversion for the S-velocity was often not possible (i.e. giving S-velocity results close to zero). The Mahogany dataset gave the best S-velocity inversion results.

To compare the image quality of the subsurface before and after decomposition (and after additional multiple elimination), conventional stacking methods with normal moveout (NMO) corrections and post-stack time migration were used on the raw data and the decomposed data (Chapters 3, 4 and 5). It must be realized, however, that by the stacking procedure in itself, some effects of the wavefield decomposition are concealed, for example angle dependent reflectivity effects. For the stacking of the horizontal component and the decomposed S-waves, asymptotic common conversion point binning was used. In general, comparison of the poststack imaging results after decomposition shows 'cleaner' datasets with a large part of multiple reflection energy, caused by the water layer, removed. The transfer of converted waves from the vertical component data to the S-wave component and from the horizontal component to the P-wave component after decomposition cannot be observed so clearly in the imaged data. It is apparent that at least the S-velocities just below the ocean-bottom, in the data examples that are used here, are low enough to already separate the S-waves on the horizontal component.

According to the processing strategy discussed in Chapter 1 (see Figure 1.2), the processing step following the wavefield decomposition is the surface-related multiple

elimination. It is possible to apply the surface-related multiple elimination procedure (Berkhout, 1982; Verschuur et al., 1992; Berkhout and Verschuur, 1997) after a small adaptation to the ocean-bottom acquisition configuration (Verschuur and Neumann, 1999). In Chapter 5, the surface-related multiple elimination was illustrated on the Mahogany dataset. Only after this step all water related multiples will have been removed from the upgoing P- and S-wavefields. Although the multiple elimination procedure correctly predicted remaining surface-related multiples in the decomposition result, the data did not contain a lot of remaining multiple energy after decomposition. The difference between an image obtained with additional surface-related multiple elimination and an image with decomposition only, was not so evident. In the Mahogany example, multiples of the strong reflections on both sides of the salt structure were not accounted for. To predict these multiples a wider aperture selection of the 2-D dataset is necessary than the aperture selection that was used.

6.2 Discussion and recommendations

Although the adaptive decomposition strategy as described in this thesis could be successfully applied to field data, there are some areas that require further investigations.

Decomposition of 3-D OBC data

In this study, the adaptive decomposition scheme has been applied to 2-D data only (after geometric spreading corrections, see section 2.7). In this situation the y -component of the geophone has not been utilized. In Chapter 2, 3-D decomposition operators have been derived. If these operators are used, the adaptive decomposition scheme would have to be modified as well. The acoustic decomposition above the bottom (stage 2) remains the same. To obtain the upgoing P- and S-waves (stage 5), an extra stressfield τ_{yz} is necessary. Moreover, to estimate these stressfields, more than two data components are needed simultaneously. But from the theoretical point of view an extension to 3-D is feasible.

For the acquisition-related issues concerning 3-D wavefield decomposition, it should be understood that the wavefield decomposition operators are in fact spatial convolution filters. A 3-D implementation of the decomposition consists of a spatial convolution of the 3-D operators with the data in both the x -direction and the y -direction. This implies that a dense receiver coverage in both directions is necessary.

In practice, a dense receiver coverage at the ocean-bottom is not yet feasible. The most common choices used for 3-D OBC acquisition are displayed in Figure 6.1. The

“inline-spread” configuration in Figure 6.1a has the shot lines (dashed lines) parallel to the receiver lines (solid lines). The spacing between receiver lines is typically in the order of 200 meters, the shot line spacing is in the order of 100 meters. The “cross-spread” configuration in Figure 6.1b has the shot lines perpendicular to the receiver lines both with a spacing in the order of 200 meters. The other possibility displayed in Figure 6.1c, is a sparse receiver coverage at the ocean-bottom with a full surface coverage of sources.

For the in-line configuration (Figure 6.1a), two situations can be distinguished. In the first situation, the shot line lies in the same vertical plane as the receiver line. The processing of such a configuration would consist of a repeated 2-D application of the decomposition procedure as was discussed in this thesis, i.e. with the 2-D decomposition operators. With this configuration, the situation can arise where the shot line does not lie in the same vertical plane as the receiver. Using the decomposition procedure as if they still were in the same plane would lead to wrong offsets, and therefore an erroneous projection of 3-D angles on the x, z -plane. For media with not too much lateral variability this could supposedly still be handled but extra research effort is required to make proper corrections for this effect.

In the case of cross-spread acquisition (Figure 6.1b), the shot and receiver lines need to be interpolated to a dense grid first, to get a good coverage. Then the 3-D decomposition operators derived in Chapter 2 could be used.

In the acquisition of Figure 6.1c, a wavefield decomposition with 3-D operators could be done, provided that the lateral variability does not prohibit the use of common-receiver gathers instead of common-shot gathers. In fact, in the discussed field data examples in this thesis this assumption was always made.

Estimation of S-velocity

The estimation of the P-velocity from the estimated optimization filters is easy. The S-velocity estimate is difficult to obtain from the data itself using the filter estimated in stage 3 of the adaptive decomposition scheme, as this filter is not so sensitive to the S-velocity. There are other possibilities for dealing with the S-velocity:

- When interface waves are present, these can provide an independent means of estimating the S-velocity. In none of the three datasets used in this thesis, interface waves (e.g. Scholte waves) were detected (possibly due to preprocessing that was already applied to the data).
- Another possibility is to decompose the data at the measurement stage, i.e. directly measure the P- and S-waves. By using dense receiver configurations with receivers at different depth levels, the horizontal and vertical derivatives

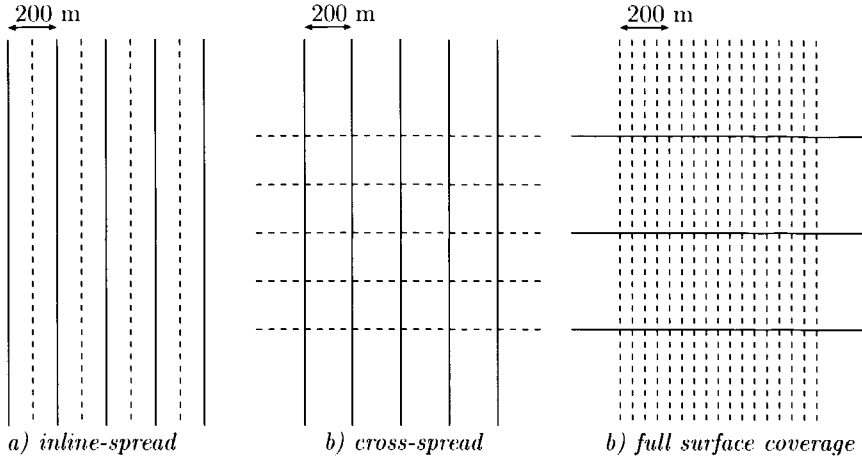


Fig. 6.1 Three different types of 3-D OBC acquisition, with (a) the shot lines (dashed lines) parallel to the receiver lines (solid lines), (b) the shot lines perpendicular to the receiver lines, and (c) a full coverage of sources at the surface.

of the recorded elastic wavefield can be estimated (Robertsson and Muyzert, 1999), and the divergence and curl of the wavefield can therefore be calculated. In this case no medium parameter estimates would be necessary.

- And finally, the S-velocity could be estimated in stage 4 of the adaptive decomposition scheme instead of in stage 3, by using optimal filters again. The elastic decomposition into down- and upgoing normal stressfields just below the bottom (stage 3) is given by

$$-\tilde{T}_{zz}^{\pm} = \frac{1}{2}\tilde{P} \pm A(\omega) \frac{\varrho_1 \beta_1}{2q_{P,1}} \tilde{V}_z. \quad (6.1)$$

The equation is implemented as

$$-2\tilde{T}_{zz}^- = \tilde{P} - \tilde{F}_3(p)A(\omega)\tilde{V}_z, \quad (6.2)$$

where, in theory, $\tilde{F}_3(p)$ is equal to the decomposition operator:

$$\tilde{F}_3(p) = \frac{\varrho_1 \beta_1}{q_{P,1}}. \quad (6.3)$$

The elastic decomposition into down- and upgoing shear stressfields just below the bottom (stage 4) is given by

$$-\tilde{T}_{xz}^{\pm} = \pm \frac{\gamma_1 p}{2q_{S,1}} \tilde{P} \pm B(\omega) \frac{\varrho_1 \beta_1}{2q_{S,1}} \tilde{V}_x. \quad (6.4)$$

Within a window over the direct arrival, equation (6.4) can be written as

$$0 = \pm \tilde{F}_4(p) \tilde{P} \pm \tilde{V}_x, \quad (6.5)$$

where

$$\tilde{F}_4(p) = \frac{\gamma_1 p}{B(\omega) \varrho_1 \beta_1} \quad (6.6)$$

The filter $\tilde{F}_4(p)$ is more sensitive to the S-velocity than $\tilde{F}_3(p)$.

Appendix A

Elastic two-way wavefield extrapolation operator

The two-way elastic extrapolation operator for homogeneous media has been derived in Wapenaar et al. (1987). Here we give the operator coefficients in the rayparameter-frequency domain. With the wave vector $\tilde{\mathbf{Q}}$ defined as

$$\tilde{\mathbf{Q}} = \begin{pmatrix} -\tilde{\tau}_{xz} \\ -\tilde{\tau}_{zz} \\ \tilde{V}_x \\ \tilde{V}_z \end{pmatrix}, \quad (\text{A.1})$$

extrapolation to a different depth level is obtained by applying

$$\tilde{\mathbf{Q}}(z_2) = \tilde{\mathbf{W}}(z_2, z_1)\tilde{\mathbf{Q}}(z_1), \quad (\text{A.2})$$

where $\tilde{\mathbf{W}}$ is a 4 x 4 matrix

$$\tilde{\mathbf{W}}(z_2, z_1) = \begin{pmatrix} W_{11} & W_{12} & W_{13} & W_{14} \\ W_{21} & W_{22} & W_{23} & W_{24} \\ W_{31} & W_{32} & W_{33} & W_{34} \\ W_{41} & W_{42} & W_{43} & W_{44} \end{pmatrix}, \quad (\text{A.3})$$

with

$$W_{11} = 2c_S^2 p^2 \cos(\omega q_P \Delta z) + (1 - 2c_S^2 p^2) \cos(\omega q_S \Delta z) \quad (\text{A.4})$$

$$W_{12} = -2j c_S^2 p q_P \sin(\omega q_P \Delta z) + \frac{jp}{q_S} (1 - 2c_S^2 p^2) \sin(\omega q_S \Delta z) \quad (\text{A.5})$$

$$W_{13} = -4j c_S^4 p^2 \varrho q_P \sin(\omega q_P \Delta z) - \frac{j\varrho}{q_S} (1 - 2c_S^2 p^2)^2 \sin(\omega q_S \Delta z) \quad (\text{A.6})$$

$$W_{14} = 2c_S^2 \varrho p (1 - 2c_S^2 p^2) [\cos(\omega q_P \Delta z) - \cos(\omega q_S \Delta z)] \quad (\text{A.7})$$

$$W_{21} = -\frac{jp}{q_P} (1 - 2c_S^2 p^2) \sin(\omega q_P \Delta z) + 2j c_S^2 p q_S \sin(\omega q_S \Delta z) \quad (\text{A.8})$$

$$W_{22} = (1 - 2c_S^2 p^2) \cos(\omega q_P \Delta z) + 2c_S^2 p^2 \cos(\omega q_S \Delta z) \quad (\text{A.9})$$

$$W_{23} = W_{14} \quad (\text{A.10})$$

$$W_{24} = -\frac{j\varrho (1 - 2c_S^2 p^2)^2}{q_P} \sin(\omega q_P \Delta z) - 4j c_S^4 p^2 \varrho q_S \sin(\omega q_S \Delta z) \quad (\text{A.11})$$

$$W_{31} = -\frac{jp^2}{\varrho q_P} \sin(\omega q_P \Delta z) - \frac{jq_S}{\varrho} \sin(\omega q_S \Delta z) \quad (\text{A.12})$$

$$W_{32} = \frac{p}{\varrho} [\cos(\omega q_P \Delta z) - \cos(\omega q_S \Delta z)] \quad (\text{A.13})$$

$$W_{33} = W_{11} \quad (\text{A.14})$$

$$W_{34} = W_{21} \quad (\text{A.15})$$

$$W_{41} = W_{32} \quad (\text{A.16})$$

$$W_{42} = -\frac{jq_P}{\varrho} \sin(\omega q_P \Delta z) - \frac{jp^2}{\varrho q_S} \sin(\omega q_S \Delta z) \quad (\text{A.17})$$

$$W_{43} = W_{12} \quad (\text{A.18})$$

$$W_{44} = W_{22} \quad (\text{A.19})$$

and

$$\Delta z = z_2 - z_1. \quad (\text{A.20})$$

Bibliography

Aki, K. and Richards, P. G. (1980). *Quantitative Seismology*. Freeman, San Francisco, CA.

Amundsen, L. and Reitan, A. (1995). Decomposition of multicomponent sea-floor data into upgoing and downgoing P- and S-waves. *Geophysics*, **60**(2), 563–572.

Auld, B. A. (1973). *Acoustic fields and waves in solids*. New York Wiley.

Barr, F. J. and Sanders, J. I. (1989). Attenuation of watercolumn reverberations using pressure and velocity detectors in a water-bottom cable. pages 653–656. SEG, Soc. Expl. Geophys., Expanded abstracts.

Berkhout, A. J. (1982). *Seismic Migration: Imaging of Acoustic Energy by Wavefield Extrapolation. A. Theoretical Aspects*. Elsevier Science Publ. Co., Inc. second edition.

Berkhout, A. J. and Verschuur, D. J. (1997). Estimation of multiple scattering by iterative inversion, Part I: Theoretical considerations. *Geophysics*, **62**(5), 1586–1595.

Berkhout, A. J. and Wapenaar, C. P. A. (1990). DELPHI: Delft philosophy on acoustic and elastic inversion. *The Leading Edge*, **9**(2), 30–33.

Brink, M., Granger, P. Y., Manin, M., and Spitz, S. (1996). Seismic methodologies for a 3-components sea-floor geophone experiment on a potential flat spot in the Vøring Basin. In *Eur. Assoc. Expl. Geophys., Abstracts*, page Session:B020.

Camp, W. and McGuire, D. (1997). Mahogany field, a subsalt legend: A tale of technology, timing and tenacity, offshore gulf of mexico. *Houston Geological Society Bulletin*.

Cho, W. H. and Spencer, T. W. (1992). Estimation of polarization and slowness in mixed wavefields. *Geophysics*, **57**(6), 805–814.

Dankbaar, J. W. M. (1985). Separation of P- and S-waves. *Geophysical Prospecting*, **33**, 970–986.

de Hoop, A. T. (1995). *Handbook of radiation and scattering of waves*. Academic press.

de Hoop, M. V. (1992). *Directional decomposition of transient acoustic waves*. Ph.D. thesis, Delft University of Technology, Netherlands.

Donati, M. S. and Stewart, R. R. (1996). P- and S-wave separation at a liquid-solid interface. *Journal of Seismic Exploration*, **5**, 113–127.

Frasier, C. W. (1970). Discrete time solution of plane P-SV waves in a plane layered medium. *Geophysics*, **35**(2), 197–219.

Gaiser, J. E. (1998). Compensating OBC data for variations in geophone coupling. pages 1429–1432, New Orleans. SEG, Soc. Expl. Geophys., Expanded abstracts.

Gras, R., Tushingham, K., and Jamieson, G. A. (1998). Interpretation of the evolution of a salt body in the gulf of mexico. *The Leading Edge*, **17**(10), 1378.

Harrison, M. P. and Stewart, R. R. (1993). Poststack migration of P-SV seismic data. *Geophysics*, **58**, 1127–1135.

Herrmann, P. (1992). *Decomposition of multi-component measurements into P and S waves*. Ph.D. thesis, Delft University of Technology, Netherlands.

Ikelle, L. T. (1998). Deghosting and free-surface multiple attenuation of multi-component OBC data. pages 1234–1237, New Orleans. SEG, Soc. Expl. Geophys., Expanded abstracts.

Ikelle, T. J. (1999). Combining two seismic experiments to attenuate free-surface multiples in OBC data. *Geophysical Prospecting*, **47**(2), 179–193.

Kennett, B. L. N. (1983). *Seismic wave propagation in stratified media*. Cambridge university press.

Li, X.-Y. and Yuan, J. (1999). Geophone orientation and coupling in three-component sea-floor data: a case study. *Geophysical Prospecting*, **47**(6), 995–1013.

Maxwell, P. (1998). personal communication. Input/Output, Inc.

Müller, G. (1985). The reflectivity method: a tutorial. *Journal of Geophysics*, **58**, 153–174.

Osen, A. (1998). *Multiple removal from ocean bottom seismic data*. Ph.D. thesis, NTNU Trondheim, Norway.

Osen, A., Amundsen, L., Reitan, A., and Helgesen, H. K. (1996). Removal of water-layer multiples from multicomponent sea-bottom data. pages 1531–1534, Denver. SEG, Soc. Expl. Geophys., Expanded abstracts.

Richwalski, S. M. (2000). *Multi-component wavefield separation with application to land seismic data*. Ph.D. thesis, Utrecht University, Netherlands.

Robertsson, J. O. A. and Muyzert, E. (1999). Wavefield separation using a volume distribution of three component recordings. *Geophysical Research Letters*, **26**, 2821–2824.

Schalkwijk, K. M., Wapenaar, C. P. A., and Verschuur, D. J. (1999). Application of two-step decomposition to multicomponent ocean-bottom data: theory and case study. *Journal of Seismic Exploration*, **8**, 261–278.

Soellner, W. and Widmaier, M. (2000). Multiple suppression and sub basalt depth imaging of OBS data. pages 2001–2004. SEG, Soc. Expl. Geophys., Expanded abstracts.

Tessmer, G. and Behle, A. (1988). Common reflection point data-stacking technique for converted waves. *Geophysical Prospecting*, **36**, 671–688.

Ursin, B. (1983). Review of elastic and electromagnetic wave propagation in horizontally layered media. *Geophysics*, **48**(8), 1063–1081.

Verschuur, D. J. (1991). *Surface-related multiple elimination, an inversion approach*. Ph.D. thesis, Delft University of Technology, The Netherlands.

Verschuur, D. J. and Neumann, E. I. (1999). Integration of OBS data and surface data for OBS multiple removal. EAGE, Eur. Ass. of Geosc. and Eng., Extended abstracts.

Verschuur, D. J., Berkhou, A. J., and Wapenaar, C. P. A. (1992). Adaptive surface-related multiple elimination. *Geophysics*, **57**(9), 1166–1177.

Vos, J. (2000). *Characterisation of laminated construction materials based on ultrasonic reflection measurements*. Ph.D. thesis, Delft University of Technology, Netherlands.

Wapenaar, C. P. A. and Berkhou, A. J. (1989). *Elastic Wavefield Extrapolation: Redatuming of Single- and Multi-Component Seismic Data*. Elsevier Science Publ. Co., Inc.

Wapenaar, C. P. A. and Haimé, G. C. (1991). Elastic wavefield decomposition: Before or after extrapolation? pages 1001–1004. SEG, Soc. Expl. Geophys., Expanded Abstracts.

Wapenaar, C. P. A., Kinneging, N. A., and J., B. A. (1987). Principle of prestack migration based on the full elastic two-way wave equation. *Geophysics*, **52**(2), 151-173.

Wapenaar, C. P. A., Herrmann, P., Verschuur, D. J., and Berkhout, A. J. (1990). Decomposition of multicomponent seismic data into primary P- and S-wave responses. *Geophys. Prosp.*, **38**(6), 633-662.

Wapenaar, C. P. A., Verschuur, D. J., and Herrmann, P. (1992). Amplitude preprocessing of single and multicomponent seismic data. *Geophysics*, **57**(9), 1178-1188.

White, J. E. (1965). *Seismic waves radiation, transmission and attenuation*. McGraw-Hill, Inc., New York.

Summary

A seismic wavefield that propagates through the Earth's subsurface consists of P-waves (with longitudinal particle motion) and two types of S-waves (with transversal particle motion). To measure the vectorial seismic wavefield, multicomponent geophones are used that record the wavefield in three orthogonal directions. With a wavefield decomposition method, the recorded wavefield can be separated into up- and downgoing wavefields as well as into P- and S-waves at a certain depth level. The wavefield decomposition procedure is basically a spatial convolution of a short filter with the data. To perform a decomposition in this way only the medium parameters at the considered depth level need to be known.

Wavefield decomposition can be used as a first step in the data processing sequence for multicomponent seismic data. Data processing of the separated waves is easier than full vector wavefield processing, and is less sensitive to errors in the macro velocity model of the subsurface.

Earlier attempts of applying wavefield decomposition to multicomponent land seismic data were complicated by the presence of an unconsolidated near-surface layer (the so-called weathered layer), leading to low data quality and geophone coupling problems. Ocean-bottom cable (OBC) data, where the source is at the sea surface and the multicomponent geophones are put at the ocean-bottom, gives access to high quality recordings of the seismic wavefield. However, application of wavefield decomposition to OBC data is not straightforward, as the medium parameters just below the ocean-bottom are unknown and measurement related issues remain, like geophone coupling and cross-talk between the different geophone components.

To apply decomposition to field data an adaptive 5-stage decomposition scheme is developed and optimized for OBC datasets from several different locations with water depths in the order of 1200, 300 and 120 meters. In the adaptive decomposition scheme the P- and S-waves are separated from each other (at the receiver side) as well as the down- and upgoing wavefields. The adaptive decomposition scheme makes use of the condition that no upgoing waves should be present in the downgo-

ing wavefield and vice versa. As an example, the downgoing waves just above the ocean-bottom contain the wave that propagates directly downwards from the source and the waves that reverberate within the water layer. Examples of upgoing waves just below the ocean-bottom are the primary reflections from deeper layers. By identifying such waves in the data and performing an optimization procedure such that the above conditions are fulfilled, any unknown factors (relative coupling, medium parameters) are estimated from the data itself. This adaptive procedure works best for ocean-bottoms with a strong step-like contrast. For a case where the adaptive decomposition scheme would have trouble, i.e. a thin sub-bottom layer, the analytic expressions of a combined extrapolation and decomposition operation are derived and inserted into the adaptive decomposition scheme. A decomposition result below the thin layer can then be obtained. This is demonstrated with synthetic data.

The adaptive decomposition procedure is applied per receiver. The extension of the method to a complete line of OBC data consists of a repeated application of the procedure for a single receiver. The resulting decomposed upgoing P- and S-wavefields are processed, yielding a poststack time migrated image of the subsurface. Comparison with the images obtained from the original (i.e., not decomposed) measurements shows that the decomposition leads to a strong attenuation of multiply reflected events at the sea surface. However, it must be noted that the poststack time section is just a possible way of displaying the decomposition results and as such conceals other effects of wavefield decomposition as for example angle-dependent amplitude effects.

Even though the wavefield decomposition has removed a lot of multiple events reflected downwards at the sea surface from the upgoing P- and S-wavefields, there remain some surface multiples after decomposition. These events can be removed by an adapted version of the surface-related multiple removal procedure, which has been developed for regular streamer data. The extension to OBC data involves an extra wavefield extrapolation from OBC measurements towards the sea surface. The resulting multiple prediction operator data can then be used for removing the multiples in all wave types. In practice considerable remaining surface multiple energy is identified in both the decomposed upgoing P- and S-wavefields. The removal of this energy is more evident on single receiver gathers than on poststack time migrated sections of the subsurface.

After application of the wavefield decomposition and additional multiple removal procedures, the data contain only events that are reflected at interfaces below the ocean-bottom and can thus be further processed to a reliable image of the subsurface.

K. M. Schalkwijk

Samenvatting

Een golfveld dat zich door de aarde voortplant bestaat uit P-golven (met longitudinale deeltjesbewegingen) en twee types S-golven (met transversale deeltjesbewegingen). Dit golfveld kan geregistreerd worden door gebruik te maken van multi-componenten geofoons die in drie orthogonale richtingen meten. Door een decompositie-algoritme toe te passen, kan het gemeten golfveld worden opgesplitst in op- en neergaande P- en S-golfvelden op een bepaalde diepte. Hiervoor is het voldoende de medium-parameters op de beschouwde diepte te kennen. Dit decompositie-algoritme is in essentie een spatiële convolutie van een kort filter met de data.

Golfveld-decompositie kan gebruikt worden als eerste stap in de dataverwerking van multi-componenten seismische data. Het is eenvoudiger om de dataverwerking toe te passen op de afzonderlijke golfvelden. Bovendien is een dergelijke procedure minder gevoelig voor fouten in het macro snelheidssmodel van de ondergrond.

Eerdere pogingen om golfveld-decompositie toe te passen op multi-componenten seismische land-data waren minder succesvol ten gevolge van de aanwezigheid van een niet-geconsolideerde laag direct onder het oppervlak (de zogenaamde verweerde laag). Deze laag zorgde voor een slechte kwaliteit van de data en veroorzaakte problemen met de koppeling tussen de gefoon en de bodem. Acquisitie van seismische data met geofoons op de zeebodem waarbij de seismische bron zich aan het wateroppervlak bevindt, zorgt voor een hoge kwaliteitsopname van het seismische golfveld. Nochthans zijn er ook met deze methode problemen door onbekende medium-parameters net onder de zeebodem, en door de imperfecte gefoonkoppeling en de overspraak tussen de verschillende gefooncomponenten .

Om het decompositie-algoritme toe te passen op gemeten data is een adaptief 5-staps decompositie-schema ontwikkeld en geoptimaliseerd voor zeebodem data op verscheidene locaties met waterdieptes van 1200, 300 en 120 meter. In het adaptieve decompositie-algoritme worden zowel de P- en de S-golven van elkaar gescheiden (bij de ontvanger) alsook het op- en neergaande golfveld. Het adaptieve decompositie-algoritme maakt alleen gebruik van de voorwaarde dat er geen opgaande golven

aanwezig kunnen zijn in het neergaande golfveld en omgekeerd. Voorbeelden van neergaande golven net boven de bodem van de oceaan zijn de directe golf die neerwaarts propageert vanaf de bron en de weerkaatsingen van de directe golf in de waterlaag. Voorbeelden van opgaande golven net onder de bodem van de oceaan zijn de primaire reflecties van de diepere lagen. Door dergelijke golven in de data te identificeren en een optimalisatie-procedure uit te voeren zodanig dat aan de hierboven vermelde voorwaarden voldaan wordt, kunnen alle onbekende factoren (relatieve koppeling, medium parameters) geschat worden uit de data zelf. Deze adaptieve procedure werkt het best voor zeebodems met een stapfunctie contrast. Wanneer de adaptieve procedure geen goede resultaten levert, bijvoorbeeld wanneer een dunne laag net onder de zeebodem aanwezig is, worden de analytische uitdrukkingen van een gecombineerde extrapolatie- en decompositie-operatie afgeleid en ingevoerd in het adaptieve decompositie-algoritme. Hiermee kan een decompositie-resultaat net onder de dunne laag verkregen worden. Dit is aangetoond met synthetische data.

De adaptieve decompositie-procedure is toegepast per ontvanger. De uitbreiding van deze methode naar een volledige lijn van zeebodem data wordt verkregen door de procedure te herhalen voor elke ontvanger. Het verkregen resultaat kan verwerkt worden tot "poststack" tijd-gemigreerde beelden van de ondergrond. De vergelijking van deze beelden met de originele beelden toont aan dat decompositie leidt tot een sterke uitdoving van de meervoudige reflecties aan het wateroppervlak. Merk op dat een poststack tijd-gemigreerd beeld slechts één mogelijke manier is om de decompositie-resultaten voor te stellen; ze kan andere effecten van de golfveld-decompositie verbergen, zoals bijvoorbeeld de hoek-afhankelijke effecten.

Hoewel de golfveld-decompositie reeds veel meervoudige oppervlakte-reflecties verwijdert, blijven er nog een aantal aanwezig. Om deze reflecties te verwijderen, wordt een procedure toegepast, vergelijkbaar met die toegepast wordt bij de verwerking van marine seismische data. De aanpassing van deze procedure op de zeebodem data-acquisitie, houdt een extra extrapolatie in van de zeebodem meting naar het wateroppervlak. De resulterende operator om de oppervlakte-reflecties te voorspellen, kan gebruikt worden om deze reflecties in alle golftypes te verwijderen. In de praktijk is er een sterke hoeveelheid energie ten gevolge van meervoudige reflecties aan het oppervlak waar te nemen in het P- en S-golfveld na decompositie. De verwijdering van deze energie kan duidelijker geobserveerd worden op de metingen van individuele ontvangers dan op de poststack tijd-gemigreerde beelden van de ondergrond.

Na toepassing van de golfveld-decompositie en de verwijdering van overblijvende oppervlakte-reflecties, bevatten de data enkel nog aankomsten van weerkaatsingen aan grensvlakken onder de zeebodem, en kunnen dus verder bewerkt worden tot een betrouwbaar beeld van de ondergrond.

K. M. Schalkwijk

Curriculum vitae

Karin Schalkwijk was born in San Diego, U.S.A., on June 14, 1972. She attended secondary school at the Lorentz Lyceum in Eindhoven, where she received the 'Gymnasium diploma' in 1990. In September of that year she started the study of Geophysics at the Utrecht University and received her M.Sc. degree ('doctorandus') in 1996. Her M.Sc. thesis was on the 'Use of scattered surface waves to detect shallow buried objects' and received the 1996 KNGMG Escher award for best Dutch M.Sc. thesis within the earth sciences. In 1996 she joined the DELPHI consortium at the faculty of applied sciences at Delft University of Technology. From september 1996 to november 2001 she has been doing a Ph.D. research.

